ULTRASONIC PROCESSING OF MAGNESIUM ALLOY MELTS

Ph.D. THESIS

by

BHINGOLE PRAMOD PANDURANG

DEPARTMENT OF METALLURGICAL AND MATERIALS ENGINEERING
INDIAN INSTITUTE OF TECHNOLOGY ROORKEE
ROORKEE- 247 667 (INDIA)
March, 2014

ULTRASONIC PROCESSING OF MAGNESIUM ALLOY MELTS

A THESIS

Submitted in partial fulfilment of the
requirements for the award of the degree
of
DOCTOR OF PHILOSOPHY

in

METALLURGICAL AND MATERIALS ENGINEERING

by

BHINGOLE PRAMOD PANDURANG

DEPARTMENT OF METALLURGICAL AND MATERIALS ENGINEERING
INDIAN INSTITUTE OF TECHNOLOGY ROORKEE
ROORKEE- 247 667 (INDIA)
March, 2014

INDIAN INSTITUTE OF TECHNOLOGY ROORKEE ROORKEE

CANDIDATE'S DECLARATION

I hereby certify that the work which is being presented in the thesis entitled **"ULTRASONIC PROCESSING OF MAGNESIUM ALLOY MELTS"** in partial fulfilment of the requirement for the award of the Degree of Doctor of Philosophy and submitted in the Department of Metallurgical and Materials Engineering of the Indian Institute of Technology Roorkee, Roorkee is an authentic record of my own work carried out during a period from July, 2009 to March, 2014 under the supervision of **Dr. G.P. Chaudhari, Associate Professor**, Department of Metallurgical and Materials Engineering, Indian Institute of Technology Roorkee, Roorkee.

The matter presented in this thesis has not been submitted by me for the award of any other degree of this or any other Institute.

(BHINGOLE PRAMOD PANDURANG)

This is to certify that the above statement made by the candidate is correct to the best of my knowledge.

(G. P. CHAUDHARI)
Superviser

Date:

The Ph. D. Viva-Voce Examination of **Mr. Bhingole Pramod Pandurang**, Research Scholar, has been held on …………………………….

Signature of Supervisor **Chairman SRC** **Signature of External Examiner**

Head of the Department/Chairman, ODC

Abstract

Magnesium alloy developments have traditionally been driven by requirements of aerospace and automobile industries. Interest in Mg based alloys stems from their low density, high strength-to-weight ratio and low inertia which results from its low density. The primary problem in all alloy systems is that dendrites are produced in normal castings because of their large freezing ranges, whereby a constitutionally undercooled region can be readily produced ahead of the growing front. Therefore, suppressing the formation of these coarse dendrites is a key issue in improving the alloy properties.

During solidification of alloys, there are generally two ways to achieve a refined microstructure. One is to break up the growing dendritic structure so that each secondary dendritic arm becomes a grain. Another way is to provide a large quantity of nuclei so that there is no excess room for each grain to grow into a dendrite. Several techniques such as inoculation, electromagnetic vibrations, and mechanical stirring are employed for the modification of grains and the grain size distribution in AZ series magnesium alloys.

Use of physical methods such as mechanical vibrations/ stirring and electromagnetic vibration techniques during solidification are known to result in finer grain size in cast products. A new effective but less practiced method of grain refinement is the ultrasonic treatment (UST). Ultrasonication is environmentally cleaner and one of the simple and effective physical methods used to refine the grain size of alloys during solidification process. Application of high intensity ultrasonic vibrations during solidification produces two effects- ultrasonic streaming of the liquid (increased convection) and ultrasound induced cavitations. These lead to various physical and indirect chemical effects in the liquid. Scientific literature documents the vast capability and potential of high power ultrasonics in materials processing.

Much work has been carried out to study the solidification behavior during ultrasonic treatment, in particular the microstructure refinement and properties of various alloys. However, it mostly concerns with the studies in aluminum alloys. A major problem with Mg-Al alloys is their large and variable grain size with coarse dendritic morphology which results in their poor mechanical properties. Unlike the Zr containing magnesium alloys, Mg-Al alloys are Zr free and no potent inoculants are available in order to obtain uniform and finer grain size.

Therefore, physical method of microstructure modification such as ultrasonication during solidification may prove useful.

Further, Al containing Mg alloy systems suffer from lack of a potent nucleating agent. In this regard, grain refining techniques such as superheating of the melt, ferric chloride inoculation (Elfinal process), and carbon inoculation have been tried with moderate success. Among these methods, carbon inoculation using reagents like C_2Cl_6, CCl_4, and graphite offer many practical advantages because of lower operating temperatures and less fading effects with long holding times, at a lower cost. Carbon black is an easily available and inexpensive form of carbon that has nano size morphology. Present work investigates the inoculation potency of these nano particles in Mg-Al alloy melts. This approach will also help replace the conventionally used toxic waste generating hexachloroethane, C_2Cl_6, grain refiner. When ultrasonic vibrations are coupled to the melts, it is expected to accelerate the wetting, de-agglomeration, and dispersion of inoculant particles and also facilitate degassing of the melts thereby reducing the microporosity.

Similarly, use of ultrasonic vibrations is also being explored in a new solidification processing technique in order to fabricate fine-grained, wear resistant MMCs reinforced with nano and microsized ceramic particles, in order to overcome the drawbacks of stir casting. In view of the potential of in situ synthesis approach and the UST, both these techniques can be coupled for the fabrication of AZ91 alloy matrix composites by the addition of suitable reactant to the melt. Such approach is expected to result in refined micro/nano composites because of the physical and concomitant chemical phenomena induced by UST.

In view of the above, there is a need to study the grain refinement, distribution of intermetallic phases and microstructure modification of magnesium alloys by high intensity ultrasonic vibration and different mechanisms operating under varying ultrasonic processing conditions. In the present work, individual and combined effects of physical (ultrasonic vibrations) and chemical (inoculation) techniques on the microstructural development and mechanical properties in AZ series magnesium alloy melts is studied. Reactively synthesized and ultrasonically processed MMCs are fabricated and their microstructural evolution, mechanical and sliding wear properties is investigated. Formation of hard oxide reinforcement particles by in situ reactions is studied. The microstructure of the composites is characterized for the uniformity in the distribution of reinforcement particles and is correlated with their mechanical properties. By evaluating the dry sliding wear behavior over a range of loads, the operating wear mechanisms are analysed.

The thesis consists of eight chapters. The first chapter consists of introduction to the topic and gives a brief idea about the overview and benefits of magnesium alloys used for different applications. The second chapter gives a comprehensive literature review on the recent developments in the field of magnesium alloys; recent processing techniques available for magnesium alloys, history of ultrasonic processing techniques and different theories related to ultrasonic processing. It also defines objectives of the present work based on literature review, scope of the work and the methodology adopted in the present investigation.

The experimental study carried out in line with the scope of the work is explained in detail in the third chapter. Results obtained are discussed in next three chapters. In the fourth chapter results of various UST parameters on the microstructural evolution and mechanical properties of magnesium alloys is discussed. Application of ultrasonic processing to the molten magnesium alloys are carried out by two different processing approached: first one is continuous cooling during the application of UST and other one is isothermal UST processing followed by cooling.

In the Fifth chapter, synergy of nano carbon black inoculation and high intensity ultrasonic processing in cast magnesium alloys is discussed. Commercial AZ series magnesium alloy containing three, six, and nine weight pct of aluminum (AZ91, AZ61 and AZ31) are investigated for their response to carbon black nano-particle inoculation and high intensity ultrasonic processing. Potency of inoculants is assessed under varying experimental conditions of untreated, carbon black treated and combined carbon black inoculation treatment followed by ultrasonic treatment conditions. Resulting grain refinement is studied and explained based on existing theories of nucleation and ultrasound induced phenomena in molten metal.

In chapter six, AZ91 and AZ31 alloys matrix composites are synthesized by in situ reactive formation of hard MgO and Al2O3 particles by the addition of 1, 5, and 10 wt pct magnesium nitrate ($Mg(NO3)_2$) as a reactant to the molten alloy. Application of ultrasonic vibrations to the melt increased the uniformity of particle distribution, avoided agglomeration, helped to reduce porosity in the castings. In situ chemical reactions were promoted and accelerated because of the ultrasound induced physical phenomena such as cavitation and liquid streaming. Presence of well dispersed, reactively formed, hard oxide and intermetallic particles increased the hardness, ultimate strength, and strain-hardening exponent of the AZ91 and AZ31 alloys matrix composites. Their improved sliding wear resistance is attributed to presence of hard oxide particles and further ultrasonic treatment produced distribution and cavitation enhanced wetting of reactively formed particles in the AZ91 and AZ31 alloys matrix.

The chapters seven and eight contain the conclusions and scope for future work, respectively.

Acknowledgement

First and foremost, I pray the Almighty God for his blessings and record my profound and sincere gratitude towards my worthy supervisor, Dr. G. P. Chaudhari, Associate Professor, Department of Metallurgical and Materials Engineering, Indian Institute of Technology Roorkee for his inspiring guidance, constant encouragement throughout the course of this research work and painstaking correction of the draft manuscript. It was an opportunity of a life time to be associated with him. Words would fail to record the invaluable moral and material support which I was privileged to receive from him on numerous occasions.

I owe my sincere gratitude to the Head, Department of Metallurgical and Materials Engineering, the staff members of his office and the faculty members of the Department of Metallurgical and Materials Engineering for the facilities and the cooperation received whenever needed.

I express my special thanks to Student Research Committee (SRC) members Prof. S. K. Nath, Prof. Anjan Sil, Department of Metallurgical and Materials Engineering and Prof. Manish Mishra, Department of Mechanical Engineering, Indian Institute of Technology Roorkee for giving valuable suggestions and guidance for the right approach of the research problem.

The financial support from Department of Science and Technology (DST), Government of India is gratefully acknowledged. My wishes to record profound gratitude to Dr. V. Pancholi, Dr. S. K. Nath and Mr. S. Kumar for their help, encouragement and support throughout the course of this study.

The author would like to express his sincere thanks to the technical and administrative staff of Department of Metallurgical and Materials Engineering especially to Mr. R. K. Sharma, Mr. Shakti Sharma, Mr. B. D. Sharma, Mr. Rajender Singh Sharma, Mr. Narendra Kumar, Mr. S. M. Giri, Mr. Dharam Pal, Mr. Ashish, Mr. T. M. Sharma, Mr. H. K. Ahuja, Mr. N. S. Rathod, Mr. Mohd Aslam and Mr. Sanjay who have helped during the work. Thanks are also due to Mr. S. D. Sharma, IIC, IITR, Roorkee for providing all necessary help at IIC.

My sincere thanks and indebtedness to colleagues and friends, Dr. Aditya Padap, Dr. Shivananda Nayak, Dr. Amrendra H. J., Dr. S. Pradeep, Mr. Nageshwar Rao, Mr. Mandal, Mr.

Banti Patel, Mr. Neeraj Shrivastava, Mr. Surya Yadao, Mr. Sanjeev Kumar Rajput, Mr. Sunil Rajput, Mr. Brij Kishor, Mr. Rahul Gupta, Mr. Himanshu panjiar and all M. Tech and research scholars (July 2009 to March 2014) of Department of Metallurgical and Materials Engineering, IITR, all of whom have rendered selfless help and support in numerous ways during the course of this study.

Special thanks to Mr. Dinesh Gond, Mr. V. K. Jinager, Mr. V. N. Shukla, Mr. P. S. Patil and Mr. N. Holkar for providing motherly affection to me during my stay in Roorkee.

I wish to record my appreciation for my wife, Poonam and son Prajwal for their painstaking support and motivation for this study.

I thankful from the core of heart to my lovable parents, Shri.Pandurang M. Bhingole and Smt. Prabhavati P. Bhingole, for their blessings to see this day. My thanks are also due to my sisters Mrs. Pratibha, Mrs. Pradnya, Mrs. Prachi and Dr. S. N. Mehtre for their unyielding support and encouragement.

Author also expresses his deep sense of gratitude to all his teachers, specially Dr. Vipin Kumar Tripathi, Professor, Department of Mechanical Engineering and Dr. N. B. Dhokey, Professor, Department of Metallurgy and Material Science, College of Engineering, Pune, for there helpful guidance and encouragement.

I also like to thank everyone who supported me for completing this work successfully and I express my apology that I could not mention everyone individually.

(BHINGOLE PRAMOD PANDURANG)

Contents

Page No.

Certificate i

Abstract iii

Acknowledgements vii

Contents ix

List of Figures xiii

List of Tables xxi

Symbols xxiii

Abbreviations xxv

List of Publications xxvii

Chapter 1

INTRODUCTION 1

Chapter 2

REVIEW OF LITERATURE 7

2.1 Evolution of magnesium alloys for engineering applications 7

2.2 Strengthening mechanisms in magnesium alloys 10

  2.2.1 Strain hardening 11

  2.2.2 Solid solution strengthening 11

  2.2.3 Strengthening by grain size reduction 12

  2.2.4 Dispersion hardening 12

2.3 Grain refinement in magnesium alloys 13

  2.3.1 Grain refinement by post solidification methods 13

  2.3.2 Grain refinement by solidification processing techniques 14

2.4 Dispersion hardening studies 35

2.5 Summary 38

2.6 Present work 40

2.7 Objectives 40

Chapter 3

EXPERIMENTAL PROCEDURE 41

3.1 Procurement of the material 41

- 3.3.1 Magnesium alloys (AZ series) 41
- 3.1.2 Raw material for carbon inoculation 42
- 3.1.3 Magnesium nitrate powder 42

3.2 Experiments 43

- 3.2.1 Experimental set up 43
- 3.2.2 Experimental procedure 43
- 3.2.3 Microstructure studies 47
- 3.2.4 Measurement of mechanical properties 51

Chapter 4

RESULTS AND DISCUSSION: ULTRASONIC PROCESSING OF AZ91 AND AZ31 ALLOYS 59

4.1 Microstructural studies 59

4.2 Ultrasonic processing of AZ91 alloy during continuous cooling 61

4.3 Ultrasonic processing of AZ91 alloy during isothermal holding 66

4.4 Ultrasonic processing of AZ31 alloy during continuous cooling 76

4.5 Ultrasonic processing of AZ31 alloy during isothermal holding 83

4.6 Discussion 91

- 4.6.1 Microstructural evolution 91
- 4.6.2 Mechanical properties 94

4.7 Summary 95

Chapter 5

RESULTS AND DISCUSSION: CARBON INOCULATION WITH ULTRASONIC PROCESSING OF AZ SERIES ALLOYS 93

5.1 Carbon inoculation results 93

5.2 Microstructural evolution 99

5.3 Mechanical behaviour 107

5.4 Summary 112

Chapter 6

RESULT AND DISCUSSION-FABRICATION OF IN SITU MMCs WITH ULTRASONIC PROCESSING 113

6.1 AZ91 alloy based MMCs 113

- 6.1.1 Microstructural evolution 113
- 6.1.2 Mechanical Behaviour 118

6.2 AZ31 alloy based MMCs 123

- 6.2.1 Microstructural evolution 123
- 6.2.2 Mechanical behaviour 124

6.3 Discussion 126

- 6.3.1 Reactive phase formation 126
- 6.3.2 Grain size and morphology 128
- 6.3.3 Distribution of in situ formed oxides 134
- 6.3.4 Mechanical properties 134
- 6.3.5 Dry sliding wear behavior 136

6.4 Summary 140

Chapter 7

CONCLUSIONS 141

Chapter 8

SCOPE OF FUTURE WORK 145

BIBLIOGRAPHY 147

List of Figures

Figure No.	Title	Page No.
2.1	Worldwide production of magnesium for the years (a) 2000, (b) 2005 and (c) 2010 [data extracted from http://www.intlmag.org].	08
2.2	Phase diagram of Mg-Al binary alloy [Friedrich, (2006)].	10
2.3	Acoustic streaming in naphthalene-camphor sytem at 45 kHz and 0.03 MPa mean pressure [Abramov, (1986)].	23
2.4	Cavitation phenomena in the melt [Eskin, (1994)].	24
2.5	Typical oscillograms for the ultrasonic treatment of melts (a) without cavitation, (b) cavitation threshold, (c) developed cavitation [Egon, (1954)].	25
2.6	Generalized effects of ultrasonic vibration on solidification process [Abramov, (1986)].	31
2.7	Schematic of rectified diffusion [Meidani, et al.(2004)].	32
2.8	Rates of removal of hydrogen from Al-Si-Mg alloy (1) chlorine salts processing, (2) UST, (3) vacuum degassing, (4) combined UST and vacuum degassing [Lierke, (1967)].	33
2.9	Dispersion of lead into aluminum, (a) Lead chloride technique, and after exposure to the sonic treatment of (b) low and (c) high intensity [Egon, (1954)].	34
3.1	Phase diagram of Mg-Al binary alloy showing alloy composition used in this work [Friedrich, (2006)].	42
3.2	Schematic of the experimental arrangement employed for ultrasonic treatment of magnesium alloys.	44
3.3	Zirconia coated ultrasonic probe (a) before processing, (b) during processing, and (c) after processing and cleaning.	44
3.4	Leica (DMI 5000M) optical microscope is used for the optical microscopy.	47
3.5	Scanning Electron Microscope actual set up used for characterization of magnesium alloy.	49

3.6	200 kV TEM is used for the analysis of carbon black nano powder.	50
3.7	Actual setup of X-ray diffraction (XRD) used for the analysis.	51
3.8	Vickers hardness tester set up used for the measuring hardness.	52
3.9	Tensile test specimens fabricated from differently cast magnesium alloys.	53
3.10	H25 K-S Tinius Olsen tensile testing machine used for the tensile test.	53
3.11	Gleeble®3800 machine used for compression testing experiments.	54
3.12	Schematic diagram of pin on disc un-lubricated wear testing machine is used in study.	55
3.13	Wear and friction (pin-on disc) machine used for conducing wear experiments.	56
3.14	Electronic balance (Mettler AJ100) having accuracy of 0.0001 g used for weighing.	56
4.1	Optical micrograph of the unprocessed cast AZ91 alloy.	59
4.2	SEM micrograph and EDS patterns corresponding to the (a) α-Mg phase, and (b) β-$Mg_{17}Al_{12}$ phase of the AZ91 alloy.	60
4.3	(a) SEM micrograph, and (b) X-ray elemental mapping of unprocessed AZ91 alloy.	61
4.4	Optical micrographs of AZ91 alloy that was subjected to UST during continuous cooling using constant ultrasonic intensity of 1.3 $kW.cm^{-2}$. UST processing time is (a) 30 s, (b) 60 s, and (c) 90 s.	63
4.5	Optical micrographs of AZ91 alloy that was subjected to UST during continuous cooling using constant ultrasonic intensity of 2.7 $kW.cm^{-2}$ and UST processing time of (a) 30 s, (b) 60 s, and (c) 90 s. Figures (d), (e) and (f) show the optical micrographs of AZ91 specimens processed using ultrasonic intensity of 4.3 $kW.cm^{-2}$ for 30, 60, and 90 s , respectively.	64
4.6	Variation in grain size of AZ91 alloy with UST processing time plotted for different ultrasonic intensities applied during continuous cooling.	65

4.7 Variation in Vickers hardness of AZ91 alloy with the UST processing time plotted for different ultrasonic intensities applied during continuous cooling. 65

4.8 The true stress-true strain tensile test curves for AZ91 alloy ultrasonically treated during continuous cooling using different ultrasonic intensity of (A) 1.3 kW.cm^{-2}, (B) 2.7 kW.cm^{-2}, and (C) 4.3 kW.cm^{-2}, for various processing duration. 67

4.9 Optical micrographs of AZ91 alloy that was subjected to UST during isothermal holding at 598 °C using constant ultrasonic intensity of 1.3 kW.cm^{-2}. UST processing time is (a) 30 s, (b) 60 s, and (c) 90 s. 69

4.10 Optical micrographs of AZ91 alloy that was subjected to UST during isothermal holding at 598 °C using constant ultrasonic intensity of 2.7 kW.cm^{-2}. UST processing time is (a) 30 s, (b) 60 s, and (c) 90 s. Figures (d), (e) and (f) show the optical micrographs of AZ91 specimens processed using ultrasonic intensity of 4.3 kW.cm^{-2} for 30, 60, and 90 s, respectively. 70

4.11 Variation in grain size of AZ91 alloy with UST processing time plotted for different ultrasonic intensities applied during isothermal treatment. 72

4.12 Variation in Vickers hardness of AZ91 alloy with the UST processing time plotted for different ultrasonic intensities applied during isothermal holding at 598 °C. 72

4.13 True stress-true strain tensile test curves for AZ91 alloy ultrasonically treated during isothermal holding using different ultrasonic intensity of (A) 1.3 kW.cm^{-2}, (B) 2.7 kW.cm^{-2}, and (C) 4.3 kW.cm^{-2}, for various processing durations. 73

4.14 Optical micrograph of the unprocessed cast AZ31 alloy. 76

4.15 (a) SEM micrograph and (b) X-ray elemental mapping of unprocessed AZ31 alloy. 77

4.16 Optical micrographs of AZ31 alloy that was subjected to UST during continuous cooling using constant ultrasonic intensity of 1.3 kW.cm^{-2}. UST processing time is (a) 30 s, (b) 60 s, and (c) 90 s. 79

4.17 Optical micrographs of AZ31 alloy that was subjected to UST during continuous cooling using constant ultrasonic intensity of 2.7 kW.cm^{-2} and UST processing time of (a) 30 s, (b) 60 s, and (c) 90 s. Figures (d), (e) and (f) show the optical micrographs of AZ31 specimens processed using ultrasonic intensity of 4.3 kW.cm^{-2} for 30, 60, and 90 s, respectively. 80

4.18 Variation in grain size of AZ31 alloy with UST processing time plotted for different ultrasonic intensities applied during continuous cooling. 81

4.19 Variation in Vickers hardness of AZ31 alloy with the UST processing time plotted for different ultrasonic intensities applied during continuous cooling. 81

4.20 The true stress-true strain tensile test curves for AZ31 alloy ultrasonically treated during continuous cooling using different ultrasonic intensity of (A) 1.3 kW.cm^{-2}, (B) 2.7 kW.cm^{-2}, and (C) 4.3 kW.cm^{-2}, for various processing duration. 82

4.21 Optical micrographs of AZ31 alloy that was subjected to UST during isothermal holding at 627 °C using constant ultrasonic intensity of 1.3 kW.cm^{-2}. UST processing time is (a) 30 s, (b) 60 s, and (c) 90 s. 84

4.22 Optical micrographs of AZ31 alloy that was subjected to UST during isothermal holding at 627 °C using constant ultrasonic intensity of 2.7 kW.cm^{-2}. UST processing time is (a) 30 s, (b) 60 s, and (c) 90 s. Figures (d), (e) and (f) show the optical micrographs of AZ31 specimens processed using ultrasonic intensity of 4.3 kW.cm^{-2} for 30, 60, and 90 s, respectively. 85

4.23 Variation in grain size of AZ31 alloy with processing time plotted for different ultrasonic intensities applied during isothermal UST treatment. 86

4.24 Variation in Vickers hardness of AZ31 alloy with the UST processing time plotted for different ultrasonic intensities applied during isothermal holding at 627 °C. 87

4.25 The true stress-true strain tensile test curves for AZ31 alloy ultrasonically treated during isothermal holding using different ultrasonic intensity of (A) 1.3 kW.cm^{-2}, (B) 2.7 kW.cm^{-2}, and (C) 4.3 kW.cm^{-2}, for various processing durations. 88

5.1 (a) TEM bright field micrograph, and (b) corresponding selected area diffraction pattern of carbon black powder used in the present work. 98
5.2 Optical micrographs of magnesium alloys under various processing conditions- unprocessed (a) AZ91, (b) AZ61, (c) AZ31, carbon inoculated (d) AZ91 (e) AZ61 (f) AZ31, and combined carbon inoculated + ultrasonic treated (g) AZ91 (h) AZ61 (i) AZ31 alloys. 101
5.3 XRD patterns for AZ31, AZ61, and AZ91 alloys processed under various conditions of inoculation and ultrasonication of the melts. 102
5.4 Grain size d vs. 1/Q for the three Mg–Al alloys. 106
5.5 Room temperature tensile behaviour of the unprocessed, carbon black inoculated, and carbon black inoculation followed by ultrasonic treatment, specimens of (a) AZ91, (b) AZ61, and (c) AZ31 alloys. 109
5.6 Variation of Vickers hardness of the unprocessed, carbon black inoculated, and carbon black inoculation followed by ultrasonically treated, specimens of AZ31, AZ61, and AZ91 alloys. 110
5.7 0.2 % proof stress as a function of d$^{-1/2}$ for the AZ31, AZ61, and AZ91 alloys. 111

6.1 Optical micrographs of AZ91 magnesium alloys in as cast condition. 114
6.2 Optical micrographs of AZ91 alloy based MMCs obtained from various processing conditions- (a) AZ91-1, (b) AZ91-5, (c) AZ91-10, (d) AZ91-1-UST, (e) AZ91-5-UST, and (f) AZ91-10-UST cast MMCs. 116

6.3 SEM micrographs of AZ91 alloy based MMCs obtained from various processing conditions- (a) AZ91-10, (b) AZ91-10-UST, and (c) AZ91-10 and (d) AZ91-10-UST, at higher magnifications. 117

6.4 XRD patterns for AZ91 MMCs processed under various conditions. 118

6.5 Variation of hardness of the ultrasonically unprocessed and processed AZ91 MMCs with wt pct of magnesium nitrate added. 119

6.6 Room temperature compressive true stress- true strain curves of variously processed AZ91 MMCs, formed from addition of different wt pct of magnesium nitrate. 119

6.7 Variation of strain hardening exponent with the wt pct of magnesium nitrate added. 120

6.8 Variation of wear volume (mm^3) with sliding distance for different normal loads in (a) AZ91, and (b) AZ91-10-UST specimens. 121

6.9 Variation of volumetric wear rate with varying normal load for (a) UST unprocessed, and (b) UST processed cast AZ91 alloy and various in situ MMCs, tested at a constant sliding speed of 1 ms^{-1}. 122

6.10 Optical micrograph of AZ31 magnesium alloy in as cast condition. 124

6.11 Optical micrographs of AZ31 alloy based MMCs obtained from various processing conditions- (a) AZ31-1, (b) AZ31-5, (c) AZ31-10, (d) AZ31-1-UST, (e) AZ31-5-UST, and (f) AZ31-10-UST cast MMCs. 127

6.12 FESEM micrographs of AZ31 alloy based MMCs obtained from various processing conditions- (a) AZ31-10, (b) AZ31-10-UST, and (c) AZ31-10 and (d) AZ31-10-UST, at higher magnifications. 128

6.13 XRD patterns for AZ31 MMCs processed under various conditions. 129

6.14 Variation of hardness of the ultrasonically unprocessed and processed AZ31 MMCs with wt pct of magnesium nitrate added. 130

6.15 Room temperature compressive true stress- true strain curves of variously processed AZ31 MMCs, formed from addition of different wt pct of magnesium nitrate. 130

6.16 Variation of strain hardening exponent with the wt pct of magnesium nitrate added. 131

6.17 Variation of wear volume (mm^3) with sliding distance for different normal loads in (a) AZ31, and (b) AZ31-10-UST specimens. 132

6.18 Variation of volumetric wear rate with varying normal load for (a) UST unprocessed, and (b) UST processed cast AZ91 alloy and various in situ MMCs, tested at a constant sliding speed of 1 ms^{-1}. 133

6.19 FESEM images of worn surfaces of (a) AZ91, (b) AZ91-10-UST for specimens tested under 14.7 N normal load, with sliding distance of 2000 m and sliding speed of $m.s^{-1}$ (c) shows the wear debris from AZ91-10-UST specimen, and (d) shows its EDS analysis. 138

6.20 FESEM images of worn surfaces of (a) AZ31, (b) AZ31-10-UST for specimens tested under 14.7 N normal load, with sliding distance of 2000 m and sliding speed of 1 $m.s^{-1}$ (c) shows the wear debris from AZ31-10-UST specimen, and (d) shows its EDS analysis. 139

List of Tables

Table No.	Title	Page No.
2.1	Summary of observed effects of inoculation treatment on various Mg alloys.	16
2.2	Summary of observed effects of ultrasonic treatment of molten materials.	19
2.3	Crystal geometry and ultrasound intensity necessary for crystal dispersion [Nastac, (2004)].	30
2.4	Comparison of efficiencies of degassing techniques used in industry for Al-Si-Mg alloy [Eskin, (1994), Lierke, (1967), Hiedemann, (1954), Junwen, et al. (2008)].	32
2.5	Dispersion and reaction kinetics observed in the different alloys by the application of UST.	34
2.6	Summary of observed effects of different reinforcements on the magnesium alloys.	37
3.1	Nominal composition of AZ31, AZ61, and AZ91 magnesium alloys [Busk, (1987)].	41
3.2	List of pin-on-disc test parameters selected for the experiments.	57
4.1	Results of EDS analysis depicting weight pct and atomic pct of elements present at different locations of Fig. 4.2 and the estimated phases.	60
4.2	Summary of the grain size and mechanical properties of AZ91 alloy UST processed using different process parameters.	75
4.3	Summary of the grain size and mechanical properties of AZ31 alloy UST processed using different process parameters.	89
5.1	Average grain size (in µm) of different Mg alloys under various processing conditions.	101
5.2	Comparison of average grain size after carbon inoculation of Mg-Al alloys from different studies.	103

5.3 Summary of tensile properties of AZ91, AZ61, and AZ31 alloys processed under different conditions. 109
5.4 Hall-Petch parameters for 0.2 % proof stress. 111
5.5 0.2 % proof stress as a function of $d^{-1/2}$ for the AZ31, AZ61, and AZ91 alloys. 102
6.1 Material designations used in the present work with AZ91 alloy and AZ31 alloy matrix composites. 114

Symbols

σ_0	Yield strength
k	Constant
σ_i	Friction stress
d	Average grain diameter
p_{max}	Pressure maximum
P_{min}	Pressure minimum
p_0	Atmospheric pressure
ρ	Density of the melt
c	Wave velocity of the melt
I	Energy of wave in the melt
P_C^v	Sound pressure
P_0	Initial air pressure
P_V	Saturation vapor pressure
R_0	Initial radius
σ_L	Liquid- vapor surface tension
ΔH	Latent heat of freezing
P	Pressure
T_m	Freezing point
V_S	Specific volumes of solid
V_L	Specific volumes of liquid
P_d	Pressure required for the fragmentation of crystals
σ_{mp}	Strength of the material near the melting point
l	Length of the crystal
r	Radius of the crystal
V	Wear volume
S	Sliding distance
W	Normal load
H	Hardness of the softer of the two materials
K	Wear coefficient

Abbreviations

ARB	Accumulative roll bonding
ASTM	American Society for Testing and Materials
CET	Columnar to equiaxed transformation
ECAE	Equal channel angular extrusion
EDS	Energy dispersive X-ray spectroscopy
FE-SEM	Field emission scanning electron microscopy
FSP	Friction stir processing
HPT	High pressure torsion
MMCs	Metal matrix composites
pct	Percentage
SEM	Scanning electron microscope
SPD	Severe plastic deformation
TEM	Transmission electron microscopy
UST	Ultrasonic treatment
UTS	Ultimate tensile strength
VHN	Vickers hardness number
wt pct	Weight percentage
XRD	X-ray diffraction

List of Publications

Papers in International Journals

1. **Bhingole, P. P**, Chaudhari G. P.,“Synergy of nano carbon black inoculation and high intensity ultrasonic processing in cast magnesium alloys”, Materials Science and Engineering A, vol. 556, pp. 954-961, 2012.
2. **Bhingole, P. P**, Patel Bantibhai, Chaudhari G. P., “Ultrasonic processing and microstructural analysis of AZ91 magnesium alloy”, Materials Science Forum; vol. 702/703, pp. 975-978, 2012.
3. **Bhingole, P. P**, Chaudhari G. P.,“Effect of ultrasonic treatment on the grain refinement and mechanical properties of AZ91 magnesium alloy”, Materials Science Forum, vol. 710, pp. 463-468, 2012.
4. **Bhingole P. P.**, Patel Bantibhai, Chaudhari G. P., “Systematic analysis of ultrasonic processing on microstructural changes in AZ91 magnesium alloy” International Journal of Materials Science and Engineering, vol. 2(1-2), pp. 33-36, 2011.

Papers Presented at International Conferences

1. **Bhingole P. P.**, Chaudhari G. P., “Mechanical and wear properties of ultrasonically processed carbon black inoculated AZ91magnesium alloy” Materials Science & Technology 2012, (MS&T 2012) Conference, 7-11October, 2012, Pittsburgh, USA.
2. **Bhingole, P. P**, Patel Bantibhai, Chaudhari G. P., “Ultrasonic processing and microstructural analysis of AZ91 magnesium alloy” 16th International Conference on Textures of Materials (ICOTOM 16), 12-17 December, 2011, Mumbai, India
3. **Bhingole P. P.**, Chaudhari G.P., “Effect of ultrasonic treatment on the grain refinement and mechanical properties of AZ91 magnesium alloy”, Advances in Metallic Materials and Manufacturing Processes for Strategic Sectors (ICAMPS), 19-21January, 2012, Trivendrum, Kerala.
4. **Bhingole P. P.**, Chaudhari G. P.,“Microstructure evaluation and mechanical properties of ultrasonicated AZ91 magnesium alloy” International Conference on Advances in Materials and Materials Processing (ICAMMP-2011), 9-11 December, 2011.
5. **Bhingole P. P.**, Chaudhari G. P., Srivastava N.,“Systematic analysis of ultrasonic processing on microstructural changes in AZ31 magnesium alloy” International Conference on Challenges and Opportunities Advances in Materials And Processing (AMPCO 2012), 2-4 Nov 2012, IIT, Roorkee.

Chapter 1

INTRODUCTION

Magnesium and its alloys are attractive material for automobile industries, aerospace engineering industries, electrical instruments, computer/laptops industries, household equipment industries, sports industries, mobile phones manufacturers and for architects, designers. This is due to their superior castability, reasonable cost, easy availability, scrap recycling, high strength-to-weight ratio, low inertia, and low density that is about two thirds that of aluminium. Some drawbacks like poor ductility and poor cold workability limit its application. It also finds limited applications at elevated temperatures because of its high oxidation rate, high chemical reactivity, low corrosion resistance and high coefficient of thermal expansion. Yet it is a most attractive problem for researchers to improve its mechanical properties and reduce its drawbacks [Blawert, et al. (2004), Kulekci, et al. (2008), Friedrich, (2006 and 1992)]. The main driving force for use of magnesium alloy in automobile industry is the reduced greenhouse gas emissions from light weighting of the vehicles. In order to maintain this momentum it is necessary to pay attention to all the processing aspects of the alloys and optimize their mechanical properties in order to increase in its use.

An easy and inexpensive way to improve mechanical properties of magnesium alloys is by a reduction in grain size. According to Hall-Petch equation, $\sigma_y=\sigma_0 + k_y d^{-1/2}$ (Where, σ_y is the yield strength, k_y is constant and d is the mean grain size diameter), yield stress of the materials is inversely related to the grain size [Hall, (1951), Petch, (1953)]. Many techniques have been used to achieve grain refinement. Depending on the processing temperatures, these can be classified in to three categories- cryogenic temperature processing, room temperature processing, and solidification processing. Solidification processing can be classified in to three categories-namely rapid quenching, chemically stimulated (particle inoculation) methods, and physical methods. Application of physical methods such as mechanical vibrations/stirring, electromagnetic vibration techniques, and ultrasonic vibrations during solidification have been promising in producing finer grain size in the cast product.

Ultrasonic vibration is a promising and effective physical method to refine grain size of alloys during solidification process. When ultrasonic vibrations are coupled to the solidifying melts, microstructural changes occur including grain refinement, increased homogeneity and reduced segregation. Various mechanisms for grain refinement under ultrasonic vibrations have been proposed. These mechanisms are related to cavitation phenomena induced by high intensity ultrasonic waves. This causes instantaneous temperature and pressure variations in the molten metal. These temperature and pressure variations encourage heterogeneous nucleation and dendrite fragmentation, through acoustic streaming by improving solute diffusion in the molten metal [Jin, et at. (2005)]. The ultrasonic vibrations of solidifying metals and alloys could lead, if applied properly, to structural refinement and improvement in their properties. The main possible effects of ultrasonic vibrations on the characteristics of as cast materials are [Djordjevic, (2003)]:

1. Reduction in grain size and primary and secondary arm spacing;
2. Promotion of columnar to equiaxed transition;
3. Alteration in the size, amount, and distribution of secondary phases;
4. Promotion of uniformity in the distribution of non-metallic inclusions; and
5. Reduction in dendritic segregation and improvement in the material homogeneity.

With ever increasing working environmental concerns, ideal methods are been sought that not only reduce pollution in the manufacturing process but also minimize the harmful effects of the end products. Compared with the traditional modification methods, this method does not pollute the working surroundings and experimented metals. Therefore, high intensity ultrasonic processing is a promising physical refining means to improve solidification structure without causing pollution.

Fine equiaxed microstructures generally exhibit optimum mechanical properties of good strength and adequate ductility along with lower susceptibility to microporosity and cracking. Grain size reduction contributes to strengthening and promotes a uniform distribution of micro constituents such as secondary phases and micro porosities, which translates in to improved chemical homogeneity and enhanced mechanical properties. Among them, the post solidification techniques involve deformation processing and severe plastic deformation techniques. Among the solidification processing techniques, rapid quenching, particle inoculation (chemically assisted), and use of physical means have shown promise. Enhanced heterogeneous nucleation by inoculation can yield fine-grained material more easily and economically because subsequent energy intensive deformation processing can be obviated.

This chemical route is easy to apply; however, there is need to identify suitable alloy specific, effective and potent inoculants. Aluminium free magnesium alloys greatly benefit from zirconium based inoculants and such inoculation is routinely practiced [Polmear, (2006)].

However, aluminium containing magnesium alloy systems suffer from lack of a potent nucleating agent [StJohn, et al. (2005)]. In this regard, grain refining techniques such as superheating of the melt, ferric-chloride inoculation (Elfinal process), and carbon inoculation have been tried with some success [Polmear, (2006), StJohn, et al. (2005)]. Among these methods, carbon inoculation using reagents like C_2Cl_6, CCl_4 and graphite offer many practical advantages because of lower operating temperatures and less fading effects with long holding times, at a lower cost [Du, et al. (2009), Jin, et al. (2009)]. Use of physical methods such as mechanical vibrations/stirring [Reddy, et al. (1985)], electromagnetic vibration techniques [Alireza, et al. (2002), Nguyen, et al. (2005)] and ultrasonic vibrations during solidification is also shown to result in finer grain size in cast products [Nastac, (2004)]. Application of high intensity ultrasonic vibrations during solidification produces two effects-ultrasonic streaming of the liquid (increased convection) and ultrasound induced cavitations. These lead to various physical and indirect chemical effects in the liquid [Suslick, et al. (1999)]. Scientific literature documents the vast capability and potential of high power ultrasonics in materials processing [Fairbanks, (1967), Swallowe, et al. (1989), Eskin, (1997)]. Another problem with Mg–Al alloys is their large and variable grain size possessing coarse dendritic solidification morphology and formation of micro porosity, which results in inhomogeneous and inferior mechanical properties [Polmear, (2006)]. Mg–Al alloys are Zr free and potent inoculants are not available in order to obtain uniform and finer grain size. Therefore, physical method of microstructure modification such as ultrasonication during solidification can prove useful [Patel, et al. (2012)]. In the present work, it is endeavoured to systematically study the individual and combined effects of physical (ultrasonic vibrations) and chemical (inoculation) techniques on the microstructural development and mechanical properties in three commercial AZ series magnesium alloys containing varying amount (3, 6 and 9 wt pct) of Al.

Carbon black is an easily available and inexpensive form of carbon that has nano size morphology. Present work investigates the inoculation potency of these nano particles in Mg-Al alloy melts. This approach will also help replace the conventionally used toxic waste generating hexachloroethane, C_2Cl_6, grain refiner [Polmear, (2006), StJohn, et al. (2005)]. When ultrasonic vibrations are coupled to the melts, it is expected to accelerate the wetting

[Tsunekawa, et al. (2001), Eskin, et al. (2003)], de-agglomeration [Yang, et al. (2004), Lan, et al. (2004)], dispersion of inoculants particles and also facilitate degassing of the melts thereby reducing the micro porosity. Mechanical properties of thus processed alloys are investigated and correlated with their microstructures.

Light metal matrix composites (MMCs) provide alternatives for improving the mechanical properties. Numerous trials are done by addition of various hard ceramic reinforcement particles to magnesium and its alloys. Superior mechanical properties, good thermal stability, increased hardness, and stiffness are reported [Paramsothy, et al. (2012)]. Ex-situ composite synthesis techniques are widely investigated for aluminium alloys by using different kinds of ceramic reinforcements like SiC, Al_2O_3, MgO and B_4C, whose properties such as refractoriness, high hardness, high compressive strength, and wear resistance etc make them suitable for use as reinforcement [Hassan, et al. (2008), Khakbiz, et al. (2009)]. Ex-situ synthesized MMCs exhibit limited improvement in their mechanical properties because of presence of large sized reinforcements and bad interface between the matrix and reinforcements [Zhang, et al.(2010)]. Ex-situ techniques usually require expensive reinforcement materials and involve complex equipments and procedures. Fabrication of MMCs by such techniques is difficult because the micron and especially nano-sized particles have much larger specific surface area. It is challenging to disperse the particles uniformly in alloy melts [Laurent, et al. (1992)]. It is reported that the potentially inexpensive in situ method offers benefits such as homogeneous distribution of the reinforcing particles, a good reinforcement-matrix interface and compatibility, and the in situ formed particles are finer [Dong, et al. (2006)]. Although this method has been extensively studied for aluminium matrix composites, it is relatively less explored for magnesium matrix composites. Hai et al. reviewed recent studies in magnesium matrix composites [Hai, et al. (2004)], and reported about Mg_2Si/Mg, MgO/Mg, TiC/Mg, and (TiB_2–TiB)/Mg composites synthesized from Mg–Si, Mg–B_2O_3, Mg–Ti–C, Mg–KBF_4–K_2TiF_6, and MgO systems, respectively. In order to eliminate the difficulties arising from poor wettability, addition of appropriate alloying elements to the matrix metal [Choh, et al. (1987), Oh, et al. (1989), Aghajanian, et al. (1989)], surface treatment on reinforcements [Rocher, et al. (1989)] and elevation of molten matrix temperature [Oh, et al. (1989)] have been widely studied. Porosity, which degrades the mechanical properties, is formed adjacent to the agglomerate particles in the MMCs when ceramic particles are transferred to the melt by stirring [Rocher, et al. (1989)], which is also caused by poor wettability. Therefore, in order to overcome the problems arising from poor wettability, novel production method for MMC components is desired. In situ reaction fabrication is one of the most economical and versatile approaches [Xiaoming, et al. (2004)].

A novel solidification processing technique involving ultrasonic treatment (UST) assisted casting process has been developed [Laurent, et al. (1992), Xiaoming, et al. (2004), Patel, et al. (2012), Tsunekawa, et al. (2001), Eskin, et al. (2003), Yang, et al. (2004), Lan, et al. (2004)]. It is efficient in dispersing the nano particles in to the melts. Poor wettability of reinforcing particles arising because of the intrinsic properties of the material such as the surface energy of the matrix and the reinforcement [Xiaoming, et al. (2004)], and the oxidation and contamination of particle surface can be overcome by the UST. It is one of the simplest and effective physical methods to homogenise and degas the melt [Patel, et al. (2012)], and to wet, de-agglomerate, and uniformly disperse the reinforcement particles [Tsunekawa, et al. (2001), Eskin, et al. (2003), Yang, et al. (2004), Lan, et al. (2004)].

In view of the aforesaid potential of in situ synthesis approach and the UST, both these techniques are coupled for the fabrication of in situ AZ91 and AZ31 alloys matrix composites by the addition of one, five, and 10-wt pct of magnesium nitrate that is easily available, low cost and easy to operate with. Formation of hard oxide reinforcement particles by in situ reactions is studied. The microstructure of the composites is characterized for the uniformity in the distribution of reinforcement particles and is correlated with their mechanical properties. By evaluating the dry sliding wear behaviour over a range of loads, the operating wear mechanisms are analysed.

Chapter 2

REVIEW OF LITERATURE

2.1 Evolution of magnesium alloys for engineering applications

After its discovery in 1808, it took about 100 years before there was a real demand for magnesium. Magnesium was not used much as a structural material. Most of the time Mg was used in Al alloys manufacturing as an alloying element and in other alloys it was used as a de-oxidation agent. During the Second World War (1939–45), with tremendous demand of metals, magnesium came into focus as structural material uses specially for aircrafts. Almost 40 to 50 years afterwards there has been renewed attention in using magnesium and magnesium based alloys.

There is a consistent increase in demand of magnesium in recent times. During the year, 2000-2010 production of primary magnesium in the world increased by almost 479,000 tons to 809,000 tons. The China Magnesium Association (CMA) reported more than 82 pct production that constituted approximately 654,000 tons of primary magnesium that was produced in 2010. Fig. 2.1 (a) shows pie chart for production of primary magnesium in the world in the year 2010. The U.S.A. produced approximately 45,000 tons of primary magnesium in the same year. Thus, as reported by the International Magnesium Association [http://www.intlmag.org], a total of approximately 809,000 tons of primary magnesium was produced in the whole world. Fig. 2.1 (a-c) shows pie diagrams of production of primary magnesium in the world in the year 2000, 2005, and 2010, respectively. It is seen that in this a decade, production increased rapidly, in year 2000 production of primary magnesium was 479,000 increased to 809,000 in the year 2010. At this time production in the USA decreased, in 2000 it were 74,000 reduce to 45,000 in 2010.

Of all metallic materials used as structural load-bearing materials, magnesium and its alloys are the lightest. Its light weight motivates automobile manufacturers, aerospace, electrical, computer, sports industries, mobile phones, and also for architectural designs in order to replace heavier and dense alloys like steels, cast irons, copper alloys, and Al alloys. Magnesium alloys have always been attractive due to their low density, (typical magnesium alloy has a density of about 1.8 g.cm^{-3} as compared to about 2.7 g.cm^{-3} for a typical aluminum alloy). It has a wide range of potential applications due to its high strength-to-weight ratio together with lower inertia which is advantageous in rapidly moving parts, for example automobile wheels, automobile parts and sports equipment. The main driving force is reduced greenhouse gas emissions from light weighting of the vehicle and efficient scrap recycling. Magnesium and its alloys have superior cast-ability, easy availability, scrap recycling, high strength-to-weight ratio, and low inertia with some disadvantages like poor ductility, poor cold workability, high chemical reactivity, inferior corrosion resistance, and high thermal expansion coefficient [Blawert, et al. (2004), Kulekci et al. (2008), Friedrich, (2006), ASM Handbook, Properties and Selection (1992)].

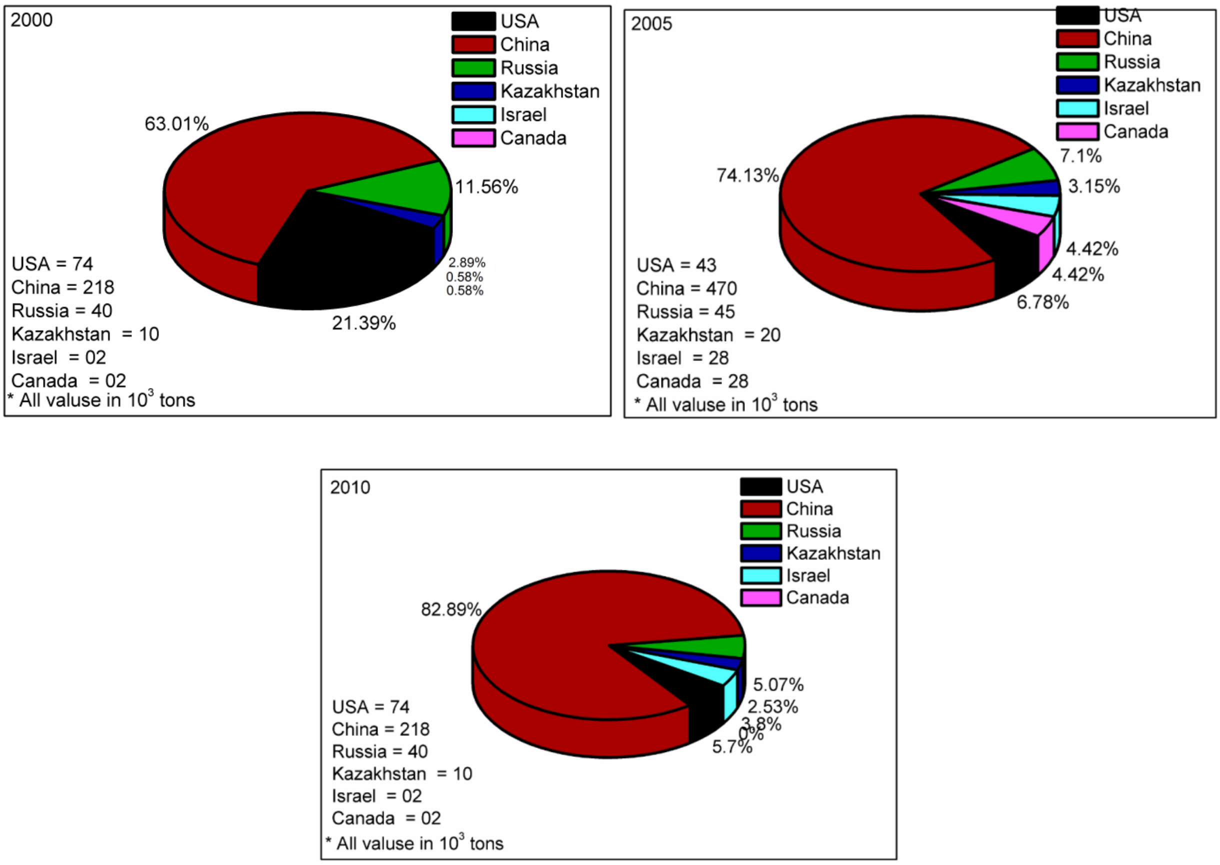

Fig. 2.1 Worldwide production of magnesium for the years (a) 2000, (b) 2005 and (c) 2010 [data extracted from http://www.intlmag.org].

In view of this increasing demand for high specific strength Mg alloys in engineering applications, it the necessary to develop stronger magnesium alloys by various methods such as grain refinement, dispersion strengthening etc. Important engineering alloys of magnesium are discussed below.

AZ series magnesium alloys

For common engineering applications, the mechanical properties of pure magnesium are not sufficient. To improve its mechanical properties, easier way is to alloy with other metals. Solid solution strengthening causes modification in the strength, ductility, elastic properties, and hardness. It is well known that when a harder intermetallic second phase is formed, it hampers the dislocation movement strengthens the alloy [Friedrich, (2006)]. Factors considered for selection of alloying element for magnesium are castability, molten metal reactivity, microstructure control, mechanical properties, corrosion behavior, manufacturability, and physical properties.

In 1909, AZ series alloys that are the Mg-Al-Zn based alloys emerged as a structural material. Aluminum and zinc were the earliest commercial alloying elements in magnesium. Germany extensively used the Mg-A1-Zn castings in the beginning of twentieth century. However, in wet or moist environments these alloys suffered corrosion related problems. Later on, this problem was overcome by a finding that corrosion resistance of Mg-A1-Zn alloys improved from small alloying additions of manganese [Wei, et al. (1990)]. For room temperature applications such as hand tools, computer casings, and portable telephone instruments the AZ series alloys have been the major die-cast Mg alloys. Of all structural applications of magnesium, the AZ and AM series alloys together constitute about 90 pct. However, for use above 150°C these alloys are unsuitable and they lose strength considerably at these temperatures [Emley, et al. (1966)]. In1960, role of Ca additions was discovered and it was [Filippov, (1960)] reported that the additions of calcium to sand cast AZ series alloys enhanced their creep resistance. Later, even in diecast AZ series alloys Ca additions were found to be effective in improving the creep resistance, without adversely affecting their corrosion resistance [Foerster, et al. (1975)].

In AZ series AZ91, AZ61, and AZ31 alloys are most widely used alloys. These alloys contain 9 wt pct, 6 wt pct and 3 wt pct, respectively, of the main alloying element, aluminum. Binary phase diagram of Mg-Al system is shown in Fig. 2.2. Aluminum has a maximum solubility of 11.5 at pct (12.7 mass pct) in magnesium. If it is in excess of six mass percentages, it can be used after heat treatment [Friedrich, (2006)]. Another common alloying element in Mg alloys is zinc. It is used in AZ series as conjunction with Al. For Mg-Al and Mg-Al-Zn series alloys, manganese is used in small amounts to reduce the solubility of iron. Presence of iron causes the increases in the yield strength; however, it also increases saltwater corrosion. Common impurities present in very small amounts are beryllium, copper, iron, nickel, and tin.

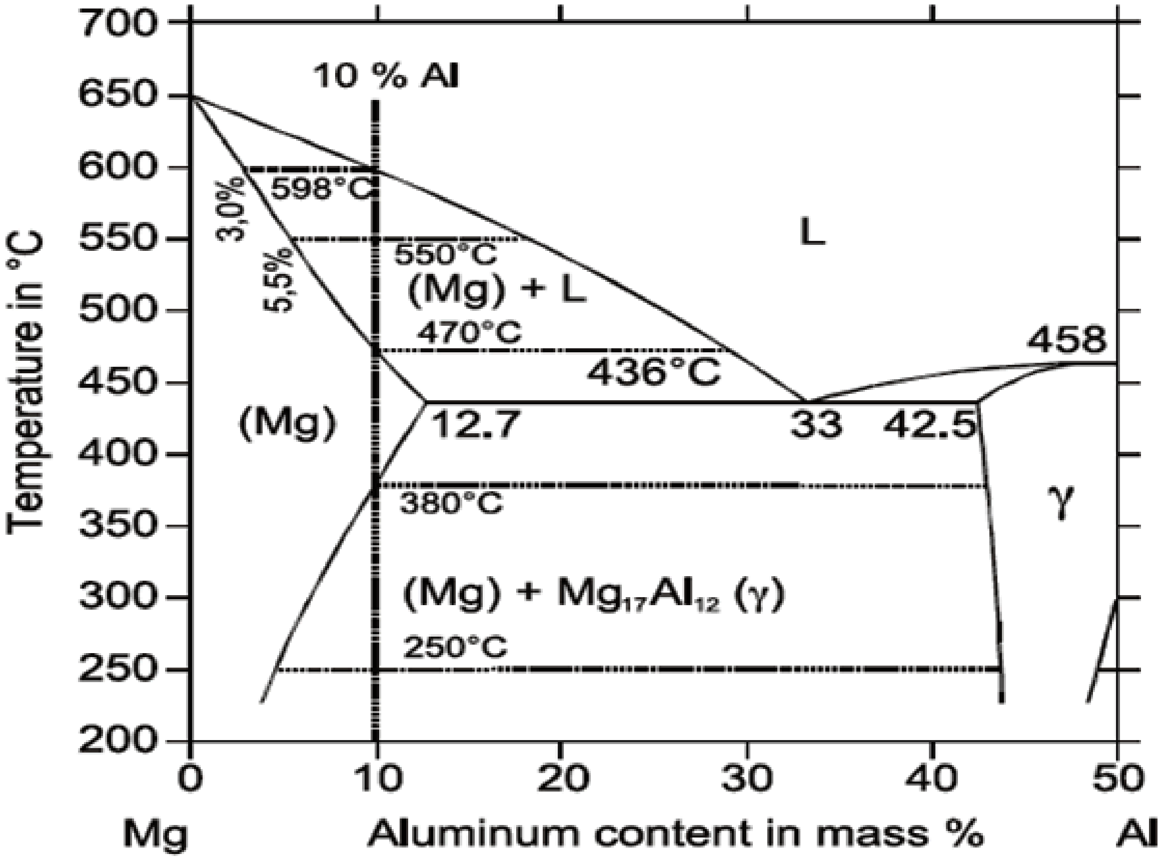

Fig. 2.2 Phase diagram of Mg-Al binary alloy [Friedrich, (2006)].

2.2 Strengthening mechanisms in magnesium alloys

Under applied external stresses, the ability of a metal to deform plastically depends on the freedom for motion of dislocations. It is well known that metals can be strengthened by putting obstructions in the path of moving dislocations. There are many ways to restrict the dislocation movement. These are solid solution strengthening, strain hardening, grain size reduction, and dispersion hardening [Dieter, (1976)]. These mechanisms may be combined together for strengthening of alloys. These are described below briefly.

2.2.1 Strain hardening

Strain hardening by cold working is used to harden metals or alloys that do not respond to heat treatment. Generally, the rate of strain hardening is lower for hcp metals than for the cubic. Increasing the test temperature also lowers the rate of strain hardening. For alloys strengthened by solute additions, the rate of strain hardening may be either increasing or decreasing compared with the behavior of the pure metal. The dislocation density increases with increased cold working strain, which in turn increases the flow stress. Moving dislocations interact with each other and produce obstacles like jogs that restrict the movement of other dislocations. Depending upon the types of interactions that occur between moving dislocations, the dislocations can produce strong or weak obstacles. The final strength of a cold worked solid-solution alloy is usually greater than that of the pure metal cold-worked to the same extent. A higher rate of strain hardening implies increased obstruction of dislocations gliding on intersecting slip systems. Strain hardening theories have been developed based on various dislocation models.

2.2.2 Solid solution strengthening

Interstitial or substitutional solid solutions can form based on Hume-Rothery rules. Upon addition of solute atoms to a solvent matrix by alloying process the solute atoms may occupy either the interstitial position or some of the solvent atom positions in the crystal lattice of the solvent resulting in either interstitial solid solution or substitutional solid solution, respectively. The formation of solutions usually results in increase in strength. The interstitial or substitutional solutes have stress fields associated with them because of the variation in their size and the size of the lattice position that they are occupying. In addition, there are other solute-solvent atom interactions such as modulus interaction, electrical and chemical interactions [Dieter, (1976)]. Dislocations interact with these stress fields to produce strengthening due to short-range dislocation solute interactions and long-range dislocation solute interactions. Dislocations can interact with solute atoms that lie on, above, or below the slip planes. The most intense interactions occur near the dislocation core. The stress fields around solute atoms and the stress fields around dislocations interact with each other. This interaction relies on reducing the overall strain energy associated with dislocations and solute atoms.

2.2.3 Strengthening by grain size reduction

In a polycrystalline material, there is misorientation between the grains where the atomic planes do not match up across the boundary. Grain boundaries impede the motion of dislocations and thereby contribute to strengthening of materials. The amount of strengthening is influenced by the structure of grain boundaries and the degree of misorientation between the grains. Grain boundary strengthening can be described by several models. However, almost all of them reduce to the original Hall-Petch relationship. Lead dislocation at the grain boundary in a dislocation pile up bears the applied shear stress and the back stress from other like dislocations in the pile up. Further, a twin boundary helps to restrict the dislocation motion [Dieter, (1976)]. Well-known Hall-Petch relation describes the relationship between yield strength (σ_o) and grain size (d) as per equation 2.1.

$$\boldsymbol{\sigma_0 = \sigma_i + kd^{-1/2}} \qquad (2.1)$$

Where σ_0 is the yield strength, k is a constant, σ_i is the friction stress and d is the average grain diameter [Hall, (1951), Petch, (1951)]. Grain refinement can be achieved by employing solidification processing techniques or by post-solidification deformation or thermomechanical processing techniques.

2.2.4 Dispersion hardening

The strength of a material can be increased by dispersed fine particles in the matrix material that impede the dislocation motion. The particles can be precipitates that are formed by suitable heat treatments involving solution treatment and aging. They can also be dispersed oxide or carbide particles that are usually not formed by following the equilibrium diagrams. Particle hardening is usually a more potent option to strengthen material as compared to solid solution strengthening. Such dispersoids or precipitates are usually more effective barriers to dislocation motion than are the single solute atoms.

The degree of strengthening is determined by particle size, shape, volume fraction, nature of the particle-matrix interface, and structure of the particle. Particle size and volume fraction determine the inter-particle spacing. A moving dislocation can either cut through the particle if the particle is small and soft or can bypass (bow around) the particles if the particles are large and strong. If stress fields are present around the dispersoids, it is akin to larger effective particle volume. In precipitation hardened materials coherency strains develop, which reduce the dislocation velocity and thus increase strength.

In the view of above mentioned strengthening mechanisms, in the present work strengthening by grain size reduction and dispersion hardening mechanisms have been investigated for magnesium alloys. Therefore, a literature review concerning these two approaches is presented in detail.

2.3 Grain refinement in magnesium alloys

Microstructures consisting of fine equiaxed grains generally exhibit a combination of good strength and good ductility. Further, if an alloy solidifies with fine grained structure it is less susceptible to micro-porosity and cracking. As discussed earlier, a decrease in the grain size contributes to strengthening. It also results in a uniform distribution of secondary phase and micro porosity. This leads to better chemical homogeneity and improved mechanical properties. Thus, grain size reduction is an easy and inexpensive way to enhance the mechanical properties of Mg alloys. Many techniques are used to achieve grain refinement in Mg alloys. These are discussed below.

2.3.1 Grain refinement by post solidification methods

Post solidification grain refinement methods include thermo mechanical treatments and severe plastic deformation (SPD) techniques [Horita, et al. (1996)]. The SPD techniques such as equal channel angular extrusion (ECAE) [Valiev, et al. (1991)] or torsion straining, accumulative roll bonding (ARB), high pressure torsion (HPT) and friction stir processing (FSP) [Feng, et al. (2009), Zhang, et al. (2007)] are carried out. The application of these SPD techniques for the achievement of ultrafine-grained metals and alloys is reviewed by Valiev et al. [Valiev, et al. (2000)]. ECAE process can produce large bulk materials with a sub-microcrystalline structure in a wide range of materials ranging from pure metals, commercial alloys, to metal matrix composites [Langdon, et al. (1998) and Langdon, et al. (2000)]. However, these processes are having following drawbacks. First, these processes require forming machines of large load capacities and expensive dies. Second, only a small volume of material can be produced with less productivity. These processes are not suitable for practical applications when large sized components / materials such as sheet materials are required [Saito, et al. (1999)]. The final product cannot be obtained through these processes; they produce only fine grain structure. For the grain refinement, the extra mechanical work has to be done on the materials. The drawback of this method is that these methods are energy intensive. Therefore, it will be useful to explore the methods of grain refinement during the solidification process that may be cost-effective [Hahato, et al. (2004)].

2.3.2 Grain refinement by solidification processing techniques

In the pre solidification process, grain refinement is carried out on the melts from the start of the solidification processes up to end or in between. Pre solidification processes are divided into three categories depending on different processes used for grain refinement. These are (i) Superheating of melt, (ii) Chemical methods, and (iii) Physical methods.

2.3.2.1 Superheating

In this process, heating of the melts carried out as above the melting temperature at around 850 °C and then it is cooled back to the pouring temperature. This phenomenon is dependent on the composition of the alloy. It has been found that in Mg alloys containing more than 1 wt pct Al, grain refinement can be obtained in this process and it is very effective when worked with a very small amount of impurities like Fe and Mn [Nelson, (1948), Tiner, (1945)]. Zn has a negligible effect on the grain refinement related with superheating process. Superheating process mechanisms are not clear in the literature. According to the Wood [Wood, (1953)], grain refinement from superheating process depends on the solubility of iron in magnesium melt and this process is greatly influenced by temperature employed. Tiner [Tiner, (1945)] observed that as wt pct of Al increases in the magnesium alloy, the liquid solubility of Fe and Mn goes on decreasing and grain refinement is less effective. Nelson, (1948) proposed a different theory to explain the phenomenon of superheating based on the change of the particle size with the variation in the temperature. Particles having size more than critical size in order to act as the inoculants start to dissolve at higher temperature. During cooling to pouring temperature, when it attains a critical size, it acts as nuclei. In this way number of nuclei increases by the superheating. In this way, superheating helps in grain refinement of alloys.

2.3.2.2 Chemical methods

Casting industries routinely practice grain refinement techniques and these determine the microstructure and properties of resulting castings (and ingots). Inoculation of melt is the most common among many different methods [Liu, et al. (2008), Cao, et al. (2005)]. In the theory of inoculation, it is well known that during the solidification process if the number of nucleating sites is increased, increased number of grains form and the ultimate result is grain refinement. Inoculation leads to enhanced heterogeneous nucleation that can readily result in a fine grained material. Further, it is economical because the post solidification intensive thermo-mechanical/ deformation processing is not required. Although the inoculation (chemical) route is easier to practice, identification of an appropriate alloy-specific, and potent inoculants with good anti-fading characteristics is a necessary requirement.

Magnesium alloys that are aluminum free are routinely and effectively inoculated with the Zr based inoculants. However, a potent nucleating agent has not been identified for magnesium alloys that contain aluminum [StJohn, et al. (2005)]. With this in view, less effective grain refining techniques like ferric chloride inoculation (Elfinal process), carbon inoculation, and superheating the melt, have been investigated and implemented with moderate results [StJohn, et al. (2005), Du, et al. (2009)].

i. Elfinal process

In this process, the molten Mg alloys at about 750 °C is treated with ferric chloride ($FeCl_3$) inoculants. It has a lower operating temperature than superheating process. This process is more effective when Mn is present in the melts and Al contained is more than 3 wt pct [Emley, (1966)]. It is also observed that in Elfinal method, formation of Fe-Mn-Al intermetallic compounds is crucial for grain refinement [Polmear, (2006)].

ii. Grain refinement by Zr additions

For grain refinement of Mg-Zn alloys, Zr addition is the most efficient inoculation method [Dahle, et al. (2010)]. The precise mechanism of grain refinement, resulting from Zr additions is still unclear. As freezing temperature is approached, α-Zr particles precipitate from the Zr saturated liquid phase that can form nuclei for the peritactic reaction between Zirconium particles and the melt and it produces α-Mg with high Zr content. Lattice parameters of Zr (hcp, a=0.320 nm, c= 0.514 nm) and Mg (hcp, a=0.323 nm, c= 0.52 nm) are close which allows this reaction to occur readily. However, it is widely known that Zr is not used for the grain refinement of the AZ series magnesium alloys. This is because high solubility of Zr is required for grain refinement that is precluded by the formation of high melting compound when Al in the melt reacts with Zr [Polmear, et al. (2006)].

iii. Carbon inoculation

Mg-Al alloys suffer from their large and variable grain size. In addition, they exhibit coarse dendritic structure and there is formation of micro porosity, which leads to their poor mechanical properties [Stjohn, et al. (2005)]. As stated earlier, these alloys cannot employ Zr because Al poisons it. For obtaining uniform and finer grain size, potent inoculants are not available. Among the inoculation methods, carbon inoculation using agents like graphite, carbon tetrachloride, and hexachloroethane are used. It is inexpensive and convenient to use them because operating temperatures are lower and fading is less that enables longer holding times [Jin, et al. (2003), Easton, et al. (2001)]. Table 2.1 presents a summary of different works related to the observed effects of inoculation treatments on various Mg alloys.

Table 2.1 Summary of observed effects of inoculation treatment on various Mg alloys.

Cited Work	**Alloy system**	**Observed Effects from inoculation**
Stjohn, et al. (2005)	Al bearing and Al-free alloys.	For Al containing magnesium alloys need for finding a new refiner is discussed.
Co, et al. (2004)	Mg-3Al and Mg-9Al	Grain refinement by Elfinal process is discussed.
Motegi, (2005)	Mg-Al-Zn	C acts as grain refiner for Mg-Al alloy, Al_4C_3 and C_2Cl_6 are formed.
Kim, et.al.(2007)	AZ91	Heterogeneous nuclei lead to grain refinement.
Qian, et al. (2005)	Mg, Mg-3Zn and Mg-3Al	The Al_4C_3-(Al-C-O) hypothesis for C addition is explained.
Ramirez, et al, (2008)	AZ31 and Mg-Zn-	Better grain refinement is obtained when carbon inoculation is done along with UST.
Du, et.al. (2009)	Mg-3Al	Sr helps in grain refinement along with C inoculation.
Yano, et.al (2003)	AZ91	C_2Cl_6 is used. Grain refining method is discussed.
Guang, et.al. (2009)	Mg-Al-Zn-Mn alloys, AZ31 and AZ63 alloys	With carbon inoculation, Al_4C_3 and Al_8Mn_5 are formed, duplex nucleation sites were detected.

In the summary, Mg alloys that contain Al cannot be inoculated effectively because no potent inoculants such as the one for Al containing alloys, is available. Therefore, as against chemical methods, the physical techniques of microstructural refinement during solidification process can prove useful [Patel, et al. (2012)]. These approaches are discussed briefly below.

2.3.2.3. Physical grain refining methods

Physical grain refining methods involve creating to new nucleation sites, breakdown of growing crystals/dendrites for multiplications and dispersion of solidifying crystals by the application of mechanical force. At the time of solidification process, as the time increases the amount of solid fraction present in the melts increases. It is well accepted that if this solid fraction of melts is broken into fine particles by using physical methods, each fine particles act as nucleation sites for growing of new grain in alloy melts and grain refining take place. It also provides favorable condition for nucleation and nuclei survival. Different methods are used to apply vibrations during casting. Physical methods are of three types- mechanical stirring [Li, et al. (2002)], electromagnetic vibration/ stirring [Li, et al. (2007)] and ultrasonic vibration processing.

Goel, et al. [Goel, et al. (1980)] investigated the influence of vibration imposed during solidification on the ingot soundness of aluminum alloys. Application of vibrations could reduce porosity in solid solution type of Al-alloys. A control of vibration parameters was felt necessary to get the beneficial effects [Shukla, et al. (1980)]. Banerjee et al. [Banerjee, et al. (1989)] superimposed mechanically induced vibrations in solidifying white cast iron melts and copper-tin alloys. It assisted the nucleation of spheroidal graphite and ensured a faster kinetics of first stage graphitization. Mechanical vibrations in the inoculated melts opposed the inoculating effect and thus prohibited graphite nucleation. In wide freezing range copper-tin alloys significant refinement of the microstructural constituents and improvements in their mechanical properties was confirmed. It altered the dendrite arm spacing values favorably and thus increased toughness [Sarkar, et al. (1985)].

One of the non contact methods used to induce vibrations inside the solidifying melt is electromagnetic vibrations. However, this method is expensive and large amount of current is required for it to be effective. Several researchers have studied the effect of electromagnetic vibrations/convection on the microstructural evolution of resulting castings. Reddy et al. [Reddy, et al. (1985)] studied the microstructure refinement in aluminum and super alloys with electromagnetic forced convection. Forced convection refined the grain size and the dendrite arm spacing. Its beneficial effect is observed when used with some other metals such as aluminum, zinc, and brass. The observed beneficial effects included production of a more homogenous metal structure, finer grain size, and reduction in shrinkage porosities. Favorable grain size distribution and modification of grain size has been obtained in AZ91 alloy using this technique [Li, et al. (2009)].

Ultrasonic treatment (UST) of molten metals is another effective physical method that has not been practiced much for grain refinement. In UST, high intensity ultrasonic vibrations with typical frequencies equal to or higher than 20 kHz are introduced in to the molten solidifying alloy. Chernov, proposed in 1878 an idea that by means of elastic oscillations produced by mechanical vibration applied to solidifying melt the quality of cast alloys can be improved. In 1936, Socolov, experimentally observed the effect of ultrasound on the solidification of molten aluminum, zinc, and tin [Eskin, (1998)]. Campbell, [Campbell, (1981)], Eskin, [Eskin, (1998)] and Abramov, [Abramov, (1987)] provide detailed reviews about the vibration treatments and UST of metals. Acoustic cavitation and streaming in the molten metal were found to be responsible for the removal of gases and refining the cast microstructure [Eskin, (1998)]. Calculations have shown that pressure created by the implosion of a cavitation bubbles are approximately (1000-4000) MPa. Such a pressure can readily cause the dispersion of crystals at the crystallization front resulting in grain refinement [Eskin, (1998), Liu, et al. (2007), Zhang, et al. (2009)].

High power ultrasonic treatment involves application of ultrasonic vibrations to melt by using a horn. When ultrasound passes through the liquid, it generates a series of expansion and compression waves. Such conditions induce two effects in the processing liquid- ultrasonic streaming of the liquid (increased convection) and ultrasound induced cavitations. These lead to various physical and indirect chemical effects in the liquid. The vast capability and potential of high power ultrasonics in materials processing has well documented in the literature [Suslick, (1999), Mason, et al. (2003)].

During solidification in metallic systems, the application ultrasonic treatment known to assist in several ways, e.g. grain refinement, dispersion of other substances into melts (improved wetting), acceleration of rate processes, homogenization, and control of segregation, and degassing of the melts. Various effects observed from the ultrasonic treatment of melts, from the literature, are summarized in Table 2.2.

Table 2.2 Summary of observed effects of ultrasonic treatment of molten materials.

Cited Work	**Alloys/ materials studied**	**Observed effects of ultrasonic treatment**
Fairbanks, et al. (1974)	Nodular Cast Iron	Decrease in size of nodular graphite, increase in no. of graphite nodules, increased hardness, retardation in the decomposition of cementite is reported.
Li, et al. (1997)	A356 alloy	Grain refinement and globular grain morphology is observed.
Feng, et al. (2008)	Hypereutectic Al–Si alloy	Removed hydrogen bubbles, refined the primary Si phase, and changed primary α-Al dendritic crystal to equiaxed crystal.
Zhong, et al. (2010)	Al alloy	Homogenized the solute distribution, decreased the start of freezing temperature of β-phase.
Puga, et al. (2010)	$AlSi_9Cu_3$ alloy	The hydrogen removal rates strongly depended upon the ultrasonic power, the processing time, and the melt temperature.
Shu-sen, et al. (2010)	Al alloy	Increased the solid solubility of the element Si in α (Al) phase, decreased the volume fraction of primary Si particles from 18.3 pct to 10.7 pct, UTS and the pct elongation of alloy increased by 34 pct and 45 pct, respectively.
Fairbanks, et al. (1967)	Nickel and Al alloys	Grain refinement, is more random orientation of grains. silica, thoria, alumina could be dispersed homogeneously.
Abramov, et al. (1997)	Hypereutectic Al-Si	Refinement in primary Si size, improved strength, and ductility post-thixoforming are observed.
Eskin, et al. (1995)	Al-6Mg alloy and 7075 alloy Al-Mn alloy.	Increased rate of degassing, promotion of non-dendritic solidification and refining of Al_6Mn phase are noticed.
Jian, et al. (2005 and 2006)	A356	Grain refinement with globular/non dendritic microstructure, refinement of eutectic Si from 26 to 2 µm, eutectic Si morphology changed from coarse plate like to rosette like.
Li, et al. (2006)	Al-1 pct Si	Grain refinement, suppression of grain boundary segregation of Si is observed.
Eskin, et al. (1995)	Al alloy with Zr addition	Without UST coarse grains (0.8-1.5 mm) formed. With UST sub-dendritic grains (~0.1 mm) formed with accompanying increase in strength and plasticity.
Pan, et al. (2000)	6063 Al alloy	Improved wettability with Al and steel inserts, and better bonding is observed.

In one of the earliest reviews, Hem, et al. (1967) reviewed the effect of ultrasound on crystallization process and discussed few theories seeking to explain the action of ultrasound. It was suggested that a lack of understanding of ultrasonic crystallization has reduced the efficiency and therefore the industrial applications of this technique.

Djordjevic et al. [Djordjevic, et al. (2003)] studied effect of ultrasound on aluminum crystallization. The study advocated that expensive modifying agents could be replaced by UST with predicted energy savings. Matsunaga, et al. [Matsunaga, et al. (2006)] observed that the decrease in the surface tension of the molten aluminum alloy and increase in its vapor pressure lead to generation of acoustic cavitation. Thus, addition of zinc of 8.7 mass pct and bismuth of 0.5 mass pct also caused to generate acoustic cavitation in aluminum alloys. Recently a number of studies also suggested improved wetting and dispersion of reinforcement particles in metallic systems from the application of ultrasonic vibrations [Yang, et al. (2004), Lan, et al. (2004), Genma, et al. (1997)].

Eskin studied the inoculation potency of uncontrolled solid inclusions existing in the melt and of modifying additions after application of UST. UST was done in the liquid pool of continuously cast aluminum ingots [Eskin, (1998)]. In the absence of UST, only inherently active modifiers and particles caused nucleation. However, particles with large wetting angles (undesired non-metallic inclusions) were also activated with the application of ultrasound, contributing to enhanced nucleation that resulted in much finer grain size.

Effect of ultrasonic vibration on the nucleation phenomenon in A356 aluminum alloy melt was investigated [Jian, et al. (2005)]. The melt was subjected to UST isothermally at various solid fractions. Globular grains could be obtained when the melt was ultrasonically treated at a temperature that is closer to the liquidus temperature followed by fast cooling. In another work by same authors, effect of UST on refinement of eutectic silicon phase of A356 aluminum alloy melt was studied. Upon UST, much-refined rosette-like eutectic silicon morphology is observed upon solidification.

Xu, et al. [Xu, et al. (2004)] studied the degassing of molten A356 aluminum alloy with high intensity ultrasound. Within a few minutes of ultrasonic vibration, a steady-state hydrogen concentration could be obtained, irrespective of the initial concentration of dissolved hydrogen.

Hydrogen evolution kinetics was studied as a function of initial hydrogen concentration, melt temperature, and processing time.

A combination of UST and electromagnetic treatment was used by Zhang et al. [Zhang, et al. (2009)] for microstructural modification of A356 alloy. Electromagnetic stirring, ultrasonic cavitation and accompanied acoustic streaming resulted in spherodization of primary aluminum dendrites, remarkable grain refinement, and refinement of eutectic silicon.

Similarly, Jeong, et al. [Jeong, et al. (2009)] had studied to evaluate the effect of ultrasound energy on microstructure of castings, and high intensity ultrasound was injected into A356 and A390 alloy melt for refinement of primary phase without adding a chemical refiner. From the study they concluded that the structure of primary phase in hypoeutectic A356 alloy could not be changed by an injection of the ultrasound into full alloy melt, however, the primary Si in hyper-eutectic A390 alloy was able to be refined and distributed uniformly in Al matrix by the same process.

In another study involving high silicon aluminum alloys, UST refined the needle like β-Al_5FeSi and plate-like δ-Al_4FeSi_2 intermetallic phases, and promoted the formation of δ phases rather than β phase [Zhong, et al. (2010)]. UST uniformly distributed the iron atoms ahead of the solidification front and the formation temperature of the β phased creased. Effective distribution of solute prevented rapid growth of δ phase in a one direction, resulting in the refinement of δ phase. In another work, morphology of $TiAl_3$ and TiC phases was changed remarkably by UST of Al–5Ti–0.25C grain refining alloy [Li, et al. (2008)]. Refinement of$TiAl_3$ particles, enhanced the nucleation potency of TiC particles, and effective dispersion of TiC particles was attributed to ultrasonic cavitation. Effect of UST on grain refinement of Zr and Ti containing Al alloys was studied [Atamanenko, et al.(2010)]. It was concluded that the efficiency of UST is significantly increased when some zirconium with small additions ($\geq$0.015 wt pct) of titanium was present in the aluminum alloy. A 20-μm amplitude of vibrations was thought to be high enough to promote cavitation.

Recently in isolated investigations, microstructure and mechanical properties of Mg alloy shave been studied after UST [Liu, et al. (2008)] [Gao, et al. (2009)]. Fine non-dendritic grains were reported in the solidified microstructures of AZ91 after UST. Acoustic cavitation and streaming, faster cooling of the melt due to the ultrasonic streaming, impurity particles activation, undercooling at the cavity/melt interfaces were the responsible reported factors. The tensile and compressive strengths, and fracture strains of the castings were improved. Potency of UST for grain refinement of some magnesium alloys was studied [Qian, et al. (2005), Qian, et al. (2010)]. Presence of adequate solute elements increased the efficiency of UST Instead of just increasing the applied ultrasonic power, increasing of solute content with lower ultrasound power was more effective. By enhancing the nucleation from activating potential nucleation sites, the UST produced the initial crystallites and contributed to grain refinement.

Although there are reports about the refinement of grain size in UST processed magnesium alloys, there is much less work commenting on the morphology of second phase in such alloys. Such phases may included intermetallics like $Mg_{17}Al_{12}$, MnFeAl(Si), Mg_2Si phases depending on the type of alloy [Ditze, et al. (1988)]. Zhiqiang, et al. [Zhiqiang, et al.(2008A) and (2008B)] investigated the effects of UST on the microstructure and mechanical properties of Mg-Ca Alloy, and Mg-9Al alloys. $Mg_{17}Al_{12}$ phase was refined and was less continuous along the grain boundaries.

This review presents the effects of UST on the microstructure of mostly aluminum alloys and a few commercial magnesium alloys. It is noticed that application of ultrasonic vibrations to solidifying melts is one of the simple, pollutants free [Breslin, et al. (1995)] and effective physical methods having fewer drawbacks. This solidification processing techniques can be especially useful for grain refinement of lightweight alloys. Along with grain refinement, reduced porosity, reduced segregation, increased homogeneity, and improved distribution of intermetallic phases can be obtained [Liu, et al. (1996)]. It is assumed that cavitation and acoustic streaming act as the two most important physical events during the treatment of the molten metal under the high intensity ultrasound field. [Oh, et al. (1989)]

Phenomena induced by propagation of ultrasound

When high intensity ultrasound propagates through liquid melts, some phenomena like acoustic streaming and cavitations arise in the molten metal, which causes the change in the morphology of the solidifying phases.

Ultrasonic streaming

Acoustic energy and loss in momentum in overcoming the melt viscosity generates streaming. It happens both in inhomogeneous sound fields and near various barriers like interfaces. The scale and velocity of streaming in a medium depends on its properties as well as on the shape and structure of its boundary. It is noteworthy that the streaming velocity increases with acoustic intensity, but is always far less than the driving ultrasonic velocity, no matter how high the intensity is [Abramov, (1986)].

There are mainly three types of acoustic streaming which are classified as: [Jian, et al. (2005)]

1. Large-scale streaming arising in a free inhomogeneous acoustic field where inhomogenities are significantly greater than the sound wavelength.
2. Streaming observed in a medium constrained by rigid walls.
3. Small-scale vortices forming in a viscous boundary layer near obstacles.

Abramov used ultrasound in 45 kHz and 100-250 kHz frequency range to study the acoustic streaming properties in the melt of transparent organic substance (the naphthalene-camphor alloys) [Abramov, (1986)]. From these experiments (Fig. 2.3), it was found that the factors that governed the scale, nature, and velocity of streaming were the melt temperature (which controls viscosity) and the ultrasonic intensity. At low ultrasonic intensity, acoustic streaming does not appear in a superheated melt. Other studies reveal that ultrasonic streaming never interacts with convective flows when ultrasonic intensity is low. By raising the vibrational velocity amplitude (to 3-8 cm.s^{-1}), streaming and convective flows begin to interact and the steady state liquid velocity is 5-10 times than that of convective flows [Abramov, (1986), Jian, et al. (2005)].

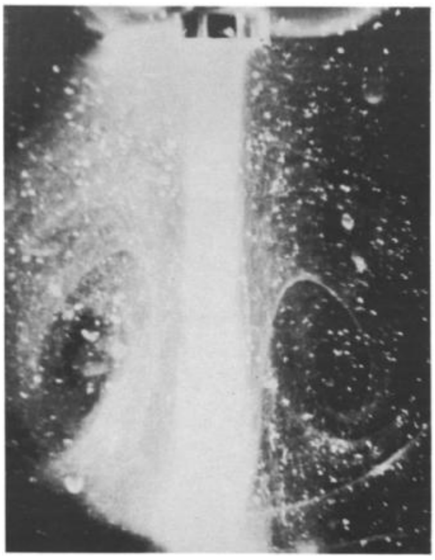

Fig. 2.3 Acoustic streaming in naphthalene-camphor system at 45 kHz and 0.03 MPa mean pressure [Abramov, (1986)].

Ultrasonic streaming affects the solidification through large-scale flows equalizing the temperature of the liquid, increasing the transfer of fine tiny solidification sites, and breaking down the crystals throughout the melt.

Ultrasonic cavitation

Acoustic energy of sufficient magnitude introduced in the melt sets up a pressure variation and initiates cavitation. In order to establish a cavitation condition where cavitation occurs and crystal dispersion takes place, an acoustic pressure of greater than 10 W.cm^{-2} at frequencies of 20 kHz is required [Eskin, (1994)].

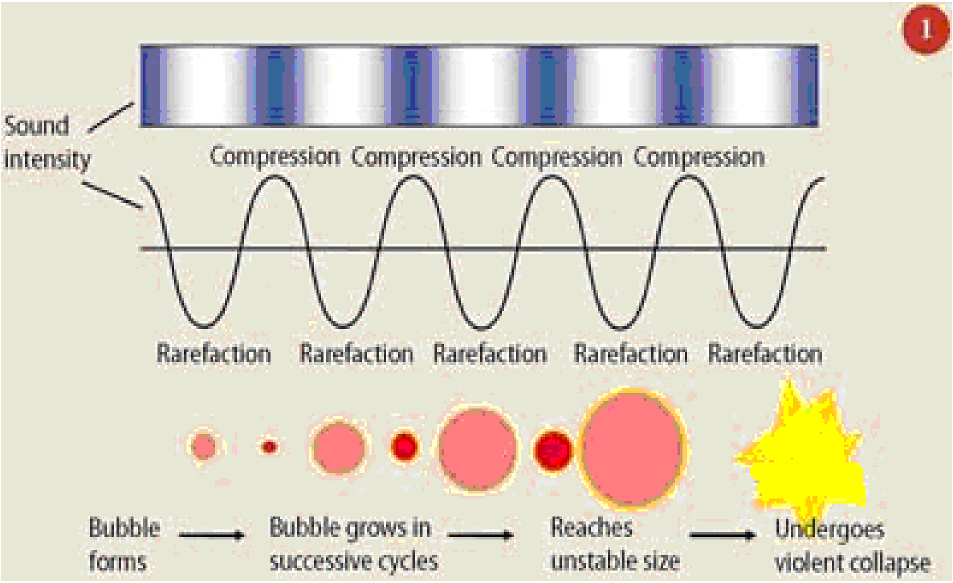

Fig. 2.4 Cavitation phenomena in the melt [Eskin, (1994)].

When ultrasound waves are transmitted through a medium, its molecular structure is alternately stretched and compressed. If the negative pressure during the stretching phase or rarefaction phase is strong enough to overcome intermolecular binding forces, it can torn apart the medium resulting in tiny cavities (micro bubbles). The cavities so formed can grow under tensile stresses in the succeeding cycles. Eventually they collapse with the release of large magnitude of energy as depicted in Fig. 2.4.

With sufficient acoustic pressure, the interface boundary that is the transition layer between the liquid and solid phases can be disrupted due to viscous friction forces. A change of state of this layer will cause the crystal nucleation and growth conditions to change [Qian, et al. (2005), Eskin, (1997), Eskin, (1994), Lierke, (1967), Egon, (1954)].

Collapsing bubbles result in mechanical and chemical effects that act in two zones:

1. One is within the bubble, and
2. Other in the immediate vicinity of the collapse where enormous shear forces are created.

The important factors controlling the intensity of cavitation are: [Qian, et al. (2005)]

Ultrasonic frequency: The lower the frequency, the more intense will be the cavitation occurrence.

Ultrasonic power: The amount of cavitation per unit of time and volume is determined by the power level. Increase in power increases the number of cavitation events. When cavitation occurs in a melt, the occurrence of pulsating cavitation bubbles can cause the dispersion of crystals and increase in the nucleation rate of crystallization.

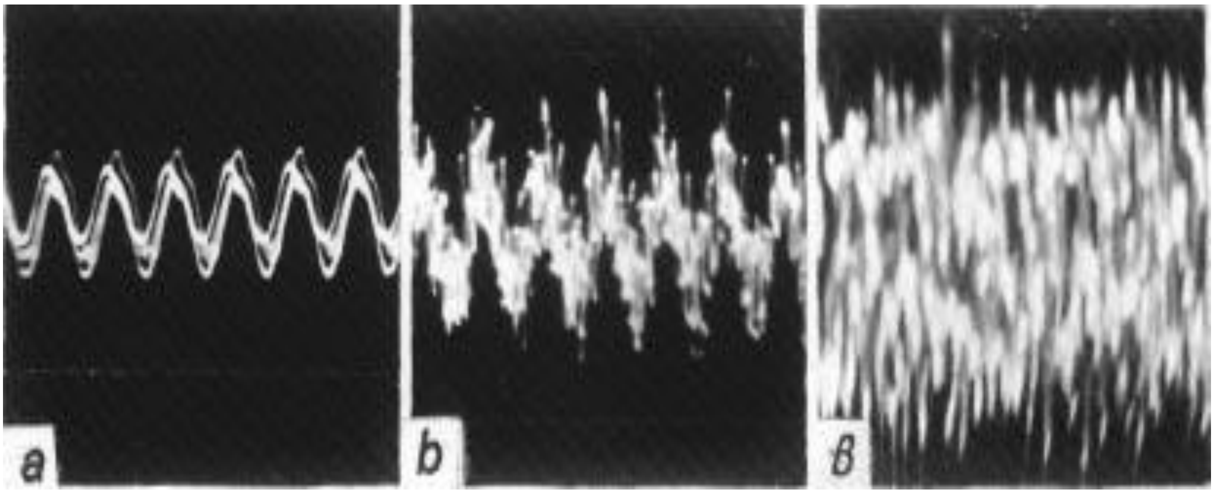

Fig. 2.5 Typical oscillograms for the ultrasonic treatment of melts (a) without cavitation, (b) cavitation threshold, (c) developed cavitation [Egon, (1954)].

The pressure created by the implosion of a cavitation bubbles is calculated as approximately (1000-4000) MPa. Such a pressure can readily cause the dispersion of crystals at the crystallization front resulting in grain refinement [Lierke, et al. (1967), Egon, (1954)]. The application of ultrasound to the melt results in variations in local pressure from minimum to maximum instantaneously. The extremities in pressures (maximum and minimum) generated in the melt are given by equation 2.2 and 2.3, respectively [Meek, et al. (2006)].

$$p_{max} = p_0 + \sqrt{2\rho c I} \tag{2.2}$$

$$p_{min} = p_0 - \sqrt{2\rho c I} \tag{2.3}$$

Where $p_0$is atmospheric pressure, ρ and c are the density and the wave velocity of the melt respectively, and I is the energy of wave in the melt. According to Abramov, a critical value of sound pressure (P_C^v) exists in order to estimate the cavitation strength of a liquid containing vapor or gas (tiny bubbles). The bubble is stable when its peak sound pressure is less than (P_C^v) or else it will grow and collapse finally according to equation 2.3 [Abramov, (1986), Abramov, (1987)].

$$P_C^{v} = P_0 - P_V + \frac{2}{3\sqrt{3}}\sqrt{\frac{(2\sigma_L/R_0)^3}{P_0 - P_V + 2\sigma_L/R_0}} \tag{2.3}$$

Where, P_0 is initial air pressure, P_V is the saturation vapor pressure, R_0 is initial radius, and σ_L is liquid- vapor surface tension. Processes such as dissolution, dispersion, diffusion, wetting, heat transfer, and mass transfer are accelerated by acoustic cavitation. Most technologies for cleaning, refining, degassing, solidification of metallic alloys are ascribed to the occurrence of such phenomena [Jian, et al. (2005), Meek, et al. (2006)].

Metallurgical effects of ultrasonic vibration in melts

Some known metallurgical effects are observed during the treatment of molten metal under the application of power ultrasound. These effects are as follows: [Egon, (1954)]

i. Solidification under ultrasonic field

    a) Reduction in grain size

    b) Non-dendritic solidification

ii. Refining of melts
    - a) Ultrasonic degassing of melts
    - b) Fine filtration in the ultrasonic field (USFIRALS process)

iii. Dispersion of other substances into the melts

iv. Acceleration of rate processes

v. Other metallurgical and related effects

i. Solidification under ultrasonic field

Structural changes observed during the solidification process under ultrasonic vibrations can be summarized as follows: [Li, et al. (2006)], [Djordjevic, et al. (2006)].

1. Promotion of transition from columnar to equiaxed structure.
2. Change in phase distribution.
3. Mean grain size is reduced.
4. Compositional homogeneity of the ingot is enhanced.
5. Liquation processes are reduced.
6. Non-metallic inclusions are distributed uniformly throughout the ingot.

a) Reduction in grain size

Different mechanisms that have been proposed are broadly classified into two groups: [Meek, et al. (2006), Li, et al. (2006).]

1. Ultrasonically induced grain nucleation.
2. Ultrasonically induced dendrite fragmentation.

Ultrasonically induced nucleation

Ultrasonic vibration may affect the nucleation in many ways. Pressure influences the liquidus temperature of an alloy. If ultrasonic energy is applied to a melt near its liquidus temperature, some regions in the molten alloy may be superheated while other regions may be undercooled. At each location the melt undergo changes from superheating to undercooling at high frequencies. This may result in the formation of an increased number of solid nuclei. Another possibility is that the grain refiners added to the melt may also be affected by ultrasonic vibration, since each foreign particle can act as a nucleus and is most effective under a certain undercooling. Nucleation under the action of ultrasound vibration may also occur in the melt at a temperature higher than the liquidus, corresponding to the increase in the pressure. It has been reported that grain size was reduced when ultrasonic vibration was applied at a temperature higher than the liquidus temperature [Abramov, (1986), Swallowe, et al. (1989), Ramirez, (2008), Jun-wen, et al. (2007)].

Possible mechanisms of crystal nucleation due to cavities are: [Li, et al. (2006)]

1. From the surface of the expanding cavity, the liquid vaporates of causing cooling of the surface
2. An increase in the melting point is produced from positive pressure pulse associated with cavity collapse
3. Cooling is caused by negative pressure associated with cavity collapse

Cavitation- enhanced nucleation is interpreted in terms of two different mechanisms discussed below [Nastac, (2004), Eskin, (1994)]:

Pressure pulse melting point (T_m) mechanism

Cavitation bubbles produced in liquid metal start to collapse, inducing the pressure pulse waves, resulting in the increase of solid-liquid equilibrium temperature. We can describe the change by using the Clausious-Clapyron equation (equation 2.4).

$$\frac{dT_m}{dP} = \frac{T_m(V_L - V_S)}{\Delta H} \tag{2.4}$$

Where, ΔH is the latent heat of freezing in J.g^{-1}, P is pressure in 10^5 Pa, T_m is freezing point in K, V_S, and V_L are the specific volumes of solid and liquid phases in cm^3.g^{-1}, respectively. Nucleation rate increases due to an increase in T_m, which is equivalent to increasing the undercooling.

Cavitation enhanced wetting

In this case, the pressure pulse fills the cavities and cracks on the surfaces of the substrates such as the mold, or impurities by molten metal. Therefore, enhanced nucleation results from these defects that can act as effective nucleation sites.

Ultrasonically induced dendrite fragmentation

The convection and shock waves created in the solidifying melt during ultrasonic vibration can promote dendrite fragmentation, which caused by melting at a dendrite root, where the solutes are segregated. The melting at a dendrite root may be the results of a local temperature increase. The diffusion of solutes away from the dendrite roots would lead to a reduction of the solute concentration and increase in the local temperature. The effect would also lead to melting at the dendrite roots. Stirring can also promote dendrite fragmentation, since it produces local temperature variations and promotes diffusion of solutes in the liquid. Furthermore, the local pressure fluctuations given by equations (2.2) and (2.3) lead to fluctuations in the melting temperature which results in the melting of the dendrite roots.

These fluctuations should aid in the melting of the dendrite roots. This will lead to more homogeneous microstructure with smaller grain size. However, if the applied ultrasonic field is strong enough to produce cavitation, then a major origin of grain refinement is the fragmentation of crystals to produce new nuclei [Jian, et al. (2005), Abramov, (1986), Thomas, et al. (2006), Tao, et al. (2006), Swallowe, et al. (1989), Ramirez, (2008), Jun-wen, et al. (2007), Nastac, (2004)]. Abramov studied the destruction/fragmentation of growing crystals due to cavitation induced by ultrasound. It has found that equation (2.5) gives the pressure (P_d) required for the fragmentation of crystals [Nastac, (2004)].

$$\mathbf{P_d = \frac{1}{4}\left(\frac{r}{l}\right)^2 \sigma_{mp} \approx \gamma\sigma_{mp}} \qquad (2.5)$$

Where σ_{mp} is strength of the material near the melting point, and l and r are the length and radius of the crystal, respectively. Table 2.3 shows that the ultrasonic intensity required for the crystal dispersion scales with the $\boldsymbol{\gamma}$ parameter. Both the alloy strength and the crystal morphology influences the dispersion of growing crystals. Table 2.3 also reveals how the crystal morphology is related to the size of the mushy zone [Nastac, (2004)].

Table 2.3 Crystal geometry and ultrasound intensity necessary for crystal dispersion [Nastac, (2004)].

Crystal growth velocity (μm.s^{-1})	**Crystal length (mm)**	**Crystal radius (mm)**	$\gamma \times 10^{-2}$	**Ultrasound intensity (W.cm^{-2})**
5	0.2	0.05	6.25	30
16	0.4	0.06	2.25	20
25	0.6	0.08	1.78	15
50	1.0	0.12	1.44	10
100	1.6	0.20	1.55	10

b) Non-dendritic solidification

The dendrites (grains) and dendrite branches (internal grain structure) are the basis for the evaluation of cast metallic structure, after the discovery of dendritic structures by Chernov. New non- dendritic structure consisting of globular grains without dendritic branching could be produced by UST. For forming the non-dendritic structure, the required main conditions are:

1. Nucleation must be accelerated, and
2. Ahead of the solidification front, excess amount of solidification sites should form.

Cavitation from the UST of the melt wets the usually uncontrolled, non- metallic impurities. Non- dendritic structure is advantageous with respect to the increased toughness with retention of strength. It is found that, large- scale crack free ingots (weighing 10 ton and measuring 1200 mm in diameter) could be obtained from structural Al alloys (2364 series) because the plasticity doubled due to UST. Irrespective of the hot deformation mode, the improved plasticity of non-dendritic ingot is retained in the deformed material [Eskin, (1994), Lierke, (1967), Hiedemann, (1954)]. Thus, the effects of UST on the solidification process can be summarized as shown in Fig. 2.6 [Abramov, (1986)].

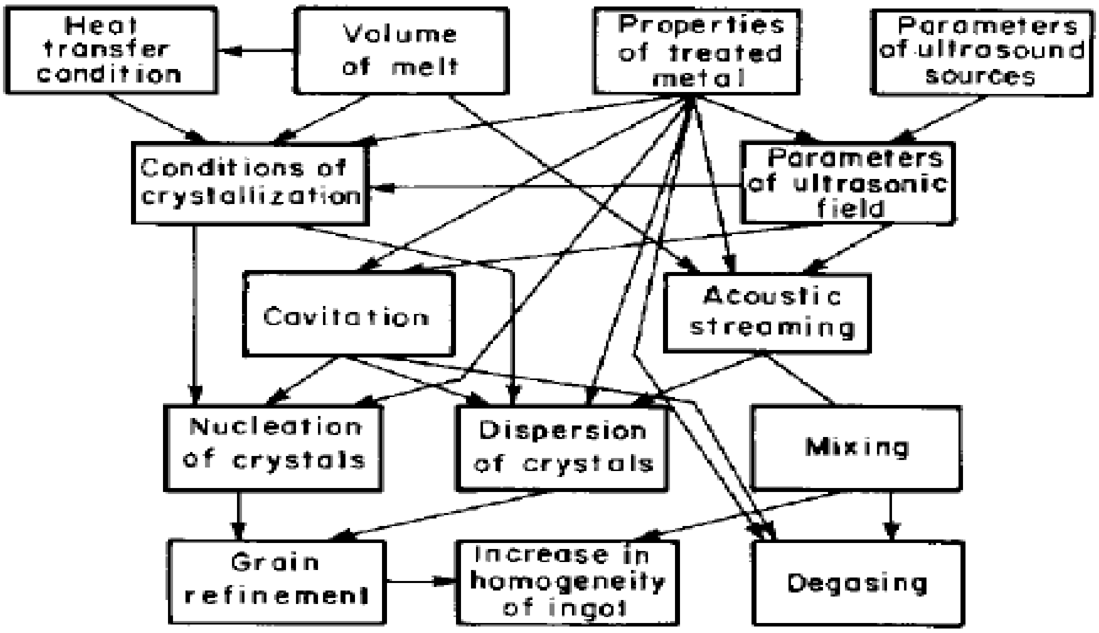

Fig. 2.6 Generalized effects of ultrasonic vibration on solidification process [Abramov, (1986)].

ii. Refining of melts

Ultrasonic melt treatment (UST), before the beginning of solidification, has a noticeable effect on melt refining processes and thereby eliminates gas and solid non-metallic inclusions [Eskin, (1994), Lierke, (1967), Hiedemann, (1954)].

a) Ultrasonic degassing of melts

The interaction of high intensity ultrasound with liquid reduces the amount of liquid contained gas, leading to degassing. This effect can be used for degassing metal melts.
Almost all molten metals often contain a suspension of submicroscopic particles that are non-wettable by the melt and their surface defects also contain some adsorbed gaseous phase. Ultrasonic degassing is relatively inexpensive and environmentally clean technique. It involves the introduction of high intensity acoustic energy in the melt, high enough to set up a pressure differences that will induce cavitations. Mass transfer of gas from the solution into the cavitation bubbles from cavitation phenomenon assisted by rectified diffusion [Junwen, et al. (2008)]. Gas transport in to the bubble is greatly improved by this directed diffusion when the cavitation threshold is exceeded. Fig. 2.4 shows the process of rectified diffusion [Meidani, et al. (2004)].

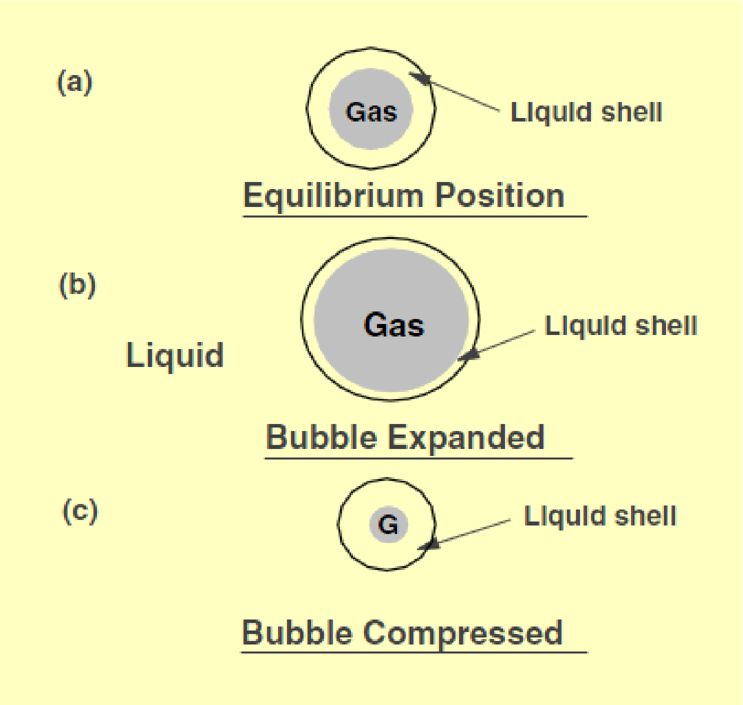

Fig. 2.7 Schematic of rectified diffusion [Meidani, et al. (2004)].

Table 2.4 Comparison of efficiencies of degassing techniques used in industry for Al-Si-Mg alloy [Eskin, (1994), Lierke, (1967), Hiedemann, (1954), Junwen, et al. (2008)].

Degassing techniques	**H_2 (cm^3 per 100 g)**	**Density (10^3 $Kg.m^{-3}$)**	**Porosity number**
Ultrasonic degassing	0.17	2.706	1-2
Vacuum degassing	0.20	2.681	1-2
Argon purging	0.26	2.667	2-3
C_2Cl_6	0.30	2.665	2-3
Universal flux	0.26	2.663	3-4
Initial melt	0.35	2.660	4

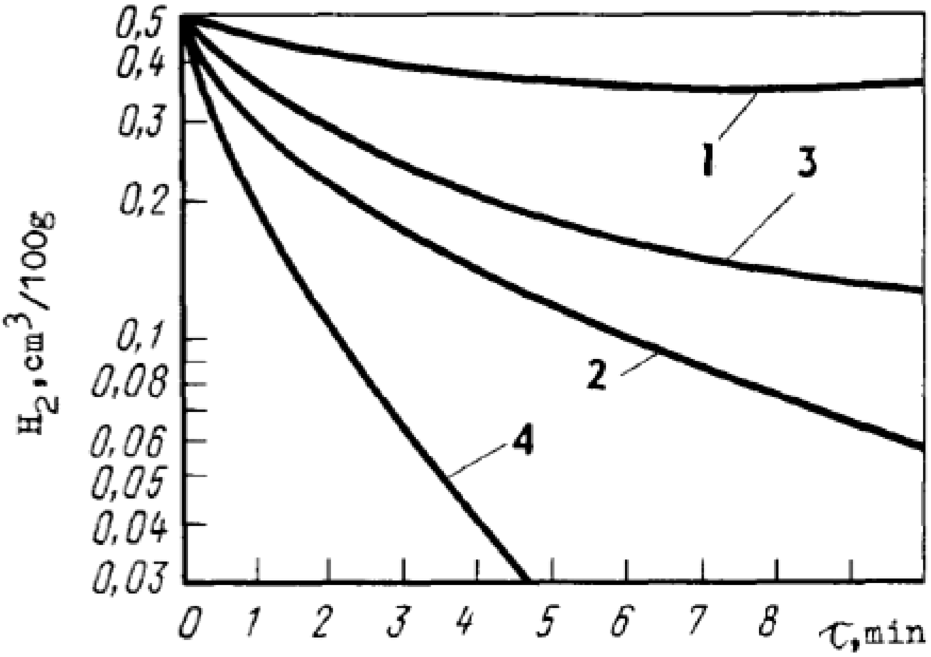

Fig. 2.8 Rates of removal of hydrogen from Al-Si-Mg alloy (1) chlorine salts processing, (2) UST, (3) vacuum degassing, (4) combined UST and vacuum degassing [Lierke, (1967)].

b) Melt filtration in ultrasonic field

For filtration of aluminum melts, mesh type alkali-free alumina-boron-silicate glass filters are widely used. However, 1×1 mm^2 mesh filter scan not filter finer inclusions. If fine filters of 0.4×0.4 mm^2 or multilayered filters are used, the capillary action performance of these filters is affected adversely. Sonocapillary effect is observed when the cavitation field from UST is formed above the filters surface. Because of this the melts is readily filtered. Refining of melt from dispersive particles of inclusions down to 1–3 μm by a multilayer filter can be effectively done using this technique called the USFIRALS-process. It allows production of high-quality blanks for magnetic disks from 5xxx (series) alloys, fine foils, sheets and other semis from 6061-type alloys sensitive to impurities. Fine filtration according to “USFIRALS-process” technique results in an improvement of service-life performances in short-transverse direction [Eskin, (1994), Lierke, (1967), Hiedemann, (1954), Junwen, (2008)].

iii. Dispersion of other substances into melts

Sometimes it is desirable to produce a fine dispersion of one metal into another. It is obvious that the dispersing effects of ultrasonic waves should be especially useful for adding constituents of low solubility or high melting point to the metal. Maring and Ritzau [Egon, (1954)] found that a treatment with ultrasound waves of 500 cycles.s^{-1} resulted in a finer distribution of Pb in Al melt than did the well-known chemical Pb-chloride process as shown in Fig. 2.9. Similarly, Egon [Egon, (1954)] also reported briefly on the ultrasonically induced dispersion of graphite into bronze used for bearings. He obtained a self-lubricating bearing by producing the contents of graphite up to 25 pct. The phenomenon of dispersion in an ultrasonic field is attributed to the action of cavitation produced in the melt. Table 2.5 summarizes the work from literature about dispersion studies conducted in the different alloys upon the application of UST.

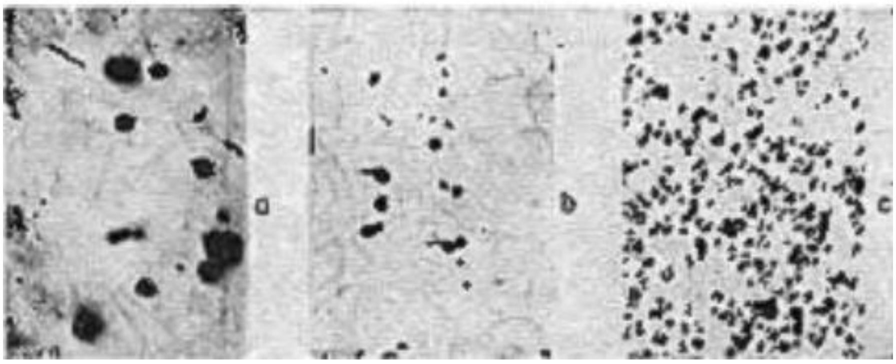

Fig. 2.9 Dispersion of lead into aluminum, (a) Lead chloride technique, and after exposure to the sonic treatment of (b) low and (c) high intensity [Egon, (1954)].

Table 2.5 Dispersion and reaction kinetics observed in the different alloys by the application of UST.

Dispersion and Reaction Kinetics		
Abramov, et al. (1995)	Al-Pb-X alloys	Uniform dispersion of finer 2-6 μm size Pb particles, ultrasonics prevents coagulation is noticed.
Tsunekawa, et al. (2001)	Al-3Mg alloy	Wettability of SiO_2 was improved increasing transfer rate and reaction rate with the melt
Eskin, et al. (2003)	Al-Si alloy based MMC	Improved wetting of non-metallic particles, reduced size of primary Si particles are studied.
Yang, et al. (2004)	A356 base MMC	Uniform dispersion of SiC nano-particles
Lan, et al. (2004)	AZ91D	Uniform dispersion of SiC nano-particles is noticed.
Han, et al. (2005)	Al-5Ti-1B	Accelerated dissolution of $TiAl_3$ and change in its morphology, accelerated reactions of Al with halide salts.

iv. Acceleration of rate processes

Numerous metallurgical processes could be carried out at a lower temperature in the presence of high-frequency oscillation without loss in efficiency. Sonic or ultrasonic vibrations do produce an increase in the rate of processes and cause processes to occur at lower temperatures [Egon, (1954)]. Ultrasonic waves have a direct effect on the rate of various metallurgical processes that can be considered as place exchanges such as diffusion, ion mobility, viscosity and thermal diffusion. The beneficial effect of power ultrasound in improving the kinetics of chemical reactions is well documented [Suslick, (1999), Han, et al. (2005)]. Table 2.5 summarizes the work from literature about reaction kinetics studies conducted in some alloys upon the application of UST.

v. Other metallurgical and related effects

Some other metallurgical effects such that the removal of dross and slag by means of sonic or ultrasonic treatment have been noticed. Ultrasonic can also be used to intensify the metal boiling. In rimmed steel ingots, especially when carbon content is more than 0.13 pct and the casting speed is increased, the depth of occurrence of honeycomb blowholes is controlled conventionally by blowing the metal stream with oxygen. However, with this technique honeycomb blowholes are difficult to control and the non-metallic inclusions content of the steel also increases. However, the intensity of boil in the steel is altered by using power ultrasonics. The molten metal surface-oxide-film breakdown and the concomitant increase in oxygen diffusion rate results in intensive boiling from UST. Further, ultrasonics is known to assist in ionization of the oxygen and as a result, the oxidizing effect is intensified. UST also reduced the slag on the metal surface in mould. Observations show that the high rate of metal boiling when rimmed steel was exposed to UST led to a reduction in oxygen consumption [Bronfin, et al. (2000)].

2.4. Dispersion hardening studies

Metal matrix composites (MMCs) of magnesium and its alloys can give better mechanical properties for various demands and applications in real practices. The addition of various hard reinforcement particles to magnesium and its alloys produces superior mechanical properties, good thermal stability, increased hardness, and stiffness. MMCs also provide flexibility in terms of required properties. According to requirement, MMCs can be designed by selecting the appropriate quantities of matrix and reinforcement materials. In the processing of MMCs, homogeneous distribution of the reinforcement phases is a common problem. Until now to achieve a defect-free microstructure in MMCs different processing techniques have been developed.

In ex-situ synthesis techniques, different kinds of ceramic materials (SiC, Al_2O_3, MgO and B_4C) are extensively used to reinforce aluminum alloy matrices. Superior properties of these ceramic materials such as refractoriness, high hardness, high compressive strength, wear resistance, etc. makes them suitable for use as reinforcement in a matrix of composites [Hassan, et al. (2008), Zhang, et al. (2009), Pen, et al. (2002), Khakbiz, et al. (2009), Dhokey et al. (2007)]. The different researchers worked in the field of Mg alloy matrix composite materials and found improvement in mechanical properties of MMCs as summarized in Table 2.6. Large size of reinforcement and bad interface between magnesium matrix and reinforcements result in only marginal improvement in the mechanical properties of MMCs prepared by ex-situ synthesis techniques [Zhao, et al. (2008)]. Further, these fabrication processes usually require expensive reinforcement materials and involve complex equipment and procedures, thus imposing a relatively high cost. Therefore, in-situ synthesis methods have come into focus as an alternative route to fabricate MMCs that is cost-effective. This method offers a number of attractive features, such as good reinforcement/matrix compatibility, homogeneous distribution of the reinforcing particles and potentially low cost [Dong, et al. (2006)].

In the in-situ MMC synthesis methods, the reinforcement is formed by controlling the chemical reactions in the matrix. In in-situ reactions, at least one of the reacting elements is reacted with the constituent of the molten matrix alloy. A series of reactions may result into fine hard ceramic or oxide powders or phases formed in the metal matrix. One of the final reaction products is the reinforcement dispersed in the matrix alloy. It is more beneficial if these in situ formed particles are coherent with the matrix and has both a finer particle size and a more homogenous distribution. These reactions have to be favourable in terms of thermodynamics. To make the fabrication process practical, reasonably fast reaction kinetics are required [Hai, et al. (2004), Nandam, et al. (2011)].

Table 2.6 Summary of observed effects of different reinforcements on the magnesium alloys.

Cited Work	**Matrix studied, reinforcement used, Size (pct).**	**Processing methods and results**
Lan, et al. (2004)	AZ91, SiC, 30 nm (2 wt pct and 5wt pct)	Cast composites based on SiC_p/AZ91D were fabricated with the help of high intensity UST. The microstructure and micro hardness of nano-sized SiC particles reinforced magnesium composites were studied.
Yao, et al. (2010)	AZ91, TiC, preform (3, 6 and 10 wt pct)	TiC/AZ91 Mg composite was formed by spray deposition. Wear properties were discussed.
Cao, et al. (2008 A)	AZ91, AlN, 25 nm (1 wt pct)	AZ91/AlN nano-composite was produced by UST. Microstructure, and room temperature and high temperature mechanical properties were studied.
Cao, et al. (2008 B)	AS21, AS41, Mg-4 pct Zn, SiC, 50 nm (2 wt pct-AS) (1.5 wt pct Mg-Zn)	SiC nano-particles reinforced Mg-(2, 4) Al-1Si was fabricated by UST. Microstructure and mechanical properties were studied.
Jayamathy, et al. (2004)	AM60, SiC, 20 μm (10 and 15 wt pct)	The influence of volume fractions of the reinforcement on mechanical properties of MMCs was discussed.
Zhao, et al. (2008)	AZ31, Mg_3N_2, 10 μm (1 wt pct)	Microstructures and mechanical properties were studied. Composite was fabricated by in-situ formation of AlN particles.
Liu, et al. (2010)	AZ91, carbon nanotubes, 20–40 nm	High-intensity ultrasonic dispersion and mechanical stirring was employed.
Yang, et al. (2004)	A356, SiC, 30 nm (0, 0.5, 1.0, 2.0 and 5 wt pct)	Bulk Al-based nano-composites with nano- sized SiC were fabricated by UST. The microstructure and mechanical properties were studied for various wt pct of SiC.

Ex-situ composite synthesis techniques are widely investigated for aluminum alloys by using different kinds of ceramic reinforcements like SiC, Al_2O_3, MgO, and B_4C, which have many desirable reinforcement properties like high hardness, refractoriness, high compressive strength, and wear resistance [Hassan, et al. (2008), Khakbiz, et al. (2009), Roy, et al. (2006)].

Ex-situ synthesized MMCs exhibit limited improvement in their mechanical properties because of the presence of large sized reinforcements and bad interface between the matrix and reinforcements [Zhang, et al. (2010)]. Ex-situ techniques usually need expensive reinforcement materials and require complex procedures and equipments. Fabrication of MMCs by such techniques is difficult because the micron and especially nano-sized particles have much larger specific surface area. It is challenging to disperse the particles uniformly in alloy melts [Laurent, et al. (1992)]. It is reported that the potentially inexpensive in situ methods offer benefits such as homogeneous distribution of the reinforcing particles, a good reinforcement-matrix interface and compatibility, and the in situ formed particles are finer [Emamy, et al. (2006), Roy, et al. (2006), Yang, et al. (2008)]. Although this method has been extensively studied for aluminum matrix composites, it is relatively less explored for magnesium matrix composites. A recent review in magnesium matrix composites [Ye, et al. (2004)] reports about TiC/Mg, MgO/Mg, (TiB_2–TiB)/Mg and Mg_2Si/Mg composites synthesized from Mg–Ti–C, Mg–B_2O_3, Mg–KBF_4–K_2TiF_6, and MgO, and Mg–Si systems, respectively. To overcome the difficulties arising from bad wettability, the addition of suitable minor alloying elements to the melt [Ye, et al. (2004), Choh, et al. (1987), Oh, et al. (1989), Yu, et al. (2012)], surface treatment on reinforcements [Rocher, et al. (1989)] and elevation of molten matrix temperature [Oh, et al. (1989)] have been widely studied. Porosity, which degrades the mechanical properties, is formed adjacent to the agglomerate particles in the MMCs when stirring transfers the ceramic particles to the melt [Rocher, et al. (1989)]. Therefore, in order to overcome the poor wettability problem, novel production method for MMCs components is desired. In this context, fabrication using in situ reaction is one of the economical and versatile approaches [Tsunekawa, et al. (2001)].

2.5 Summary

1. An easy and inexpensive way to improve mechanical properties of magnesium alloys is by reduction in grain size.
2. Ultrasonic treatment has a significant influence on the structural modification and corresponding improvement in the properties from microstructural refinement, melt degassing, and reduction in elemental segregation.
3. In the specimens processed using ultrasonic vibrations, the dominant mechanism for the grain refinement is the cavitation led heterogeneous nucleation and fragmentation of growing crystals by acoustic streaming. Few studies have addressed the fundamental

nucleation mechanisms and the growth of grains during ultrasonically induced solidification. There are only limited systematic studies involving UST of Mg alloys in order to refine their grain size and there is scope for further exploration.

4. Ultrasonic treatment approach possesses the advantages of being environment friendly, cost effective, and amenable for combination with other physical processing technologies for liquid metal.
5. Grain refining techniques such as superheating the melt, ferric chloride inoculation (Elfinal process), and carbon inoculation have been tried with some success. Among these methods, carbon inoculation using agents like C_2Cl_6, CCl_4, and graphite offer many practical advantages because of lower operating temperature and less fading.
6. Nano carbon black powder inoculation can be an effective grain refining method for Mg-Al-Zn magnesium alloy than the conventional polluting hexacholoroethane treatments. Inexpensive nano carbon black that has a high surface-area-to-volume ratio and it can readily form the inoculating phase particles in larger number.
7. Use of grain refiner with the combination of ultrasonic vibrations can further refine the alloy structure. This combined effect approach has not been explored so far. High intensity ultrasonic treatment can help to accelerate the wetting, de-agglomeration, and dispersion of carbon black nano particles and can improve the kinetics of inoculating phase formation. Its beneficial effects can be synergistic considering the physical capabilities of UST and there is a scope for initiating research in this direction.
8. Light metal matrix composites (MMCs) provide many options for improving the mechanical properties of materials. Many trials have been made by the addition of various hard ceramic reinforces particles to the magnesium and its alloys. Magnesium alloy MMCs possess superior mechanical properties, good thermal stability, increased hardness, and stiffness compared to base alloys.
9. In situ technique has potential to offer advantages over ex-situ synthesis technique. This approach offers a number of attractive benefits such as finer reinforcing particles, homogeneous distribution of the particles, a good matrix/reinforcement compatibility, and lower cost. Studies involving in-situ fabrication Mg alloy matrix MMCs are scarce.
10. Ultrasonic treatment (UST) has potential of being one of the simplest and effective physical methods that can homogenize and degas the melt and increase the wettability of reinforcement particles in the fabrication of magnesium alloy based MMCs.

2.6 Present work

Ultrasonic technology is an effective means of treating the solidifying metal that can significantly affect heat and mass transfer in melts, modify the structure and properties of solidified alloy. These structural changes arise due to the processes in the molten metal such as crystal nucleation, dispersion, and homogenization induced from the ultrasound. This work is concerned with the evolution of microstructure and study of properties of commercial magnesium alloys after treatment with high intensity ultrasound.

2.7 Objectives

Following are the objectives of this work.

1. To study the microstructural evolution in AZ91 and AZ31 magnesium alloys upon application of high intensity ultrasonic vibrations to their melts. Study and optimization of various ultrasonic processing parameters like ultrasonic intensity, processing time, and different (isothermal and non-isothermal) processing conditions on the solidified microstructures and mechanical properties of these Mg alloys will be done.
2. To study the individual and combined effect of nano carbon black inoculation and high intensity ultrasonic processing in cast magnesium alloys (AZ31, AZ61, and AZ91) and to compare the mechanical properties of differently processed alloys.
3. To fabricate reactively synthesized and ultrasonically processed in situ Mg alloy MMCs and to study their microstructural evolution, mechanical properties, and sliding wear properties.

Chapter 3

EXPERIMENTAL PROCEDURE

In this chapter, the experimental procedures used in the present investigation are discussed in detail. The experiments were carried out on the AZ series alloys with varying aluminium contents in the alloy.

3.1 Procurement of the material

3.1.1 Magnesium alloys (AZ series)

Magnesium alloy is procured in the form of cast ingots supplied by M/s. Exclusive Magnesium Private Limited, A. P., India. To analyse the effect of Al content on microstructure and mechanical properties of ultrasonicated AZ series magnesium alloys AZ31, AZ61, and AZ91alloys are selected for investigation. Their nominal composition is given in Table 3.1.

Table 3.1 Nominal chemical composition of AZ31, AZ61, and AZ91 magnesium alloys [Busk (1987)].

Magnesium alloys	**Element content (wt %)**						
	Mg	**Al**	**Zn**	**Mn**	**Fe**	**Si**	**Ni**
AZ31	Balance	2.95	0.73	0.30	0.07	0.05	0.004
AZ61	Balance	5.91	0.73	0.30	0.07	0.05	0.004
AZ91	Balance	8.91	0.73	0.30	0.07	0.05	0.004

Mg-Al phase diagram is shown in Fig. 3.1. From the equilibrium diagram, the approximate liquidus and solidus temperatures of the AZ91 alloy are determined as 602 °C and 490 °C, respectively. Liquidus and solidus temperatures of the AZ31 alloy are 632 °C and 598 °C and for AZ61 alloy 618 °C and 527 °C, respectively.

3.1.2 Raw material for carbon inoculation

Carbon black powder having average particle size of 0.042 µm, 99.9 pct metal basis purity (Alfa Aesar, USA) is used for carbon inoculation of the magnesium alloy melts.

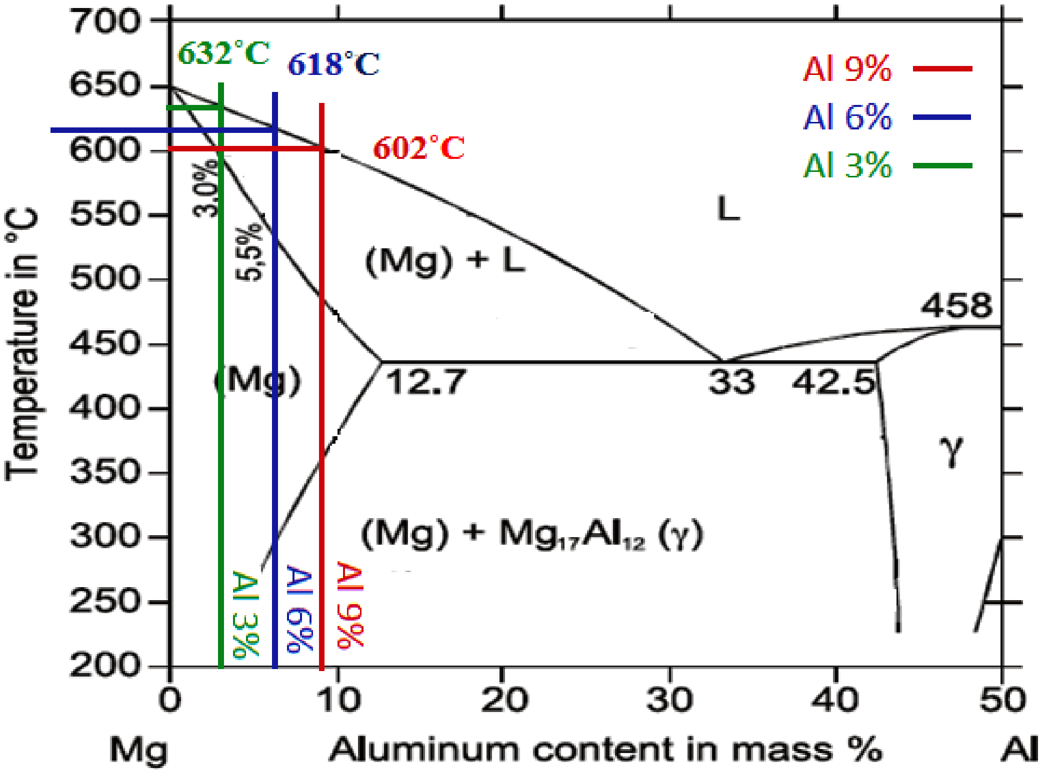

Fig. 3.1 Phase diagram of Mg-Al binary alloy showing alloy composition used in this work. [Friedrich, (2006)]

3.1.3 Magnesium nitrate powder

Magnesium nitrate ($Mg\ (NO_3)_2$) powder is used as a reactant in order to form reinforcement particles from in-situ reaction with AZ series of magnesium alloys.

3.2 Experiments

3.2.1 Experimental set up

A schematic of the experimental apparatus for ultrasonic treatment is shown in Fig. 3.2. The ultrasonic system consisted of a high power ultrasonic probe unit (Model VCX1500, Sonics and Materials, USA). It consists of a 1.5 kW electric power supply, a 20 kHz acoustic generator, an air-cooled converter that is made from piezoelectric lead zirconate titanate crystals and an acoustic radiator made of Ti-6Al-4V titanium alloy. The ultrasonic probe vibration intensity could be continuously adjusted from 0 to 5.4 $kW.cm^{-2}$, which is the maximum intensity of the unit. During the treatment, temperature of the melt and the time of application of the ultrasonic vibrations were precisely controlled. The radiator is coated with zirconia baked at 100 °C, for inertness and to protect it from deterioration that might occur at high working temperature. The coating remained intact after the ultrasonic processing of melts. After ultrasonic processing, it is observed that the zirconia coating provides enough protection to probes from damage (Fig. 3.3).

3.2.2 Experimental procedure

Melting of magnesium alloys was carried out in a mild steel crucible, in an atmosphere controlled electric resistance furnace. In each experiment, charge was melted in furnace at a temperature that was about 75 ºC higher than its liquidus temperature, in order to allow complete dissolution. It was maintained at that temperature for an half an hour. In order to prevent oxidation of molten magnesium, continuous flow of argon was maintained through the sealed furnace chamber. A thermocouple was inserted into the molten metal to acquire the temperature throughout the process. Before ultrasonic processing, the ultrasonic probe is preheated to the processing temperature. As soon as the melt was cooled down to the processing temperature, the ultrasonic probe was quickly lowered into the melt and subjected to ultrasonic vibration for a specific period. A few experiments were performed by varying ultrasonic intensity and processing time in order to study their effect on the grain refinement of magnesium alloys [Panigrahi, et al. (2012)]. During these experiments other variables such as temperature, composition, cooling conditions etc. were kept constant. After the processing, the crucible was quenched immediately in water. For comparison, control specimen (without subjecting to ultrasonic vibrations) castings were made similarly. The cooling conditions were consistent among all the experiments in order to ensure that the difference in the microstructure obtained results almost exclusively from the difference in the irradiation conditions.

In present work, three different methods were used for microstructural refinement and to improve the mechanical properties of magnesium alloys by using UST. These were-

I. UST processing under isothermal holding and continuous cooling conditions
II. Carbon inoculation combined with UST processing
III. In-situ magnesium alloy MMCs fabrication.

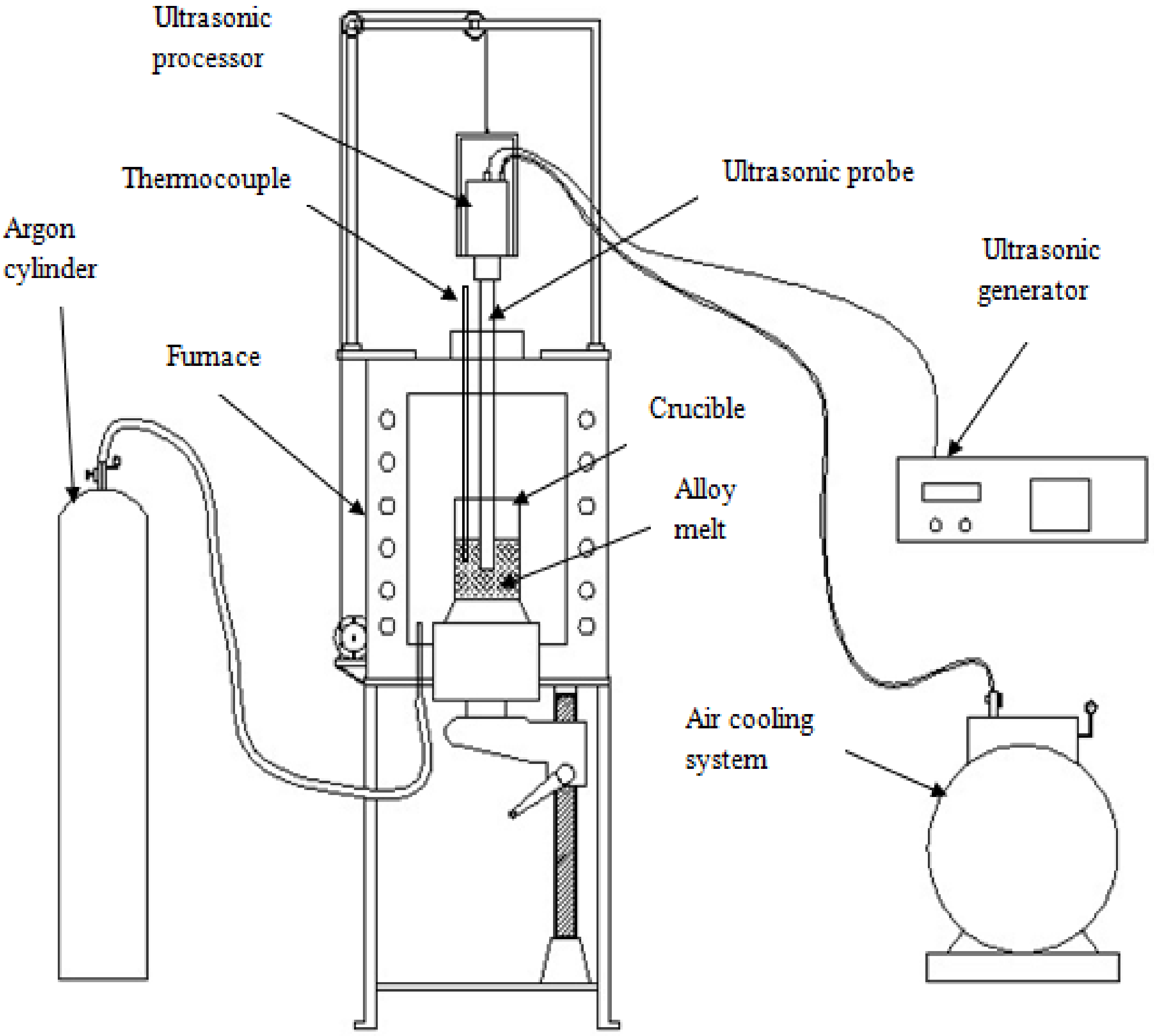

Fig. 3.2 Schematic of the experimental arrangement employed for ultrasonic treatment of magnesium alloys.

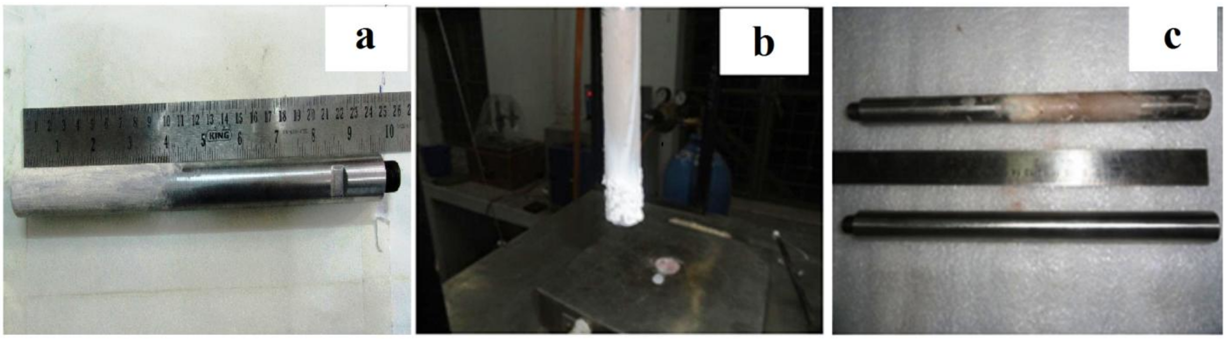

Fig.3.3 Zirconia coated ultrasonic probe. (a) before processing, (b) during processing, and (c) after processing and cleaning.

I. Ultrasonic processing under isothermal and continuous cooling conditions

Experiments were performed under high intensity ultrasonic vibrations with varying amplitude from 0-4.31 kW.cm^{-2} intensity. Grain refinement in AZ91 and AZ31 alloys is studied under different melt conditions. One when the ultrasonic vibrations were applied under isothermal conditions and other under continuous cooling conditions.

Melting of AZ91 and AZ31 alloys was carried out in the mild steel crucible having diameter of 50 mm and a height of 110 mm, heated in an atmosphere controlled electric resistance furnace. In each experiment, 200 g of charge was melted in furnace at 670°C and 705°C, that is about 75°C higher than its liquidus temperature of AZ91 and AZ31 respectively, in order to allow complete dissolution. The melt was cooled down to the processing temperature (that is 598 °C and 627 °C for AZ91 and AZ31, respectively) the ultrasonic probe was quickly lowered into the melt and subjected to ultrasonic vibrations for a specific period. Experiments were carried out with different processing conditions like, varying processing intensity and processing time. Different ultrasonic probe vibration amplitudes of 15 µm, 30 µm and 45 µm were employed which correspond to ultrasonic intensities of 1.3 kW.cm^{-2}, 2.7 kW.cm^{-2}, and 4.3 kW.cm^{-2}, respectively. The intensity of ultrasound is calculated using equation (3.1) [Eskin, (1998)].

$$\mathbf{I = \frac{1}{2}\rho C(2\pi f A)^2} \tag{3.1}$$

Where, ρ is liquid density in (1.584 for liquid magnesium) g.cm^{-3}, C is speed of sound (1500 m.s^{-1} in molten Mg), f is ultrasonic frequency (20 kHz), A is amplitude of ultrasound.

In isothermal processing, temperature of the molten magnesium alloy was kept constant below its liquidus temperature, corresponding to estimated 10 pct solid fraction present at the time of processing. After ultrasonic processing, the crucible was withdrawn from the furnace and immediately quenched in water. For comparison, the control specimen (without ultrasonic vibration) castings were made similarly. In continuous cooling processing, when molten alloys reach to the processing temperature, the crucible was withdrawn from the furnace and ultrasonically processed in an inert atmosphere where alloy was cooled continuously. After ultrasonic processing, the crucible was immediately quenched in water.

II. Carbon inoculation processing combined with the UST

Melting of magnesium alloys was carried out in the mild steel crucible (height - 70 mm, diameter-50 mm and wall thickness- 3 mm), heated in an atmosphere controlled electric resistance furnace. In each experiment, 250 g (AZ91, AZ61 and AZ31 alloys) of charge was melted in the electric furnace at 700 °C, a temperature higher than the liquidus temperature in order to allow for complete dissolution and melt was maintained at 700 °C for 30 minutes. After the processing, the crucible was withdrawn from the furnace and immediately cooled in water. Experiments were performed at 700 °C with three different conditions. These were- carbon black addition alone with manual stirring, carbon black addition coupled with ultrasonic processing, and the control specimen (without ultrasonic vibration and no carbon addition). After the charge dissolved completely, 0.25 wt pct of inoculants was added to the melt. Ultrasonic processing was performed nearly isothermally at 700 °C using processing time of 180 s. Constant ultrasonic vibration amplitude of 48 μm was used.

III. In-situ MMCs processing

These experiments were performed on 400 g AZ91 (and AZ31) alloy melts at 700°C with three different conditions. These were- magnesium nitrate additions accompanied with manual stirring, magnesium nitrate additions coupled with ultrasonic processing, and the control specimen (without magnesium nitrate additions and without application of ultrasonic vibrations). At 700°C, when the charge is liquid, magnesium nitrate (1, 5 and 10 pct by weight) was added to the both the alloy melts for the in situ formation of particles. Manual or ultrasonic stirring was done for uniform distribution of in situ formed particles. Before UST, the manual stirrer or ultrasonic probe was preheated to the processing temperature. Ultrasonic processing was performed isothermally at 700 °C for 180 s by using ultrasonic intensity of 4.3 $kW.cm^{-2}$. After application of different processing conditions mild steel crucible (size-height - 70 mm, diameter- 50 mm and wall thickness- 3 mm) was immediately cooled in water. The heating and cooling conditions were consistent among all the experiments in order to ensure that the difference in the microstructure and mechanical properties results exclusively from the difference in process control variables.

3.2.3 Microstructural studies

Microstructural characterization of unprocessed and UST processed magnesium alloy and its MMCs was performed by using optical light microscope, field emission scanning electron microscope (FE-SEM), along with an energy dispersive X-ray (EDAX) spectrometer, X-ray diffraction (XRD) and transmission electron microscopy (TEM).

A. Optical microscopy

It is an instrument is used to obtain magnified image of cast samples using visible light. In general, it consists of light source, objective lens, condenser and ocular or eyepiece. A recording device can replace the eyepieces. In research, optical microscopy is used for the inspection, analysis, and testing of microstructure of materials, analysis of phase distribution and in MMCs, it is used for determination of distribution of reinforcements. A Leica DMI 5000M microscope was used for optical microscopy (Fig. 3.4).

Fig. 3.4 Leica (DMI 5000M) optical microscope was used for optical microscopy.

Following were the steps involved to prepare sample for optical microscopy.

(i) Sample cutting

After casting, specimens were cut from the centre of the longitudinal section of each casting by using diamond cutter. To ascertain if the ultrasonic processing effects were uniform across the magnesium alloy casting, specimens from different positions were also selected for optical microscopy.

(ii) Grinding or pre-polishing

After cutting, the specimens were flattened by using belt grinder. This grinding also removes the strain-hardened layer produced by cutting process.

(iii) Paper polishing

After grinding, the specimens were polished manually by using different grades of polishing papers (paper grades used were P600, P800, P1000, P1200, P2000 and P2500). Specimens were polished on same paper until the removal of previous scratch marks. While shifting to the next grade emery paper, specimen was rotated by 90°. In this way each specimens was polished up to finest emery paper.

(iv) Diamond polishing

After paper polishing, for finer polishing the specimen were polished using diamond paste. Diamond paste is a type of polishing compound made up of fine grounded powder of diamond particles in pest form. This paste is applied on polishing cloth of polishing machine and diamond polishing extender fluid is used for distribution of diamond paste evenly on the polishing cloth. In present study, two grades of diamond paste were used 1 µm and 0.25 µm.

(v) Cleaning and drying

After diamond paste polishing, specimens were cleaned with ethanol and dried by blowing air on specimen.

(vi) Etching

After cleaning with pure ethanol, the specimens were etched by swabbing with a solution of acetic picral (10 ml acetic acid, 4.2 g picric acid, 10 ml H_2O and 70 ml ethanol) in order to increase the contrast between the primary phase and the intermetallic phases. By using this method optical and SEM specimens were prepared.

(vii) Average grain size measurement

The mean linear intercept method was used to determine the average grain size [Metals Handbook, (1973)].

B. The field emission scanning electron microscope (FESEM)

A FEI-Quanta 200 FE-SEM (Fig. 3.5) was used in secondary electron imaging mode. An energy dispersive X-ray (EDAX) spectrometer was used for detecting different elements. EDS was used for elemental mapping of magnesium alloys.

Fig. 3.5 Scanning electron microscope used for characterization of magnesium alloys.

C. The transmission electron microscope (TEM)

The transmission electron microscope in bright Field (BF)/Dark Field (DF) modes provides information about the size, morphological, compositional, and crystallographic characteristics. In present study, the Tecnai G^2 20 S-twin TEM (FEI Neitherlands) was used for the analysis of carbon black nano powder (Fig.3.6).

D. X-ray diffraction (XRD)

X-ray diffraction (XRD) is used for phase identification in specimens. A Bruker D8 (advance) X-ray diffractometer was used (Fig. 3.7). It was used for the confirmation of new in situ formed phases in the cast MMCs. X-ray diffraction patterns were obtained by employing Cu, Kα radiation with 2θ ranging from 20º to 120º. For all the diffraction peaks and corresponding values of 2θ, the inter-planer spacing, d, was calculated using the Bragg’s law. For identifying the various phases, inorganic JCPDS X-ray diffraction database was used.

Fig. 3.6 200 kV TEM is used for the analysis of carbon black nano powder.

3.2.4 Measurement of mechanical properties

A. Hardness

Hardness tests were performed using a FIE-VM50 PC Vickers hardness tester by employing 5 kg load. The requirements for the testing are that the samples should be properly ground and polished for precise measurement of indentation. Hardness testing was done on Vickers hardness testing machine shown in Fig. 3.8, which has a software for accurate measurement of VHN. At least five hardness readings were obtained and the average is reported along with standard deviation.

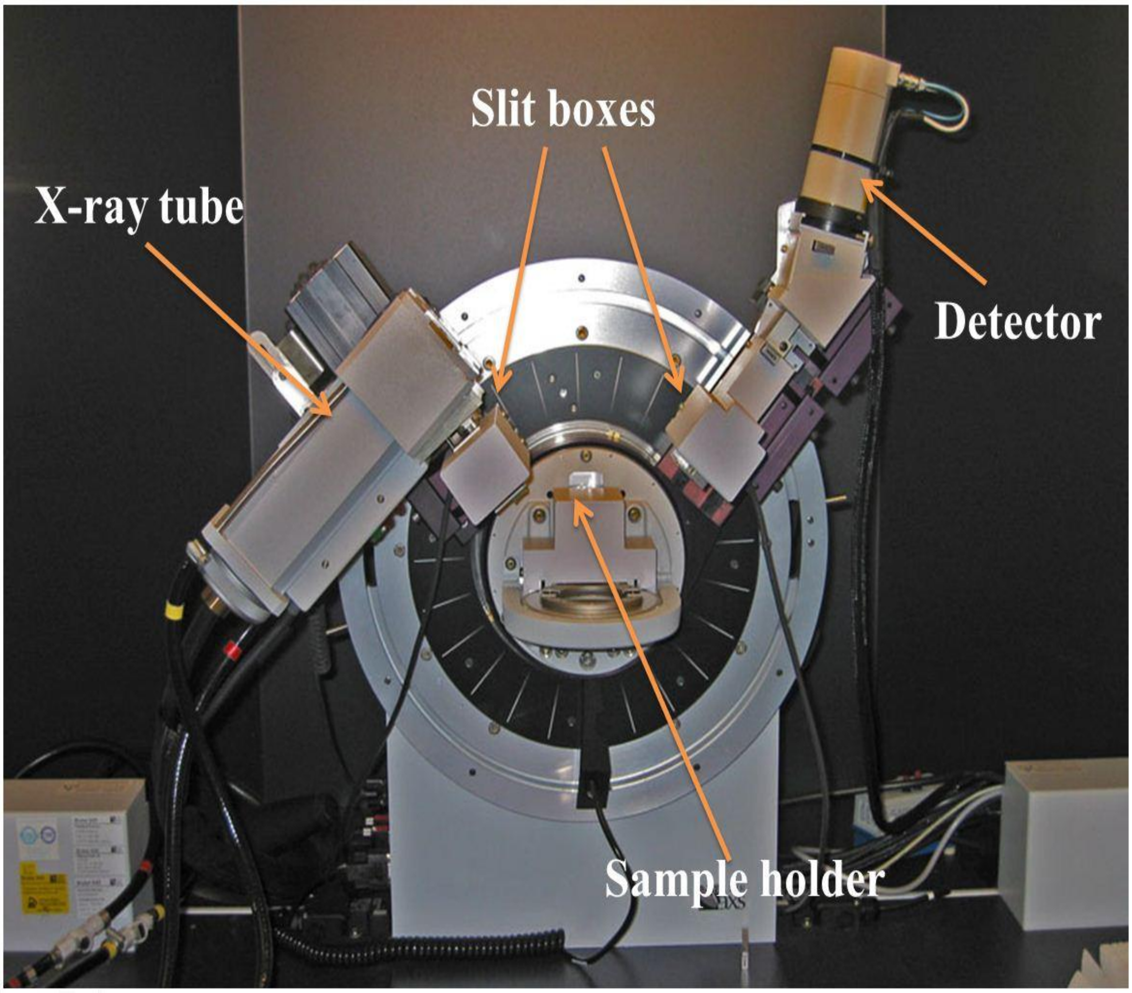

Fig. 3.7 Actual setup of X-ray diffraction (XRD) used for the analysis.

B. Tensile testing

Fig. 3.9 shows the tensile test specimens used for testing that were fabricated from differently cast magnesium alloys. Tensile test specimens round in cross section (diameter- 4 mm and a gauge length of 20 mm) were machined from each casting. Tensile tests were conducted at room temperature by employing a constant crosshead speed of 0.1 mm.min^{-1}, using a H25 K-S Tinius Olsen tensile testing machine as shown in Fig. 3.10.

C. Compression testing

Compression tests were performed on MMCs using Gleeble® 3800 thermomechanical simulation machine that is shown in Fig. 3.11, at room temperature using strain rate of 9.5×10^{-4} s^{-1}. The specimens used for compression testing were 10 mm in diameter and 12 mm in gauge length. Three specimens were tested for each condition. Yield stress (σ_y) is estimated from the stress-strain data taking the flow stress at 0.2 % offset strain while σ_{max} is maximum value of flow stress.

Fig. 3.8 Vickers hardness tester set up used for the measuring hardness.

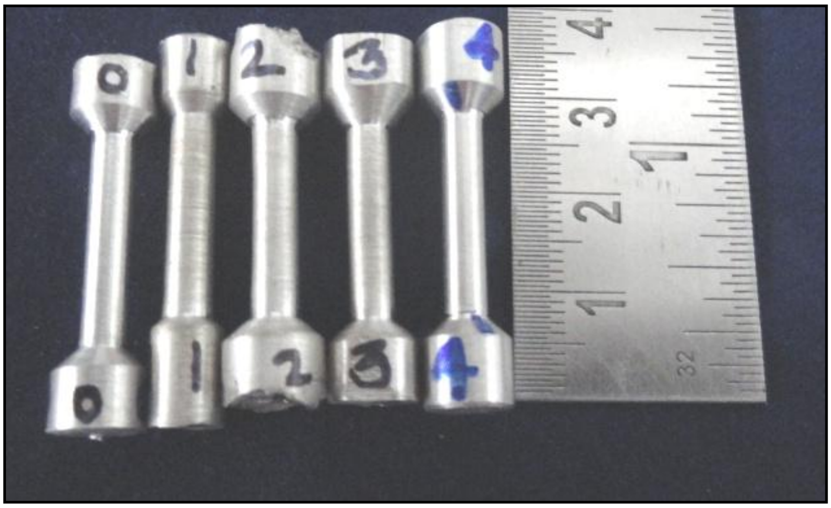

Fig. 3.9 Tesnile test specimens fabricated from differently cast magnesium alloys.

Fig. 3.10 H25 K-S Tinius Olsen tensile testing machine used for the tensile testing.

Fig. 3.11 Gleeble®3800 machine used for compression testing experiments.

Dry sliding friction and wear test (Pin-on-Disc test rig)

The machine used for wear testing of in-situ magnesium alloy was wear and friction monitor TR-20 (pin on disc machine) manufactured by M/s. Ducom, Bangalore. Pin samples were made from in-situ magnesium alloys reacted with magnesium nitride having different wt pct and ultrasonically processed/unprocessed conditions. The pin specimen was kept stationary, while the circular disc rotated during the testing. The wear tests were performed under unlubricated conditions at room temperature referring ASTM G99 standard. The wear disc, made up of EN32 steel disc of 215 mm diameter was used for the wear test. The test sample was clamped in a holder and holder clamped on loading arm against the rotating disc, as shown in schematic diagram of Fig. 3.12. Wear and friction machine with monitor used for experiments is shown in Fig. 3.13.

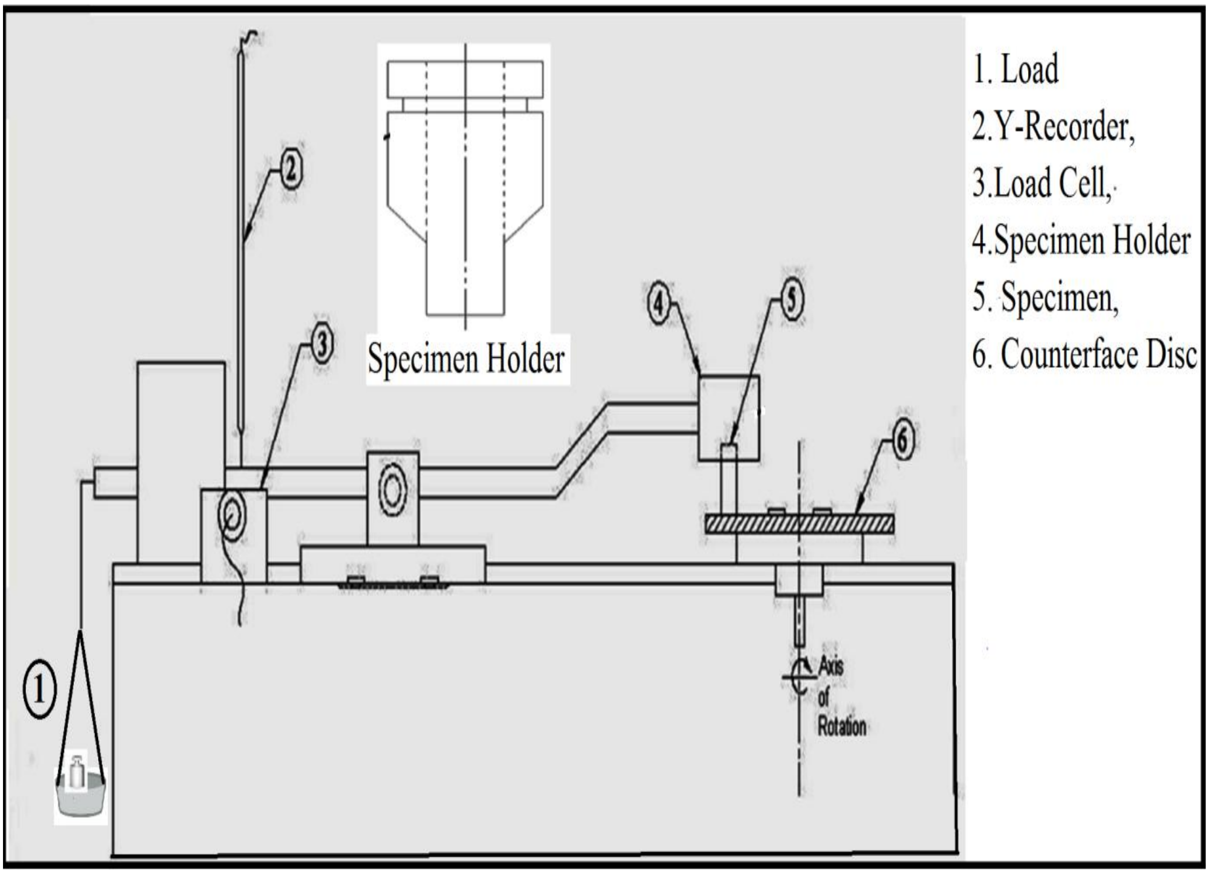

Fig. 3.12 Schematic diagram of pin on disc un-lubricated sliding wear testing machine is used in study.

Preparation of specimens for wear testing

Pin specimens were fabricated form cast magnesium alloy in the size of 12 mm in height and 5 mm in diameter. The surface roughness of the counter face of specimens and wear disc were maintained similar by polishing with 1000 grit paper. Specimen and disc both were cleaned with acetone before and after the test in order to remove any possible surface contamination. Table 3.2 shows the pin-on-disc test parameters used for the wear test for the AZ91 and AZ31 alloys and its MMCs. Before and after each wear test, after cleaning and drying, the specimen was weighed by using electronic balance (Mettler AJ100) having accuracy of 0.0001 g. The reading of frictional force was noted after equal interval of time directly from the display of load cell (Fig. 3.12).

The worn surfaces were observed by using FEI-Quanta 200 FE-SEM. Debris was collected after each test and it was studied using FEI-Quanta 200 FE-SEM, and Bruker D8 XRD for analysis of phases involved in the wear phenomenon. A separate specimen was used for each test and three tests were performed for each material condition. After wear test, the mass loss was measured and the average of three samples is recorded.

Fig. 3.13 Wear and friction (pin-on disc) machine used for conducing wear experiments.

Fig. 3.14 Electronic balance (Mettler AJ100) having accuracy of 0.0001 g used for weighing.

Table 3.2 List of pin-on-disc test parameters selected for the experiments.

Wear disc material	EN32 grade steel
Pin specimen	AZ91 alloy, AZ31 alloy and AZ31 alloy based in-situ MMCs
Applied force	4.9 N, 9.8 N and 14.7 N
Velocity	1 ms^{-1}
Test length (sliding distance)	500 m,1000 m and 2000 m
Temperature	23 °C
Humidity	40 pct

Chapter 4

RESULTS AND DISCUSSION:

ULTRASONIC PROCESSING OF AZ91 AND AZ31 ALLOYS

4.1 Microstructural studies

Unprocessed AZ91 alloy

Fig. 4.1 shows the optical micrograph of AZ91 alloy cast by cooling the crucible in a water bath, without ultrasonic treatment. Coarse dendrites with branch lengths as long as 250 μm in length can be noticed. It shows dendrites of primary α-Mg phase and a second phase is present in the inter-dendritic areas. These phases are estimated using EDS analysis as follows.

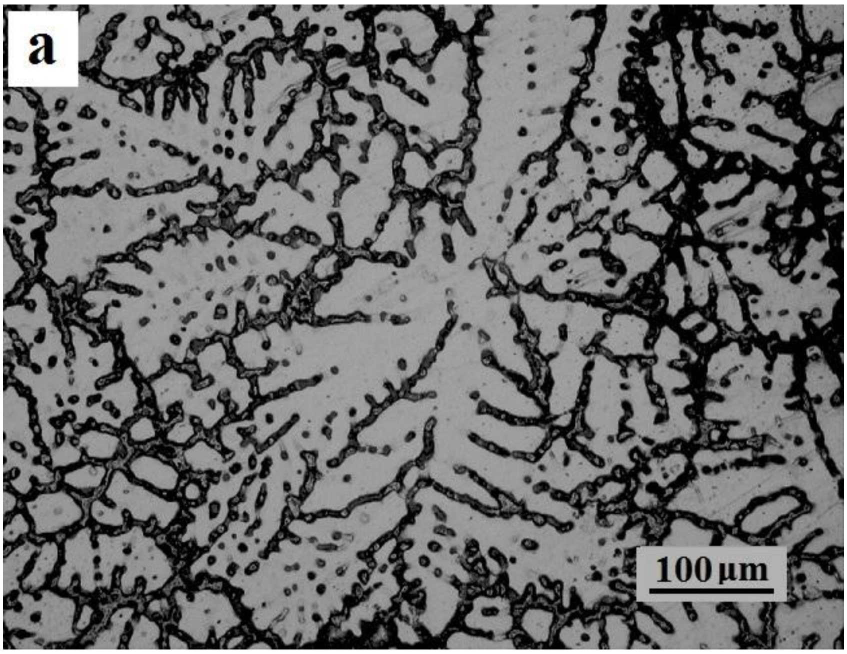

Fig. 4.1 Optical micrograph of the unprocessed cast AZ91 alloy.

Microstructures were characterized for the composition and distribution of various phases in order to evaluate the effect of UST. Fig. 4.2 shows SEM micrograph and EDS patterns corresponding to the identified regions shown by arrow, of the AZ91 alloy. Table 4.1 presents the results of semi-quantitative EDS analysis of the phases marked in Fig. 4.2. It can be observed that the microstructure is a composed of the primary α-Mg phase with β-$Mg_{17}Al_{12}$ phase segregated along the grain boundaries.

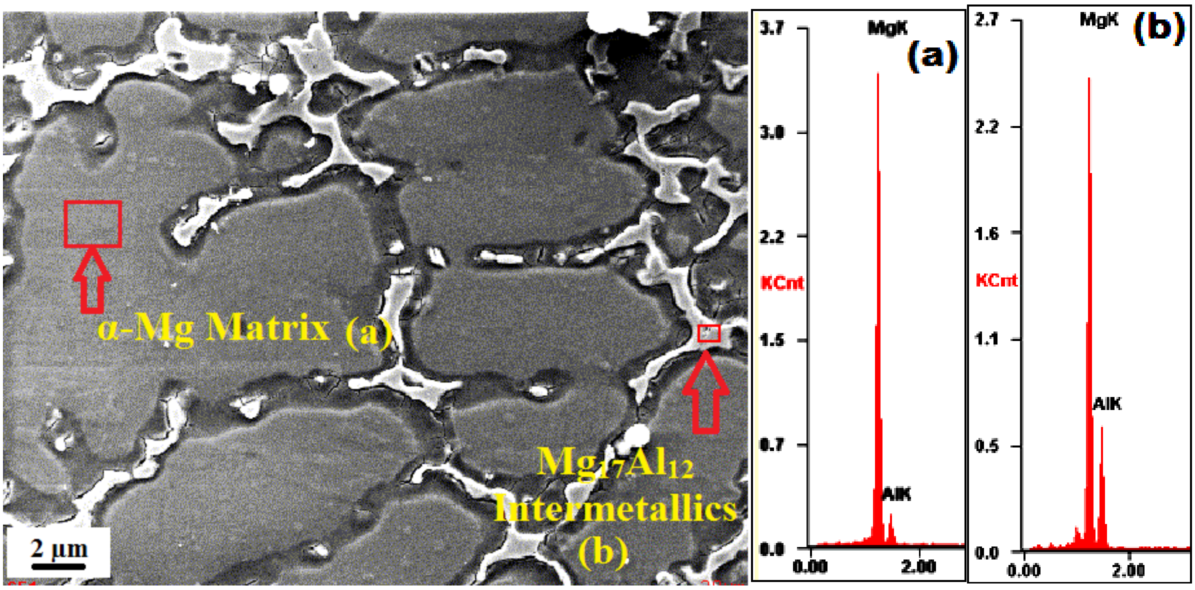

Fig. 4.2 SEM micrograph and EDS patterns corresponding to the (a) α-Mg phase, and (b) β-$Mg_{17}Al_{12}$ phase of the AZ91 alloy.

Table 4.1 Results of EDS analysis depicting weight pct and atomic pct of elements present at different locations of Fig. 4.2 and the estimated phases.

Phase	**Normalized Composition**			**Estimated Phase**
	Element	**Weight pct**	**Atomic pct**	
(a)	Mg	89.6	91.0	α-Mg Matrix
	Al	09.5	08.7	
	Zn	0.89	0.34	
(b)	Mg	62.1	66.1	$Mg_{17}Al_{12}$ Intermetallics
	Al	33.6	32.2	
	Zn	04.3	1.7	

In order to determine the distribution of phases, X-ray elemental mapping is performed. Fig. 4.3 shows the SEM micrograph and X-ray elemental mapping of AZ91. AZ91 alloy shows pronounced dendritic growth (Fig. 4.3a). Figs. 4.2b shows that aluminium element is present only along the grain boundary as secondary $Mg_{17}Al_{12}$ phase and small amount of Zn present throughout the matrix.

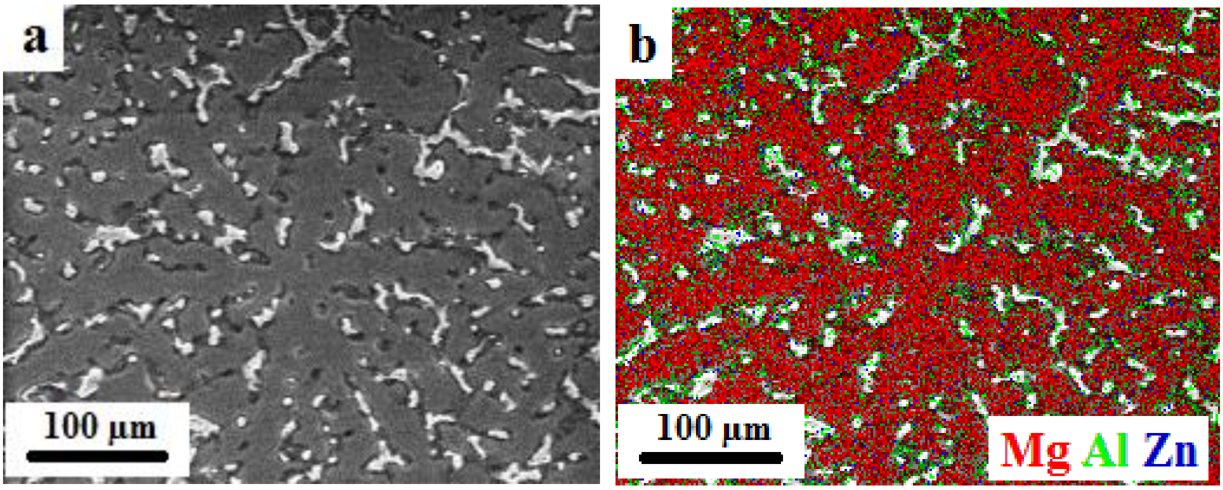

Fig. 4.3 (a) SEM micrograph, and (b) X-ray elemental mapping of unprocessed AZ91 alloy.

4.2 Ultrasonic processing of AZ91 alloy during continuous cooling

Fig. 4.4 shows the optical micrographs of AZ91 alloy that was subjected to UST during continuous cooling. The UST is performed at a constant vibration intensity of 1.3 $kW.cm^{-2}$ and varied processing time of 30, 60, and 90 s was used. It is noticed that at constant intensity, UST processing time has significant effect on the microstructure. Increased grain refinement occurred with UST processing time. Compared with unprocessed AZ91 alloy, 30 s UST processed alloy shows grain refinement with grain size reduced to an average of 110 µm (Fig. 4.4-a). It still exhibits dendritic growth but the dendrites are smaller. UST processing for 60 s resulted in further refinement with average grain size reduced to 79 µm, which is a 65 pct reduction as compared with base alloy. It has a mixed structure of smaller dendrites and some equiaxed grains. UST processing for 90 s resulted in more equiaxed microstructure and caused further grain refinement, with average grain size reduced to 66 µm.

Fig. 4.5 shows the optical micrographs of AZ91 alloy that was subjected to UST at a constant intensity of 2.7 $kW.cm^{-2}$ and 4.3 $kW.cm^{-2}$ for various durations during continuous cooling. Fig 4.5a shows that for 2.7 $kW.cm^{-2}$ intensity and 30 s of UST processing time, AZ91 alloy became almost dendrite free with grain size reduction of 61 pct. With an increase in the processing time to 60 s (Fig. 4.5 b-d), grains became globular with 73 pct reduction in the grain size compared with that of the unprocessed AZ91 alloy. Further, after 90 s of UST processing time grains are globular in shape and appear more uniform (Fig. 4.5 c). Average grain size is reduced to 56 μm that is 75 pct reduction compared with the base alloy. Fig. 4.5d-f are the optical micrographs of AZ91 alloy ultrasonically processed at constant intensity 4.3 kW.cm^{-2}. It is observed that at maximum intensity with 30 s processing time the microstructure contained a mixture of fine and large grains. Microstructures are more refined after 60 s and 90 s of ultrasonic processing time. After 60 s of UST time, dense and fine grains are observed. Maximum grain refinement is observed in specimens processed for 90 s using 4.3 kW.cm^{-2} intensity.

Grain size and hardness

Fig 4.6 shows the variation in grain size of AZ91 alloy with UST processing time when different ultrasonic intensities were applied during continuous cooling. It is observed that as the ultrasonic intensity and ultrasonic processing times are increased the grain size decreased sharply in the beginning and moderately later. Fig. 4.7 shows the variation in Vickers hardness (HV) with the UST processing time at different ultrasonic intensities for the continuous cooling condition. As the ultrasonic processing time increased, the hardness of the AZ91 alloy increased at a higher rate in the beginning and moderately at higher UST times for low ultrasonic intensities. Interestingly for the high intensity of 4.3 kW.cm^{-2}hardness increased monotonously with time. Maximum hardness that is found in specimen UST processed with 90 s processing time and constant intensity of 4.3 kW.cm^{-2} is 160 pct higher than that of the AZ91 alloy. Thus, grain refinement resulted in increase in hardness according to the Hall- Petch strengthening.

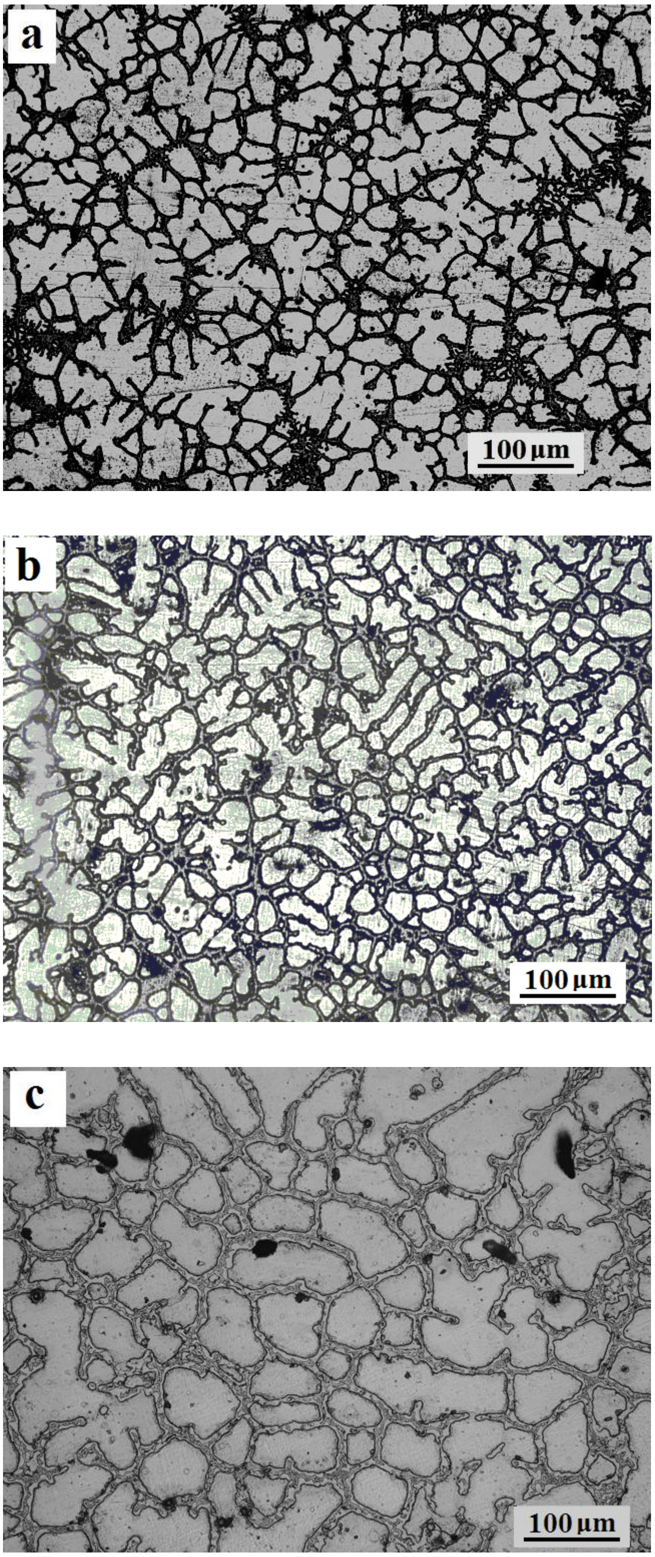

Fig. 4.4 Optical micrographs of AZ91 alloy that was subjected to UST during continuous cooling using constant ultrasonic intensity of 1.3 kW.cm^{-2}. UST processing time is (a) 30 s, (b) 60 s, and (c) 90 s.

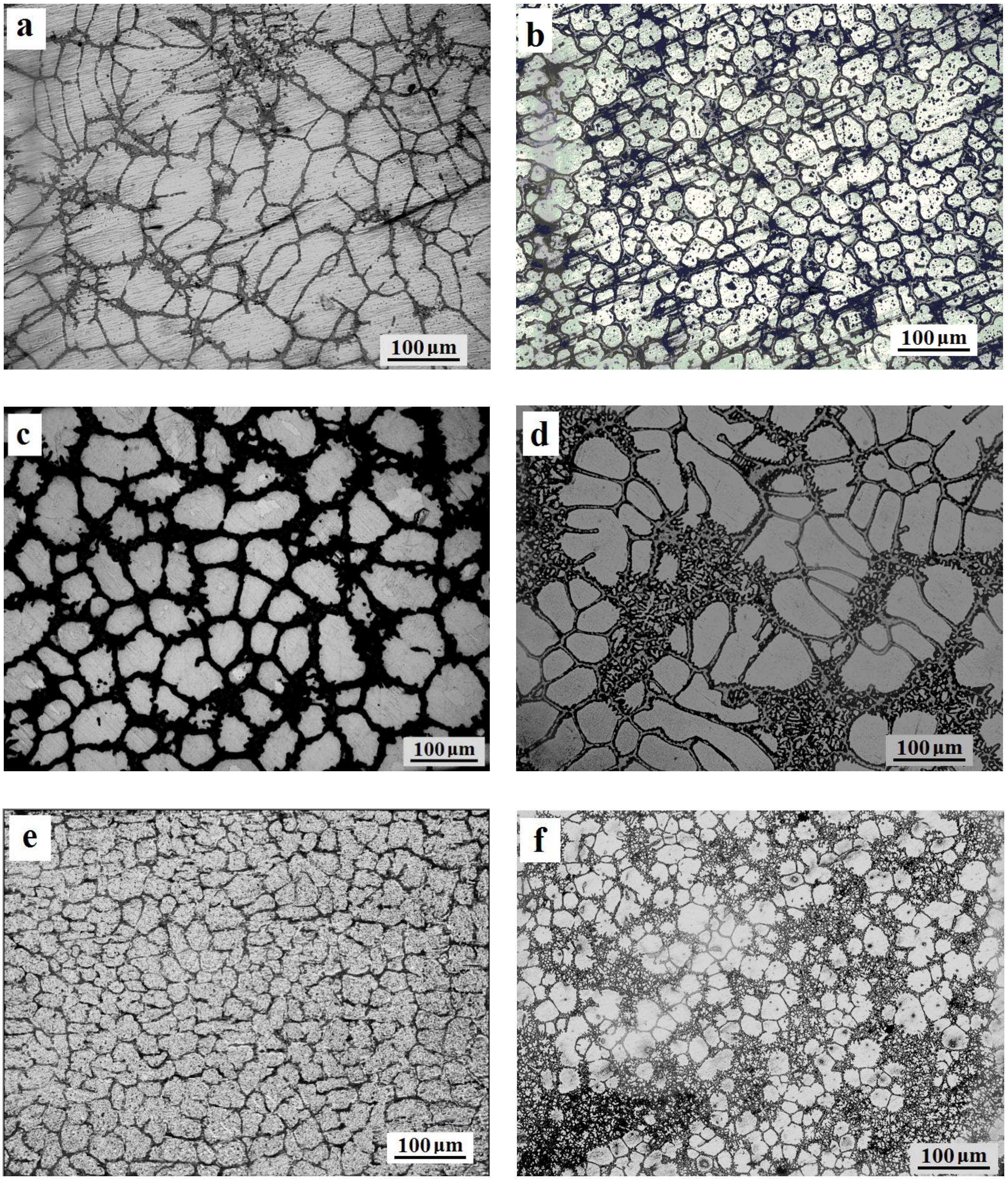

Fig. 4.5 Optical micrographs of AZ91 alloy that was subjected to UST during continuous cooling using constant ultrasonic intensity of 2.7 kW.cm^{-2} and UST processing time of (a) 30 s, (b) 60 s, and (c) 90 s. Figures (d), (e) and (f) show the optical micrographs of AZ91 specimens processed using ultrasonic intensity of 4.3 kW.cm^{-2} for 30, 60, and 90 s, respectively.

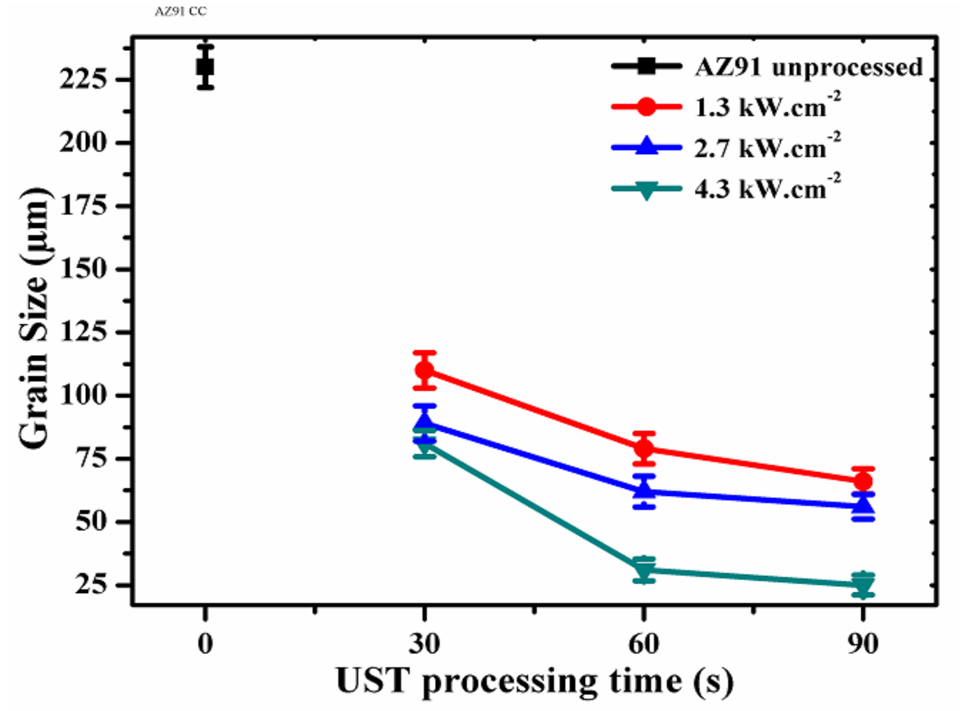

Fig. 4.6 Variation in grain size of AZ91 alloy with UST processing time plotted for different ultrasonic intensities applied during continuous cooling.

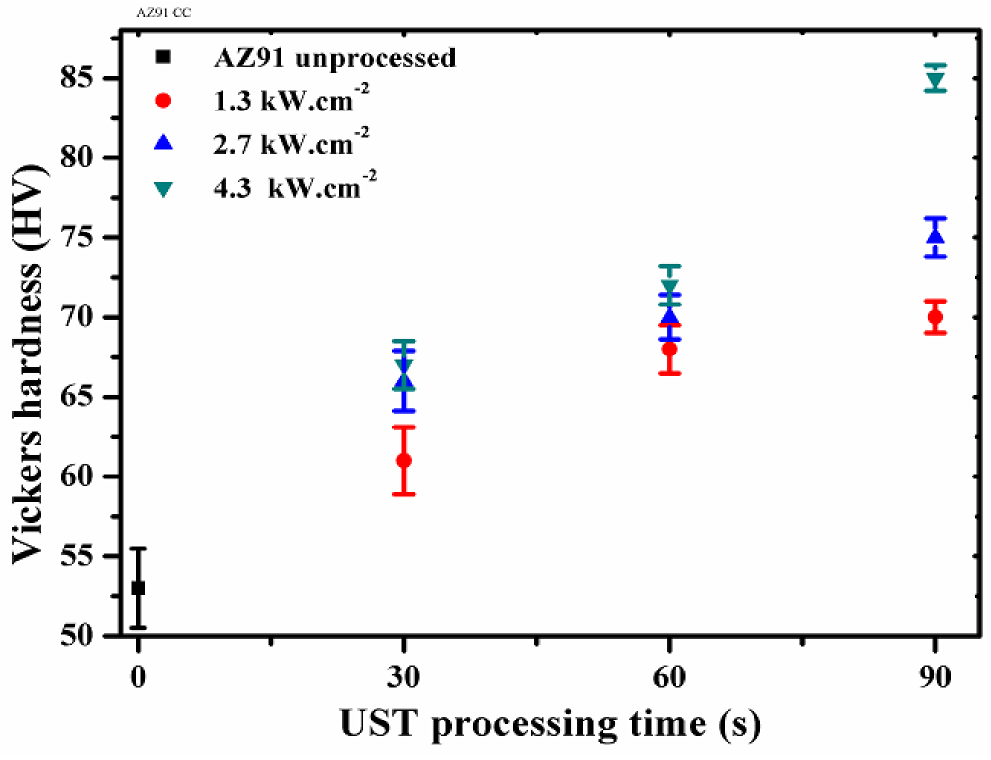

Fig. 4.7 Variation in Vickers hardness of AZ91 alloy with the UST processing time plotted for different ultrasonic intensities applied during continuous cooling.

Tensile test

Figs. 4.8-A,B,C shows the true stress-true strain curves obtained from the tensile tests performed on unprocessed AZ91 alloy, and the AZ91 alloys UST treated at different intensity and different UST processing times. From these three graphs, it is noticed that as UST intensity increases, proof stress, UTS, and total pct elongation of AZ91 alloy increased. This is summarized later in Table 2. Fig. 4.8A shows that at constant intensity (1.3 kW.cm^{-2}), proof stress, UTS, and elongation of AZ91 alloys increased with the UST processing time. At 1.3 kW.cm^{-2} intensity, the highest increment in proof stress, UTS and elongation is observed in 90s UST processing specimen that is 18 pct, 22 pct and 34 pct increase, respectively compared with unprocessed AZ91 alloy. Fig. 4.8-B shows that at constant UST intensity of 2.7 kW.cm^{-2}, proof stress, UTS, and elongation of AZ91 alloys increased with the UST processing time. Again, highest increment of 28 pct, 28 pct, and 42 pct was observed in the proof stress, UTS, and total pct elongation, respectively in specimen UST processed for 90 s as compared with unprocessed AZ91 alloy. Fig. 4.8-C shows that UST performed using 4.3 kW.cm^{-2} intensity for 90 s was most effective. It showed 59 pct, 93 pct, and 92 pct increment in proof stress, UTS, and elongation to failure, respectively, as compared to the unprocessed AZ91 alloy.

4.3 Ultrasonic processing of AZ91 alloy during isothermal holding

A few experiments were performed with ultrasonic treatment done under isothermal conditions at a temperature where 10 pct solid fraction is present in the mushy freezing range. Fig. 4.9 shows the optical micrographs of AZ91 alloy that was subjected to UST during isothermal holding at 598 °C. The UST is performed at a constant vibration intensity of 1.3 kW.cm^{-2} and variable processing time of 30, 60, and 90 s was used. Increased grain refinement occurred with UST processing time. Compared with unprocessed AZ91 alloy (225 μm), 30 s UST processed alloy shows grain refinement with grain size reduced to an average of 102 μm (Fig. 4.9a). UST processing for 60 s resulted in further refinement with average grain size reduced to 73 μm, which is a 67 pct reduction as compared with base alloy (Fig. 4.9b). It has a mixed structure of smaller dendrites and some equiaxed grains. UST processing for 90 s resulted in a microstructure consisting of more globular grains and it caused further grain refinement (Fig. 4.9c), with average grain size reduced to 50 μm that is a 77 pct reduction compared with unprocessed AZ91 alloy.

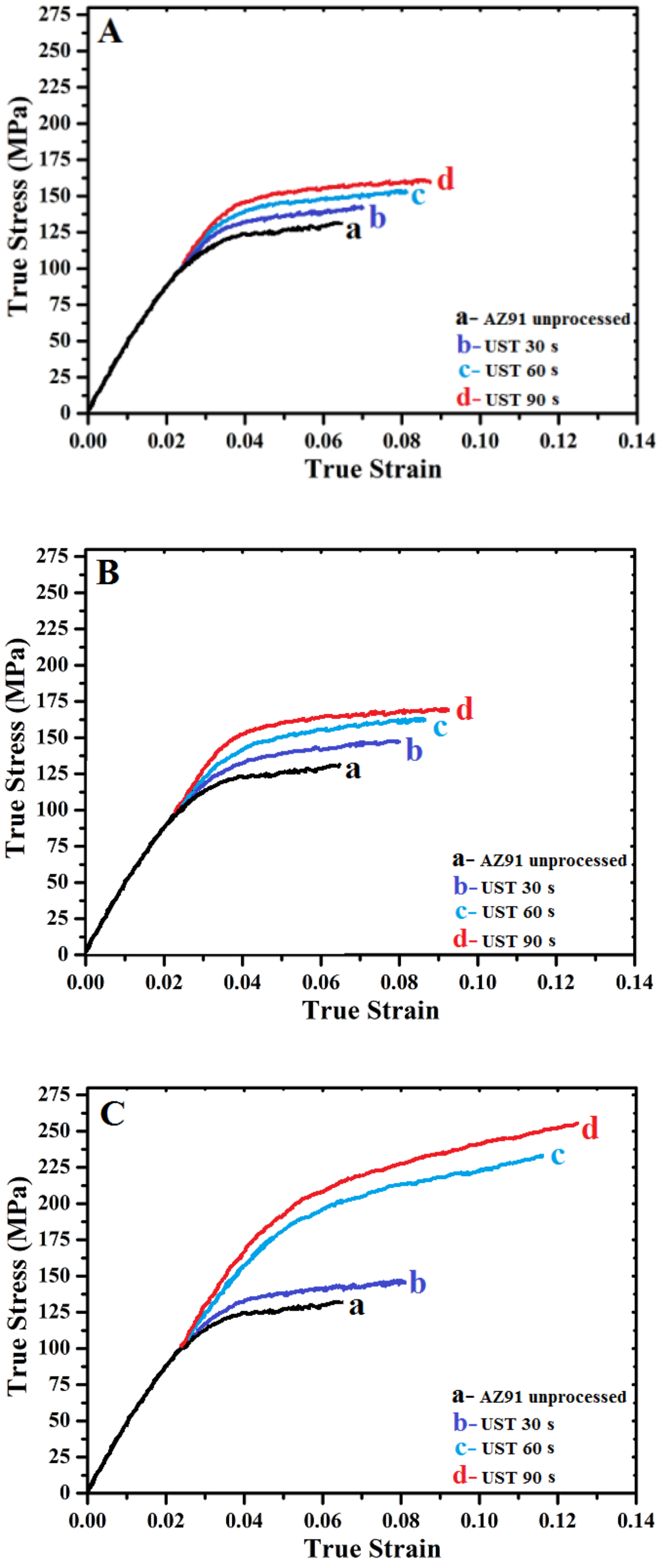

Fig. 4.8 The true stress-true strain tensile test curves for AZ91 alloy ultrasonically treated during continuous cooling using different ultrasonic intensity of (A) 1.3 kW.cm^{-2}, (B) 2.7 kW.cm^{-2}, and (C) 4.3 kW.cm^{-2}, for various processing durations.

Fig. 4.10 shows the optical micrographs of AZ91 alloy that was subjected to UST at constant temperature of 598°C, and using a constant intensity of 2.7 kW.cm^{-2} and 4.3 kW.cm^{-2} for various durations. Fig 4.10-a shows that at intensity 2.7 kW.cm^{-2} and after 30 s of UST processing time, microstructure of AZ91 alloy became dendrite free accompanied with grain refinement. Increase in the processing time from 30 s to 60 s grains resulted in more globular grains. The reduction in the grain size is 66 pct and 77 pct, respectively when compared with AZ91 alloy (Fig. 4.10 a-b).

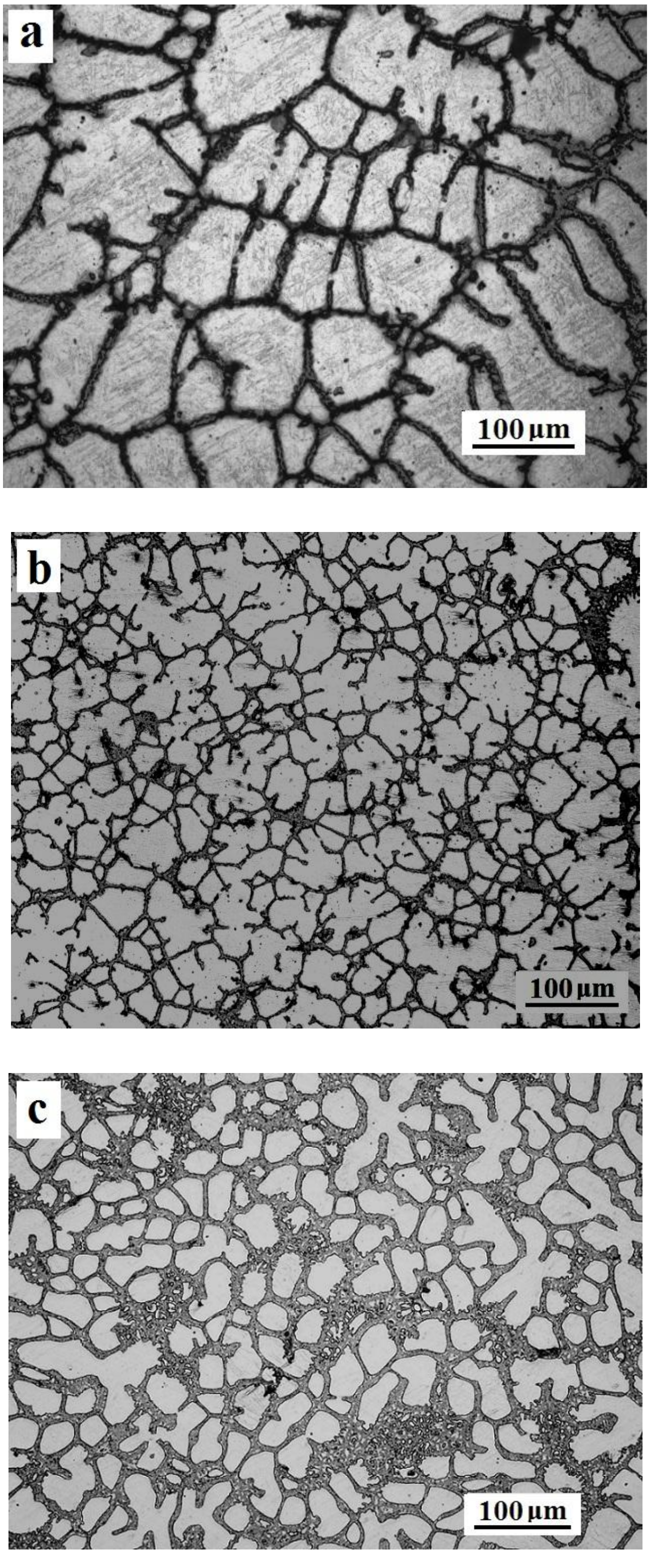

Fig. 4.9 Optical micrographs of AZ91 alloy that was subjected to UST during isothermal holding at 598 °C using constant ultrasonic intensity of 1.3 kW.cm^{-2}. UST processing time is (a) 30 s, (b) 60 s, and (c) 90 s.

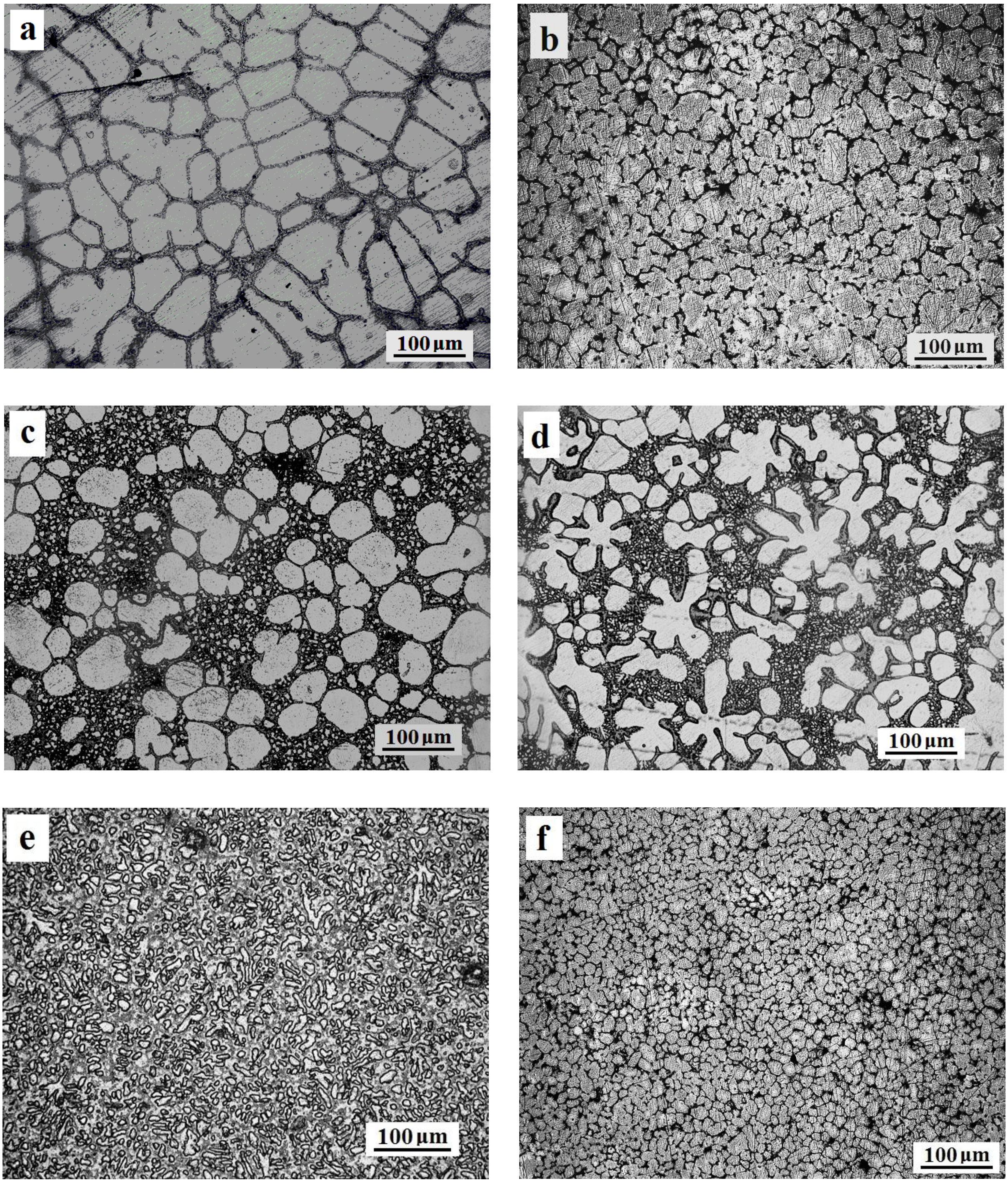

Fig. 4.10 Optical micrographs of AZ91 alloy that was subjected to UST during isothermal holding at 598°C using constant ultrasonic intensity of 2.7 kW.cm^{-2}. UST processing time is (a) 30 s, (b) 60 s, and (c) 90 s. Figures (d), (e) and (f) show the optical micrographs of AZ91 specimens processed using ultrasonic intensity of 4.3 kW.cm^{-2} for 30, 60, and 90 s, respectively.

With further increase in the processing time to 90 s, grains become globular in shape and having a mixture of small and large grains (Fig. 4.10-c). Grain size reduced to 42 μm that is about 81 pct reduction compared with the base alloy. Fig. 4.10 d-f are the optical micrographs of AZ91 alloy UST processed using a constant intensity 4.3 kW.cm^{-2}. It is seen that with a 30 s processing time, there is a mixture of fine and larger dendritic grains having average grain size 61 μm. Microstructures are more refined after 60 s and 90 s processing time. After 60 s of processing time fine grains are observed, however, they are random in size and smallest average grain size of 17 μm is noticed. Better grain refinement is observed after 90 s of processing time with 4.3 kW.cm^{-2} intensity. Compared with the unprocessed AZ91 alloy, it is 91 pct reduction in grain size.

Grain size and hardness

Fig. 4.11 shows the variation in grain size of AZ91 alloy with UST processing time when different ultrasonic intensities were applied during isothermal holding. It is observed that as the ultrasonic intensity and ultrasonic processing times are increased the grain size decreased sharply in the beginning and moderately later. At 4.3 kW.cm^{-2}, most refined microstructure is observed after 60 s of processing time. The average grain size is 17 μm that is about 92 pct smaller than the unprocessed AZ91 alloy. Fig. 4.12 shows the variation in Vickers hardness with the UST processing time, under isothermal holding condition at different ultrasonic intensities. It is observed that as ultrasonic intensity and ultrasonic processing time increased hardness of the UST processed AZ91 alloy increased. Maximum hardness is exhibited by the alloy that was treated for 60 s processing time using a constant intensity of 4.3 kW.cm^{-2}. Hardness is 163 pct higher than that of the unprocessed AZ91 alloy. Thus, grain refinement resulted in increase in hardness according to the Hall- Petch strengthening.

Tensile properties

Fig. 4.13A-C shows the true stress-true strain curves from the tensile tests of unprocessed AZ91 alloy, UST treated at different intensity and different UST processing times under isothermal holding condition. From these three graphs, it is noticed that as the UST intensity increases, the proof stress, UTS, and elongation to failure of AZ91 alloy increased as compared with base alloy. The properties are summarized later in Table 2. Fig. 4.13-A shows that at constant low UST intensity of 1.3 kW.cm^{-2}, the proof stress, UTS, and elongation to failure of AZ91 alloys increased with the UST processing time. It is observed that after 90 s of

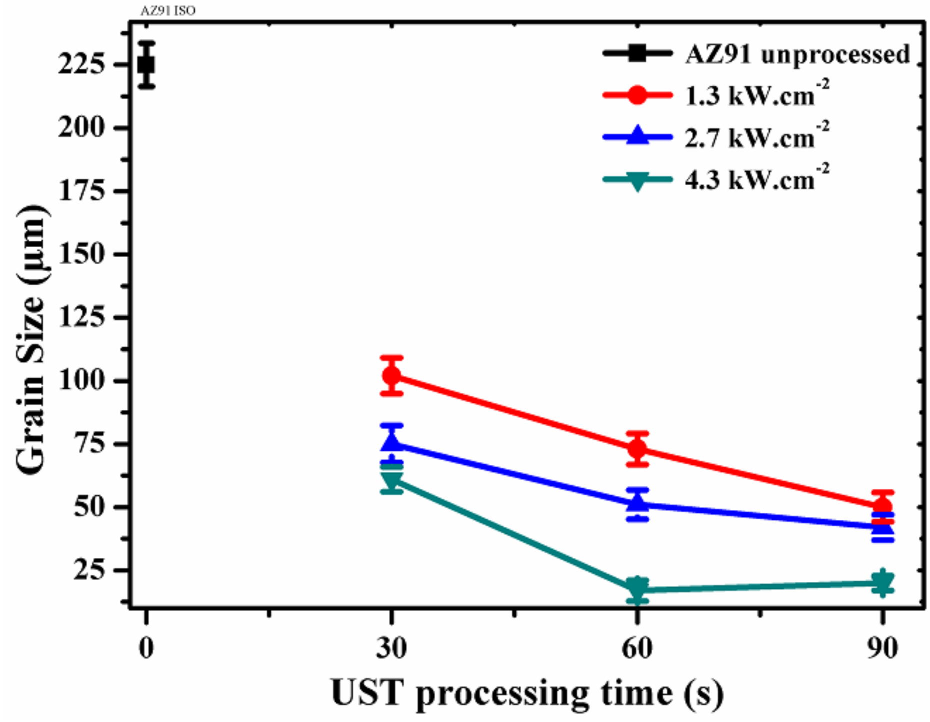

Fig. 4.11 Variation in grain size of AZ91 alloy with UST processing time plotted for different ultrasonic intensities applied during isothermal treatment.

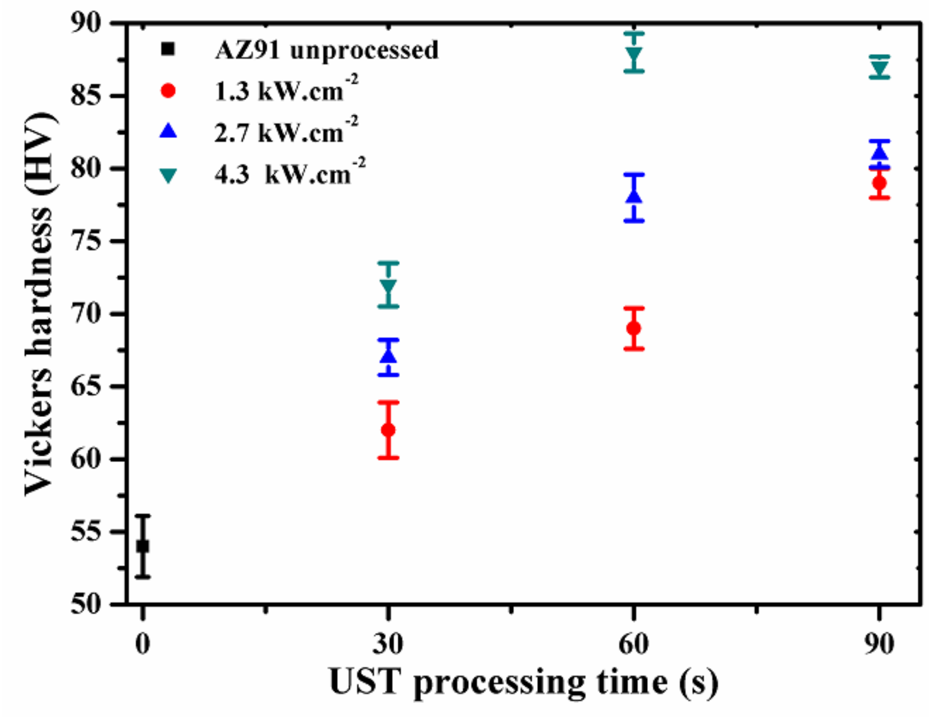

Fig. 4.12 Variation in Vickers hardness of AZ91 alloy with the UST processing time plotted for different ultrasonic intensities applied during isothermal holding at 598 °C.

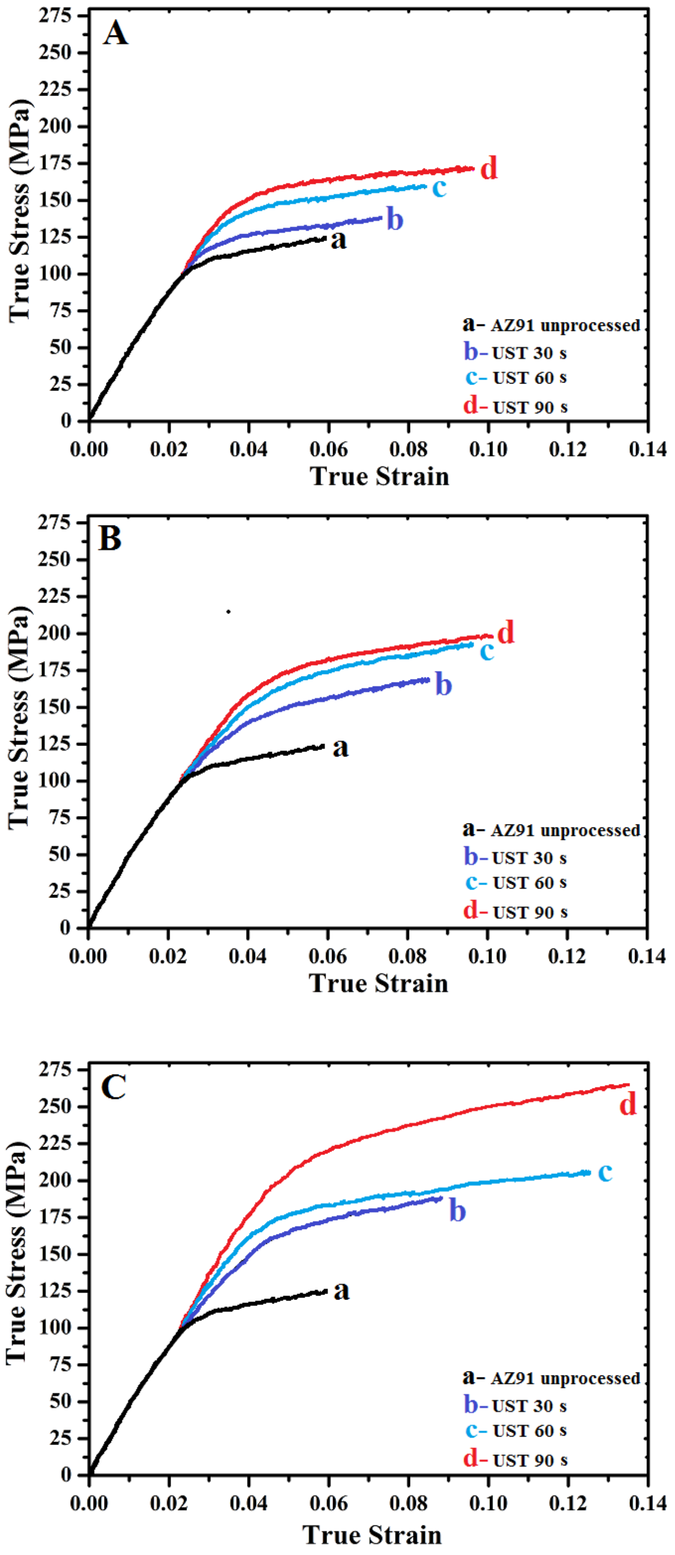

Fig. 4.13 True stress-true strain tensile test curves for AZ91 alloy ultrasonically treated during isothermal holding using different ultrasonic intensity of (A) 1.3 kW.cm^{-2}, (B) 2.7 kW.cm^{-2}, and (C) 4.3 kW.cm^{-2}, for various processing durations.

UST processing at 1.3 kW.cm^{-2} highest increments of 32 pct, 36 pct and 31 pct in proof stress, UTS and elongation to failure, respectively, are obtained when compared with the unprocessed AZ91 alloy.

Fig. 4.13-B shows that at constant UST intensity of 2.7 kW.cm^{-2}, the proof stress, UTS, and elongation to failure of AZ91 alloy increased with processing time. UST processing at 2.7 kW.cm^{-2} for 90 s, increased the proof stress, UTS, and elongation to failure by 37 pct, 58 pct and 38 pct, respectively, when compared with the unprocessed AZ91 alloy. Fig. 4.13-C shows the tensile properties for constant UST intensity of 4.3 kW.cm^{-2} with a variation in the processing time. A highest increment is observed after 60 s of UST processing, which is 68 pct, 112 pct and 84 pct increase in proof stress, UTS, and elongation, respectively, as compared to that of the unprocessed AZ91 alloy.

Table 4.2. Summary of the grain size and mechanical properties of AZ91 alloy UST processed using different process parameters..

Materials	Processing condition	UST intensity	Processing time	Grain size (µm)	Hardness (HV)	Proof stress (MPa)	UTS (MPa)
AZ91	Continuous cooling condition	1.3 kW.cm^{-2}	0	230	53	95	120
			30	110	61	109	142
			60	79	68	114	153
			90	66	70	118	160
		2.7 kW.cm^{-2}					
			30	89	66	112	147
			60	62	70	120	164
			90	56	75	128	169
		4.3 kW.cm^{-2}					
			30	81	67	113	146
			60	31	72	148	233
			90	25	85	159	256
	Isothermal condition	1.3 kW.cm^{-2}					
			30	102	62	106	138
			60	73	69	116	159
			90	50	79	130	171
		2.7 kW.cm^{-2}					
			30	75	67	118	169
			60	51	78	124	193
			90	42	81	135	198
		4.3 kW.cm^{-2}					
			30	61	72	121	188
			60	17	88	165	265
			90	20	86	163	260

Unprocessed AZ31 alloy

Fig. 4.14 shows the optical micrograph of AZ31 alloy cast by cooling the crucible in a water bath, without ultrasonic treatment. Coarse dendritic structure with dendrite branch lengths as long as 235 μm can be seen along with an inter-dendritic second phase.

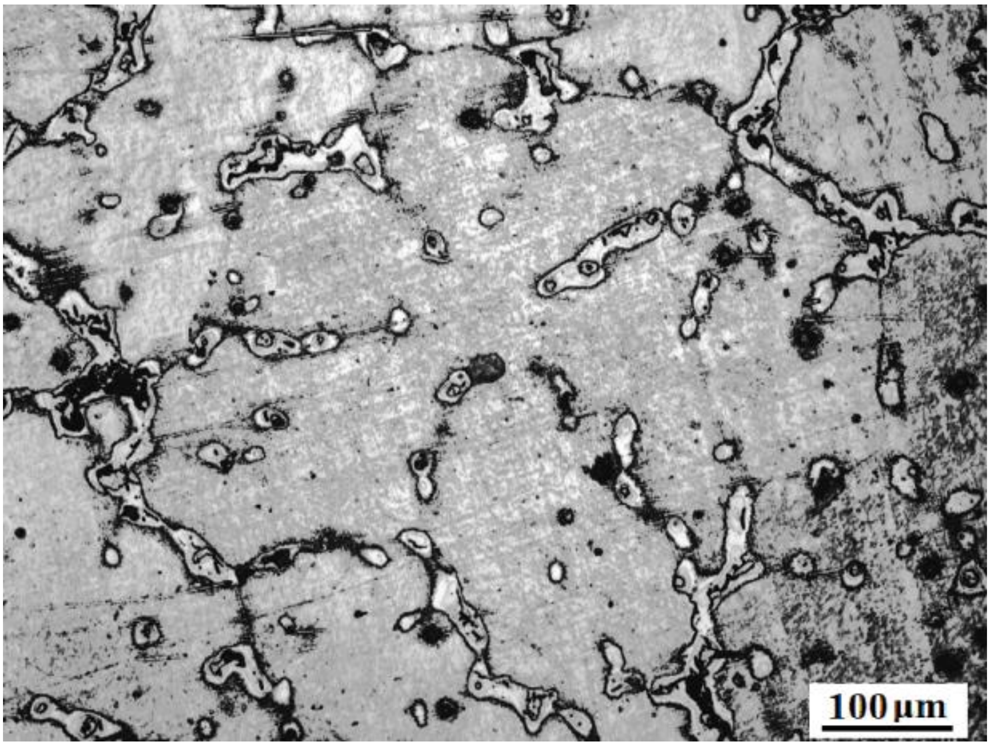

Fig. 4.14 Optical micrograph of the unprocessed cast AZ31 alloy.

In order to determine the distribution of phases, X-ray elemental mapping is performed. Fig. 4.15 shows the SEM micrograph and X-ray elemental mapping of cast AZ31 alloy. It exhibits less significant dendritic growth (Fig. 4.15a) as compared to the AZ91 alloy. Fig. 4.15b shows that aluminium is present mainly along the grain boundary as secondary $Mg_{17}Al_{12}$ intermetallic phase and small amount of Zn present throughout the matrix of alloy.

4.4 Ultrasonic processing of AZ31 alloy during continuous cooling

Microstructural evolution

Figs. 4.16 a-c shows the optical micrographs of AZ31 alloy that was subjected to UST during continuous cooling. The UST is performed at a constant vibration intensity of 1.4 $kW.cm^{-2}$ and varied processing time of 30, 60, and 90 s was used. Increased grain refinement occurred with UST processing time. Compared with unprocessed AZ31 alloy, 30s UST processed alloy shows grain refinement with grain size reduced to an average of 151 μm (Fig. 4.16-a). It still exhibits dendritic growth but the dendrites are smaller. UST processing for 60 s resulted in further refinement with average grain size reduced to 108 μm (Fig. 4.16-b), which is a 54 pct reduction as compared with base alloy. It has a mixed structure of smaller dendrites and some equiaxed grains. UST processing for 90 s is resulted in a globular microstructure and caused further grain refinement, with average grain size reduced to 84 μm which represents 64 pct reduction as compared to the base alloy (Fig. 4.16-c).

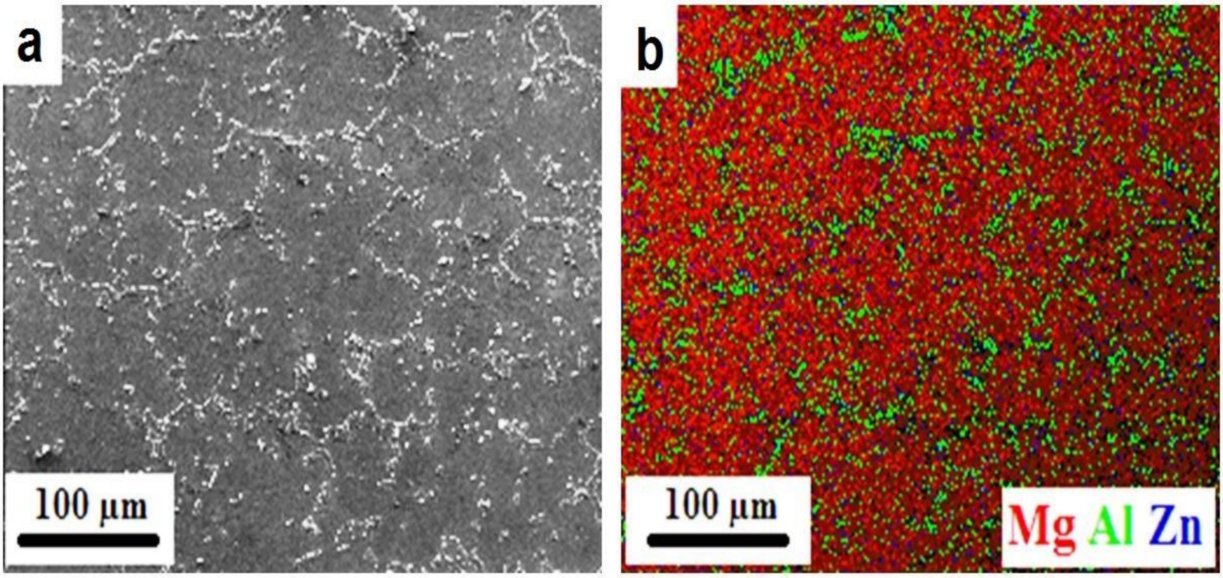

Fig. 4.15 (a) SEM micrograph and (b) X-ray elemental mapping of unprocessed AZ31 alloy.

Fig. 4.17 shows the optical micrographs of AZ31 alloy that was subjected to UST at a constant intensity of 2.7 kW.cm^{-2} and 4.3 kW.cm^{-2} during continuous cooling for various durations. Fig 4.17a shows that for 2.7 kW.cm^{-2} intensity and 30 s of UST processing time, AZ31 alloy became almost dendrite free with grain size reduction of 55 pct. With increase in the processing time to 60 s grains became predominantly globular with a 57 pct reduction in the grain size compared with AZ31 base alloy (Fig. 4.17 b-d). Further, after 90 s of UST processing time grains are partly globular and partly dendritic in shape (Fig. 4.17 c). Average grain size is reduced to 81 μm that is 65 pct reduction compared with the base alloy.

Fig. 4.17d-f are the optical micrographs of AZ31 alloy ultrasonically processed using ultrasonic vibration intensity of 4.3 kW.cm^{-2}. It is observed that at maximum intensity with 30 s processing time the microstructure contained a mixture of fine and large grains.

Microstructures are more refined after 60 s and 90 s of ultrasonic processing time. After 60 s of UST time, dense and fine grains are observed. Maximum grain refinement is observed in specimens processed for 90 s using 4.3 kW.cm^{-2}.

Grain size and hardness

Fig. 4.18 shows the variation in grain size of AZ31 alloy with UST processing time when different ultrasonic intensities were applied during continuous cooling. It is observed that as the ultrasonic intensity and ultrasonic processing times are increased the grain size decreased sharply in the beginning and moderately later. Fig. 4.19 shows the variation in Vickers hardness (HV) with the UST processing time at different ultrasonic intensities for the continuous cooling condition. For high ultrasonic intensities as the ultrasonic processing time increased, the hardness of the AZ31 alloy increased at a higher rate in the beginning and moderately at higher UST times. For the low intensities, the hardness increased monotonously with time. Maximum hardness that is found in specimen UST processed with 90 s processing time and constant intensity of 4.3 kW.cm^{-2} is 153 pct higher than that of the AZ31 alloy.

Tensile properties

Figs. 4.20-A,B,C shows the true stress-true strain curves from the tensile tests performed on unprocessed AZ31 alloy, and alloys UST treated at different intensity and different UST processing times. From these three graphs, it is noticed that as thee UST intensity increases, proof stress, UTS, and total pct elongation to failure of AZ31 alloy increased. It is summarized later in Table 3. Fig. 4.20A shows that at constant intensity (1.3 kW.cm^{-2}), proof stress, UTS, and elongation of AZ31 alloys increased with the UST processing time. At 1.3 kW.cm^{-2} intensity, the highest increment in proof stress, UTS, and elongation is observed in 90 s UST processed specimen that is 17 pct, 36 pct and 13 pct increase, respectively compared with unprocessed AZ31 alloy. Fig. 4.20-B shows that at constant UST intensity of 2.7 kW.cm^{-2}, proof stress, UTS, and elongation of AZ31 alloys increased with the UST processing time. Again, highest increment of 20 pct, 38 pct, and 25 pct was observed in the proof stress, UTS, and total pct elongation, respectively in specimen UST processed for 90 s as compared with unprocessed AZ31 alloy. Fig. 4.20-C shows that UST performed using 4.3 kW.cm^{-2} intensity for 90 s was most effective. It showed 25 pct, 56 pct, and 46 pct increment in proof stress, UTS, and elongation to failure, respectively, as compared to the unprocessed AZ31 alloy.

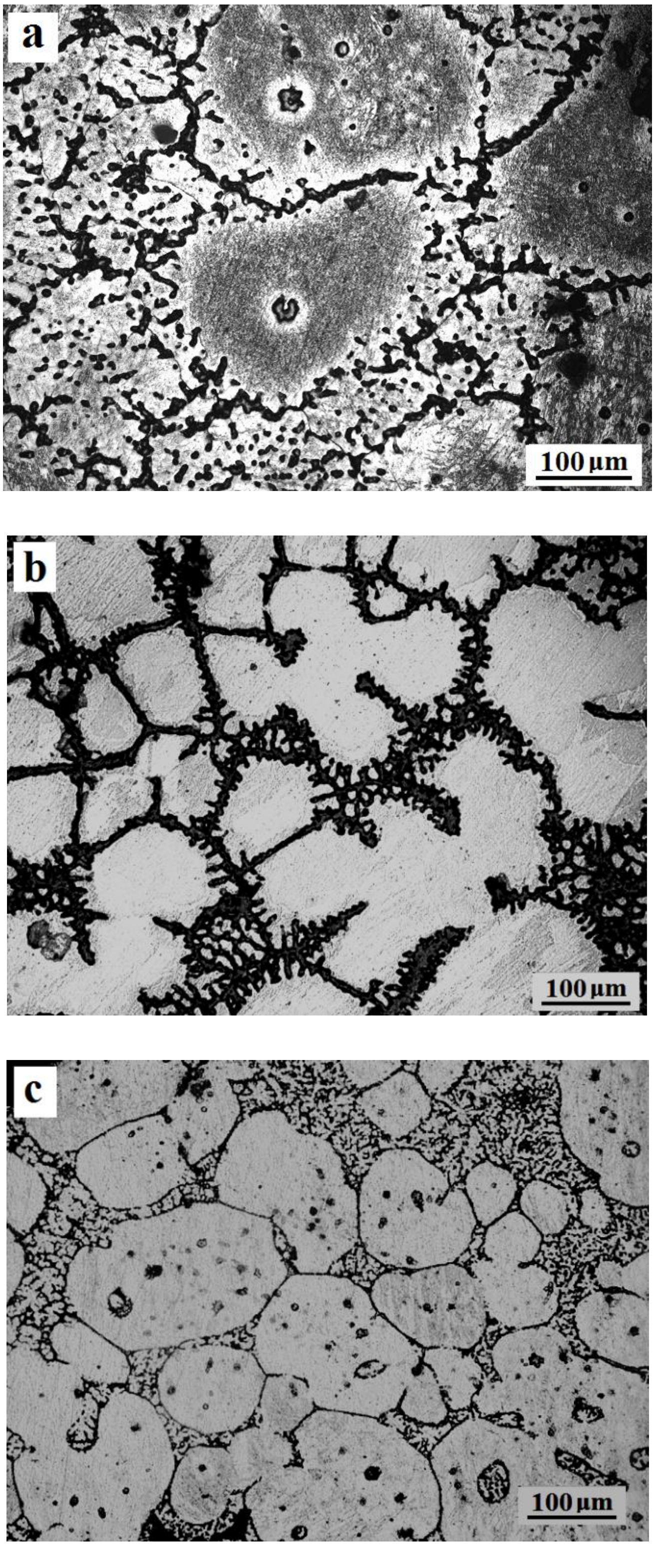

Fig. 4.16 Optical micrographs of AZ31 alloy that was subjected to UST during continuous cooling using constant ultrasonic intensity of 1.3 kW.cm^{-2}. UST processing time is (a) 30 s, (b) 60 s, and (c) 90 s.

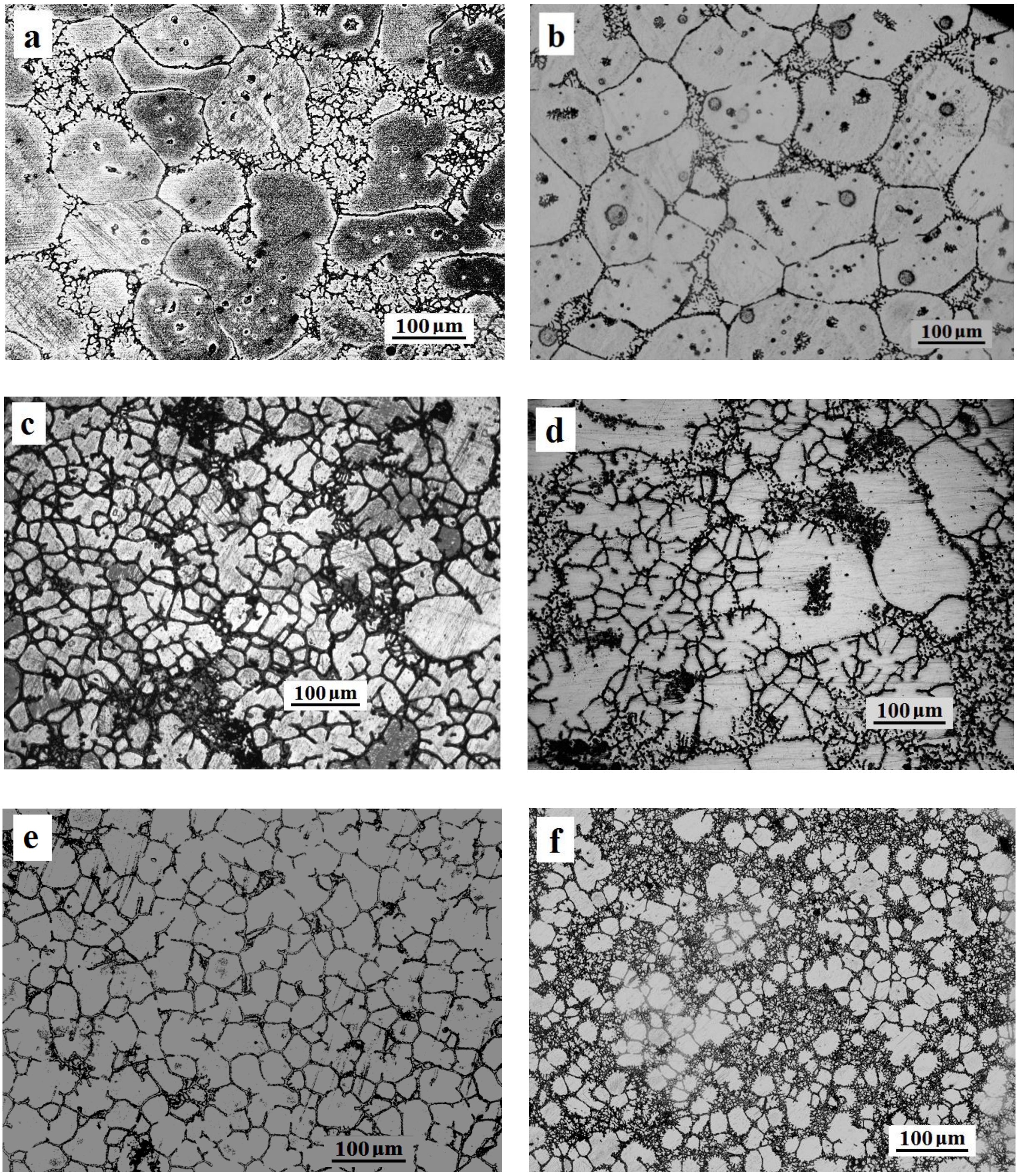

Fig. 4.17 Optical micrographs of AZ31 alloy that was subjected to UST during continuous cooling using constant ultrasonic intensity of 2.7 kW.cm^{-2} and UST processing time of (a) 30 s, (b) 60 s, and (c) 90 s. Figures (d), (e) and (f) show the optical micrographs of AZ31 specimens processed using ultrasonic intensity of 4.3 kW.cm^{-2} for 30, 60, and 90 s, respectively.

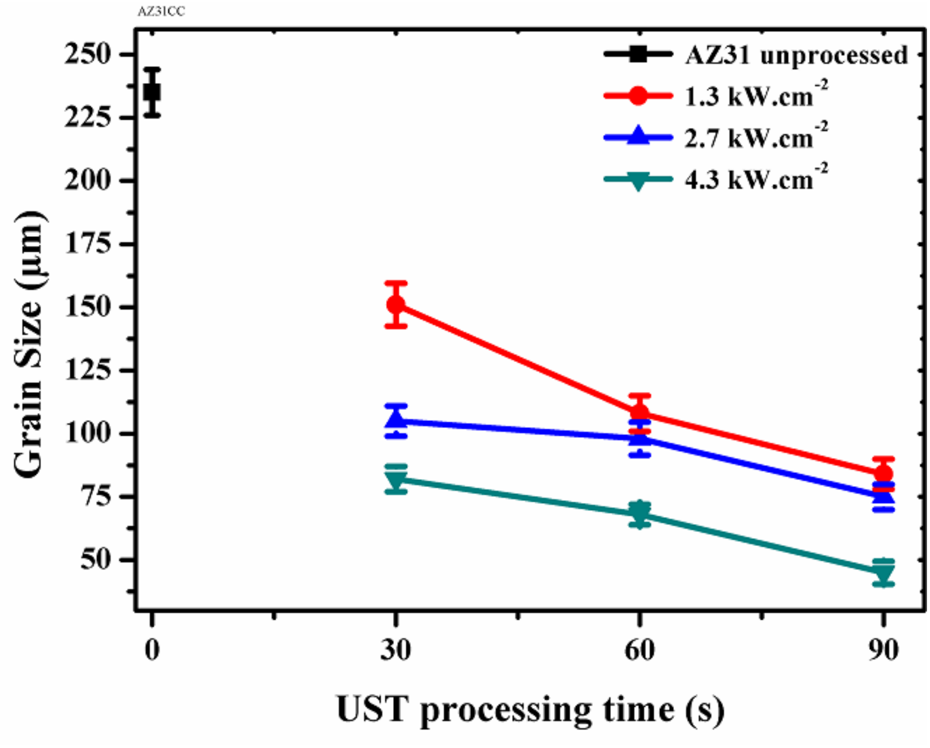

Fig. 4.18 Variation in grain size of AZ31 alloy with UST processing time plotted for different ultrasonic intensities applied during continuous cooling.

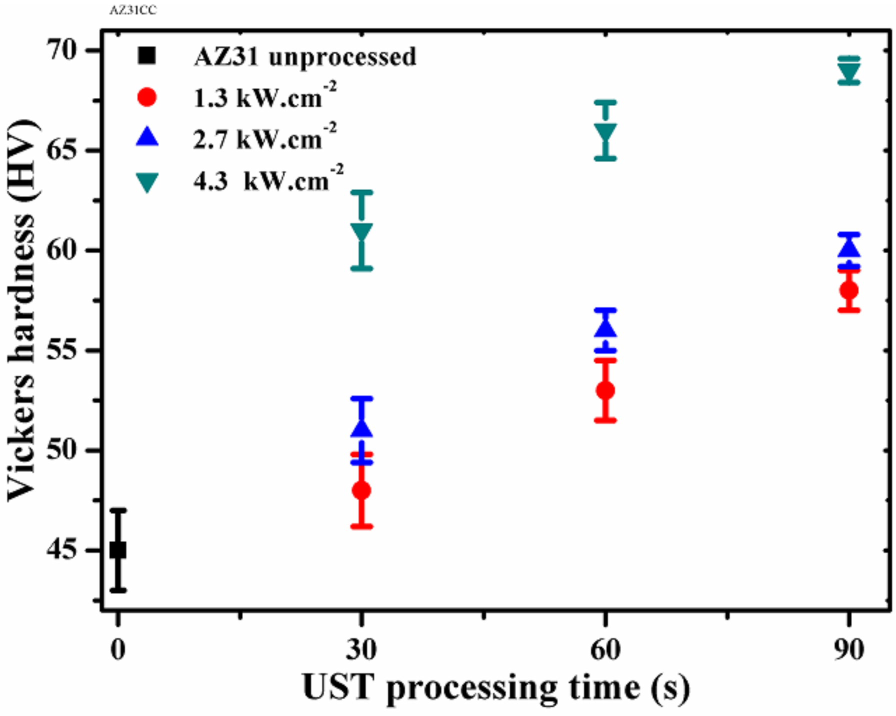

Fig. 4.19 Variation in Vickers hardness of AZ31 alloy with the UST processing time plotted for different ultrasonic intensities applied during continuous cooling.

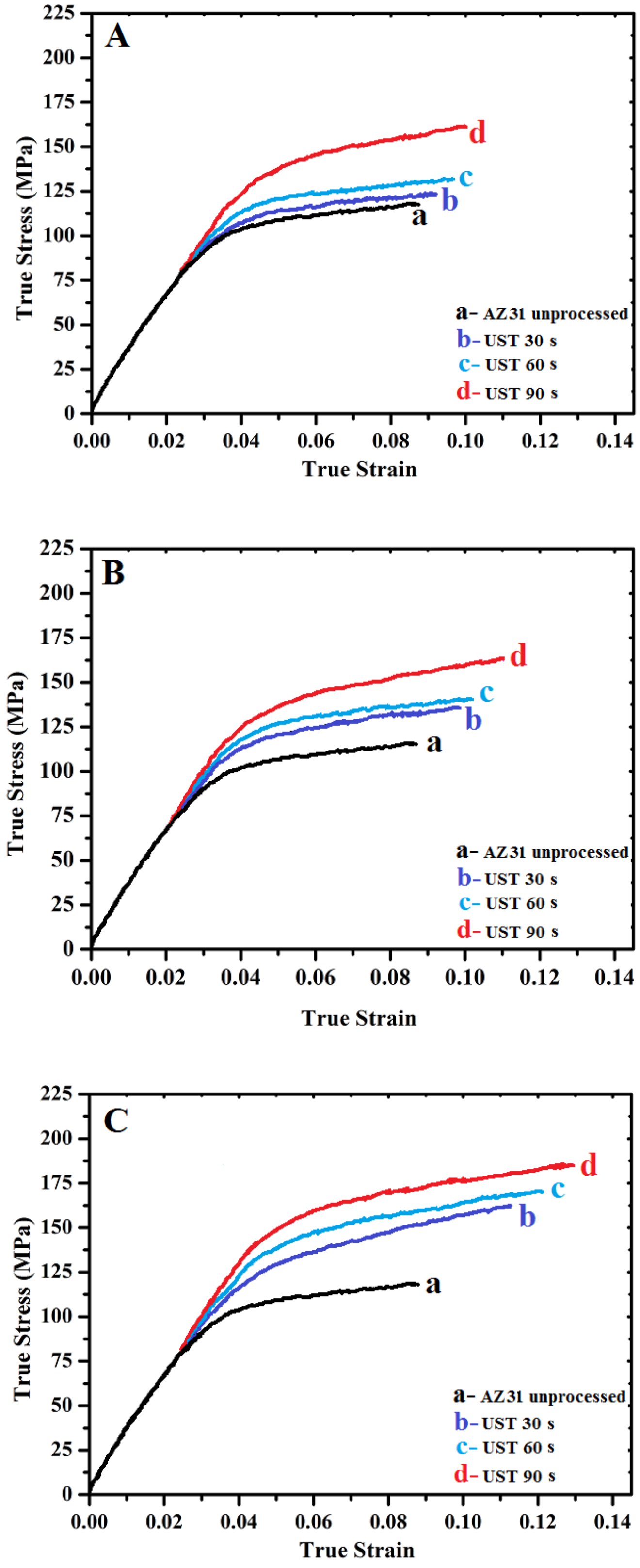

Fig. 4.20 The true stress-true strain tensile test curves for AZ31 alloy ultrasonically treated during continuous cooling using different ultrasonic intensity of (A) 1.3 kW.cm^{-2}, (B) 2.7 kW.cm^{-2}, and (C) 4.3 kW.cm^{-2}, for various processing durations.

4.5 Ultrasonic processing of AZ31 alloy during isothermal holding

A few experiments were performed with ultrasonic treatment done under isothermal conditions at a temperature where 10 pct solid fraction is present in the mushy freezing range. Fig. 4.9 shows the optical micrographs of AZ91 alloy that was subjected to UST during isothermal holding at 627°C. The UST is performed at a constant vibration intensity of 1.3 kW.cm^{-2} and variable processing time of 30, 60, and 90 s was used. Increased grain refinement occurred with UST processing time. Compared with unprocessed AZ31 alloy (average grain size = 240 μm), 30 s UST processed alloy shows grain refinement with grain size reduced to an average of 210 μm (Fig. 4.21a). UST processing for 60 s resulted in further refinement with average grain size reduced to 125 μm, which is a 48 pct reduction as compared with base alloy (Fig. 4.21b). It has a mixed structure of smaller dendrites and some equiaxed grains. UST processing for 90 s resulted in a microstructure consisting of more globular grains and caused further grain refinement (Fig. 4.21c), with average grain size reduced to 82 μm that is a 65 pct reduction compared with unprocessed AZ31 alloy.

Fig. 4.22 shows the optical micrographs of AZ31 alloy that was subjected to UST at constant temperature of 627 °C, and using a constant intensity of 2.7 kW.cm^{-2} and 4.3 kW.cm^{-2} for various durations. Fig 4.22-a shows that at intensity 2.7 kW.cm^{-2} and after 30 s of UST processing time, AZ31 alloy become dendrite free concomitant with grain refinement. Increase in the processing time from 30 s to 60 s grains resulted in more globular grains. The reduction in the grain size is 69 pct and 71 pct, respectively when compared with AZ31 alloy (Fig. 4.22a-b). With further increase in the processing time to 90 s grains become globular in size and having a mixture of small and large grains (Fig. 4.22-c). Grain size reduced to 65 μm, i.e. about 73 pct reduction is observed compared with base alloy. Figs. 4.22 d-f are the optical micrographs of AZ31 alloy UST processed using a constant intensity 4.3 kW.cm^{-2}. It is seen that with a 30 s processing time, there is a mixture of fine and larger dendritic grains having average grain size of 68 μm. Microstructures are more refined after 60 s and 90 s processing time. After 60 s of processing time fine grains are observed, however, they are random in size and smaller average grain size of 32 μm is noticed. Best gain refinement is observed in 90 s processing time with constant 4.3 kW.cm^{-2} intensity, compared with unprocessed AZ91 alloy. It shows 88 pct reduction in grain size.

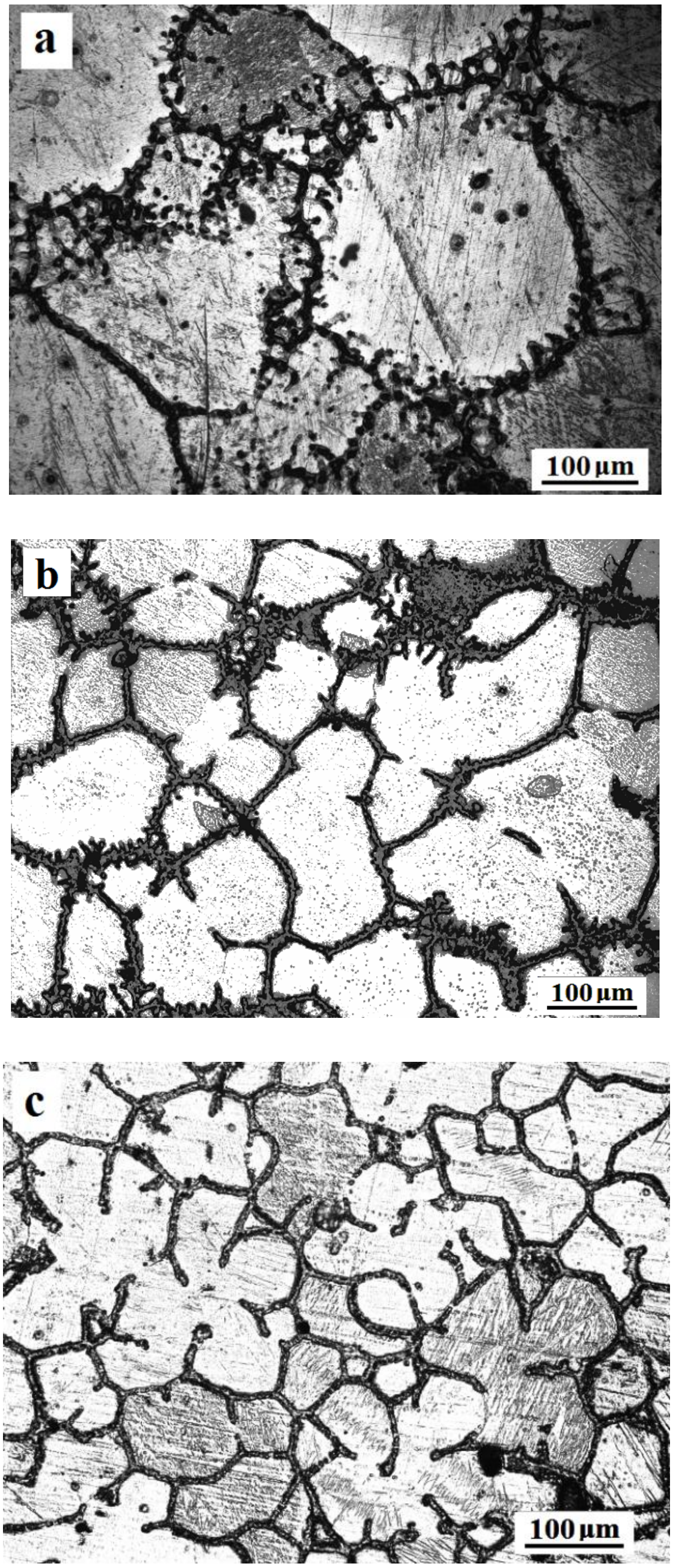

Fig. 4.21 Optical micrographs of AZ31 alloy that was subjected to UST during isothermal holding at 627°C using constant ultrasonic intensity of 1.3 kW.cm^{-2}. UST processing time is (a) 30 s, (b) 60 s, and (c) 90 s.

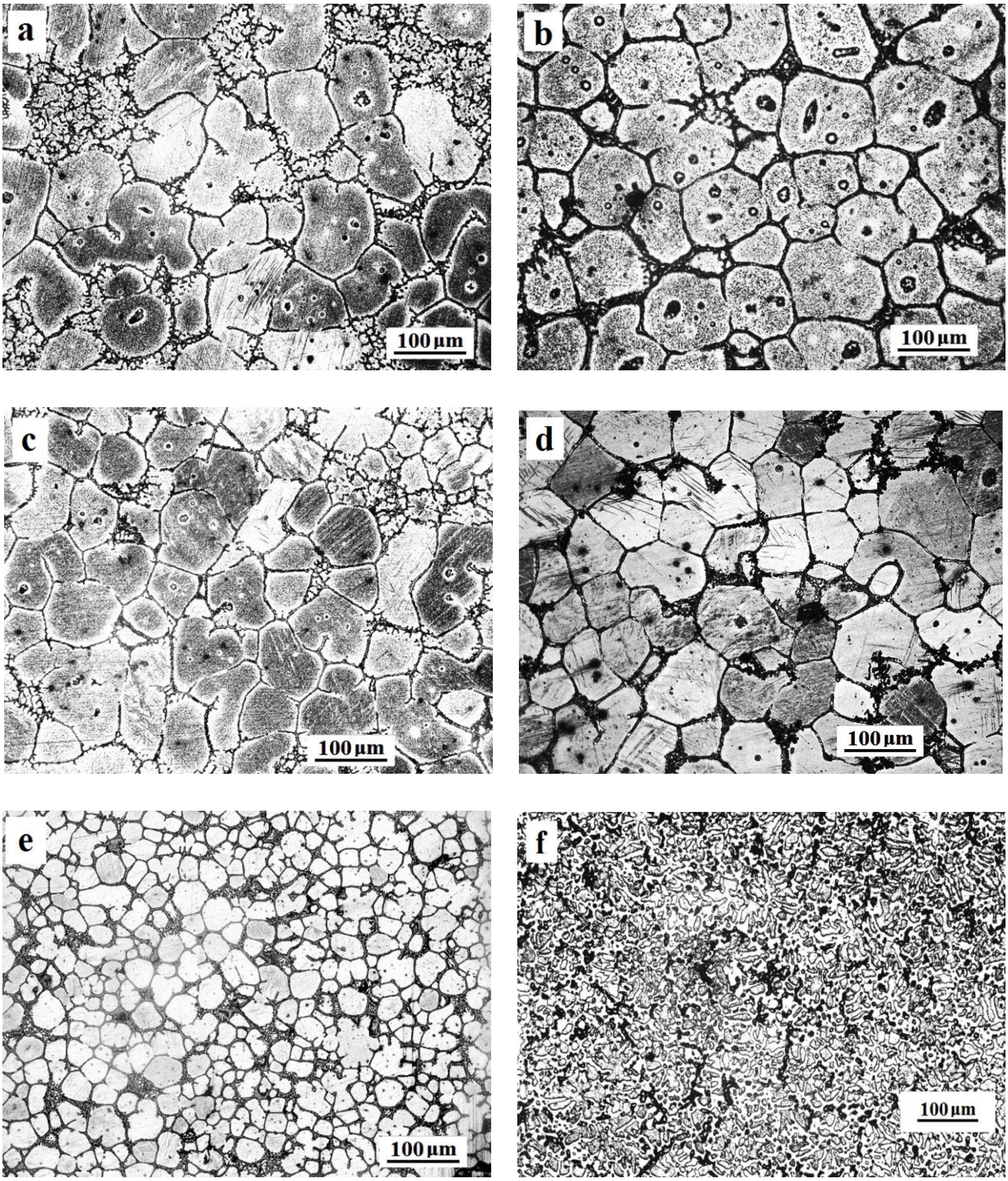

Fig. 4.22 Optical micrographs of AZ31 alloy that was subjected to UST during isothermal holding at 627°C using constant ultrasonic intensity of 2.7 kW.cm^{-2}. UST processing time is (a) 30 s, (b) 60 s, and (c) 90 s. Figures (d), (e) and (f) show the optical micrographs of AZ31 specimens processed using ultrasonic intensity of 4.3 kW.cm^{-2} for 30, 60, and 90 s, respectively.

Grain size and hardness

Fig. 4.23 shows the variation in grain size of AZ31 alloy with UST processing time when different ultrasonic intensities were applied during isothermal holding. For lower ultrasonic intensity of 1.3 kW.cm^{-2} the grain size reduced monotonously with UST processing time. However, for higher UST intensities of 2.7 kW.cm^{-2} and 4.3 kW.cm^{-2}, it is observed that as the ultrasonic processing time is increased the grain size decreased sharply in the beginning and moderately later. Most refined microstructure is observed after 90 s of processing time, i.e. the smallest grain size is 28 μm that is found to be 88 pct smaller than that of the unprocessed alloy. Fig. 4.24 shows the variation in Vickers hardness with the UST processing time, under isothermal holding condition at different ultrasonic intensities. As the ultrasonic intensity and ultrasonic processing time increased, the hardness of the UST processed AZ31 alloy increased. Maximum hardness is found in the alloy treated for 90 s processing time and constant intensity of 4.3 kW.cm^{-2}. Hardness is 171 pct higher than that of the unprocessed AZ31 alloy.

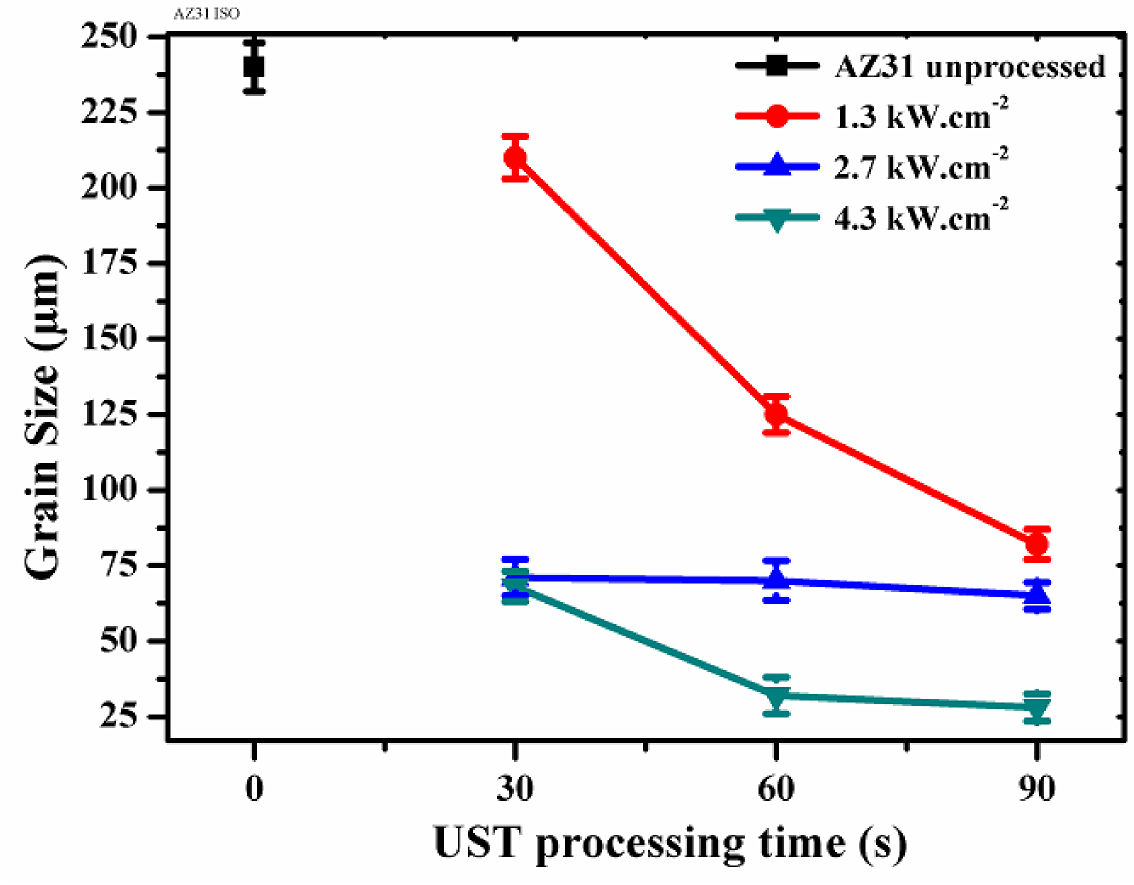

Fig. 4.23 Variation in grain size of AZ31 alloy with processing time plotted for different ultrasonic intensities applied during isothermal UST treatment.

Tensile properties

Figs. 4.25A-C show the true stress-true strain curves from the tensile tests of unprocessed AZ31 alloy, alloy UST treated using different intensity and different UST processing times under isothermal holding condition. From these three graphs, it is noticed that as the UST intensity increased, the proof stress, UTS, and total elongation to failure of AZ31 alloy increased as compared with the base alloy. These properties are summarized later in Table 4.3. Fig. 4.25-A shows that at constant low UST intensity of 1.3 kW.cm^{-2}, the proof stress, UTS, and elongation to failure of AZ31 alloys increased with the UST processing time. It is observed that after 90 s of UST processing at 1.3 kW.cm^{-2} highest increments of 46 pct, 44 pct and 36 pct in proof stress, UTS and elongation to failure, respectively, are obtained when compared with the unprocessed AZ31 alloy.

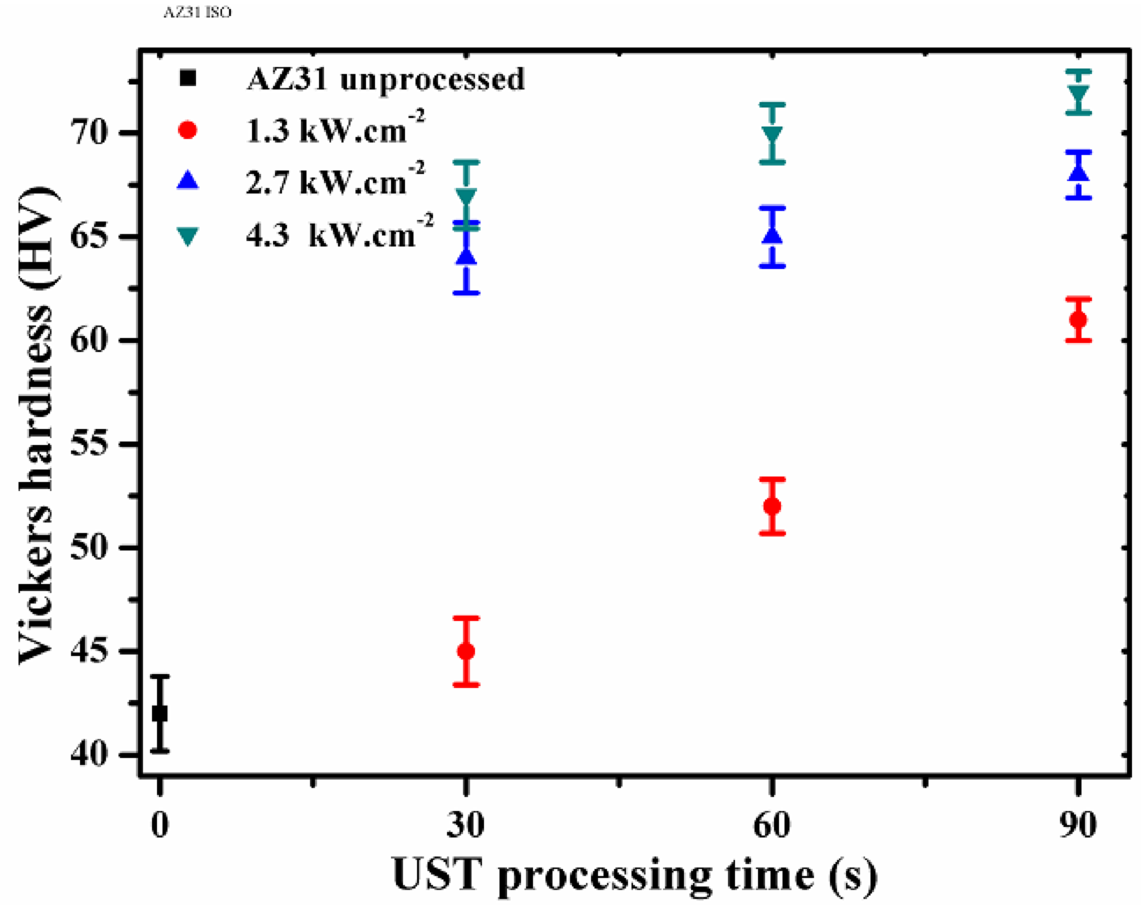

Fig. 4.24 Variation in Vickers hardness of AZ31 alloy with the UST processing time plotted for different ultrasonic intensities applied during isothermal holding at 627 °C.

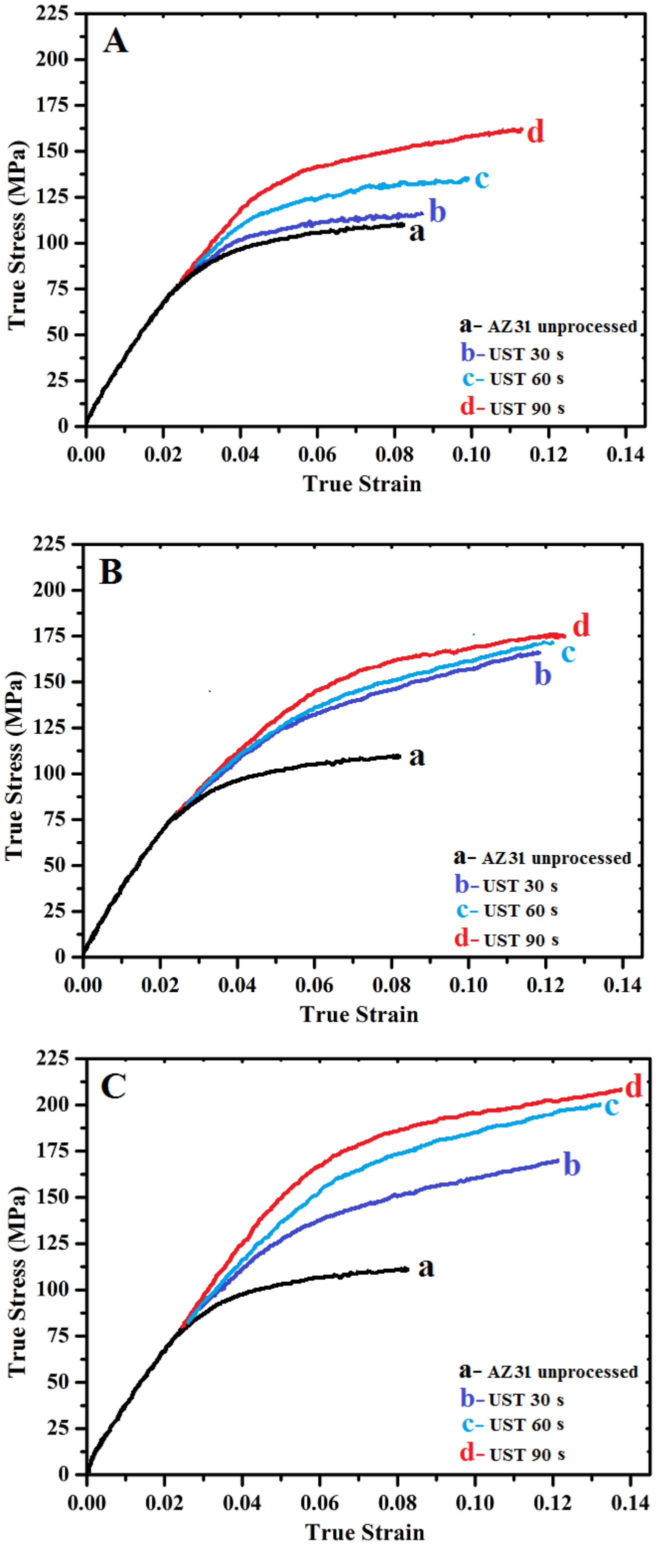

Fig. 4.25 The true stress-true strain tensile test curves for AZ31 alloy ultrasonically treated during isothermal holding using different ultrasonic intensity of (A) 1.3 kW.cm^{-2}, (B) 2.7 kW.cm^{-2}, and (C) 4.3 kW.cm^{-2}, for various processing durations.

Table 4.3. Summary of the grain size and mechanical properties of AZ31 alloy UST processed using different process parameters.

Fig. 4.25-B shows that at constant UST intensity of 2.7 kW.cm^{-2}, the proof stress, UTS,

Materials	Processing conditions	UST intensity	Processing time	Grain size (µm)	Hardness (HV)	Proof stress (MPa)	UTS (MPa)
AZ31	Continuous cooled condition	1.3 kW.cm^{-2}	0	235	45	88	118
			30	151	48	94	122
			60	108	53	99	131
			90	84	58	103	161
		2.7 kW.cm^{-2}					
			30	105	51	100.5	137
			60	102	52	101	139
			90	81	60	105.5	163
		4.3 kW.cm^{-2}					
			30	82	61	105	162
			60	68	66	107	170
			90	45	69	110	185
	Iso-thermal condition	1.3 kW.cm^{-2}					
			30	210	45	84	116
			60	125	52	97	135
			90	82	61	105	162
		2.7 kW.cm^{-2}					
			30	71	64	106	169
			60	70	65	106.3	169.5
			90	65	68	107.8	172
		4.3 kW.cm^{-2}					
			30	68	67	107	170
			60	32	70	112	201
			90	28	72	114	208

and elongation to failure of AZ31 alloy increased with processing time. UST processing at 2.7 kW.cm^{-2} for 90 s increased the proof stress, UTS, and elongation to failure by 49.7 pct, 53 pct and 52 pct, respectively when compared with the unprocessed AZ31 alloy. Fig. 4.25-C shows the variation in tensile properties with the processing time for constant UST intensity of 4.3 kW.cm^{-2}. Maximum improvement is observed after 60 s of UST processing, which corresponds to a 58 pct, 85 pct and 67 pct increase in proof stress, UTS, and elongation, respectively, as compared to that of the unprocessed AZ31 alloy.

4.6 Discussion

4.6.1 Microstructural evolution

Optical micrographs of AZ91 and AZ31 cast magnesium alloys shown in Fig. 4.3 and Fig. 4.13, respectively support the common observation regarding AZ series magnesium alloys that the cast structures are fully coarse dendritic in nature with a large variation in grain size. This results in non-uniform microstructures and hence inferior mechanical properties (Table 4.2 and 4.3). Ultrasonic processing of AZ91 and AZ31 alloys under continuous cooling and isothermal holding conditions leads to considerable grain refinement the magnitude of which is a function of a combination of applied ultrasonic intensity, processing time, and the solute (Al) content. It is seen that pronounced dendritic solidification is observed in AZ91 alloy as compared to AZ31 alloys. This is readily apparent from the Mg-Al binary phase diagram that indicates wider freezing range for 9 wt pct Al alloy. According to the classical nucleation theory the grain size of a casting can be refined in two ways- by increased constitutional undercooling during solidification at the advancing solid/liquid interface, and by increasing the number of potent nuclei in the melt [Du, et al. (2009)]. To understand the former effect, it is instructive to consider the microstructures of unprocessed alloys. For the unprocessed alloys, with an increase in solute (Al) content, the grain size decreased progressively from AZ31 to AZ91 alloys. Thus, the effect of solute concentration in the melt on resulting grain refinement is significant. The segregation of the solutes such as Al and Zn in these alloys is expected to result in strong constitutional undercooling in the diffusion layer in front of the advancing solid/liquid interface. In particular, Al is known to have stronger segregating power leading to grain refinement in magnesium alloys [Dahle, et al. (2001)]. In high Al containing AZ91 alloy, enhanced nucleation results ahead of the solidification front as the constitutional undercooling enables more and more nuclei to form and survive.

Application of ultrasonic vibrations to solidifying melts results in the refinement of microstructure that is widely reported for other alloys [Nastac, (2004), Fairbanks, (1967), Swallowe, et al. (1989), Eskin, (1997)]. A number of grain refinement mechanisms are proposed which are discussed below in the context of present work. When alloy melts are ultrasonically treated after the onset of solidification, ultrasound induced cavitation and accompanying streaming phenomena cause dendrite fragmentation and their dispersion into the melt [Han, et al. (2005)]. Since the UST is performed below the liquidus temperature (about 10 pct solid fraction present at the time of UST processing) in the present work, dendrite fragmentation effect is expected to be a contributing factor in the grain refinement.

The convection and shock waves created in the solidifying melt during the application of ultrasonic vibrations can promote dendrite fragmentation, which is caused by melting at the dendrite root, where the solutes are segregated. The melting at a dendrite root may be the results of a local temperature increase. The diffusion of solutes away from the dendrite roots would lead to a reduction of the solute concentration and an increase in the local temperature. The effect would also lead to melting at the dendrite roots. Stirring can also promote dendrite fragmentation, since it produces local temperature variations and promotes diffusion of solutes in the liquid. Furthermore, the local pressure fluctuations lead to fluctuations in the melting temperature which results in the melting of the dendrite roots. These fluctuations should aid in the melting of the dendrite roots. This will lead to more homogeneous microstructure with smaller grain size. However, if the applied ultrasonic field is strong enough to produce cavitation, then a major origin of grain refinement is the fragmentation of crystals to produce new nuclei [Jian, et al. (2005), Abramov, (1986), Thomas, et al. (2006), Tao, et al. (2006), Swallowe, et al. (1989), Ramirez, (2008), Jun-wen, et al. (2007), Nastac, (2004)].

However, according to cavitation enhanced heterogeneous nucleation theory [Eskin, (1997), Xu, et al. (2004), Easton, et al. (2001)], the grain refinement from ultrasonic processing could be explained by three different mechanisms. First one is based on the pressure pulse-melting point (T_m) mechanism, where the pressure pulse arising from the collapse of bubbles increases T_m according to the Clausius-Clapyron equation. An increase in T_m is equivalent to increasing the undercooling, so that enhanced nucleation events are expected (equation 2.4).

$$\frac{dT_m}{dP} = \frac{T_m(V_L - V_S)}{\Delta H} \tag{2.4}$$

Where, T_m is freezing point in K, P is pressure in 10^5 Pa, V_L and V_S are the specific volume of liquid and solid phase in $cm^3.g^{-1}$ respectively. ΔH is the latent heat of freezing in $J.g^{-1}$. An increase in T_m is equivalent to increasing the undercooling and hence increasing the nucleation rate.

Second mechanism is based on cavitation enhanced wetting which assumes that any molten alloy always contains vast amount of insoluble particles such as oxides, ultrafine particles of some intermetallics, which are not normally wettable by the alloy melt. During the collapse of the cavitation bubbles high pressure pulses are generated. Under the action of high pressure pulses, the wettability of these impurity particles is improved by filling of the microcracks and defects at their surfaces with the melt. Therefore, most of the insoluble impurity particles throughout the melt become active and get involved in the solidification process as nuclei, which leads to the heterogeneous nucleation easily upon a slight undercooling. Another mechanism proposes that during the expansion of cavitation bubbles, there is endothermic vaporization of the surrounding melt into the bubbles. This decreases the temperature on the surface of the bubbles and local supercooling occurs. Therefore, the nuclei form around the bubbles during solidification, which increases the nucleation rate and refines the grain size [Eskin, (1997), Eskin, et al. (2003), Suslick, et al. (1999), Su, et al. (2012)]. One or more of these three mechanisms may be responsible for increased density of active nuclei with higher UST duration, which resulted in finer microstructures observed in the present work.

Figs. 4.4, 4.5, 4.15, 4.16 show the optical micrographs of the specimens obtained after UST done in continuous cooling condition for the AZ91 and AZ31 alloys. In continuous cooled condition, with the progress of UST processing, tempereture decreases with time. Thus the solid fraction present in the melts goes on increasing with the time. Therefore, it causes more dendrite fragmentation in the melt, however there is gradual reduction in the acoustic streaming phenomena in the slurry. Dendrite fragmentation from the UST produces more nucleation sites for grains to form in continuous cooled condition. As the UST processing time and intensity increased, the dendritic fragmentation phenomena worked more efficiently for causing grain refinement in solidifying alloy melts in continuous cooled condition.

Figs. 4.9, 4.10, 4.21, and 4.22 show the optical micrographs of the specimens obtained after UST done under isothermal holding condition for the AZ91 and AZ31 alloys, respectively. Isothermal processing for an alloy is carried out little below its liquidus temperature, where at the time of isothermal ultrasonic processing, a calculated amount of solid fraction is present in the melt. In this processing approach, both the dendrite fragmentation and acoustic streaming effectively take part in the grain refinement of alloys. Solid fraction available at the time of UST processing is broken in to numerous nuclei and acoustic streaming carries these nuclei in to the bulk of the melt. This resulted in maximum refinement at highest vibration amplitude and longest processing time in the present experiments.

Comparing the microstructural evolution in magnesium alloy specimens UST processed under continuous cooling condition and isothermal holding conditions, the former exhibits less grain refinement and less improvement in mechanical proparties. This is becasuse the dendrite fragmentation caused in the continuous cooled conditionis is totally dependent on the remelting of the secondary dendrite arms. Since latent heat is needed to remelt the secondary dendrite arms at their roots, remelting of a solid is usually a slower process. Further, because the pressure and temperature fluctuations occur at a high frequency of 20 kHz in the present work, they may be too fast for dendrite fragmentation [Jian et al. (2005)]. On the other hand, in near isothermal UST processing, the acoustic streaming caused heterogeneous nucleation is observed to be the leading mechanism for the formation of a globular microstructure in the magnesium alloys. Therefore, much enhanced grain refinement and improved mechanical properties are observed after isothermal UST processing of the melts.

4.6.2 Mechanical properties

Vickers hardness values (VHN) are influenced by processing conditions and they increased with increase in solute concentration, ultrasonic intensity, and processing time. The increase in hardness is attributed to the grain refinement produced after application of UST. Grain refinement results in increase the grain boundary area in the alloy and it acts as barrier to the dislocation motion produced under the applied stress. In the case of ultrasonically treated AZ alloys, improved distribution of secondary phase, because of UST applied to the alloys can further impede the dislocation motion. The increase in the hardness is related to the Hall-Petch relationship and uniform distribution of hard intermetallic phases as explained earlier.

From Tables 4.2 and 4.3, it is obvious that the unprocessed AZ91 alloy has better mechanical properties than unprocessed AZ31 alloy. This follows from its higher solute content (Al content). In unprocessed AZ91 alloy grains are fine as compared with unprocessed AZ31 alloy. It can be seen that 0.2 % proof stress, UTS, and total elongation to fracture values are lowest for all the unprocessed alloys and as UST intensity and time increases tensile properties of the alloys increases. This can be explained by the Hall-Petch equation (equation 2.1.)

$$\boldsymbol{\sigma_0 = \sigma_i + kd^{-1/2}} \tag{2.1}$$

Where, σ_0 is the yield strength, k is constant, σ_i is the friction stress and d is the mean grain size diameter. Thus, the yield stress of metallic materials varies inversely with their grain size. In the case of ultrasonically treated alloys, the grain refinement is dependent on the process variables such as UST intensity, processing time, processing conditions and solute content. Significant change in the microstructure with respect to the distribution of $Mg_{17}Al_{12}$ intermetallic phase, which is brittle in nature, has significant effect on the mechanical properties magnesium alloys. UST produces discontinuity, an increase in the sphericity, and a decrease in the size of the $Mg_{17}Al_{12}$ intermetallic phase, which helps to improve the spheroidization of $Mg_{17}Al_{12}$ intermetallic phase [Aghayani, (2010)]. This reduces the stress raiser points in these alloys. The collective effects of globular/equiaxed grain morphology, grain size reduction, and spheroidization of $Mg_{17}Al_{12}$ intermetallic phase has significantly improved the tensile properties, especially total elongation to failure of the investigated magnesium alloys. It holds true for alloy specimens obtained under both the continuous cooled condition and isothermal processing conditions.

4.7 Summary

1. UST processing time has significant effect on the microstructure refinement of AZ91 and AZ31 alloys. Increased grain refinement occurred with increased UST processing time. The $Mg_{17}Al_{12}$ phase is found to be well distributed along the grain boundaries after the ultrasonic treatment of the both AZ91 and AZ31 alloys.
2. Isothermal holding and continuous cooling conditions at the time of ultrasonic treatment of AZ91 and AZ31 alloys, produced microstructures with nearly non-dendritic equiaxed and globular grains and the grain refinement is attributed to the dendrite fragmentation phenomena.
3. After maximum processing time i.e. 90 s of UST processing, as ultrasonic intensity is increased to 4.3 $kW.cm^{-2}$, the average grain size decreased to 17 µm in isothermal ultrasonically processed AZ91 alloy and the average grain size decreased to 28 µm in isothermal ultrasonically processed AZ31 alloy.
4. During UST of AZ91 and AZ31 alloys, when intensity is increased to 4.3 $kW.cm^{-2}$, the average grain size decreased to 20 µm in isothermal ultrasonically processed AZ91 alloy and it decreased to 45 µm in continuously cooled UST processed AZ31 alloy. Thus, isothermal UST resulted in greater degree of grain refinement.
5. Interestingly for the high intensity of 4.3 $kW.cm^{-2}$ hardness increased monotonously with processing time, although the decrease in grain size was abrupt in the beginning. Highest hardness found in the AZ91 specimen UST processed with 90 s processing time and constant intensity of 4.3 $kW.cm^{-2}$ in continuous cooling conditions is 160 pct higher than that of the AZ91 base alloy.
6. The Vickers hardness of the ultrasonically processed AZ91 and AZ31 alloys increased with increase in ultrasonic intensity applied and applied duration of

processing during the solidification. The increase is attributed to the ultrasound induced dendrite fragmentation leading to grain refinement.

7. For the AZ31 alloy, maximum Vickers hardness is observed when high intensity of 4.3 kW.cm^{-2} and higher processing duration that is 90 s is used during isothermal UST processing. It is 177 pct higher than that of the unprocessed AZ31 alloy. For the similar UST parameters used in continuous cooling condition, 153 pct higher Vickers hardness is observed as compared to the AZ31 base alloy.
8. Vickers hardness values (VHN) increased with increase in solute concentration, ultrasonic intensity, processing time, and is influenced by processing conditions. The increase in hardness is attributed to the Hall-Petch strengthening from grain refinement produced after application of UST.
9. It can be seen that 0.2 % proof stress, UTS, and total elongation to fracture values are lowest for all the unprocessed alloys and as UST intensity and UST time increased tensile properties of the alloys increased. Improvement in tensile properties with respect to enhanced proof strength, tensile strength, and total elongation to failure can be correlated to the morphology of primary α-phase, its grain size, and the morphology of secondary intermetallic phase.

Chapter 5

RESULTS AND DISCUSSION: CARBON INOCULATION WITH ULTRASONIC PROCESSING OF AZ SERIES ALLOYS

In the present work, it is endeavored to systematically study the individual and combined effects of chemical (inoculation) and physical (ultrasonic vibrations) techniques on the microstructural development and mechanical properties in three magnesium alloys. Commercial AZ series magnesium alloys containing three, six, and nine weight pct of aluminum (AZ31, AZ61 and AZ91) are investigated for their response to carbon black nano-particle inoculation and high intensity ultrasonic processing. Potency of inoculants is assessed under varying experimental conditions of untreated, carbon black treated and combined carbon black inoculation treatment followed by ultrasonic treatment conditions. Resulting grain refinement is studied and explained based on existing theories of nucleation and ultrasound induced phenomena in molten metals. It is observed that ultrasonic treatment helps to accelerate the wetting, de-agglomeration, and dispersion of inoculant particles, thereby resulting in refined microstructures. The hardness and tensile properties are evaluated and correlated with microstructural evolution during each of the processing approaches. Effect of Al solute content on mechanical properties of AZ series magnesium alloys is also studied.

5.1 Carbon inoculation results

Fig. 5.1a shows a bright field TEM micrograph of the carbon black nanopowder used for inoculation. It shows elemental carbon arranged as aciniform (grape-like) particle cluster. The average size of the particles in the cluster matches well with the manufacturer specified average particle size of 42 nm. That the particles are amorphous is evident from the selected area diffraction pattern (Fig. 5.1b) which shows a diffuse ring pattern.

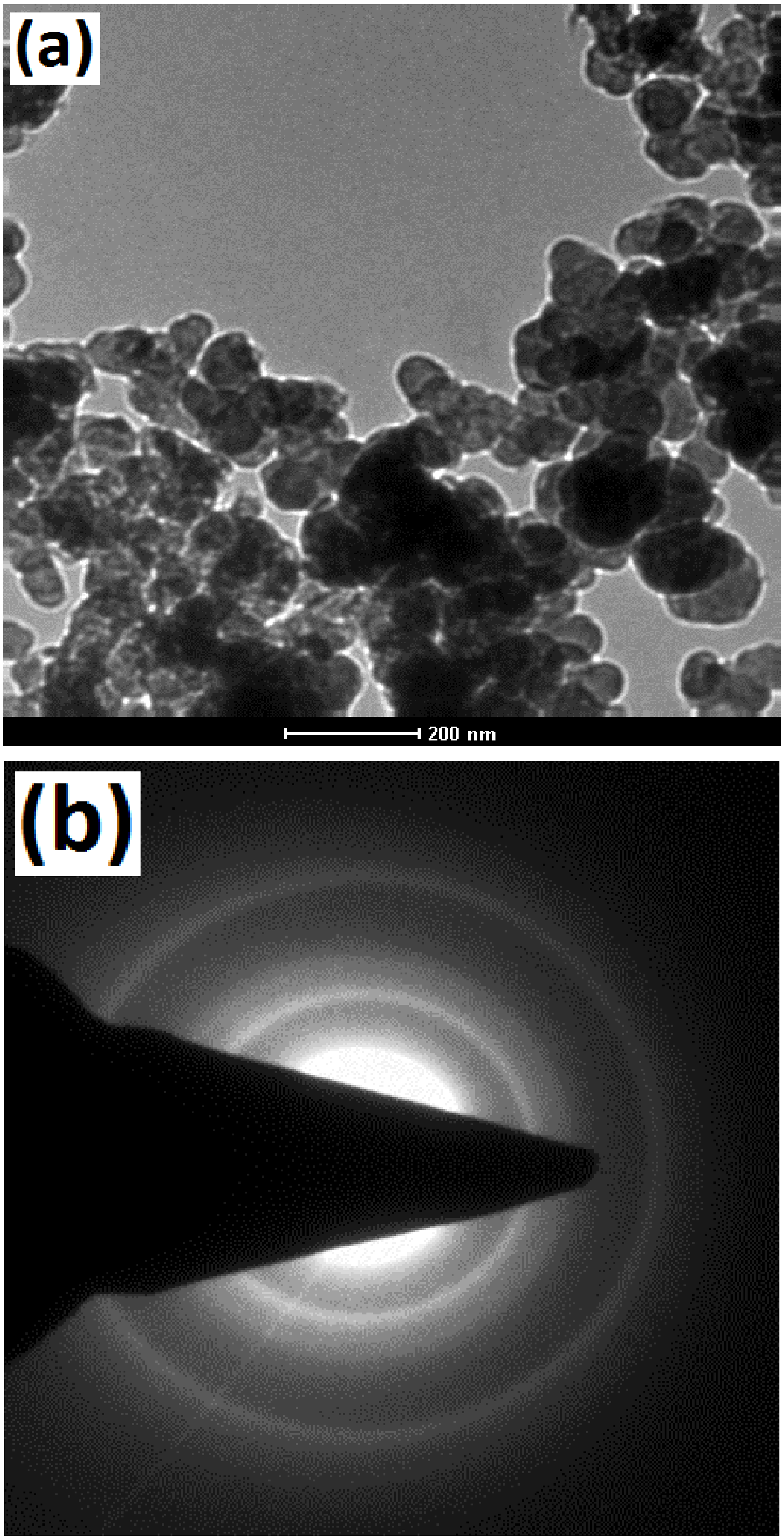

Fig. 5.1 (a) TEM bright field micrograph, and (b) corresponding selected area diffraction pattern of carbon black powder used in the present work.

5.2 Microstructural evolution

Fig. 5.2 shows the microstructures of AZ series alloys with varying Al contents cast at 700 °C under various processing conditions. Pronounced dendritic solidification is observed in AZ91 alloy as compared to AZ61 and AZ31 alloys. This is readily apparent from the Mg-Al binary phase diagram that shows a wider freezing range for 9 wt pct Al alloy. It is further observed that in all the alloys studied in this work, the grain size reduced progressively from unprocessed alloys to carbon inoculated alloys and further to combined carbon inoculated and ultrasonicated alloys (Table 5.1).

The grain size of a casting can be refined in two ways- by increased constitutional undercooling at the advancing solid/liquid interface during solidification, and by increasing the number of potent nuclei in the melt [Du, et al. (2009)]. To understand the former effect, it is instructive to consider the microstructures of unprocessed alloys (Fig. 5.2a-c). For the unprocessed alloys, with an increase in the solute (Al) content, the grain size decreased progressively from AZ31 to AZ91 alloys. Thus, the effect of solute concentration in the melt on resulting grain refinement is obvious. The segregation of solutes such as Al and Zn in these alloys is expected to result in strong constitutional undercooling in the diffusion layer in front of the advancing S/L interface. In particular, Al is known to have stronger segregating power leading to grain refinement in magnesium alloys [Dahle et al. (2001)]. In high Al containing AZ91 alloy, enhanced nucleation results ahead of the solidification front as the constitutional undercooling enables more and more nuclei to form and survive.

In order to understand the latter effect, i.e. the effect of having large number of potent nuclei in the melt, the reader is referred to Figs. 5.2d-f. Inoculation is routinely practiced in important engineering alloys in order to refine their grain size. Inoculants provide additional nuclei that are generally required to increase the frequency of heterogeneous nucleation. As seen in Figs. 5.2d-f, there is a significant decrease in the grain size with the addition of carbon black to the melt. Upon inoculation, the grain size reduced consistently by almost 50 pct in all the alloys studied in this work (Table 5.1). Regarding carbon inoculation in Mg-Al alloys, a number of hypotheses are proposed to explain the mechanism [Lee, et al. (2000), Nimityongskula, et al. (2010)]. So far, Al_4C_3 that forms during the carbon treatment is widely accepted as the nucleating phase. It is reported that the compound Al_4C_3 forms upon the treatment of Mg-Al melts using hexachloroethane, according to the reaction (5.1).

$$4Al + 3C = Al_4C_3 \tag{5.1}$$

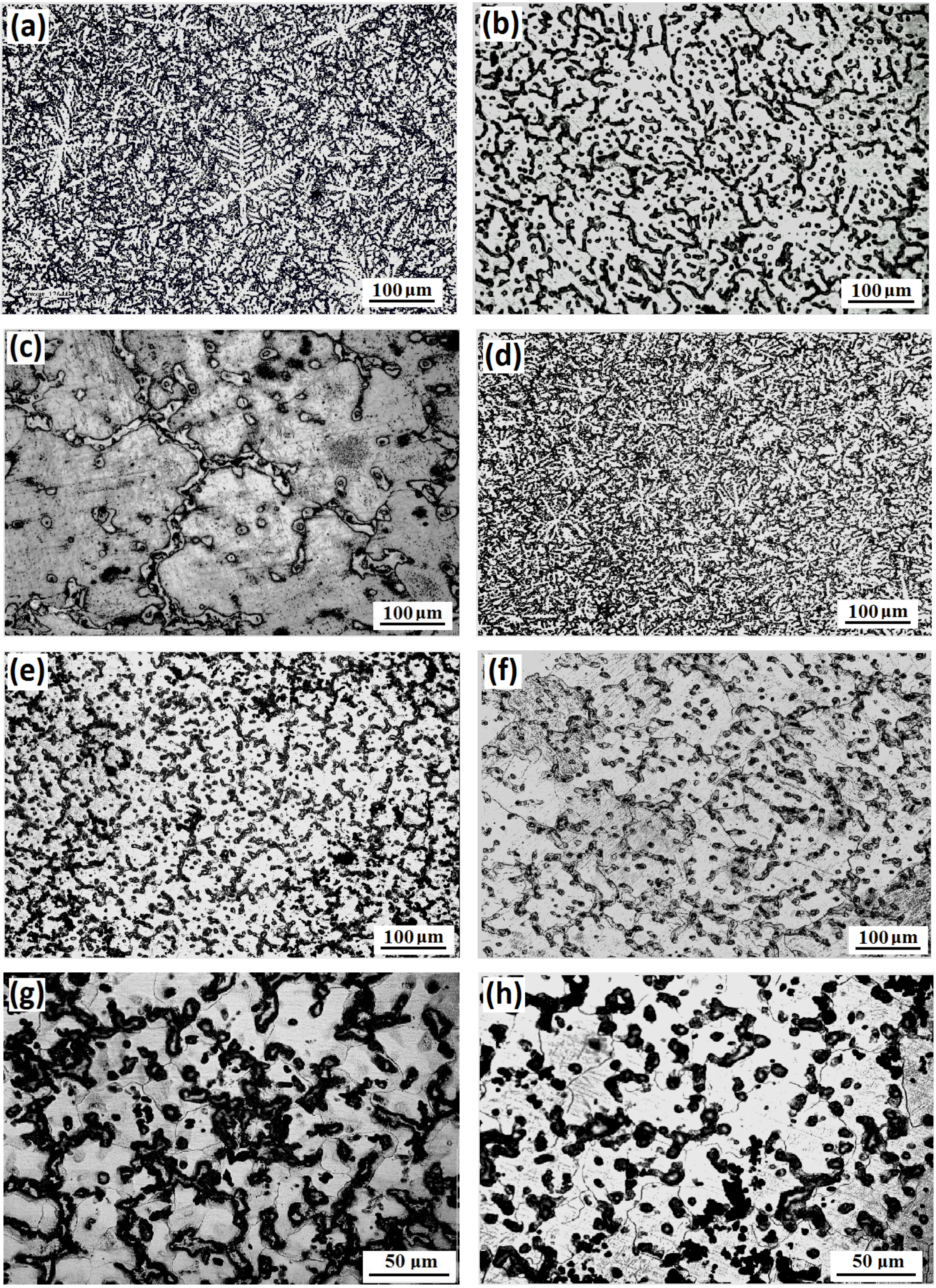
(a)
100 µm
(b)
100 µm
(c)
100 µm
(d)
100 µm
(e)
100 µm
(f)
100 µm
(g)
50 µm
(h)
50 µm

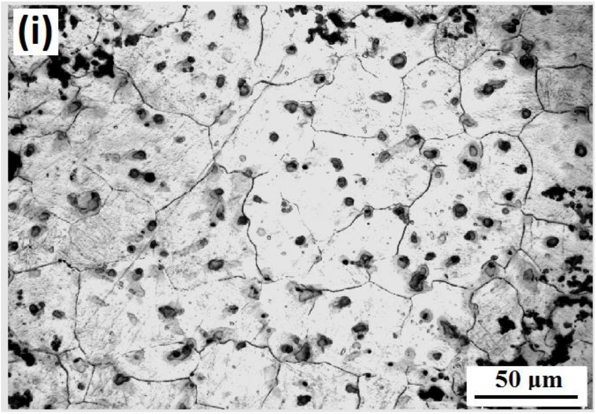

Fig. 5.2 Optical micrographs of magnesium alloys under various processing conditions- unprocessed (a) AZ91, (b) AZ61, (c) AZ31, carbon inoculated (d) AZ91 (e) AZ61 (f) AZ31, and combined carbon inoculated + ultrasonic treated (g) AZ91 (h) AZ61 (i) AZ31 alloys.

Table 5.1 Average grain size (in µm) of different Mg alloys under various processing conditions.

Alloy	**Unprocessed**	**C inoculated**	**C inoculated + Ultrasonicated**
AZ31	200	90	35
AZ61	125	65	32
AZ91	101	50	30

However, some researchers reported that Al_4C_3 is not found in the magnesium alloys [Lee, et al. (2000), Motegi, (2005), Qian, et al. (2005)]. One of the reasons advocated is that Al_4C_3 is extremely reactive with water and oxygen in the Al_2OC is introduced during polishing by combining with H_2O as per the following chemical reaction [Motegi, (2005)].

$$Al_4C_3 + 12H_2O = 3CH_4 + 4Al(OH)_3 \tag{5.2}$$

In the present work, too, Al_2OC and not the Al_4C_3 phase is observed in the XRD analysis shown in Fig. 5.3. This observation matches with many of the earlier observations stated above. There is considerable controversy in the literature about whether Al_4C_3 or Al_2OC is the inoculating phase [Lee, et al. (2000), Nimityongskula, et al. (2010), Motegi, (2005), Qian, et al. (2005)] and it is not the aim of this work to verify it. An interesting comparison of the average grain size of AZ series alloys after carbon inoculation as reported in different studies is presented in Table 5.2 along with the results from present work. Although the casting conditions may vary among different studies, it is apparent that relatively smaller average grain size is obtained in the AZ series alloys studied in the present work. This can be explained from the fact that carbon black, which is a form of fine and amorphous carbon, has high surface area to volume ratio (Fig. 5.1). This is expected to increase the kinetics of its chemical reaction with Al. Thus, when added to molten Mg-Al alloys the inoculating phase particles form readily and in large number, thereby resulting in the extensive grain refinement observed in this work.

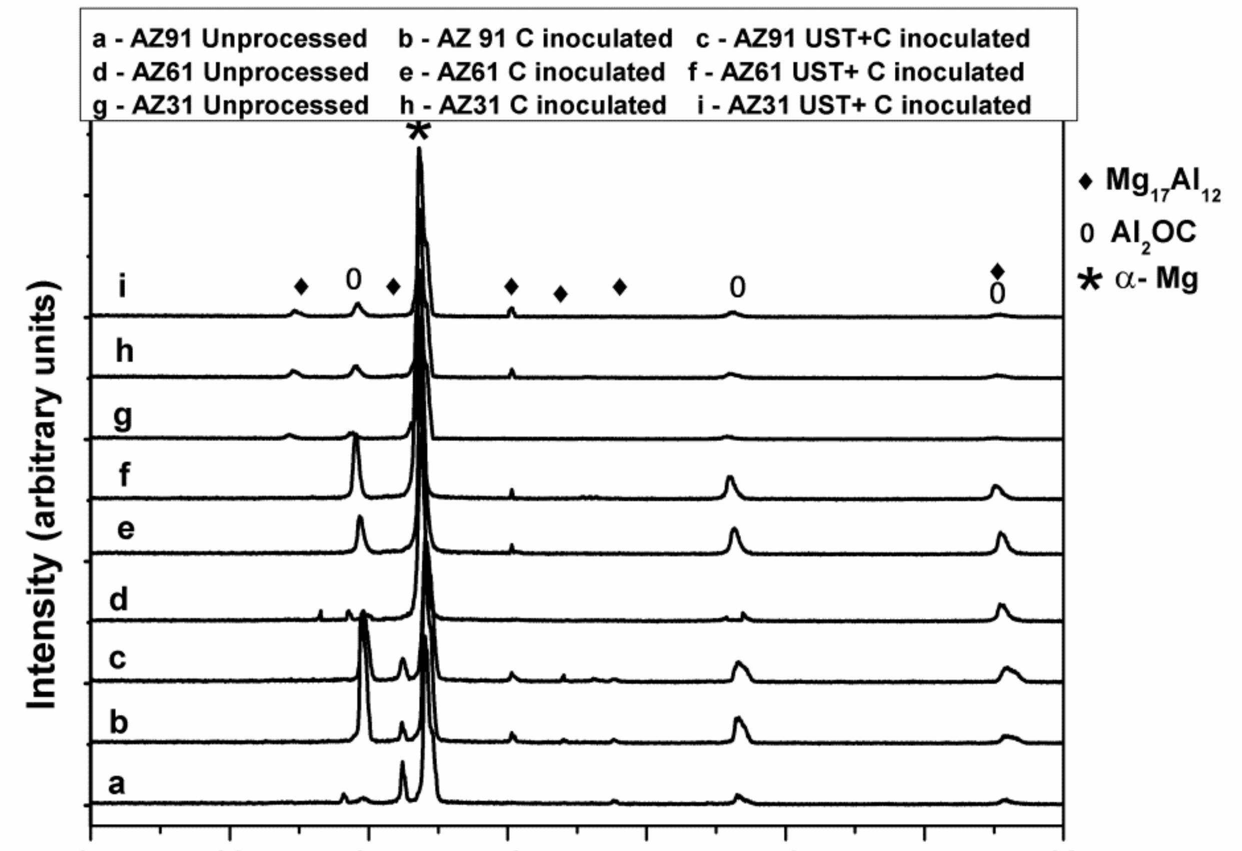

Fig. 5.3 XRD patterns for AZ31, AZ61, and AZ91 alloys processed under various conditions of inoculation and ultrasonication of the melts.

Application of ultrasonic vibrations to solidifying melts also results in the refinement of microstructure [Nastac, (2004), Fairbanks, (1967), Swallowe, et al. (1989), Eskin, (1997)]. A number of grain refinement mechanisms are proposed which are discussed below in the context of present work. When the alloy melts are ultrasonically treated after the onset of solidification, ultrasound induced cavitation and accompanying streaming phenomena cause dendrite fragmentation and their dispersion into the melt [Han et al. (2005)]. Since the UST is performed above the liquidus temperature in the present work, dendrite fragmentation effect is not expected to be a contributing factor in the grain refinement.

Table 5.2 Comparison of average grain size after carbon inoculation of Mg-Al alloys from different studies.

Work and reference	**Mg-Al alloy studied**	**Average grain size after carbon inoculation, μm**
Motegi, (2005)	AZ91E	75
Yano et al.(2001)	AZ91	70
Renger et al. (2003)	AZ91	190
Guang, et al. (2009)	AZ31	150
Ramirez, et al. (2008)	AZ31	250
	AZ61	350
	AZ91	500
Present work	AZ31	90
	AZ61	65
	AZ91	50

According to the cavitation enhanced heterogeneous nucleation theory [Eskin, (1997), Xu, et al. (2004), Easton, et al. (2001)], there could be three different mechanisms responsible for grain refinement. First one is based on the pressure pulse melting point (T_m) mechanism, where the pressure pulse arising from the collapse of bubbles increases T_m according to the Clausius-Clapeyron equation 2.4 [Swallowe et al. (1989)]. An increase in T_m is equivalent to increased undercooling so that increased frequency of nucleation events is expected.

$$\frac{dT_m}{dP} = \frac{T_m \left(V_L - V_S \right)}{\Delta H} \qquad (2.4)$$

Where, T_m is the freezing point, P is the pressure, V_L and V_S are the specific volume of liquid and solid phases, respectively, and ΔH is the latent heat of freezing. Although this explanation is advanced in some alloy solidification studies [Xu, et al. (2004),], it is not likely to be responsible for the observed grain refinement in this study since the metals studied in this work are alloys having wider freezing range. Thus, they do not exhibit a unique melting point and this mechanism of grain refinement applies only to pure metals [Swallowe et al. (1989)].

Second mechanism proposes that during the expansion of cavitation bubbles, there is endothermic vaporization of the surrounding melt into the bubbles. This lowers the temperature on the surface of the bubbles and local undercooling occurs. This leads to the formation of nuclei around the bubbles during solidification, which increases the nucleation rate and refines the grain size [Xu, et al. (2004), Easton, et al. (2001)]. Third mechanism is based on ultrasonic cavitation-induced enhanced wetting of particles. It assumes that alloy melts always contain large number of ultrafine insoluble non-metallic particles such as oxides, intermetallics etc and normally these are not wettable by the melt [Eskin, et al. (2003), Patel et al. (2012)]. Collapse of cavitation bubbles generates high-pressure pulses in the melt. Under the action of high-pressure pulses, the wettability of these impurity particles is improved by filling of melt in to their surface micro cracks and surface defects. Enhanced wetting activates most of these insoluble impurity particles, involving them in the solidification process as nuclei. Therefore, heterogeneous nucleation occurs easily upon slight undercooling. It is noteworthy that in addition to the usually present non-metallic particles, Mg-Al melts in the present work also contain added carbon black nanoparticles. Based on previous works on UST of molten alloys [Tsunekawa, et al. (2001), Eskin, et al. (2003), Yang, et al. (2004), Lan, et al. (2004)], it can be concluded that the high intensity ultrasonic vibrations applied to inoculated melts would result in enhanced wetting of carbon black nano-particles. More importantly, the cavity collapse and concomitant streaming of melts would de-agglomerate and disperse them throughout the melt. The beneficial effect of power ultrasound on improving the kinetics of chemical reactions is well documented [Suslick, (1999), Su, et al. (2012)]. Therefore, the UST of AZ alloys is also expected to accelerate the kinetics of inoculating phase formation in the present work. As compared to the base alloys, there is about 70-80 pct reduction in the grain size of all the alloys subjected to combined inoculation and UST (Table 5.1). Thus, it is very likely that one, the other, or both of the later two mechanisms along with efficient de-agglomeration and dispersion of inoculants in the melt might be responsible for increased density of active nuclei with UST, which resulted in the finer microstructures observed in the present work.

Assuming that heterogeneous nucleation develops progressively along with the development of constitutional undercooling ahead of the growing grains, Easton et al [Li, et al. (2008)] theoretically derived an equation relating the grain size, d, of a solidified alloy to growth restriction factor, Q, as

$$d = a + \frac{b}{Q} \tag{5.3}$$

$$Q = m(k-1)C_0 \tag{5.4}$$

Where, m is the slope of the liquidus on a binary phase diagram, k is the solute partition coefficient and C_0 is the solute concentration. When similar casting conditions are used, the intercept, a, is related to the number of the active nucleants. A smaller “a” represents a large number of active nucleants. Slope, b, is shown to represent the potency of the active nucleants. A smaller “b" corresponds to higher potency [StJohn, et al. (2005)]. This equation is used for evaluation of grain refining processes [StJohn, et al. (2005), Xu, et al. (2004)] because it enables the analysis based on the number and potency of active nucleants that exist during the solidification of melts. This approach is used in the present work in order to assess the efficacy of grain refinement in variously processed Mg alloys containing different Al contents.

Figure 5.4 shows the plots of grain size d vs. 1/Q for the three Mg–Al alloys solidified as base alloys, carbon inoculated alloys, and combined carbon inoculated and ultrasonically processed alloys. A linear relationship is observed for all the alloys studied, agreeing well with equation (5.3). Large intercept ($a \approx 88$ μm) obtained for the base alloys (line 1) indicate that there are fewer active nucleants operating during the solidification. This is consistent with microstructures of all the base alloys (Fig. 5.2a-c). It implies that the constitutional undercooling generated during solidification of the alloys was inadequate to activate the nucleants existing in each commercial alloy. In literature, it has been shown that, carbon inoculation can induce good grain refinement because of the formation of the mildly potent

Al_4C_3 nucleants [Polmear, (2006), StJohn, et al. (2005), Du et al. (2009), Jin, et al. (2003)]. In the present work, this is evident from the lowering of the values for slope and intercept for the line 2. However, UST together with carbon inoculation (line 3) demonstrated significantly higher potency than carbon inoculation alone as revealed by the sharp decrease in the slope from line 2 to line 3. In addition, the number of the active nucleants is increased as suggested by a smaller intercept of line 3. This is supported by the much finer grain structures obtained after UST with carbon inoculation (Figs. 5.2g-i).

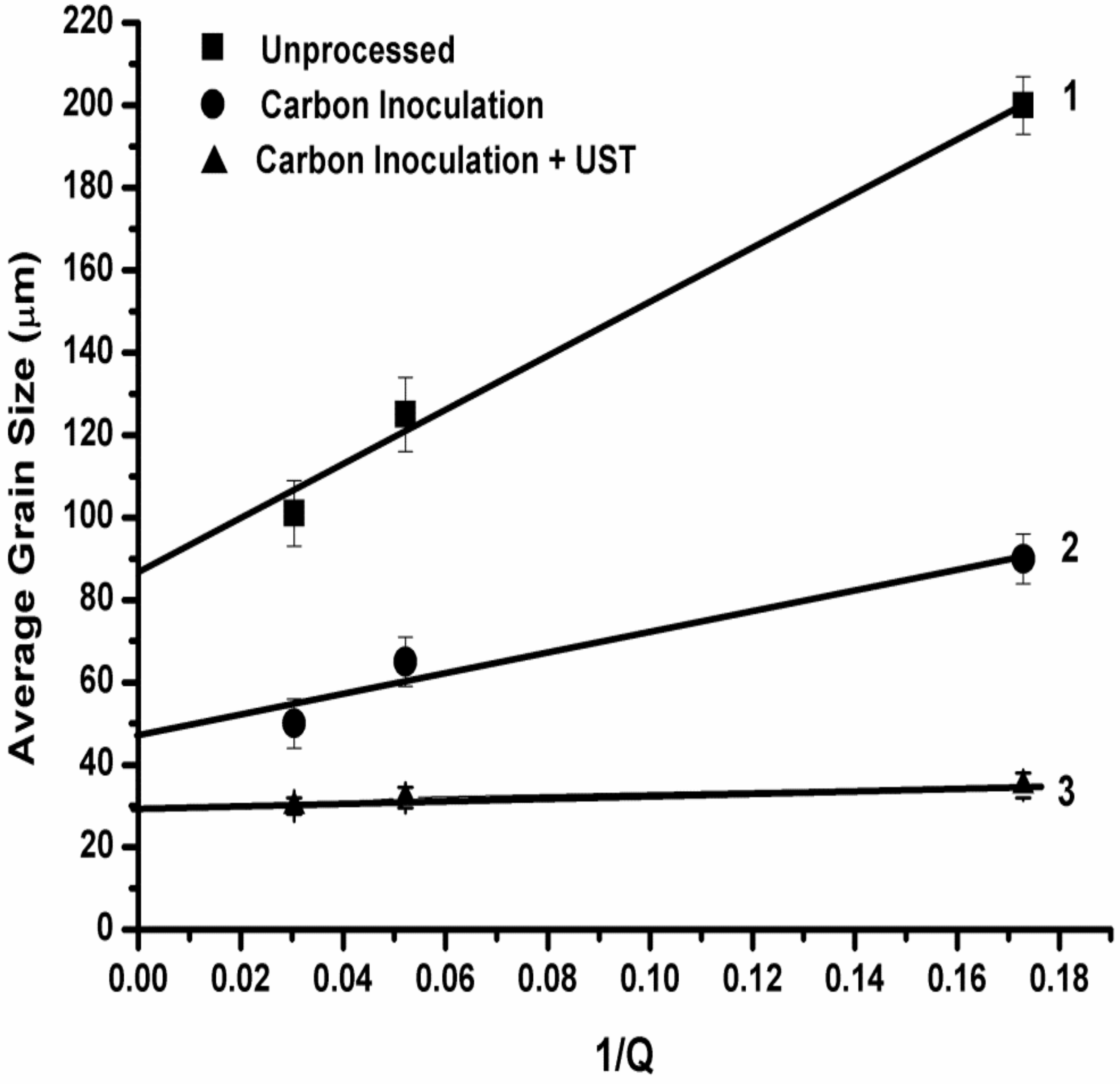

Fig. 5.4 Grain size d vs. 1/Q for the three Mg–Al alloys.

5.3 Mechanical behaviour

Figs. 5.5a-c show the true stress-true strain curves obtained from tension tests performed on samples of variously processed AZ91, AZ61, and AZ31 alloys, respectively. Table 5.3 shows a summary of the tensile properties obtained from these curves. Among all the alloys, AZ91 shows the highest 0.2 % proof stress and UTS values for all the processing conditions. This follows from its higher solute content (Al content) and more refined microstructure (Figs. 5.2a,d,g), the effect of which is further discussed later using the Hall-Petch relationship. It can also be seen that the 0.2% proof stress, the UTS, and total elongation to fracture values are lowest for all the unprocessed alloys. These values are intermediate for all the carbon inoculated alloys and are highest for all the combined carbon inoculated and ultrasonically treated alloys. These results correlate well with the microstructural refinement observed after subjecting these alloys to various processing conditions. The finer the microstructure the higher is the 0.2 % proof stress and total elongation to failure. Thus, the proof stress, UTS and true strain to failure of the AZ91, AZ61 and AZ31 magnesium alloys exhibit an obvious linear dependence on microstructure. Ultrasonic treatment of molten metals is known to result in reduced microporosity [Eskin, (1997), Tsunekawa, et al.(2001), Eskin, et al. (2003), Eskin, et al. (1998), Easton, et al. (2001), Ye, et al. (2004)]. It was shown that in Al-Si alloys minimum porosity was observed when the melt was treated for 180s using ultrasonic intensity of 150 W [Nie, et al. (2011)]. In the present work, higher intensity (4.3 kW) UST was carried out for 180s. The resulting cavitation phenomena might have resulted in increased degassing of the melt and hence reduced porosity. Thus, the higher total elongation to failure in ultrasonically processed alloys can also be ascribed to the expected reduced microporosity in them, although no detailed porosity evolution studies are performed in this work.

Fig. 5.6 shows the variation of Vickers hardness of the specimens of AZ31, AZ61, and AZ91 alloys in unprocessed, carbon black inoculated, and carbon black inoculation followed by ultrasonic treatment conditions. It is observed that carbon inoculation treatment improves hardness of magnesium alloys by about 15 to 25 pct as compared to that of the corresponding unprocessed base alloys. Carbon inoculation treatment coupled with the ultrasonic processing has largest improvement in hardness (about 30-50 pct) as compared to that of the unprocessed alloys. The variation in Vickers hardness follows the same trend as the variation in proof stress for all the alloys treated under all the conditions. The improvement in the Vickers hardness and the proof stress of the alloys with decrease in grain size can be explained using the Hall-Petch relationship.

(a)

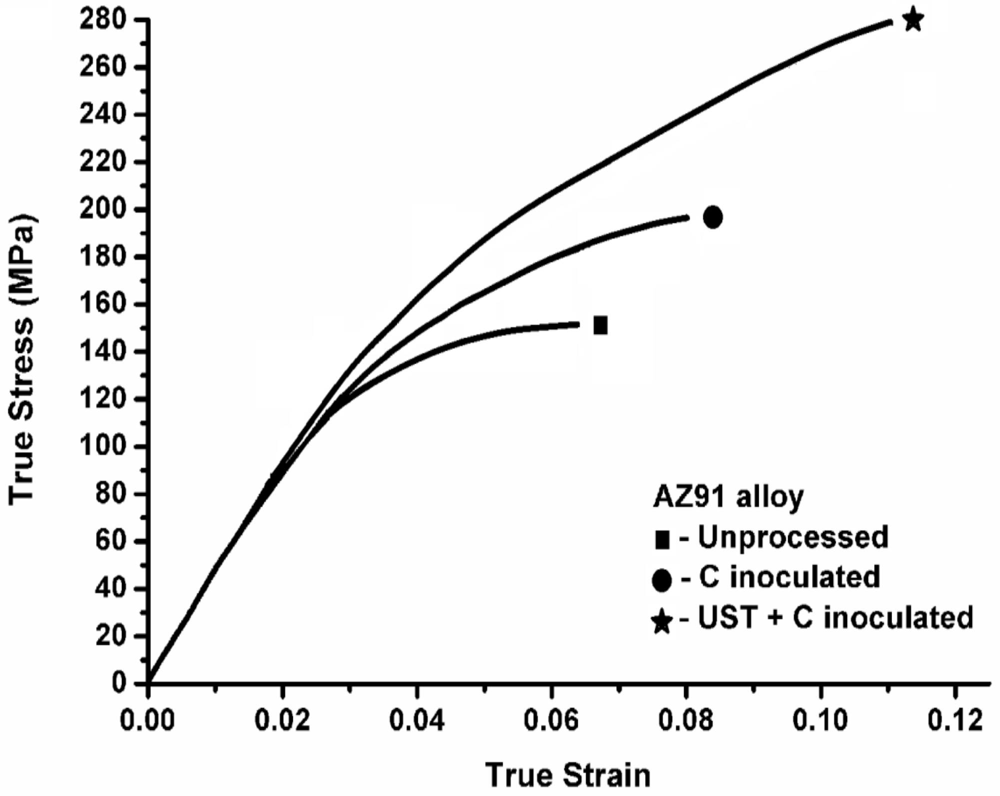
True Stress (MPa)
0
20
40
60
80
100
120
140
160
180
200
220
240
260
280
0.00
0.02
0.04
0.06
0.08
0.10
0.12
True Strain
AZ91 alloy
■ - Unprocessed
● - C inoculated
★ - UST + C inoculated

(b)

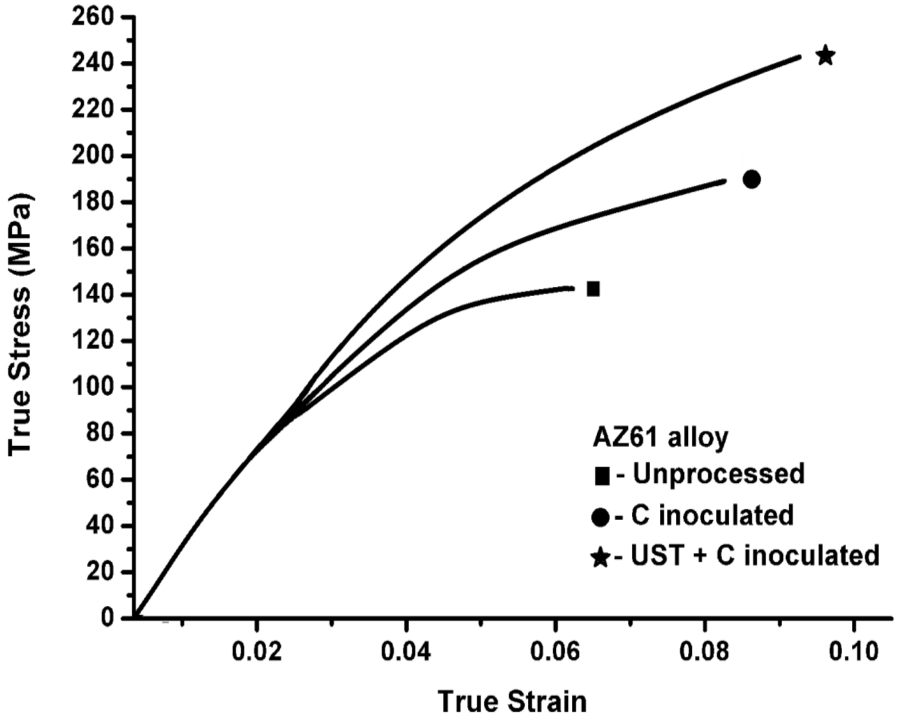
True Stress (MPa)
0
20
40
60
80
100
120
140
160
180
200
220
240
260
0.02
0.04
0.06
0.08
0.10
True Strain
AZ61 alloy
■ - Unprocessed
● - C inoculated
★ - UST + C inoculated

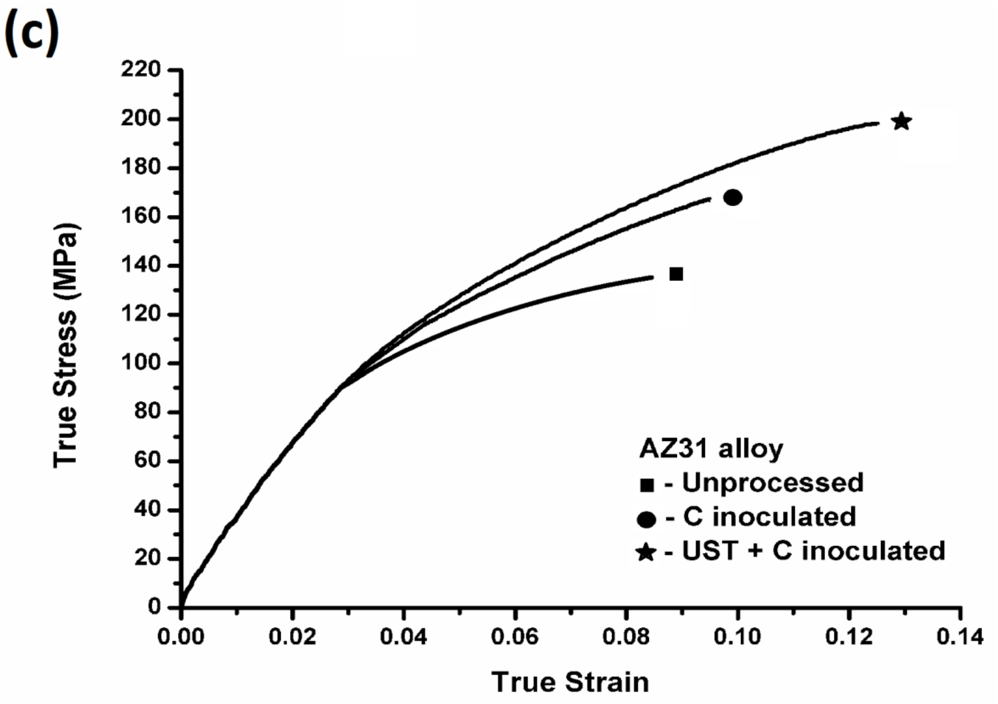

Fig. 5.5 Room temperature tensile behaviour of the unprocessed, carbon black inoculated, and carbon black inoculation followed by ultrasonic treatment, specimens of (a) AZ91, (b) AZ61, and (c) AZ31 alloys.

Table 5.3 Summary of tensile properties of AZ91, AZ61, and AZ31 alloys processed under different conditions.

Material	**Processing Condition**	**0.2 % proof stress (MPa)**	**UTS (MPa)**	**True strain to failure**
AZ91	Unprocessed	111	142	0.07
	Carbon inoculated	123	182	0.08
	C inoculated +UST	154	249	0.12
AZ61	Unprocessed	94	134	0.06
	Carbon inoculated	105	174	0.09
	C inoculated +UST	115	220	0.10
AZ31	Unprocessed	90	120	0.09
	Carbon inoculated	104	167	0.1
	C inoculated +UST	110	198	0.13

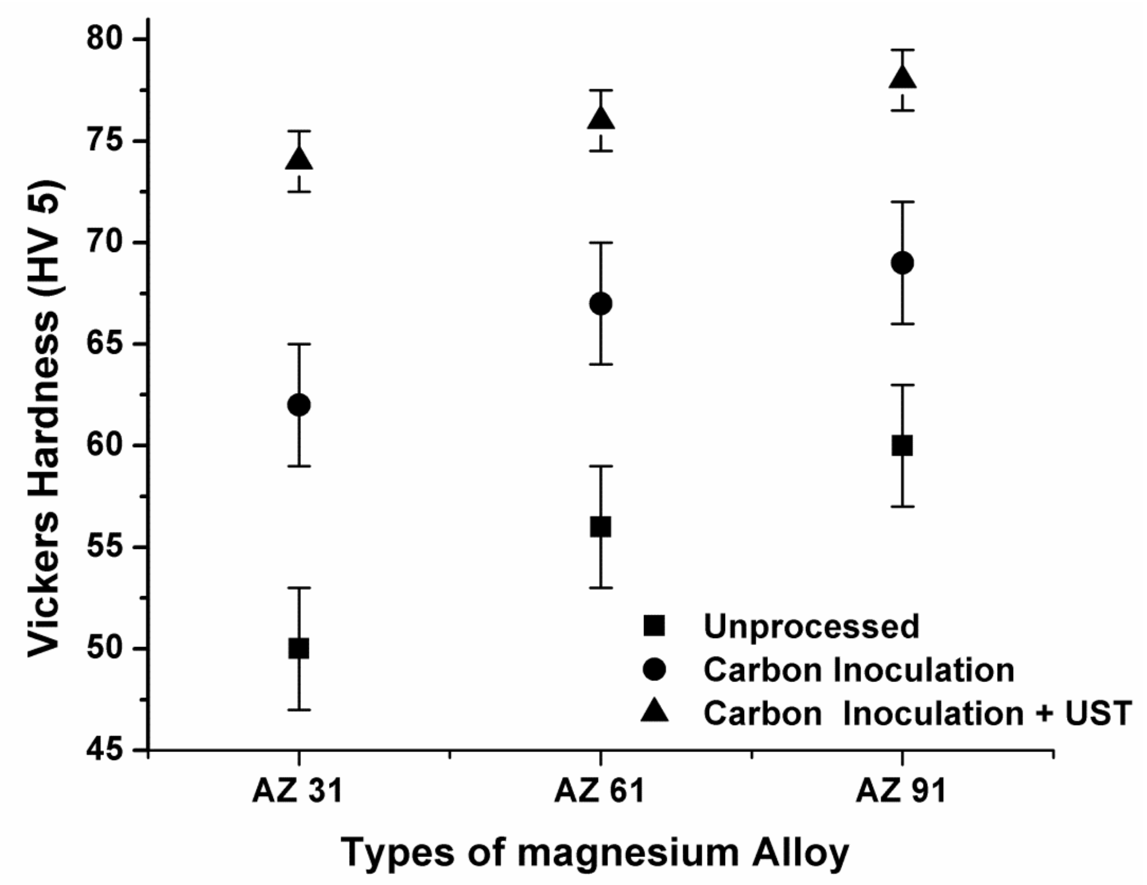

Fig. 5.6 Variation of Vickers hardness of the unprocessed, carbon black inoculated, and carbon black inoculation followed by ultrasonically treated, specimens of AZ31, AZ61, and AZ91 alloys.

According to Hall-Petch equation (equation 2.1) $\sigma_0 = \sigma_i + kd^{-1/2}$ (where, σ_0 is the yield strength, k is constant, σ_i is the friction stress and d is the mean grain diameter), yield stress of metallic materials varies inversely with their grain size. Figure 5.7 shows a plot of 0.2 % proof stress as a function of average grain size ($d^{-1/2}$). From the plots, the locking parameter (slope, k) and the friction stress ($\boldsymbol{\sigma_0}$) needed to move unlocked dislocation along the slip plane, are derived and the values are summarised in Table 5.4. Value of slope k is dependent on the number of slip systems. It is higher for HCP metals than for FCC and BCC metals [Lee, (2007)]. Since α-Mg matrix of all the magnesium alloys studied in this work has HCP structure, the grain size affects the yield strength significantly [Nil et al. (2011)]. The locking parameter of the AZ91 alloy in the Hall-Petch relation in this study is highest 0.52 (MPa $m^{1/2}$), much higher than that of the AZ61 (0.24 MPa $m^{1/2}$) and AZ31 (0.19 MPa $m^{1/2}$) alloys. This suggests that the strengthening effect by grain refinement is more significant in the AZ91alloy than in AZ61 and AZ31 magnesium alloys [Lee, (2007)]. Largest improvement in the mechanical properties of the combined processed alloys is attributed to the synergistic grain refinement effect of nano-carbon black inoculation and ultrasonic treatment of the melt, as discussed earlier.

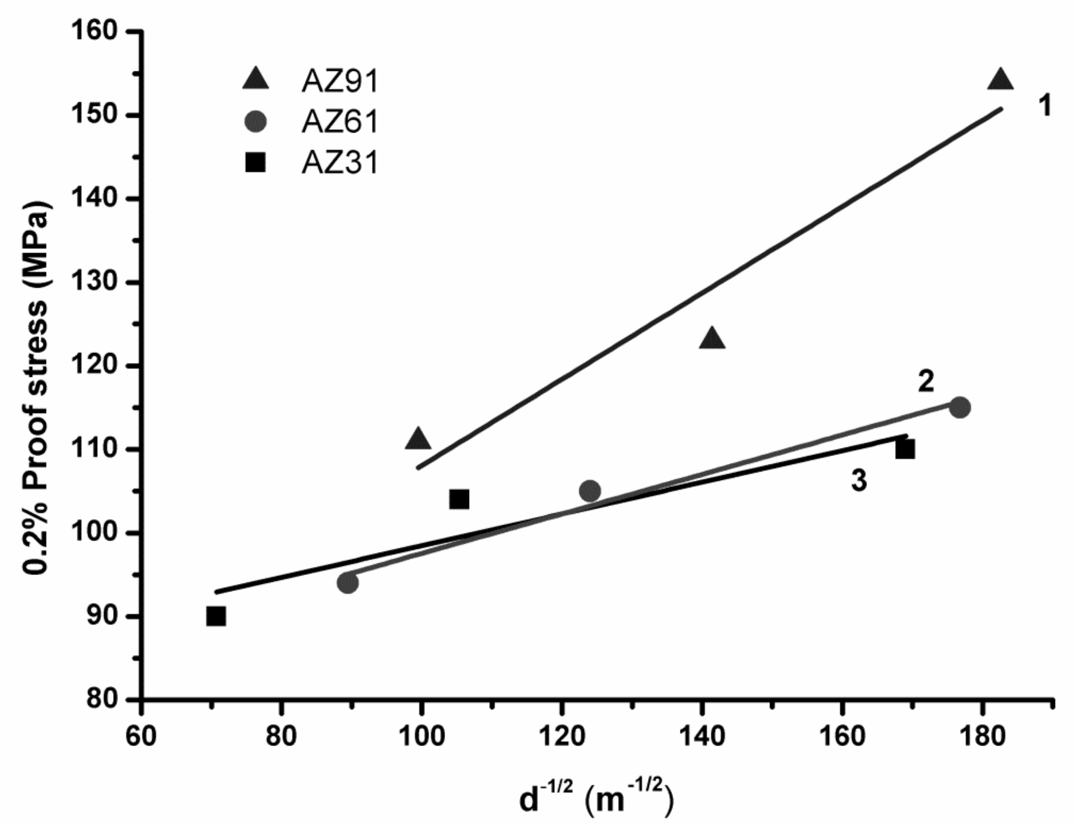

Fig. 5.7 0.2 % proof stress as a function of d$^{-1/2}$ for the AZ31, AZ61, and AZ91 alloys.

Table 5.4 Hall-Petch parameters for 0.2 % proof stress.

Material	**Friction stress, σ_0 (MPa)**	**Slope, k (MPa m$^{1/2}$)**
AZ91	56.4	0.52
AZ61	73.9	0.24
AZ31	79.4	0.19

5.4 Summary

Three commercial Mg-Al alloy melts are subjected to carbon black inoculation and ultrasonic treatment before solidification. Following conclusion are drawn from the present work.

1. Nano carbon black powder inoculation is a more effective grain refiner for Mg-Al-Zn magnesium alloy than the conventional environmentally polluting hexacholoroethane treatments. Inexpensive nano carbon black that has a high surface area to volume ratio readily forms the inoculating phase particles in larger number, thereby resulting in the more extensive grain refinement observed in this work.
2. High intensity ultrasonic treatment applied along with carbon black inoculation increases the number of particles that actually nucleate grains and the potency of nuclei. After such treatment, the average grain size of all the AZ alloys decreased by about 70-80 pct. This is ascribed to the fact that UST accelerates the wetting, de-agglomeration, and dispersion of carbon black nano-particles and also improves the kinetics of inoculating phase formation.
3. The 0.2 % proof stress, UTS, and total elongation to fracture values are highest for all the Mg alloys that were subjected to carbon black inoculation followed by ultrasonic treatment. This is because of the grain refinement resulting from the synergy of nano carbon black inoculation and high intensity ultrasonic processing.

Chapter 6

RESULT AND DISCUSSIONS-FABRICATION OF IN SITU MMCs WITH ULTRASONIC PROCESSING

A novel solidification processing technique involving ultrasonic treatment (UST) assisted casting process has been developed. It is efficient in dispersing the nano particles in to the melts. Poor wettability of reinforcing particles arising because of the intrinsic properties of the material such as the surface energy of the matrix and the reinforcement, and the oxidation and contamination of particle surface can be overcome by the UST. It is one of the simplest and effective physical methods to homogenise and degas the melt, and to wet, de-agglomerate, and uniformly disperse the reinforcement particles. In view of the potential of in situ synthesis approach and the UST, both these techniques are coupled for the fabrication of AZ91 alloy matrix composites by the addition of one, five, and 10-wt pct of magnesium nitrate that is easily available, low cost and easy to operate with. Formation of hard oxide reinforcement particles by in situ reactions is studied. The microstructure of the composites is characterized for the uniformity in the distribution of reinforcement particles and is correlated with mechanical properties. By evaluating the dry sliding wear behaviour over a range of loads, the operating wear mechanisms are analysed.

6.1 AZ91 alloy based MMCs

6.1.1 Microstructural evolution

Light optical micrographs of the cast AZ91 alloy and its MMCs are shown in Fig. 6.1. Optical micrograph of unprocessed AZ91 alloy is shown in Fig. 6.1a. It shows large dendritic primary α-Mg phase having dendrite arm lengths of 150 μm to 175 μm. Secondary $Mg_{17}Al_{12}$ phase is seen bordering the primary α-Mg dendrites. Figs. 2b-d are optical micrographs of AZ91 alloy matrix composites processed without UST. It shows in situ formed oxide particles (dark, shown by arrow) at isolated locations in the agglomerated form. The size and amount of these agglomerates increased with increase in the amount of magnesium nitrate added. Optical micrographs of AZ91 alloy matrix composites processed with UST are shown in Figs. 6.1e-g. The oxide agglomerates are absent. It is likely that the oxide particles are finely distributed in the alloy matrix and hence are not resolved using optical microscopy. This is further verified by the FESEM studies. Material designation used in the present work for different processing conditions is shown in Table 6.1.

Table 6.1 Material designations used in the present work with AZ91 alloy and AZ31 alloy matrix composites.

Magnesium Nitrate Addition (wt pct)	**Ultrasonic Processing condition**	**Material Designation for AZ91**	**Material Designation for AZ31**
0	Unprocessed	AZ91	AZ31
1	Unprocessed	AZ91-1	AZ31-1
1	Ultrasonically processed	AZ91-1-UST	AZ31-1-UST
5	Unprocessed	AZ91-5	AZ31-5
5	Ultrasonically processed	AZ91-5-UST	AZ31-5-UST
10	Unprocessed	AZ91-10	AZ31-10
10	Ultrasonically processed	AZ91-10-UST	AZ31-10-UST

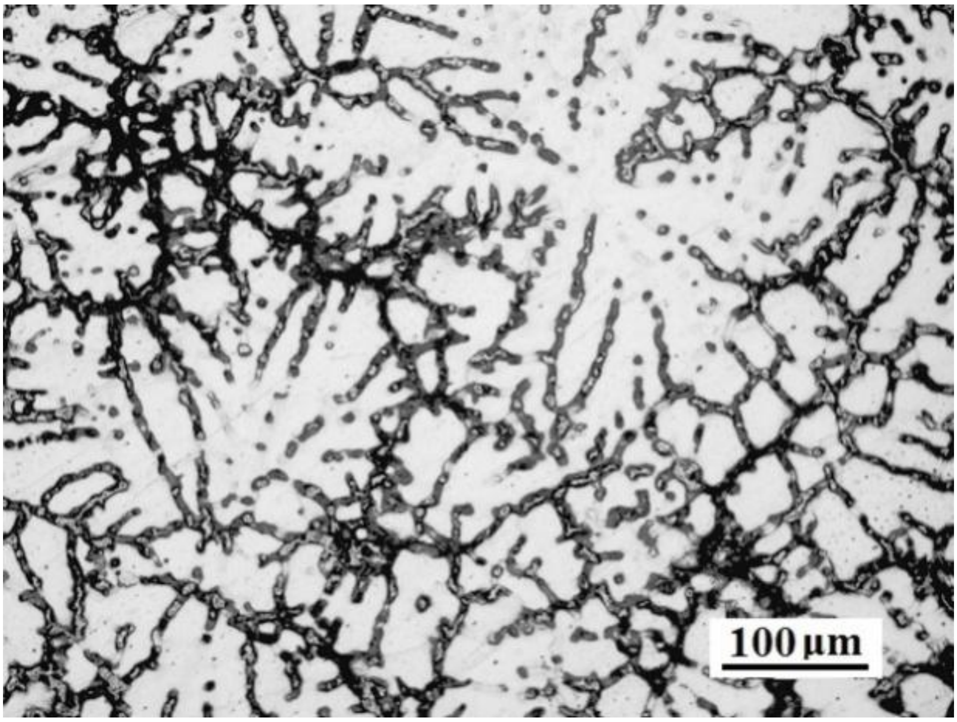

Fig. 6.1 Optical micrographs of AZ91 magnesium alloys in as cast condition.

Optical micrograph of unprocessed AZ91 alloy is shown in Fig. 6.1. It shows large dendritic primary α-Mg phase having dendrite arm lengths measuring about 150 µm to 175 µm. Secondary $Mg_{17}Al_{12}$ phase is seen bordering the primary α-Mg dendrites. Figs. 6.2a,b,c show the optical micrographs of AZ91 alloy matrix composites processed without UST. It shows in situ formed oxide particles (dark, shown by arrow) at specific locations in the agglomerated form. The size and amount of these agglomerates increased with the amount of magnesium nitrate added. Optical micrographs of AZ91 alloy matrix composites processed with UST are shown in Figs. 6.2d,e,f. The oxide agglomerates are absent. It is likely that the oxide particles are finely distributed in the alloy matrix and hence are not resolved using optical microscopy. This is further verified by the FESEM studies. The Figs. 6.3a-b shows the FESEM micrographs of AZ91-10 and AZ91-10-UST MMCs, respectively. In these micrographs, the dark areas correspond to α- Mg phase and the light to the β-phase ($Mg_{17}Al_{12}$). Also seen along the grain boundaries are the scattered magnesium oxide and aluminium oxide particles, which were semi-quantitatively verified using the EDS analysis. It is also noticeable that the distribution of in situ formed oxide particles is not uniform in the MMCs processed without UST as compared those processed with the UST.

Figs. 6.3c-d show the high magnification micrographs of AZ91-10 and AZ91-10-UST MMC specimens, respectively. It is clear from Fig. 6.3c that in-situ formed particles are nano sized but they are in agglomerated form in the ultrasonically unprocessed MMCs. With the application of UST, the in situ formed oxide particles are well distributed in AZ91 alloy matrix (Fig. 6.3d, shown by arrow). XRD analysis of the processed MMCs and the base alloy is shown in Fig. 6.4. Figs 6.4b-g show the presence of in situ formed $MgAl_2O_4$, Mg_2Al_3, MgO, Al_2O_3 phases in the matrix of α-Mg and $Mg_{17}Al_{12}$ phase of the parent AZ91 alloy. Peaks corresponding to these oxides are absent in the AZ91 base alloy (Fig. 6.4a).

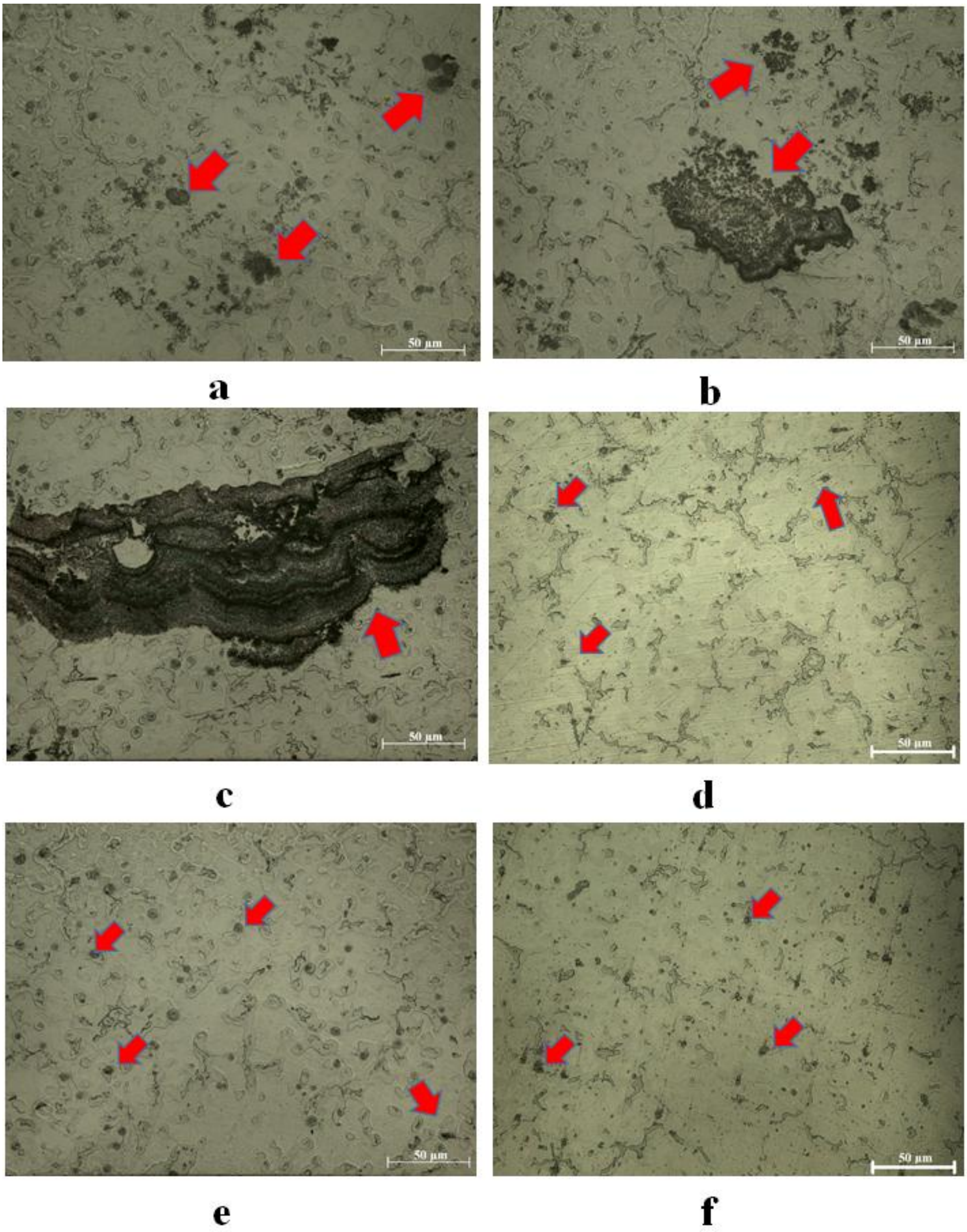

Fig. 6.2 Optical micrographs of AZ91 alloy based MMCs obtained from various processing conditions- (a) AZ91-1, (b) AZ91-5, (c) AZ91-10, (d) AZ91-1-UST, (e) AZ91-5-UST, and (f) AZ91-10-UST cast MMCs.

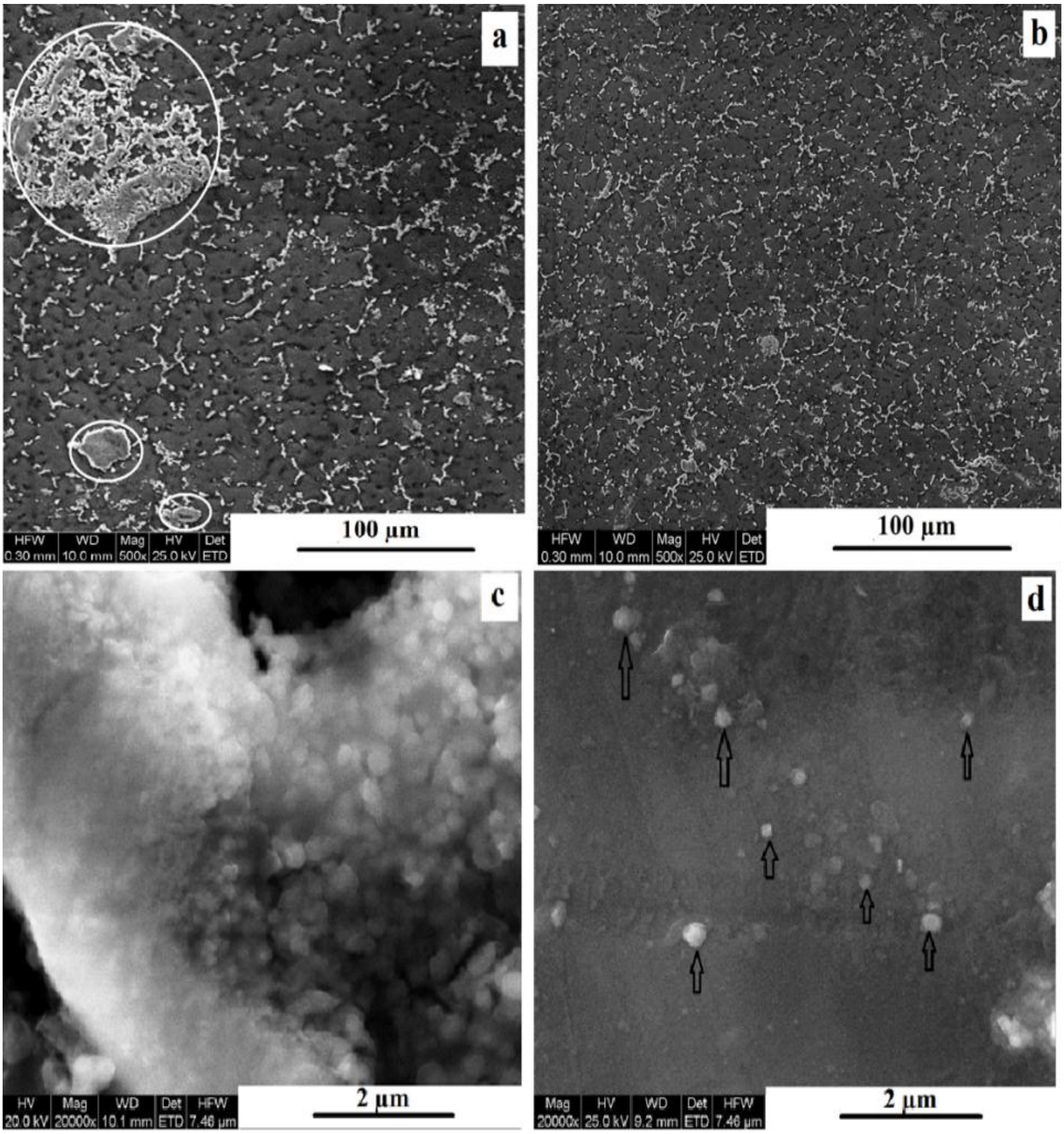

Fig. 6.3 SEM micrographs of AZ91 alloy based MMCs obtained from various processing conditions- (a) AZ91-10, (b) AZ91-10-UST, and (c) AZ91-10 and (d) AZ91-10-UST, at higher magnifications.

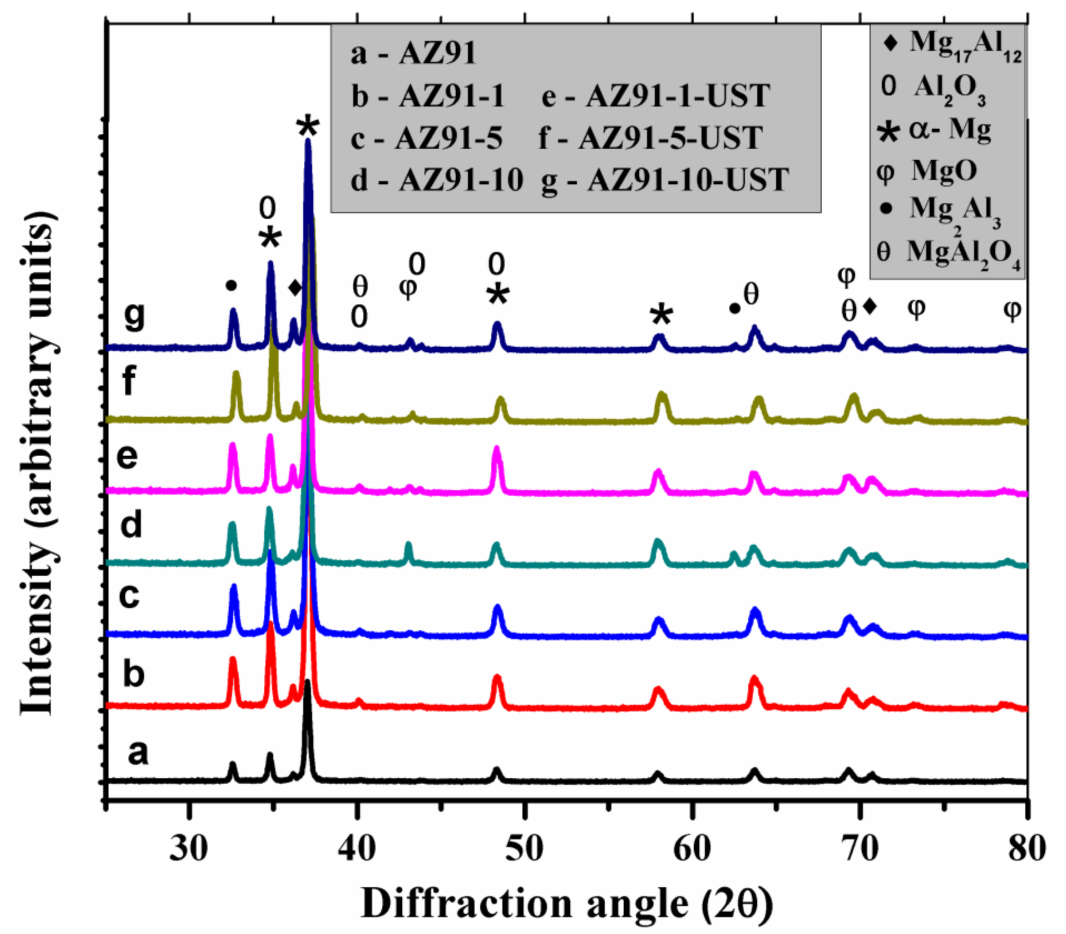

Fig. 6.4 XRD patterns for AZ91 MMCs processed under various conditions.

6.1.2 Mechanical behaviour

Fig. 6.5 shows the variation in the Vickers hardness of the cast AZ91 alloy and variously processed MMCs. It is observed that hardness of the MMCs increased with the wt pct of magnesium nitrate added in the melt. AZ91-10-UST composite specimens exhibit highest hardness. Its hardness is about 64 pct higher as compared to that of the AZ91 alloy. Fig. 6.6 shows room temperature true stress-true strain curves of the AZ91 alloy and the MMCs. It is seen that the yield strength follows similar trend as the hardness. AZ91-10-UST specimens exhibit the highest yield strength, which is 43 pct higher as compared with AZ91 alloy. Fig. 6.7 shows the variation of strain hardening exponent (n) with composition of the MMC. The n value increases continuously with wt pct of reinforcement added in the matrix. It is higher for UST processed MMCs as compared to the unprocessed MMCs for all melt additions. Highest nvalue is exhibited AZ91-10-UST specimens, which is 115 pct higher as compared with the n value of AZ91 alloy.

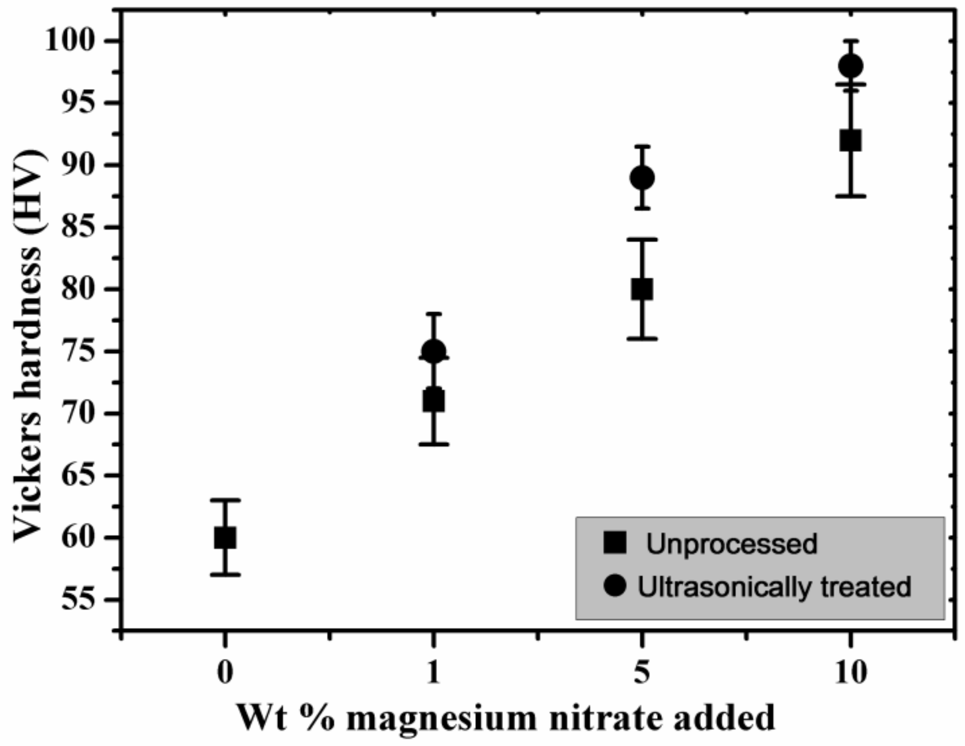

Fig. 6.5 Variation of hardness of the ultrasonically unprocessed and processed AZ91 MMCs with wt pct of magnesium nitrate added.

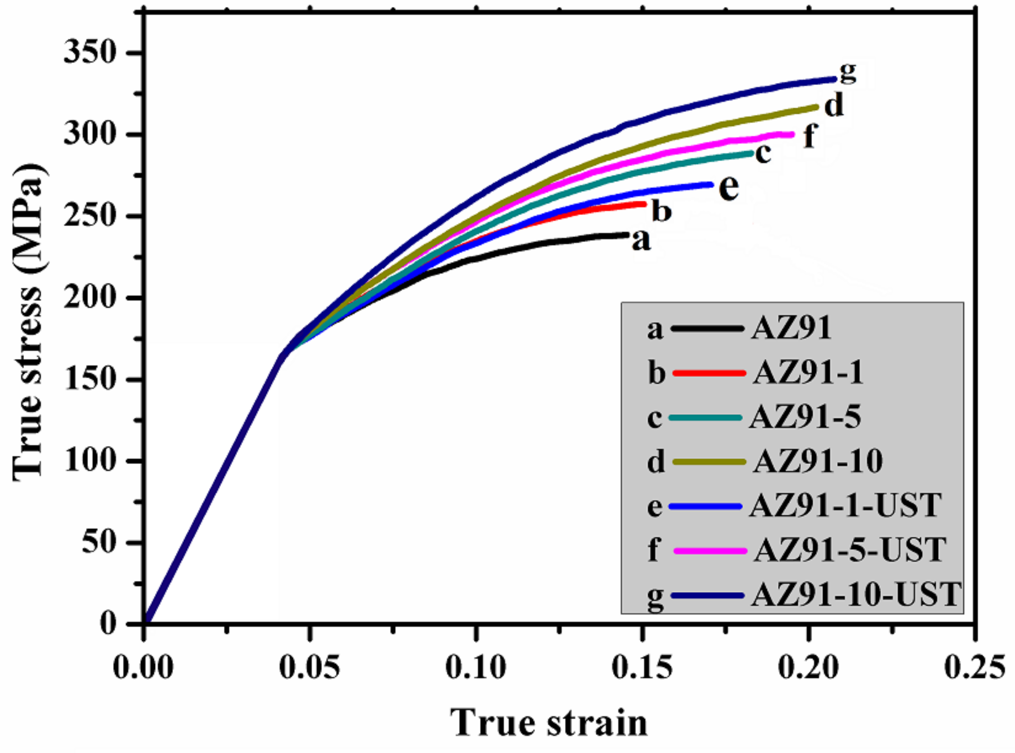

Fig. 6.6 Room temperature compressive true stress- true strain curves of variously processed AZ91 MMCs, formed from addition of different wt pct of magnesium nitrate.

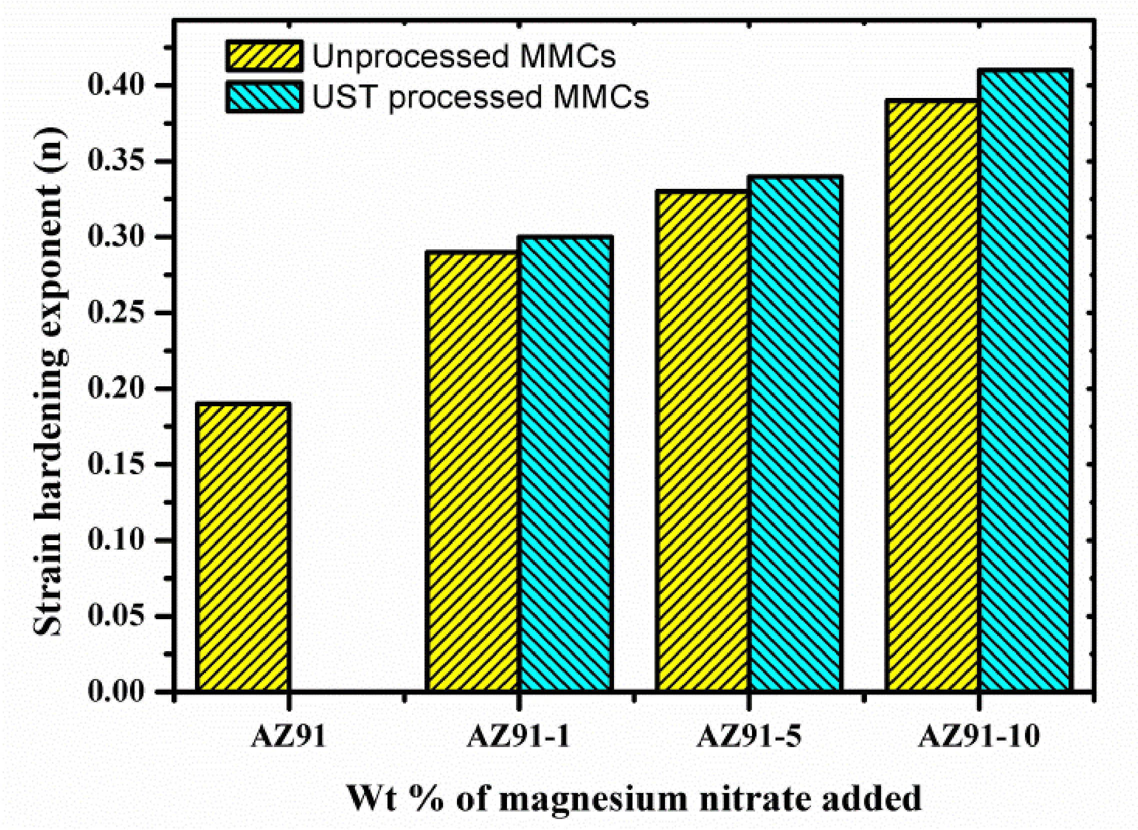

Fig. 6.7 Variation of strain hardening exponent with the wt pct of magnesium nitrate added.

Representative plots of variations of wear volume with sliding distance under different normal loads and at a fixed sliding speed of 1 ms^{-1} for AZ91 alloy and AZ91-10-UST samples are shown in Figs. 6.8a and 6.8b, respectively. It is observed that wear volume increases linearly with sliding distance at the all normal load applied.

At given sliding distance as the normal load increased, the wear volume increases. Linear variation of wear volume with sliding distance helps in analyzing the wear data within the framework of Archard wear equation. These observations indicate that they obey the Archard law. Maximum wear volume is observed in AZ91 alloy and minimum is observed in AZ91-10-UST specimen for all the loads and all the sliding distances. A 28 pct reduction in the wear volume of AZ91-10-UST specimen is observed at 14.9 N load and 2000 m sliding distance compared with AZ91 alloy for same load and sliding distance. From the above graphs, wear rate was determined as the slope of each line at respective loads for each type of material. Variation of wear rate of AZ91 alloy, MMCs and the UST processed MMCs is plotted against the normal loads (Fig. 6.9a-b).

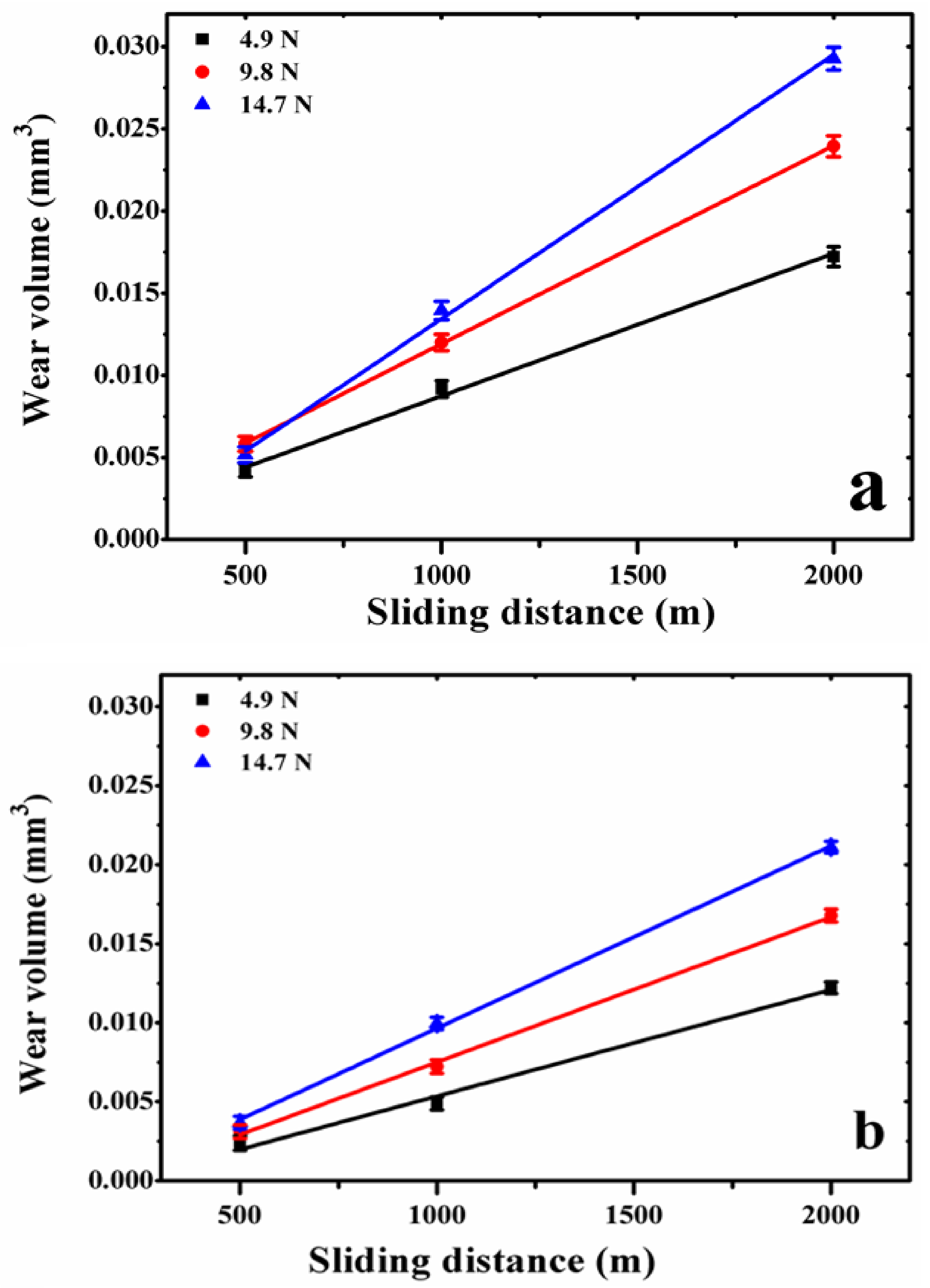

Fig. 6.8 Variation of wear volume (mm^3) with sliding distance for different normal loads in (a) AZ91, and (b) AZ91-10-UST specimens.

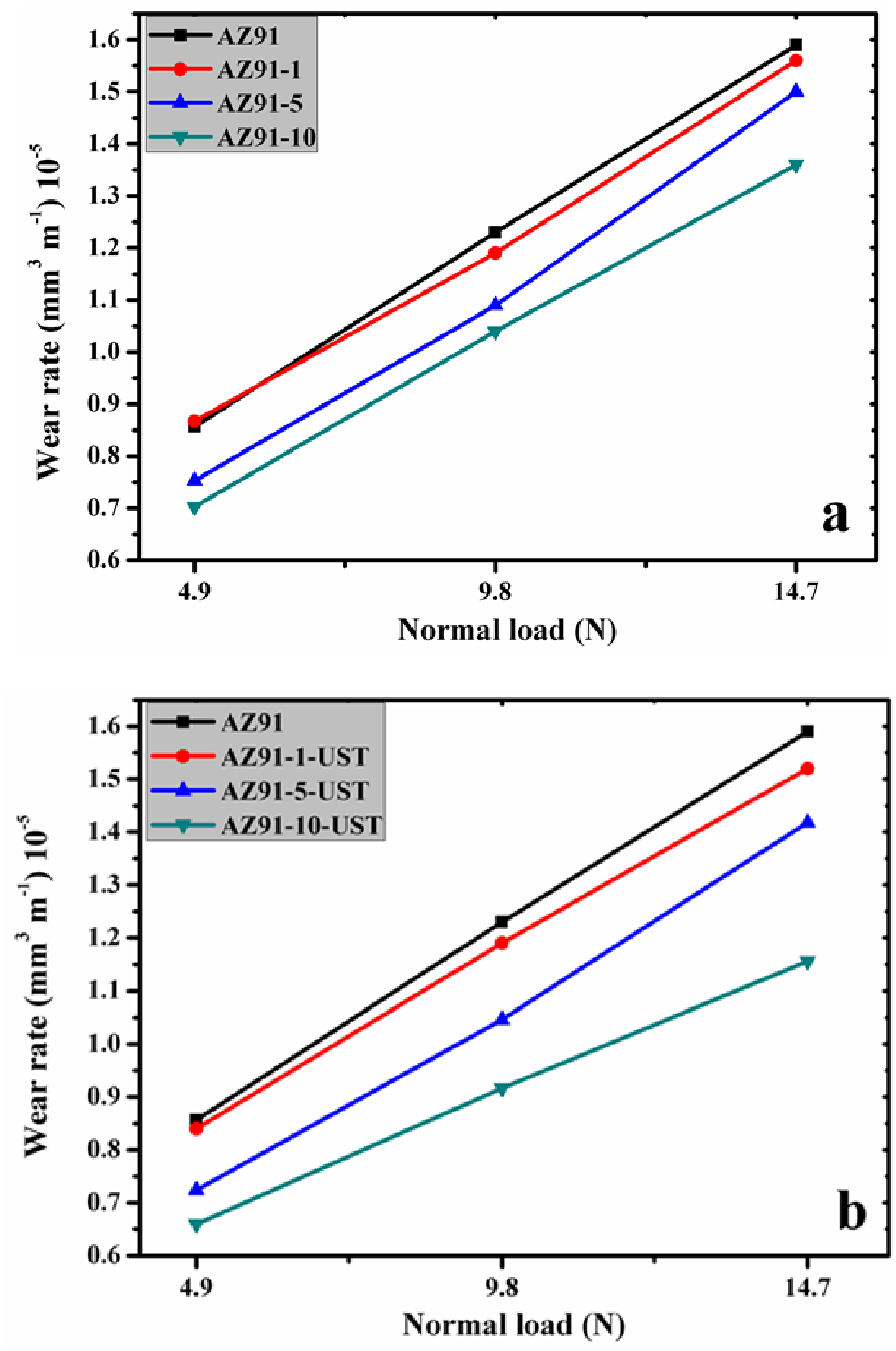

Fig. 6.9 Variation of volumetric wear rate with varying normal load for (a) UST unprocessed, and (b) UST processed cast AZ91 alloy and various in situ MMCs, tested at a constant sliding speed of 1 ms^{-1}.

In Fig. 6.9a it is observed that wear rate of AZ91 alloy and the MMCs follow a linear relationship with normal loads. It indicates that wear rate increases with increase in the normal load. Lowest wear rate is observed in AZ91-10 specimens that is 15 pct lower as compared with AZ91 alloy at 14.7 N loads. Similarly Fig. 6.9b shows that the wear rate of AZ91-10-UST MMC is 27 pct lower as compared with AZ91 alloy at 14.7 N loads. All these MMCs and AZ91 alloy follows Archard's equation. Maximum wear rate is observed in the base AZ91 alloy. It is also noticed that for a given normal load, the wear rate decreased with an increase in the wt pct of reinforcement added. Further, it is interesting that all the UST processed MMCs exhibit lower wear rates. AZ91-10-UST composite exhibited highest wear resistance among all the tested MMCs.

6.2 AZ31 alloy based MMCs

6.2.1 Microstructural evolution

Optical micrograph of unprocessed AZ31 alloy is shown in Fig. 6.10. It shows large dendritic primary α-Mg phase having dendrite arm lengths measuring about 150 μm to 175 μm. Secondary $Mg_{17}Al_{12}$ phase is seen bordering the primary α-Mg dendrites. Figs. 6.11a,b,c show the optical micrographs of AZ31 alloy matrix composites processed without UST. It shows in situ formed oxide particles (dark, shown by arrow) at specific locations in the agglomerated form. The size and amount of these agglomerates increased with the amount of magnesium nitrate added. Optical micrographs of AZ31 alloy matrix composites processed with UST are shown in Figs. 6.11d,e,f. The oxide agglomerates are absent. It is likely that the oxide particles are finely distributed in the alloy matrix and hence are not resolved using optical microscopy. This is further verified by the FESEM studies.

The Figs. 6.12a-b shows the FESEM micrographs of AZ31-10 and AZ31-10-UST MMCs, respectively. In these micrographs, the dark areas correspond to α- Mg phase and the light to the β-phase ($Mg_{17}Al_{12}$). Also seen along the grain boundaries are the scattered magnesium oxide and aluminium oxide particles, which were semi-quantitatively verified using the EDS analysis. It is also noticeable that the distribution of in situ formed oxide particles is not uniform in the MMCs processed without UST as compared those processed with the UST. Figs. 6.12c-d show the high magnification micrographs of AZ31-10 and AZ31-10-UST MMC specimens, respectively.

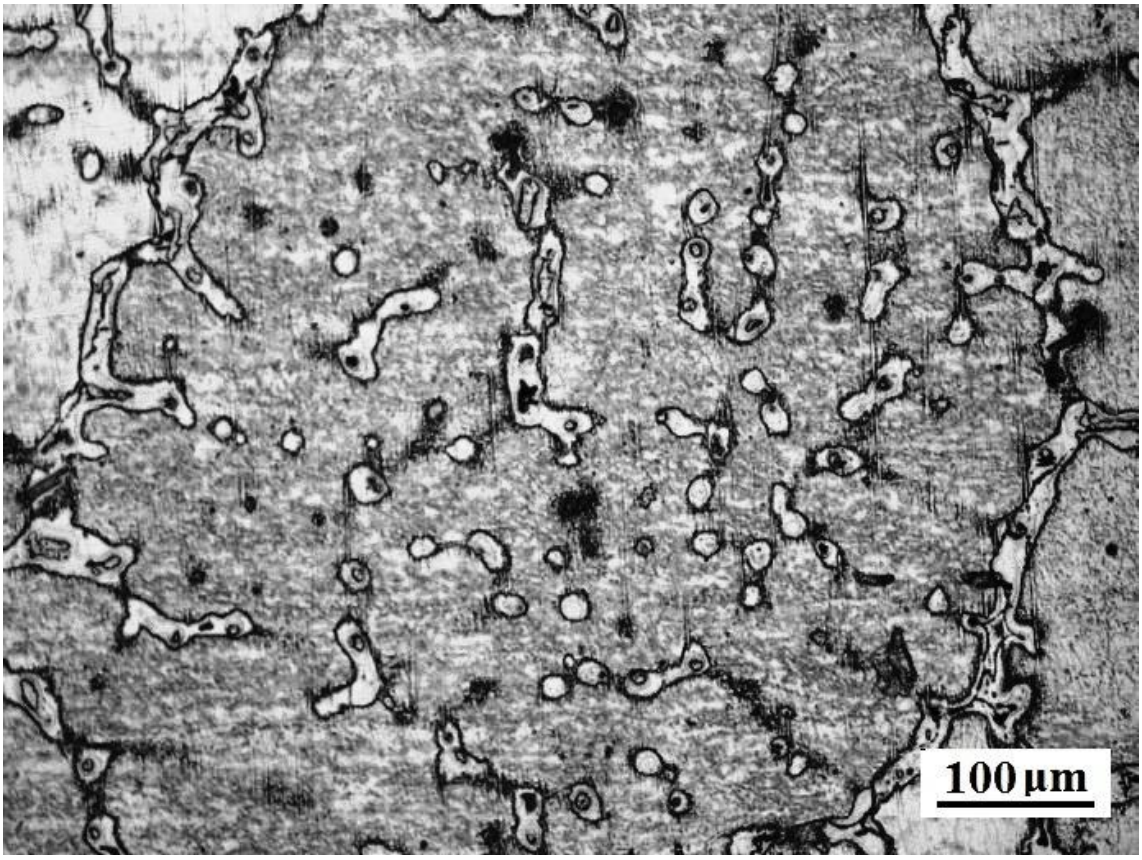

Fig. 6.10 Optical micrograph of AZ31 magnesium alloy in as cast condition.

It is clear from Fig. 6.12c that in situ formed particles are nano sized but they are in agglomerated form in the ultrasonically unprocessed MMCs. With the application of UST, the in situ formed oxide particles are well distributed in AZ31 alloy matrix (Fig. 6.12d, shown by arrow). XRD analysis of the processed MMCs and the base alloy is shown in Fig. 6.13. Figs 6.13b-g show the presence of in situ formed $MgAl_2O_4$, Mg_2Al_3, MgO, Al_2O_3 phases in the matrix of α-Mg and $Mg_{17}Al_{12}$ phase of the parent AZ31 alloy. Peaks corresponding to these oxides are absent in the AZ31 base alloy (Fig. 6.13a).

6.2.2 Mechanical behaviour

Fig. 6.14 shows the variation in the Vickers hardness of the cast AZ31 alloy and variously processed MMCs. It is observed that hardness of the MMCs increased with the wt pct of magnesium nitrate added in the melt. AZ31-10-UST composite specimens exhibit highest hardness. Its hardness is about 94 pct higher as compared to that of the AZ31 alloy. Fig. 6.15 shows room temperature true stress-true strain curves of the AZ31 alloy and the MMCs. It is seen that the yield strength follows similar trend as the hardness. AZ31-10-UST specimens exhibit the highest yield strength, which is 35 pct higher as compared with AZ31 alloy. Fig. 6.16 shows the variation of strain hardening exponent (n) with composition of the MMC. The n value increases continuously with wt pct of reinforcement added in the matrix. It is higher for UST processed MMCs as compared to the unprocessed MMCs for all melt additions. Highest n value is exhibited AZ31-10-UST specimens, which is 109 pct higher as compared with the n value of AZ31 alloy.

Representative plots of variations of wear volume with sliding distance under different normal loads and at a fixed sliding speed of 1 ms^{-1} for AZ31 alloy and AZ31-10-UST samples are shown in Figs. 6.17a and 6.17b, repsectively. It is observed that wear volume increases linearly with sliding distance at the all normal load applied. At given sliding distance as the normal load is increased, the wear volume increases. Linear variation of wear volume with sliding distance helps in analyzing the wear data within the framework of Archard wear equation. These observations indicate that they obey the Archard law. Maximum wear volume is observed in AZ31 alloy and minimum is observed in AZ31-10-UST specimen for all the loads and all the sliding distances. A 17 pct reduction in the wear volume of AZ31-10-UST specimen is observed at 14.9 N load and 2000 m sliding distance compared with AZ31 alloy for same load and sliding distance. From the above graphs, wear rate was determined as the slope of each line at respective loads for each type of material. Variation of wear rate of AZ31 alloy, MMCs and the UST processed MMCs is plotted against the normal loads (Fig. 6.18a-b). In Fig. 6.18a it is observed that wear rate of AZ31 alloy and the MMCs follow a linear relationship with normal loads. It indicates that wear rate increases with increase in the normal load. Lowest wear rate is observed in AZ31-10 specimens that is 13.5 pct lower as compared with AZ31 alloy at 14.7 N loads. Similarly Fig. 6.18b shows that the wear rate of AZ31-10-UST MMC is 17 pct lower as compared with AZ31 alloy at 14.7 N loads. All these MMCs and AZ31 alloy follows Archard’s equation. Maximum wear rate is observed in the base AZ31 alloy. It is also noticed that for a given normal load, the wear rate decreased with an increase in the wt pct of reinforcement added. Further, it is interesting that all the UST processed MMCs exhibit lower wear rates. AZ31-10-UST composite exhibited highest wear resistance among all the tested MMCs.

6.3 Discussion

6.3.1 Reactive phase formation

At 700°C, MgO, Al_2O_3 and $MgAl_2O_4$ particles are formed in the AZ91 and AZ31 alloys melts. The added magnesium nitrate decomposes and supplies oxygen into the melt. The generated oxygen reacts with magnesium and aluminum to form MgO and Al_2O_3 according to reactions (6.1, 6.2)[Rao, et.al. (2009)].

$$2Mg + O_2 \rightarrow 2\,MgO \quad , \Delta G = -569\ kJ.mol^{-1} \tag{6.1}$$

$$2Al + 3O_2 \rightarrow 2Al_2O_3 \quad , \Delta G = -1532\ kJ.mol^{-1} \tag{6.2}$$

This newly formed magnesium oxide and aluminum oxide react with each other and form spinel $MgAl_2O_4$ as per reactions (6.3,6. 4)[Ma et.ai.(2011)].

$$3Mg + 4Al_2O_3 \rightarrow MgAl_2O_4 + 2Al, \Delta G = -231\ kJ.mol^{-1} \tag{6.3}$$

$$MgO + Al_2O_3 \rightarrow MgAl_2O_4 \quad , \Delta G = -33\ kJ.mol^{-1} \tag{6.4}$$

The negative Gibbs energy values for reactions 6.1 to 6.4 confirm the formation of these compounds. Formation of $MgAl_2O_4$ spinal in the presence oxygen-supplying agent is reported in [Sreekumar, etal. (2007)]. It is reported that in situ stoichiometric spinel can be generated at low temperatures (at 700-800°C) using oxygen-supplying sources in aluminum alloys. In the present work, diffraction peaks corresponding to $MgAl_2O_4$ phase are observed in the XRD analysis of AZ91 MMCs. Thus, it can be concluded that magnesium nitrate acts as an oxygen source for the formation of stable oxides like MgO, $MgAl_2O_4$ and Al_2O_3 in the AZ91 MMCs. The beneficial effect of power ultrasound in improving the kinetics of chemical reactions aided by accelerated diffusion of atomic species is well documented [Sreekumar, et al. (2007), Chan, et al. (2013)]. Application high power ultrasonic vibrations to the melt in the present work must have favourably influenced the reaction kinetics. These in situ particles are seen as black spots in the optical micrographs of AZ91-1, AZ91-5, AZ91-10 andAZ31-1, AZ31-5, AZ31-10 specimens shown in Figs. 6.2a, 6.2b, and 6.2c, and Figs. 6.11a, 6.11b, and 6.11c, respectively. Their formation is also confirmed from XRD analysis as shown in Fig. 6.4 for the AZ91 alloy and Fig. 6.13 for the AZ31 alloy. From the optical images of AZ91 and AZ31 alloy (Fig. 6.2a,b,c and Fig. 6.11a,b,c) it is observed that as wt pct of magnesium nitrate increases the amount of reactively formed in situ particles increases.

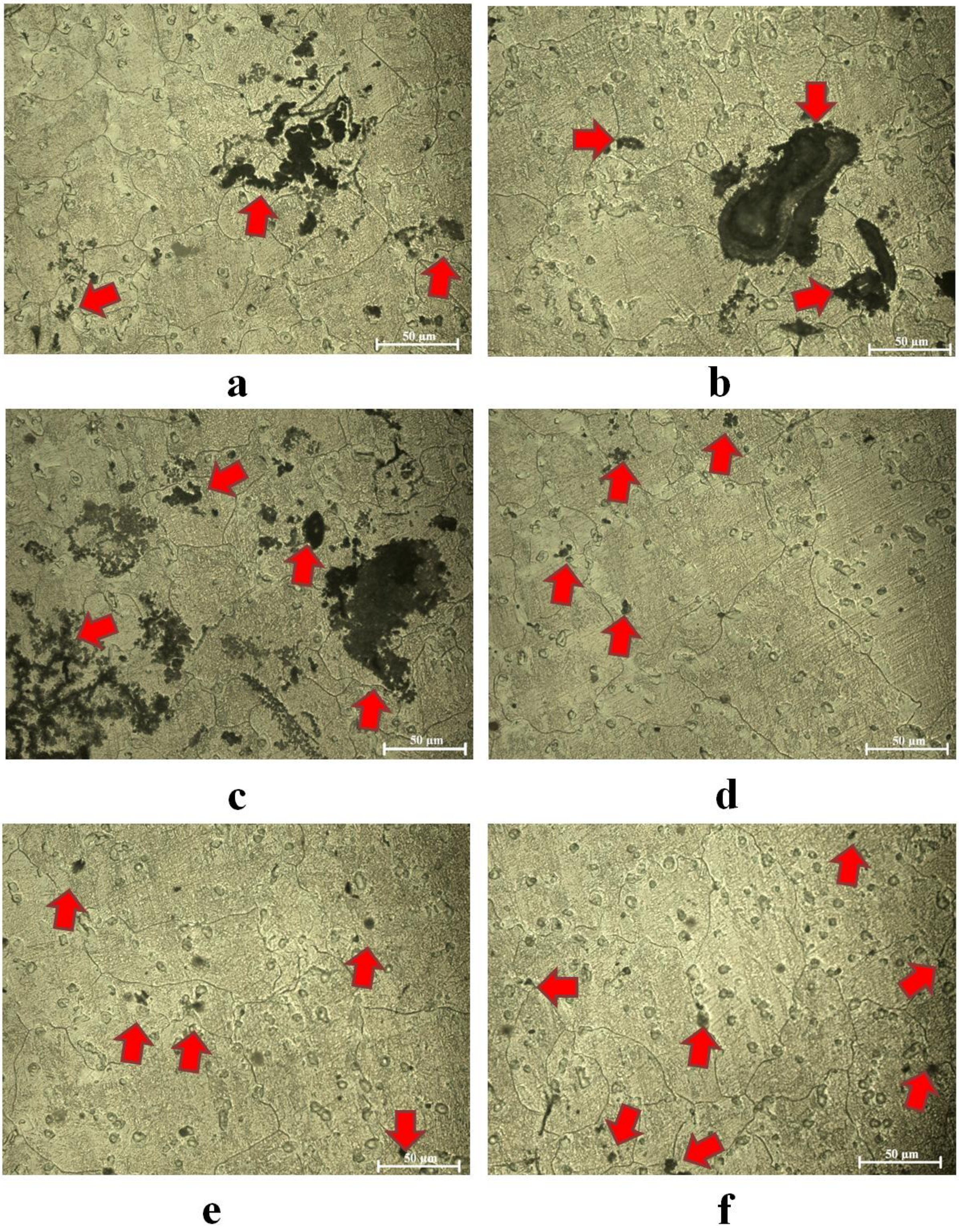

Fig. 6.11 Optical micrographs of AZ31 alloy based MMCs obtained from various processing conditions- (a) AZ31-1, (b) AZ31-5, (c) AZ31-10, (d) AZ31-1-UST, (e) AZ31-5-UST, and (f) AZ31-10-UST cast MMCs.

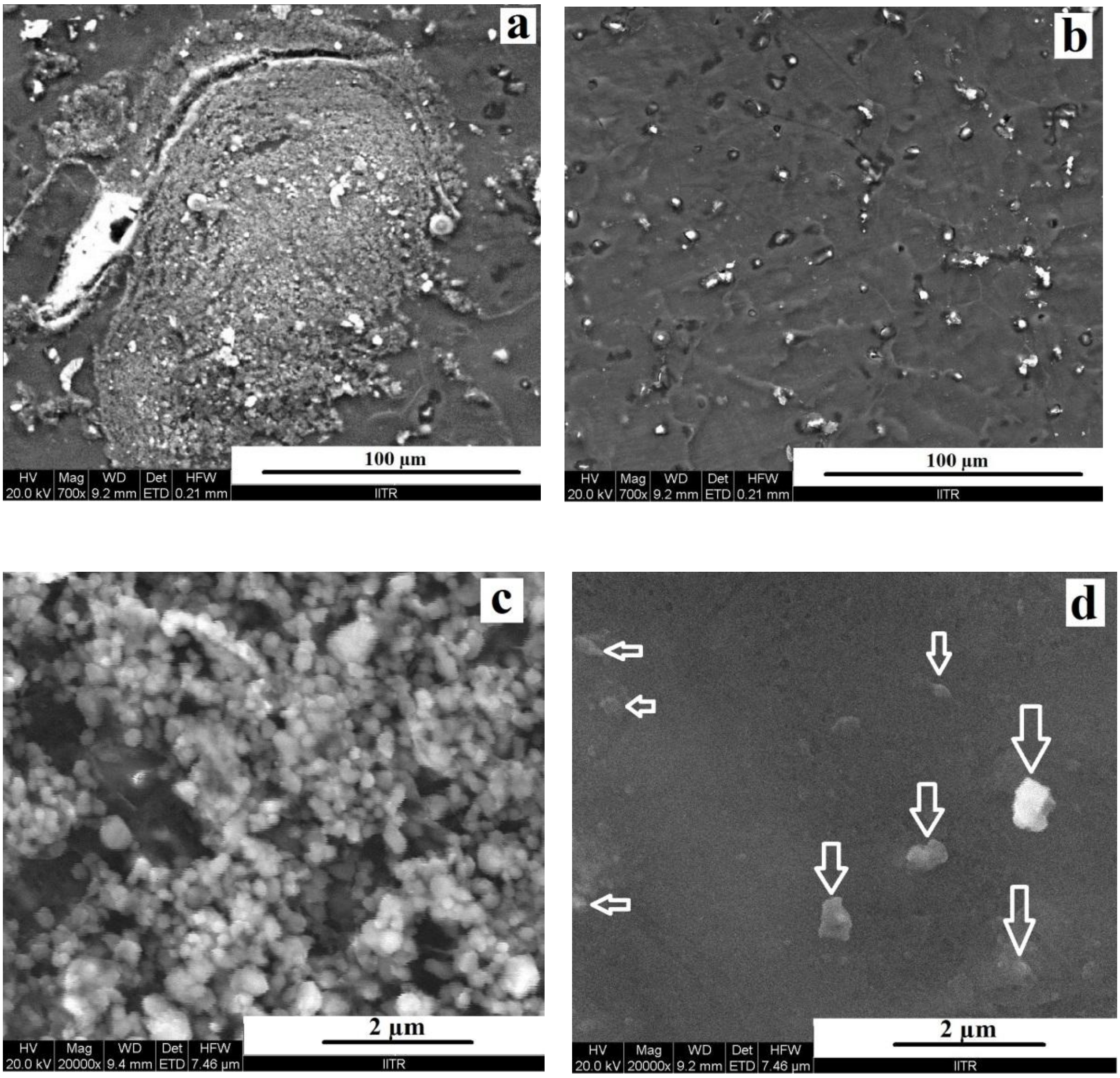

Fig. 6.12 FESEM micrographs of AZ31 alloy based MMCs obtained from various processing conditions- (a) AZ31-10, (b) AZ31-10-UST, and (c) AZ31-10 and (d) AZ31-10-UST, at higher magnifications.

6.3.2 Grain size and morphology

Among all the micrographs of Fig. 6.1, Fig. 6.2 of AZ91 and Fig. 6.10, Fig. 6.11 of AZ31 alloys, it is observed that the dendritic structure is coarse in unprocessed alloy (Fig. 6.1 and Fig. 6.10). It is relatively finer in AZ91 and AZ31 alloy metal matrix composite prepared by the addition of magnesium nitrate and without UST (Figs. 6.2a,b,c, and Figs. 6.11a,b,c). It is finest in the MMCs processed with the UST in both the alloys (Figs. 6.2d,e,f and Figs. 6.11d,e,f). It shows that the microstructure is refined after the UST. This may be attributed to a variety of reasons. The newly formed oxide particles could have acted as effective inoculating agents. Among the oxides, MgO is formed more easily due to the higher diffusion coefficient of Mg as compared to Al in the melt. The diffusion coefficients of these elements in oxides at temperatures between 700-800 °C are very small and the reaction products are extremely fine crystals [Ma, et al. (2011)]. The UST ensures the de-agglomeration and uniform distribution of these in situ formed oxide particles, thereby providing an increased number of nucleation sites.

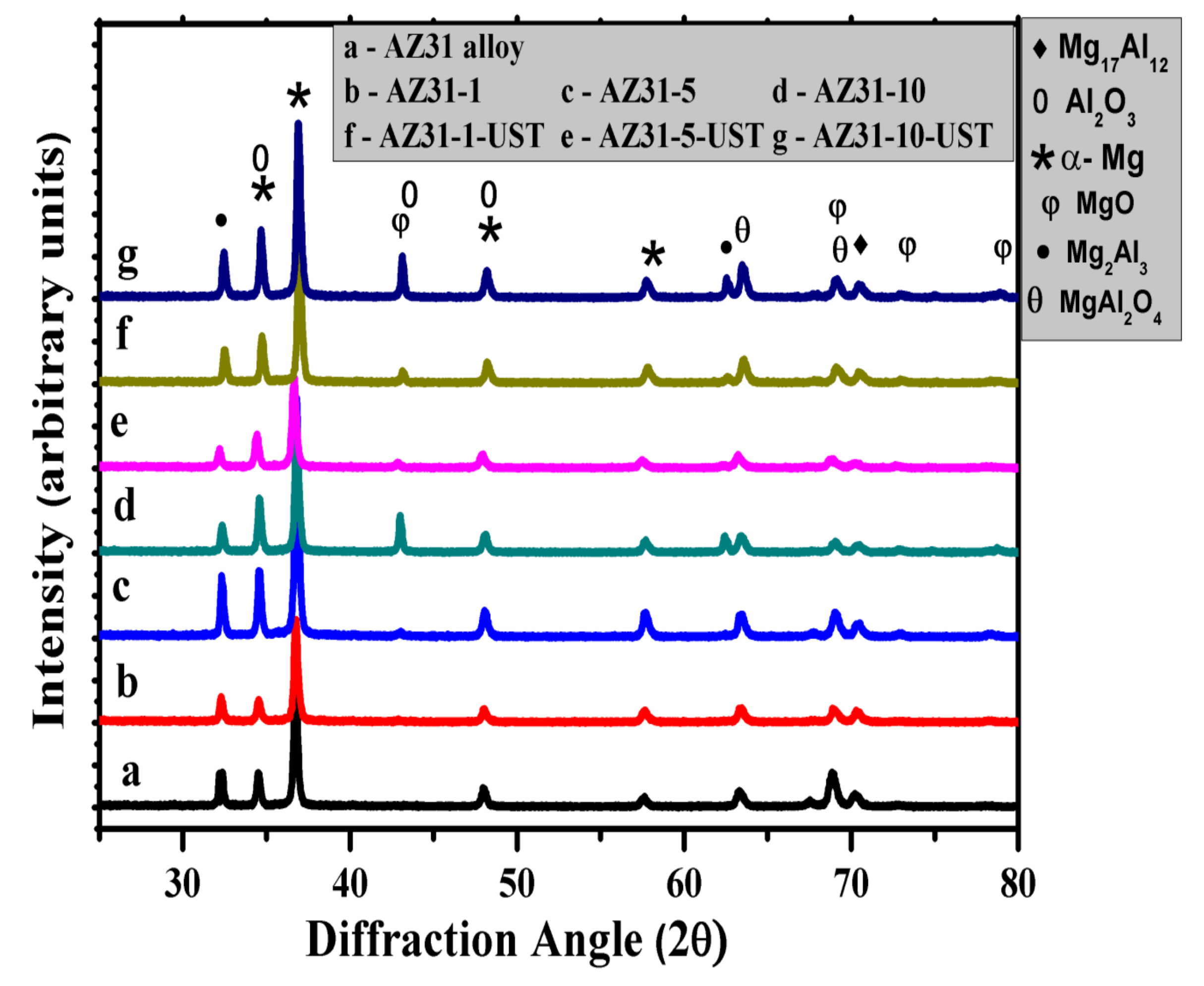

Fig. 6.13 XRD patterns for AZ31 MMCs processed under various conditions.

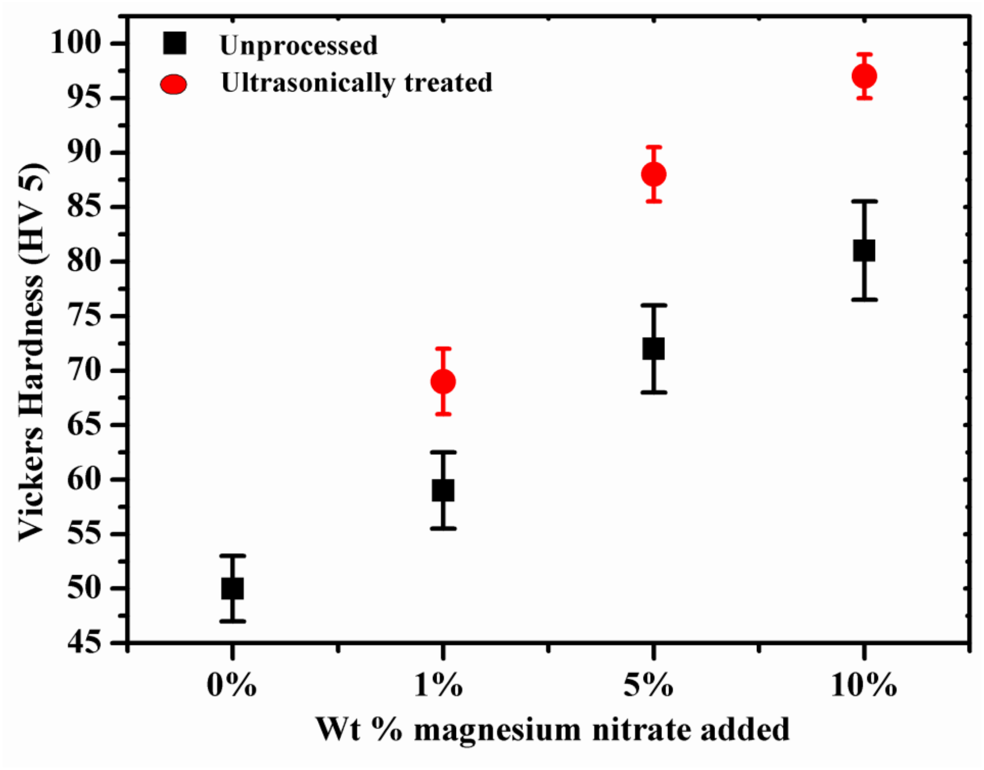

Fig. 6.14 Variation of hardness of the ultrasonically unprocessed and processed AZ31 MMCs with wt pct of magnesium nitrate added.

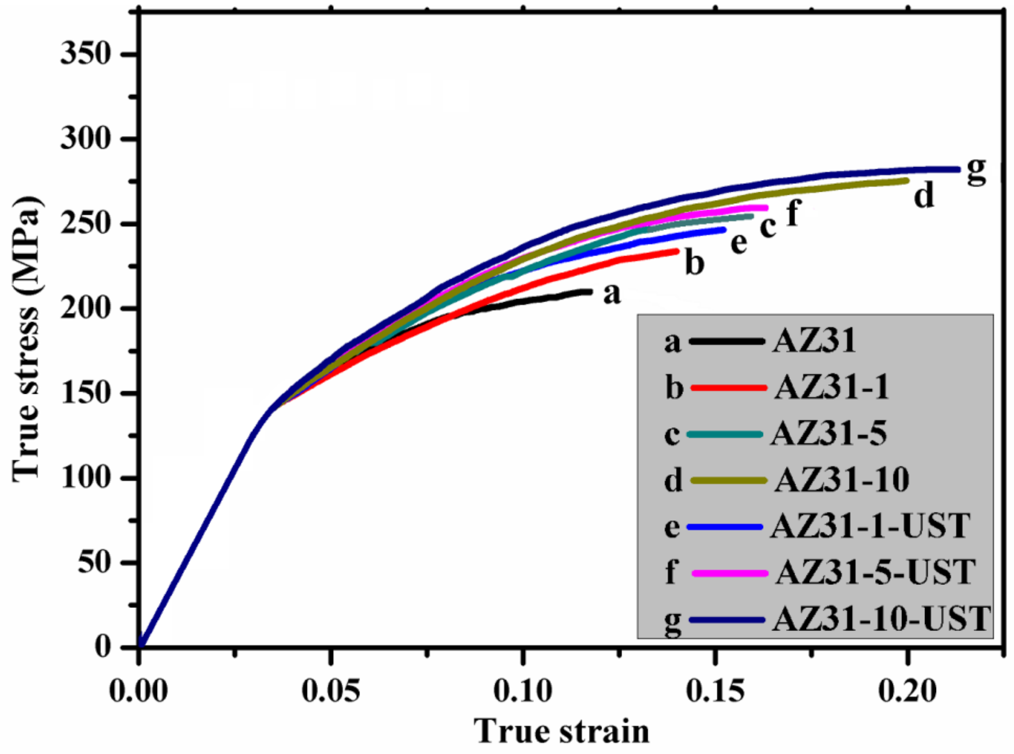

Fig. 6.15 Room temperature compressive true stress- true strain curves of variously processed AZ31 MMCs, formed from addition of different wt pct of magnesium nitrate.

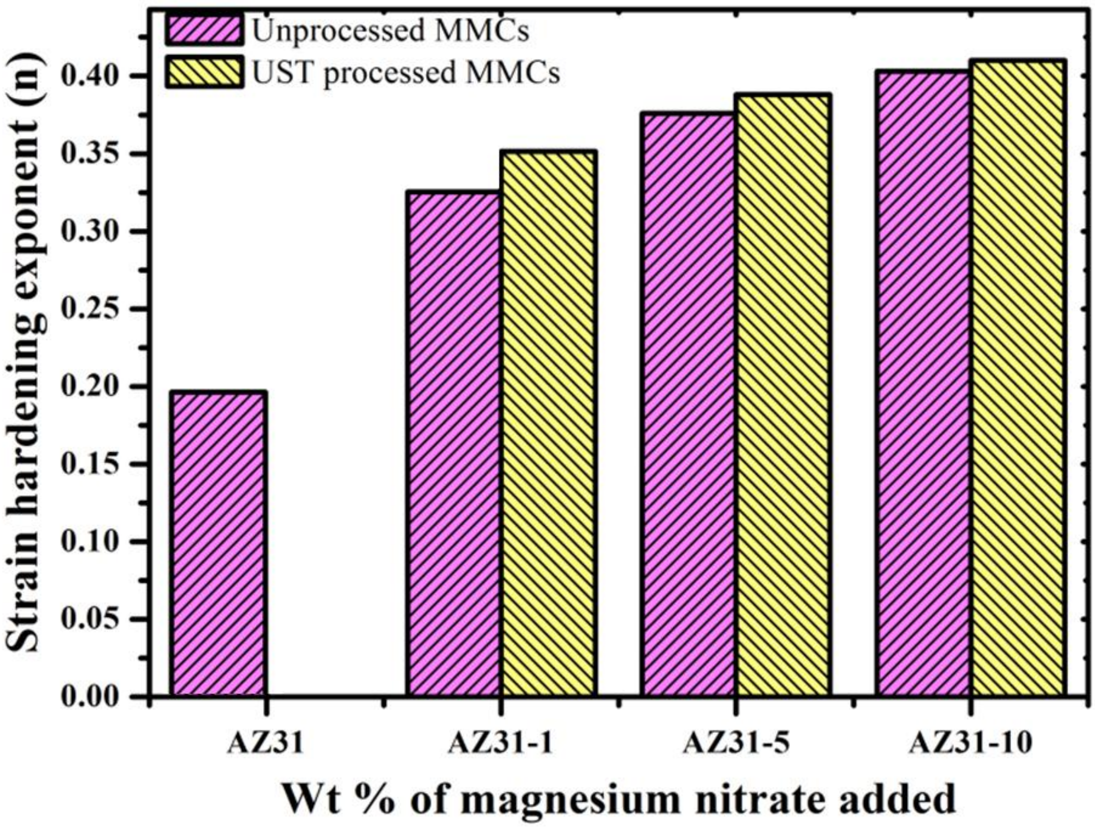

Fig. 6.16 Variation of strain hardening exponent with the wt pct of magnesium nitrate added.

Further, UST of melts results in cavitation phenomenon and there can be cavitation enhanced wetting of reactively formed magnesium and aluminum oxide particles [Tsunekawa, et al. (2001), Eskin, et al. (2003), Lan, et al. (2004), Ma, et ai. (2011), Chan, et al. (2013)]. Enhanced heterogeneous nucleation can also occur due to an increase in the melting point that is given by the Clausius-Clapeyron equation (2.4) [Swallowe, et al. (1987)].

$$\frac{dT_m}{dP} = \frac{T_m(V_L - V_S)}{\Delta H} \qquad (6.5)$$

Where T_m is the freezing point, P is the pressure, V_L, V_S are the specific volume of the liquid and the solid phase, respectively and ΔH is the latent heat of freezing. Alternately, there can be cavitation induced endothermic vaporization of liquid inside the expanded bubble [Xu, et al. (2004), Swallowe, et al. (1987)]. This decreases the temperature on the surface of the bubbles and local undercooling occurs. One or more of these ultrasonic cavitation and streaming induced mechanisms may be additionally responsible for finer microstructures observed in the present work.

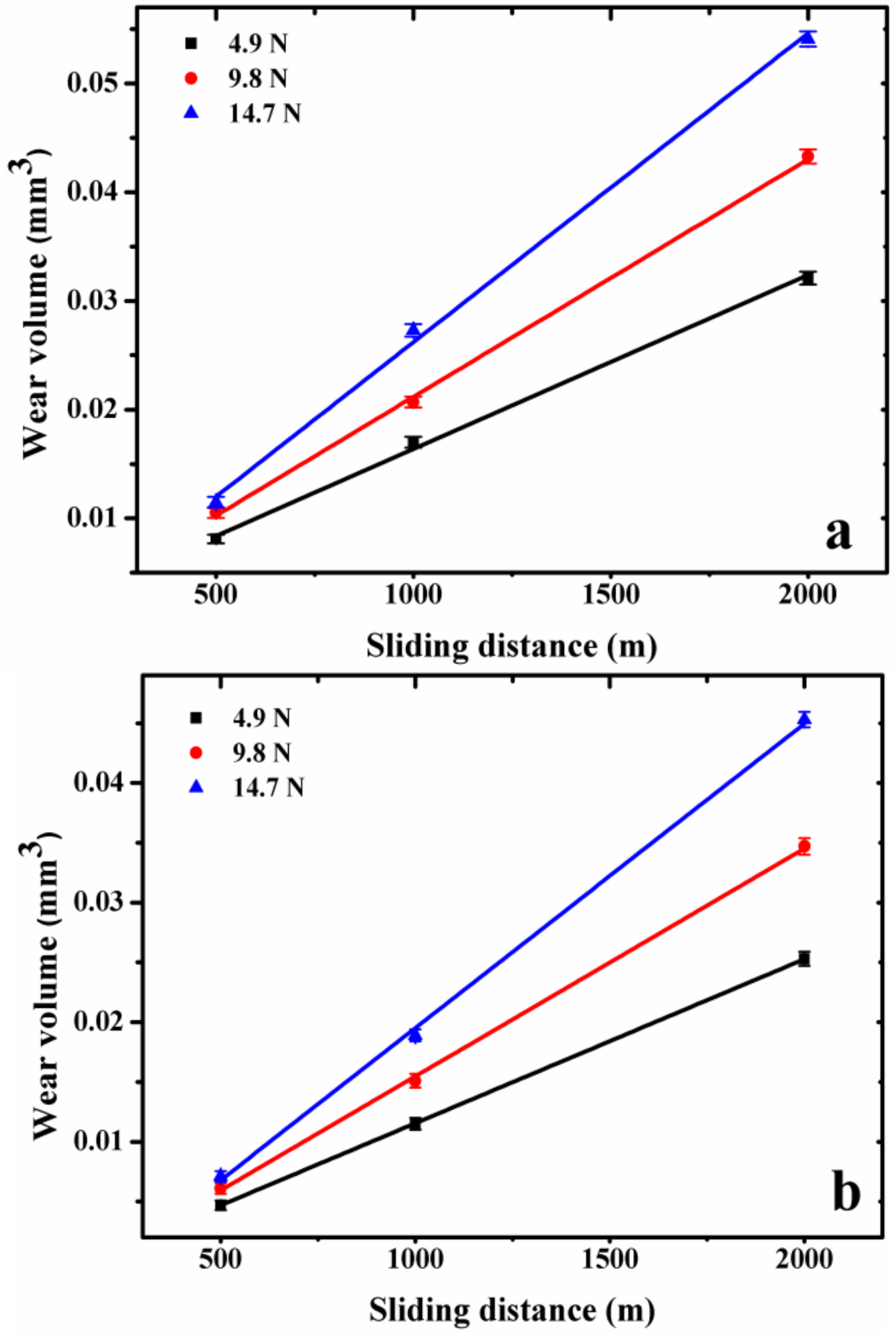

Fig. 6.17 Variation of wear volume (mm^3) with sliding distance for different normal loads in (a) AZ31, and (b) AZ31-10-UST specimens.

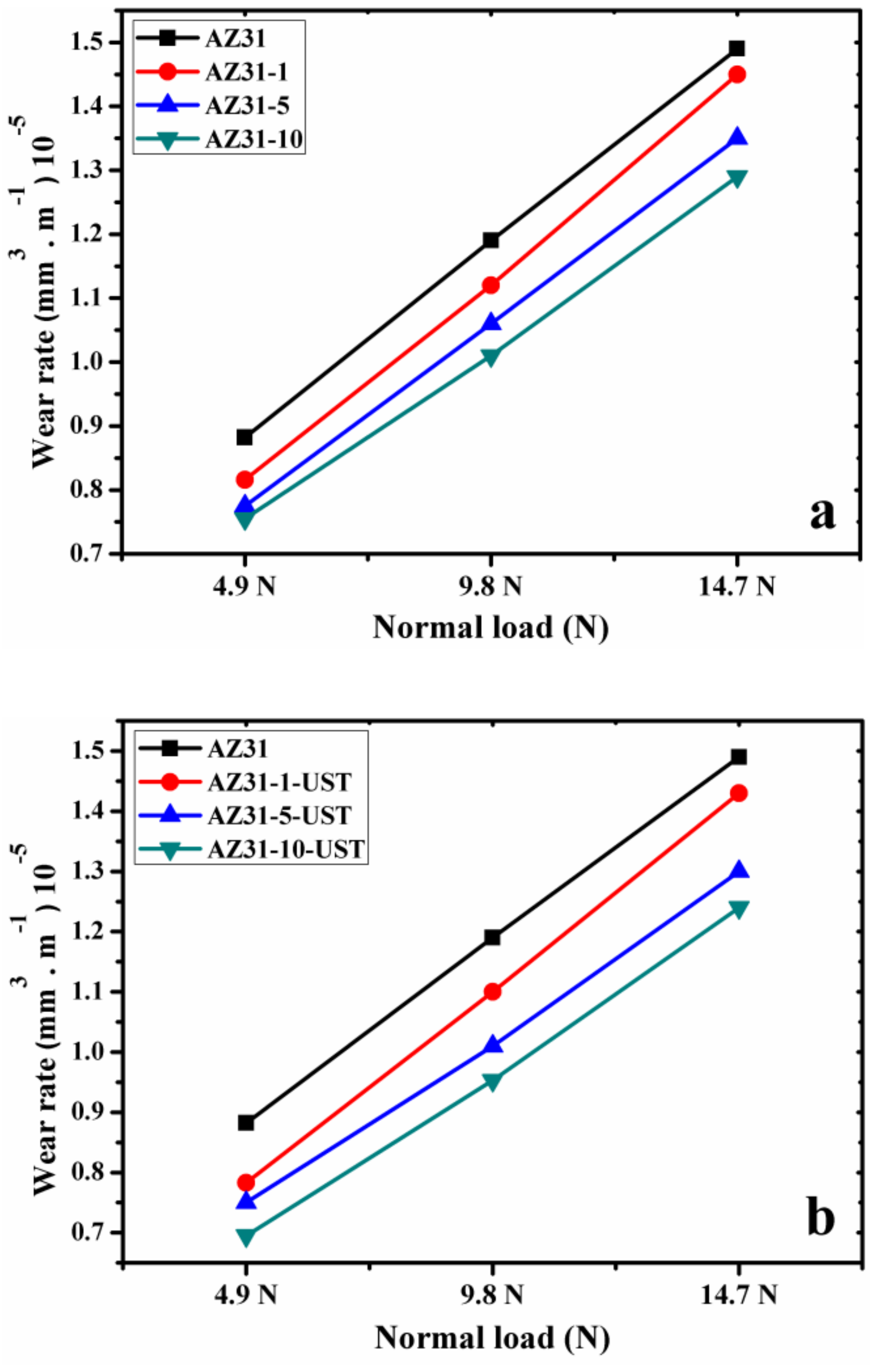

Fig. 6.18 Variation of volumetric wear rate with varying normal load for (a) UST unprocessed, and (b) UST processed cast AZ91 alloy and various in situ MMCs, tested at a constant sliding speed of 1 ms^{-1}.

6.3.3 Distribution of in situ formed oxides

In UST processed MMCs, in situ formed magnesium and aluminum oxides are uniformly distributed which can be seen from the absence of oxide agglomerates in the optical micrographs (Figs. 6.2d,e,f and Figs. 6.11d,e,f). Few hypotheses are available suggesting that UST helps in better distribution of reinforced particles in MMCs. During the collapse of the cavitation bubbles generated from high intensity ultrasonic vibrations, high-pressure pulses are generated. These results in enhanced wetting of in situ formed insoluble non-metallic particles that may be normally not wettable by the alloy melt [Eskin, et al. (2003)]. Under the action of high-pressure pulses, their wettability is improved by filling of the micro cracks and defects present on their surfaces [Eskin, et al. (2003)]. Improved wettability prevents the particle-melt separation and promotes incorporation of particles in the melt. Further, the implosion of cavities generates microjets having velocities of the order of 100 s of m.s^{-1} directed at the surface of the solid. It has two effects. One is the de-agglomeration of oxide particles and the other is the streaming of molten metal [Chan, et al. (2013)]. This result in improved distribution of in situ formed hard oxide particles in the UST processed MMCs. Other works on the ultrasonic processing of MMCs support this hypothesis [Lan, et al. (2004), Patel, et al. (2012), Rao, (2009), Sreekumar, et al. (2007), Eskin, (1997), Bhingole, et al. (2012)].

6.3.4 Mechanical properties

Hardness of the AZ91 and AZ31 alloy matrix composites is higher than that of the base alloy, irrespective of the type of processing. It is observed that as pct of magnesium nitrate in the melts increases, hardness of the MMCs is increased resulting in an increase of almost 64 pct in AZ91-10-UST samples as compared the AZ91 alloy (Fig. 6.5). Similar results are observed in the AZ31 alloy MMCs, an increase of almost 94 pct in AZ31-10-UST samples as compared the AZ31 alloy (Fig. 6.14). This increase in hardness of the MMCs is attributed mainly to the in situ formed harder oxide/intermetallic particles in the matrix, and uniform distribution of these particles throughout matrix aided by high intensity UST. In the MMCs, when forces act upon the matrix they are sustained by these in situ formed particles [Khakbiz, et al. (2009), Abramov, (1987)] and these particles provide resistance to the movement of dislocations that results in increase in hardness. Further, UST minimizes the inter-dendritic segregation and improves the material homogeneity [Abramov, (1987)], which may result in the higher hardness. For the same reasons the in situ synthesized AZ91 and AZ31 matrix composites also exhibit higher yield strengths and ultimate compressive strengths (Fig. 6.6 and Fig. 6.15). In general, the yield strength of a composite material is the stress required to operate dislocation sources and is governed by the presence and number of all the obstacles that restrict the motion of dislocations in the matrix. The increase in yield strength of the MMCs with the increase in volume fraction and improved distribution of reinforcement (resulting from the UST) is because of the higher dislocation density as discussed later. Further increase results from smaller free path for dislocation movement due to smaller inter particle spacing. This is apparent in higher values of yield strength for ultrasonically treated composite specimens that contain well-distributed and finer reinforcing particles, as compared to the untreated composites [Zhang, et al. (2006)].

The strain-hardening rate of the light metal composites is an important parameter for various applications especially for armour applications and those requiring crashworthiness. Strain hardening exponent, n, of the composites is higher than that of the base alloy in both, the AZ91 and AZ31 alloys (Fig. 6.7 and Fig. 6.16). This can be explained as follows. MMCs are a mixture of ductile α-Mg phase and rigid oxide and intermetallic particles. Strain hardening occurs when the stress required to produce further plastic deformation is increased because of prior plastic strain. Microscopic flow behavior of alloy that is strongly dependent on the dislocation density largely influences the strain-hardening exponent. Dislocation density in the matrix phase of MMC is likely to be higher than that of the AZ91 alloy and same is true for the AZ31 alloy. There is elastic and plastic incompatibility between the phases especially at the interfacial regions. When stressed, the incompatibility result in the generation of interaction stress in the constituent phases that leads to the generation of geometrically necessary dislocations in addition to the statistical dislocations in the matrix. Furthermore, thermal residual stress of large magnitude is expected to be present in the matrix owing to large differences in the coefficient of thermal expansion of the constituent phases (oxides/intermetallics) and the matrix phase. It leads to generation of more dislocations. “n” is also found to increase significantly with the amount of reinforcement. The particles are coarse enough so that the dislocations are unable to cut through them, thus providing effective pinning action. Higher the amount of reinforcement, smaller is the inter particle spacing and higher is the pinning action. Further, the UST results in de-agglomeration and more uniform distribution of the reinforcing particles thereby further reducing the inter particle spacing. The dislocation density in the soft matrix can be reduced by annihilation of dislocations. Dislocation annihilation can occur by their absorption at the interface if the interface is weak. In addition, the shear stress imposed at the interface by dislocations may relax by sliding of the interfaces under the support of diffusion processes [Fukuda, et al. (1981)]. Strong interface bonding may prevent dislocation annihilation and sliding of the interfaces, thereby resulting in a higher n value [Mondal, et al. (2007)]. It is widely accepted that the interfaces formed by in situ formation of phases are often stronger. Thus, the in situ composites processed in this work exhibit very large increase in n value as compared to the base alloy.

6.3.5 Dry sliding wear behavior

Lower wear rates are observed in unprocessed MMCs as well as ultrasonically processed MMCs as compared to the AZ91 alloy and similar results are observed in AZ31 alloy. This is attributed to the presence of hard MgO, Al_2O_3 and $MgAl_2O_4$ particles in the matrix. The improvement is more in UST processed MMCs because distribution of these particles is improved by application of high intensity ultrasound, as discussed earlier. It is also well accepted that when high power ultrasound is coupled with solidifying alloys degassing take place, which results in reduction of porosity [Patel, et al. (2012), Abramov, (1987), Abramov, (1987), Fairbanks, (1967), Jain, et al. (2011)]. This may further improve the mechanical properties especially hardness. Hardness of the material and volume of wear are related by Archard’s equation (6.6) [Archard (1953), Anbuselvan, et al. (2010), Tyagi, et al. (2003)].

$$\boldsymbol{\frac{V}{S} = \frac{KW}{H}} \qquad (6.6)$$

Where V is the wear volume, S the sliding distance, W the normal load, H the hardness of the softer of the two materials (AZ91 alloy, AZ31 alloy and there MMCs in the present work) in contact and K is the wear coefficient. From Archard’s equation, it is observed that the wear volume decreases with an increase in pin sample hardness. In Fig. 6.5 for the AZ91 alloy and Fig. 6.14 for the AZ31 alloy, it is clearly seen that the hardness of UST processed MMCs is higher than unprocessed MMCs and the base alloy. Therefore, improvement in wear resistance of UST processed MMCs is caused by an increase in its hardness and strength [Chen, et al. (2012)].

In dry sliding wear under low load conditions (4.9 N-14.7 N), the hard MgO and Al_2O_3 reinforcement particles have an excellent load sustaining ability to bear stress without undergoing plastic deformation or fracture. This may hinder the subsurface flow and improve the anti-adhesion ability. If the plastic deformation of the material is minimized, surface damage can be prevented at the contact interface and the wear rate can be reduced [Archard

(1953)]. This is true if the hardness and wear resistance of these reinforcement phases is markedly higher and thus the reinforcement phase has grinding and micro-scouring effect on the counter disc, leading to the generation of iron debris. The iron debris is mechanically mixed with the pin material at the sliding interface and is oxidized at elevated temperatures during sliding. Some of the debris is deposited on the pin surface and is tamped into a hard transfer layer. This effectively protects the pin surface in the sliding process [Faraji, et al. (2011), Hokkirigawa, et al. (1988)]. Thus there is decrease in wear rate of the AZ91 alloys matrix composites and the AZ31 alloys matrix composites.

For better understanding of the tribological behaviour and to find out different wear mechanisms operating in the wear of AZ91 alloy, AZ31 alloy and there MMCs, worn pin sample surfaces are examined by using FESEM. Figs. 6.19a-c shows the FESEM micrographs of worn pin samples and debris for the AZ91 alloy and its MMCs. At almost all the loads AZ91 alloy shows enhanced wear mainly because of micro ploughing. AZ91 is the softest material and hence is more susceptible to micro welding during sliding wear. These microwelds break and reform thereby generating wear debris, which may be oxidized during further sliding. These can result in ploughing. Worn surfaces of all the specimens are covered with grooves parallel to the sliding direction. These are typical features associated with abrasive wear, in which hard asperities on the steel counter face, or hard particles in between the pin and disc, plough or cut into the pin, causing wear by the removal of small fragments or ribbon-like strips (shown by arrow in Fig. 6.19a) of material [Lim, et al. (1987)]. Deeper grooves in AZ91 alloy, as shown in Fig. 6.19a, indicate that there was a higher degree of penetration by hard asperities, which together with the minimal displacement of material on both sides of the grooves, suggest a primarily cutting mode of abrasion at the lower loads. The relatively brittle hcp structure of the α-Mg matrix also favors abrasive wear through micro cutting. Same results are observed in AZ31 alloy Figs. 20a-c.

As suggested by Archard [Archard, (1953)], harder composites are better able to resist wear by abrasion. Differences in the extent of grooving is observed with the variation in the hardness of MMCs. Well-defined deep grooves change to shallower scratches accompanied by plastic deformation in the MMCs having higher hardness (Fig. 6.19b and Fig. 6.20b).

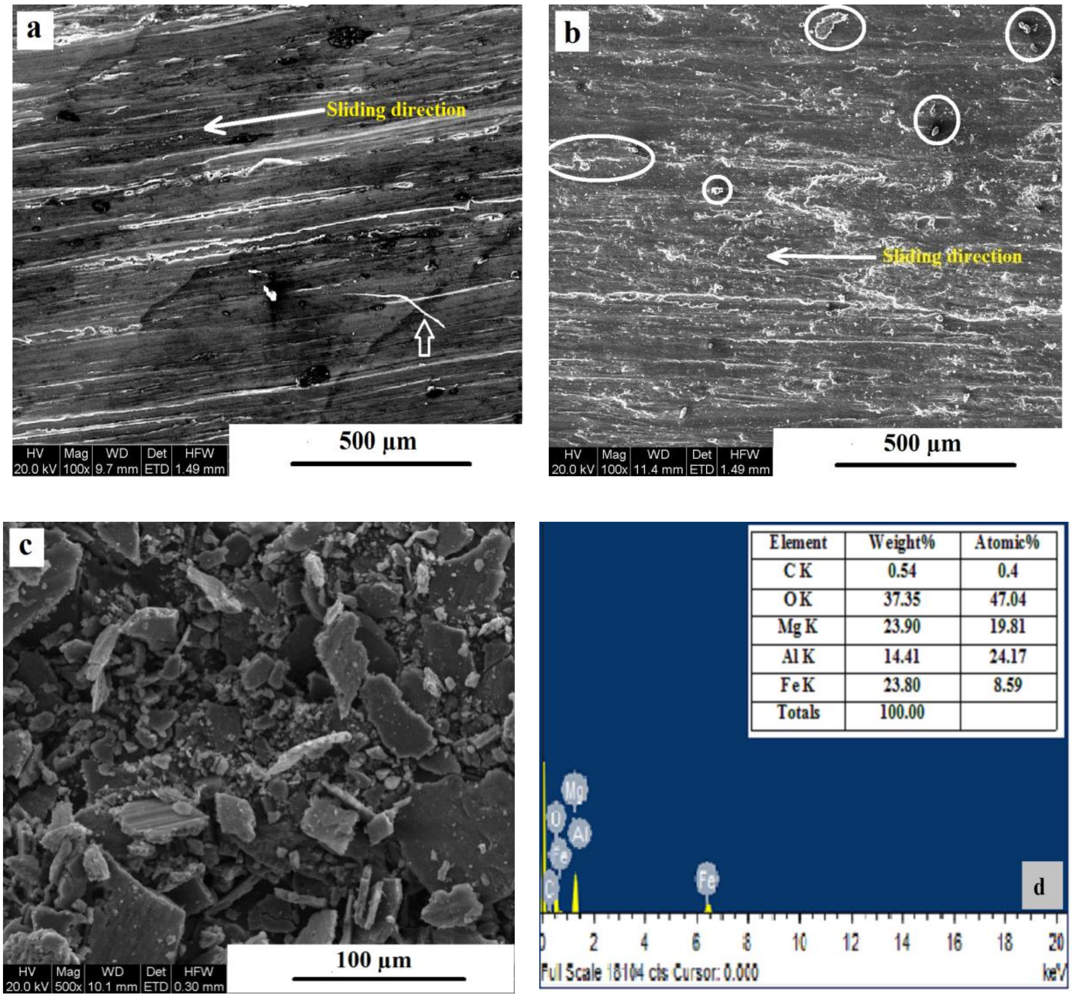

Element	Weight%	Atomic%
C K	0.54	0.4
O K	37.35	47.04
Mg K	23.90	19.81
Al K	14.41	24.17
Fe K	23.80	8.59
Totals	100.00	

Fig. 6.19 FESEM images of worn surfaces of (a) AZ91, (b) AZ91-10-UST for specimens tested under 14.7 N normal load, with sliding distance of 2000 m and sliding speed of m.s^{-1} (c) shows the wear debris from AZ91-10-UST specimen, and (d) shows its EDS analysis.

Naked-eye inspection revealed that the worn surfaces of these pins appear dark. FESEM studies showed that fine particles cover these dark surfaces extensively. EDS studies identified strong oxygen peak along with Al and Mg peaks, suggesting that these particles contain oxides (Fig. 6.19d and Fig. 6.20d). The wear debris in case of composites can contain the oxide reinforcement particles and the worn oxidized product of wear. Fig. 6.19c and Fig.6.20c shows the FESEM images of wear debris produced after pin on disc test conducted on AZ91 and AZ31 alloys respectively. Wear debris contains particles of MMCs and particles of oxides and very small amount of iron particles from the worn steel counter face. These characteristics are indicative of oxidative wear mechanism taking part in the wear of MMCs. Over repeated

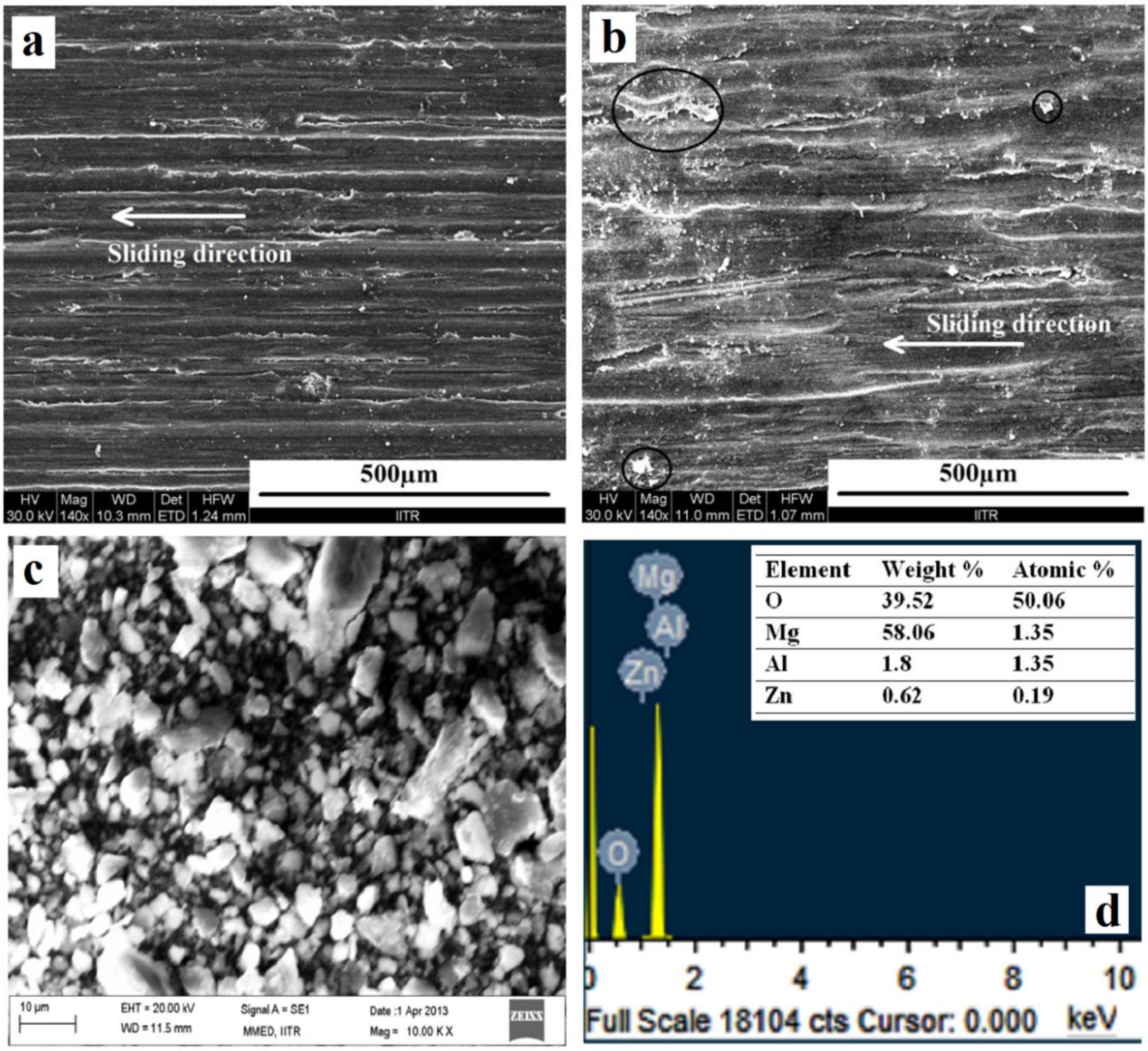

Element	Weight %	Atomic %
O	39.52	50.06
Mg	58.06	1.35
Al	1.8	1.35
Zn	0.62	0.19

Fig. 6.20 FESEM images of worn surfaces of (a) AZ31, (b) AZ31-10-UST for specimens tested under 14.7 N normal load, with sliding distance of 2000 m and sliding speed of 1 $m.s^{-1}$ (c) shows the wear debris from AZ31-10-UST specimen, and (d) shows its EDS analysis.

sliding, the oxide-rich wear debris fills up the valleys on the pin surface. It gets compacted into a protective layer [Hokkirigawa, et al. (1988)]. This prevents the metallic contact and the wear rates drop accordingly, in case of the composites, as compared to the base AZ91 alloy and the base AZ31 alloy.

6.4 Summary

1. Upon ultrasonic treatment, AZ91 alloy matrix composites and AZ31 alloy matrix composites could be successfully synthesized by in situ formation of hard MgO and Al_2O_3 particles, by using magnesium nitrate ($Mg(NO_3)_2$) as an oxygen supplying agent to the molten AZ91alloy and AZ31 alloy.
2. Microscopic studies revealed that high intensity ultrasonic vibrations applied to the melt resulted in enhanced wetting, de-agglomeration and dispersion of in situ formed hard oxide particles throughout the matrix. In addition, the ultrasonic treatment of the melt led to refined cast microstructures.
3. AZ91-10-UST composite specimens exhibited best mechanical properties with its hardness, yield strength and strain-hardening exponents higher by 64 pct, 43 pct, and 115 pct, respectively, as compared to the AZ91 alloy. This is ascribed to the presence of in situ formed harder and finer oxide particles in the matrix, and uniform distribution of these particles throughout matrix aided by high intensity ultrasonic treatment.
4. AZ31-10-UST composite specimens exhibited best mechanical properties with its hardness, yield strength and strain-hardening exponents higher by 94 pct, 35 pct, and 109 pct, respectively, as compared to the AZ31 alloy. This is ascribed to the presence of in situ formed harder and finer oxide particles in the matrix, and uniform distribution of these particles throughout matrix aided by high intensity ultrasonic treatment.
5. Sliding wear resistance of MMCs is better as compared to that of the base alloy. As the amount of reinforcement increased, the MMCs became more wear resistant. Among the AZ91 alloy and its MMCs, AZ91-10-UST shows highest wear resistance and for AZ31 and its MMCs, AZ91-10-UST shows highest wear resistance. Mechanism of wear identified under low load conditions in the base alloy is abrasion and in MMCs, oxidation mechanism operates at higher normal loads observed in both the AZ91 and AZ31 alloys.

Chapter 7

CONCLUSIONS

Following are the main conclusions drawn from this work.

1. UST processing time has significant effect on the microstructure refinement of AZ91 and AZ31 alloys. Increased grain refinement occurred with increased UST processing time. The $Mg_{17}Al_{12}$ phase is found to be well distributed along the grain boundaries after the ultrasonic treatment of the both AZ91 and AZ31 alloys.
2. Isothermal holding and continuous cooling conditions at the time of ultrasonic treatment of AZ91 and AZ31 alloys, produced microstructures with nearly non-dendritic equiaxed and globular grains and the grain refinement is attributed to the dendrite fragmentation phenomena.
3. After maximum processing time i.e. 90 s of UST processing, as ultrasonic intensity is increased to 4.3 kW.cm^{-2}, the average grain size decreased to 17 µm in isothermal ultrasonically processed AZ91 alloy and the average grain size decreased to 28 µm in isothermal ultrasonically processed AZ31 alloy.
4. During UST of AZ91 and AZ31 alloys, when intensity is increased to 4.3 kW.cm^{-2}, the average grain size decreased to 20 µm in isothermal ultrasonically processed AZ91 alloy and it decreased to 45 µm in continuously cooled UST processed AZ31 alloy. Thus, isothermal UST resulted in greater degree of grain refinement.
5. Interestingly for the high intensity of 4.3 kW.cm^{-2} hardness increased monotonously with processing time, although the decrease in grain size was abrupt in the beginning. Highest hardness found in the AZ91 specimen UST processed with 90 s processing time and constant intensity of 4.3 kW.cm^{-2} in continuous cooling conditions is 160 pct higher than that of the AZ91 base alloy.
6. The Vickers hardness of the ultrasonically processed AZ91 and AZ31 alloys increased with increase in ultrasonic intensity applied and applied duration of processing during the solidification. The increase is attributed to the ultrasound induced dendrite fragmentation leading to grain refinement.

7. For the AZ31 alloy, maximum Vickers hardness is observed when high intensity of 4.3 $kW.cm^{-2}$ and higher processing duration that is 90 s is used during isothermal UST processing . It is 177 pct higher than that of the unprocessed AZ31 alloy. For the similar UST parameters used in continuous cooling condition, 153 pct higher Vickers hardness is observed as compared to the AZ31 base alloy.

8. Vickers hardness values (VHN) increased with increase in solute concentration, ultrasonic intensity, processing time, and is influenced by processing conditions. The increase in hardness is attributed to the Hall-Petch strengthening from grain refinement produced after application of UST.

9. It can be seen that 0.2 % proof stress, UTS, and total elongation to fracture values are lowest for all the unprocessed alloys and as UST intensity and UST time increased tensile properties of the alloys increased. Improvement in tensile properties with respect to enhanced proof strength, tensile strength, and total elongation to failure can be correlated to the morphology of primary α-phase, its grain size, and the morphology of secondary intermetallic phase.

10. Nano carbon black powder inoculation is a more effective grain refining technique for Mg-Al-Zn magnesium alloy than the conventional hexacholoroethane treatments. Inexpensive nano carbon black which has a high surface-area-to-volume ratio readily forms the inoculating phase particles in larger number, thereby resulting in the more extensive grain refinement observed in this work.
11. High intensity ultrasonic treatment applied with carbon black inoculation increases the number of particles that actually nucleate grains and the potency of inoculants. UST accelerates the wetting, de-agglomeration, and dispersion of nano particles of carbon black particles and also improves the kinetics of inoculating phase formation.
12. The 0.2 % proof stress, UTS, and total elongation to fracture values are highest for all the Mg alloys that were subjected to carbon black inoculation followed by ultrasonic treatment. This is ascribed to the grain refinement resulting from synergy of nano carbon black inoculation and high intensity ultrasonic processing.
13. Upon ultrasonic treatment, AZ91 and AZ31 alloy matrix composites could be successfully synthesized by in situ formation of hard MgO and Al_2O_3 particles, by using magnesium nitrate ($Mg(NO_3)_2$) as an oxygen supplying agent to the molten AZ91 alloy.

14. Microscopic studies revealed that high intensity ultrasonic vibrations applied to the melt resulted in enhanced wetting, de-agglomeration and dispersion of in situ formed hard oxide particles throughout the matrix. In addition, the ultrasonic treatment of the melt led to refined cast microstructures.
15. AZ91-10-UST composite specimens exhibited best mechanical properties with its hardness, yield strength and strain-hardening exponents higher by 64 pct, 43 pct, and 115 pct, respectively, as compared to the AZ91 alloy. Similarly, AZ31-10-UST composite specimens exhibited best mechanical properties with its hardness, yield strength and strain-hardening exponents higher by 94 pct, 35 pct, and 109 pct, respectively, as compared to the AZ31 alloy. This is ascribed to the presence of in situ formed harder and finer oxide particles in the matrix, and uniform distribution of these particles throughout matrix aided by high intensity ultrasonic treatment.
16. Sliding wear resistance of MMCs is better as compared to that of the base alloy. As the amount of reinforcement increased, the MMCs became more wear resistant. AZ91-10-UST shows highest wear resistance among all AZ91 based MMCs and AZ31-10-UST shows highest wear resistance among all AZ31 alloy based MMCs. Mechanism of wear identified under low load conditions in the base alloy is abrasion and in MMCs, oxidation mechanism operates at higher normal loads.

Chapter 8

SCOPE OF FUTURE WORK

Further studies could include investigation of the following:

1) Effect of solute content on the grain refinement of other low melting alloys such as Al alloys, along with application of ultrasonic vibrations can be investigated in order to develop a universal approach to grain refinement from ultrasonic vibrations assisted solidification processing.
2) Numerical simulation of acoustic pressure field for ultrasonic grain refinement of AZ series magnesium alloys can be done and studied.
3) In view of the remarkable ability of wetting and dispersion of nanoparticles from ultrasonic cavitations, lightweight magnesium alloy composites reinforced with stable phases for the high temperature applications can be developed and the mechanisms studied.

BIBLIOGRAPHY

1. Abramov V., Abramov O., Sommer F., Orlov D., “ Properties of Al-Pb base alloys applying electromagnetic forces and ultrasonic vibration during casting”, Materials Letters, vol. 23, pp.17-20, 1995.
2. Abramov, O. “Action of high intensity ultrasound on solidifying metal”, Ultrasonics, vol. 25.2, pp. 73-82, 1987.
3. Abramov, V., Abramov, O., Straumal, B., Gust, W., “Hypereutectic Al-Si based alloys with a thixotropic microstructure produced by ultrasonic treatment”, Materials and Design, vol. 18(4), pp. 323-326. 1997.
4. Aghajanian M., Burke J., White D., Nagelberg A., “A new infiltration process for the fabrication of metal matrix composites”, Sampe Quarterly, vol. 20(4), pp. 43-46, 1989.
5. Alireza R., Kenji M., “Structural refinement of gray iron by electromagnetic vibrations”, Metallurgical and Materials Transactions A, vol. 33A, pp. 3025-3030, 2002.
6. Anbuselvan S., Ramanathan S., “A comparative study of the wear behavior of as-cast and hot extruded ZE41A magnesium alloy”, Journal of Alloys and Compounds, vol. 502(2), pp. 495-502, 2010.
7. Archard J., “Contact and rubbing of flat surfaces” Journal of Applied Physics, vol. 24, pp. 981-988, 1953.
8. Arenas M., He M., Acoff V., “Effect of flux on the wetting characteristics of SnAg, SnCu, SnAgBi, and SnAgCu lead-free solders on copper substrates”, Journal of Electronic Materials, vol. 35-7, pp. 1530-1536, 2006.
9. ASM Handbook. Properties and Selection: Non-ferrous alloys and special- purpose materials. ASM international vol. 2, pp. 1424-1588, 1992.
10. Atamanenko, T., Eskin, D., Zhang, L., Katgerman L., “Criteria of grain refinement induced by ultrasonic melt treatment of aluminum alloys containing Zr and Ti”, Metallurgical and Materials Transactions A, vol. 41(8), pp. 2056-2066, 2010.
11. Avedesian M., Baker H., “ASM specialty handbook, magnesium and magnesium alloys”, ASM International, Materials Park, OH, 1999.
12. Banerjee M., Seal A., “Effect of vibration on the solidification process of white cast iron”, Crystal Properties and Preparation, vol. 22-25(2), pp. 783-93, 1989.

13. Bhingole P., Chaudhari G., “Synergy of nano carbon black inoculation and high intensity ultrasonic processing in cast magnesium alloys”, Materials Science and Engineering A, vol. 556, pp. 954-961, 2012.
14. Blawert C., Hort N., Kainer K., “Automotive application of magnesium and its alloys”, Transactions of the Indian Institute of Metals - Springer, vol. 57, pp. 397-408, 2004.
15. Brandon D., Kaplan W. D. “Microstructure characterization of materials book” Technology & Engineering, page no.1-3, 2008.
16. Breslin M., Ringnalda J., Xu L., Fuller M., Seeger J., Daehn G., Otani T., Fraser H., “Processing, microstructure, and properties of co-continuous alumina-aluminum composites”, Materials Science and Engineering A, vol. 195, pp. 113-119, 1995.
17. Busk R., “Nomenclature and specifications, magnesium products design”, Ch. 3, Marcel Dekker, New York, (1987).
18. Campbell J., “Effects of vibration during solidification”, International Metals Reviews, vol. 2, 1981.
19. Cao G., Konishi H., Li X., “Mechanical properties and microstructure of SiC-reinforced Mg-(2,4)Al-1Si nano composites fabricated by ultrasonic cavitation based solidification processing”, Materials Science and Engineering A, vol. 486, pp. 357–362, 2008.
20. Cao P., Qian M., StJohn D., “Effect of iron on grain refinement of high-purity Mg–Al alloys”, ScriptaMaterialia, vol. 51(2), pp. 125-129, 2004.
21. Cao P., StJohn D., Qian M., “The Effect of Manganese on the Grain Size of Commercial AZ31 Alloy”, Materials Science Forum, vol. 488-489, pp.139-142, 2005.
22. Cao, G., Choi, H., Oportus, J., Konishi, H., Li, X., “Study on tensile properties and microstructure of cast AZ91D/AlN nano composites”, Materials Science and Engineering: A, vol. 494(1), pp. 127-131. 2008.
23. Chen T., Wang R., Ma Y., Hao Y., “Grain refinement of AZ91D magnesium alloy by Al-Ti-B master alloy and its effect on mechanical properties”, Materials and Design, vol. 34, pp. 637–648, 2012.
24. Chen X., Yan J., Gao F., Wei J., Xu Z., Fan G., “Interaction behaviors at the interface between liquid Al-Si and solid Ti-6Al-4V in ultrasonic-assisted brazing in air”, Ultrasonics Sonochemistry, vol. 20(1), pp. 144-154, 2013.
25. Choh T., Kobashi M., Nakata H., Kaneda H., “Fabrication of metal matrix composite by spontaneous infiltration and subsequent in situ reaction processes”, Materials Science Forum, vol. 217-222(1), pp. 353-358, 1996.

26. Choh T., Oki T., “Wettability of SiC to aluminium and aluminium alloys”, Materials Science and Technology, vol. 3(5), pp. 378-385, 1987.
27. Dahle A., “Nucleation and Grain Refinement”, Materials Science Forum, vol. 649, pp. 287-293. 2010.
28. Dahle A., Lee Y., Nave M., Schaffer P., StJohn, D., “Development of the as-cast microstructure in magnesium-aluminium alloys”, Journal of Light Metals, vol. 1, pp. 61-72, 2001.
29. Dhokey N., Sapate S., Paretkar R., “Influence of operating parameters on dry sliding wear of copper based SiC composites”, Journal of Tribology, vol. 221, pp.105-114, 2007.
30. Dieter G., “Mechanical metallurgy”, New York: McGraw-Hill, vol. 3, 1976.
31. Ditze A., Scharf C., “Recycling of Magnesium”, Ditze&Scharf, 2008.
32. Djordjevic S., “The effect of Ultrasonic solidification on aluminium”, Journal of Mining and Metallurgy, vol. 39(3-4) B, pp. 527-532, 2003.
33. Dong L., Wu Y., Dou C., Xu G., Wang L., “Structural characterization and property of in-situ synthesized AZ91-Mg_2Si composite”, Transactions of Nonferrous Metals Society of China, vol. 16(Z3), pp. 1845−1847, 2006.
34. Du J., Yang J., Kuwabara M., Li, W., Peng J. “Effect of strontium on the grain refining efficiency of Mg–3Al alloy refined by carbon inoculation”, Journal of Alloys and Compounds, vol. 470(1), pp. 228-232, 2009.
35. Easton, M., and StJohn D., “A model of grain refinement incorporating alloy constitution and potency of heterogeneous nucleant particles." ActaMaterialia, vol. 49(10), pp. 1867-1878, 2001.
36. Emamy M., Mahta M., Rasizadeh J., “Formation of TiB_2 particles during dissolution of $TiAl_3$ in Al-TiB_2 metal matrix composite using an in situ technique”, Composites Science and Technology, vol. 66(7–8), pp. 1063-1066, 2006.
37. Emley E., “Principles of magnesium technology”, Per-gamon Press, London, 1966.
38. Eskin G., “Broad prospects for commercial application of the ultrasonic (cavitation) melt treatment of light alloys”, Ultrasonics Sonochemistry, vol. 8, pp. 319-325, 2001.
39. Eskin G., “Principles of ultrasonic treatment: Application for light alloys melts”, Advanced Performance Materials, vol. 4, pp. 223-232, 1997.
40. Eskin G., “Ultrasonic treatment of light alloy melts”, CRC Press, 1998.

41. Eskin G., Makarov G., Pimenov Y., “Effect of ultrasonic processing of molten metal on structure formation and improvement of properties of high-strength Al-Zn-Mg-Cu-Zr alloys” Advanced Performance Materials, vol. 2(1), pp. 43-50, 1995.
42. Eskin, G., “Influence of cavitation treatment of melts on the processes of nucleation and growth of crystals during solidification of ingots and castings from light alloys” Ultrasonics Sonochemistry, vol. 1(1), pp. S59-S63, 1994.
43. EskinG., Eskin D., “Production of natural and synthesized aluminum-based composite materials with the aid of ultrasonic (cavitation) treatment of the melt”, Ultrasonic Sonochemistry, vol. 10, pp. 297-301, 2003.
44. Fairbanks H., “Acoustic drying of coal”, IEEE Trans. on Sonics and Ultrasonics, vol. SC-14(2), pp. 53-59, 1967.
45. Fairbanks H., “Influence of ultrasonics on some metallurgical processes”, IEEE Transactions on Sonics and Ultrasonics, vol. SC-14(2), pp. 53-59, 1967.
46. Fairbanks H., Dakan J., “The effects of adding ultrasound during the production of nodular cast iron”, Ultrasonics Symposium Proceedings, IEEE Cat.74 CHO 896-lSV, pp. 664-666, 1974.
47. Faraji G., Asadi P., “Characterization of AZ91/alumina nano composite produced by FSP”, Materials Science and Engineering A, vol. 528(6), pp. 2431–2440, 2011.
48. Feng A., Ma Z., “Microstructural evolution of cast Mg–Al–Zn during friction stir processing and subsequent aging”, ActaMaterialia, vol. 57(14), pp. 4248-4260, 2009.
49. Feng H., Yua S., Li Y., Gong L., “Effect of ultrasonic treatment on microstructures of hypereutectic Al–Si alloy”, Journal of Materials Processing Technology, vol. 208, pp. 330–335, 2008.
50. Filippov, I. I., Liteznoje Proiswodstwo 2, vol. S10, 1960.
51. Foerster G., “Improved Magnesium Die-casting”, The 8th SDCE International Die-casting Exposition and Congress, Detroit, MI, USA, 1975.
52. Friedrich H., Mordike B., “Magnesium Technology-Metallurgy, Design Data, Applications”, Springer- verlag berlin Heidelberg, Chp 2, pp. 63-78, 2006.
53. Friedrich H., Mordike B., “Magnesium Technology-Metallurgy, Design Data, Applications”, Germany: Springer-Verlag Berlin Heidelberg, Chp 2, pp. 80-84, 2006.
54. Fukuda H., Chou T., “An advanced shear-lag model applicable to discontinuous fiber composites”, Journal of Alloys and Compounds, vol. 15(1), pp. 79-91, 1981.

55. Gao D., Li Z., Han, Q., Zhai Q., “Effect of ultrasonic power on microstructure and mechanical properties of AZ91 alloy”, Materials Science and Engineering A, vol. 502(1), pp.2-5, (2009).
56. Genma Y., Tsunekawa Y., Okumiya M., Mohri N., “Incorporation of alumina particles with different shapes and sizes ingot molten aluminum alloy by melt stirring with ultrasonic vibration”, Materials Transactions, JIM, vol.38(3), pp.232-239, (1997).
57. Goel D., Shukla D., Pandey P., “Effect of vibration during solidification on GR in Aluminium alloys”. Trans. Indian Inst. of Met., vol. 33(3), pp. 196–199, (1980).
58. Guang H., Xiangfa L., “Duplex nucleation in Mg–Al–Zn–Mn alloys with carbon inoculation”, Journal of Alloys and Compounds, vol. 487(1-2), pp. 194–197, 2009.
59. Guang H., Xiangfa L., Haimin D. “Grain refinement of Mg-Al based alloys by a new Al–C master alloy”, Journal of Alloys and Compounds, vol. 467(1), pp. 202-207, 2009.
60. Hai Z., Xing Y. “Review of recent studies in magnesium matrix composites”, Journal of Materials Science, vol. 39(20), pp. 6153 – 6171, 2004.
61. Hall E., “The hall-petch relationship”, Proceedings of the Physical Society B, vol. 64, pp. 747-753, 1951.
62. Han Y., Li K., Wang J., Shu D., Sun B., “Influence of high-intensity ultrasound on grain refining performance of Al-5Ti-1B master alloy on aluminium”, Materials Science and Engineering A, vol. 405, pp. 306-312, 2005.
63. Hassan S., Aponbiede O., Aigbodion V., “Precipitation hardening characteristics of Al–Si–Fe/SiC particulate composites”, Journal of alloys and Compounds, vol. 466(1), pp. 268-272, 2008.
64. Hem S. “The effect of ultrasonic vibrations on crystallization processes”, Ultrasonics, vol. 5(4), pp. 202-207, 1967.
65. Hokkirigawa K., Kato K., “An experimental and theoretical investigation of ploughing, cutting and wedge formation during abrasive wear”, Tribology International, vol. 21(1), pp.51–57, 1988.
66. Horita Z., Smith D. J., Furukawa M., Nemoto M., Valiev R., Langdon T. “An investigation of grain boundaries in submicrometer-grained Al-Mg solid solution alloys using high-resolution electron microscopy” ,Journal of Materials Research, vol. 11(8) , pp. 1880-1890, 1996.
67. Jain M., Subrahmanyam J., Ray S., “Ductile refractory metal foil reinforced MoSi2 matrix laminated composites: processing, microstructure and mechanical behaviour”

Symposium and 22nd annual General Meeting Materials Research Scoiety of India (MRSI), Advanced Materials and Processed Research Institute, Bhopal, Feb 14-16, 2011.

68. Jayamathy, M., Seshan S., Kailas S., Kumar K., Srivatsan T., “Influence of reinforcement on microstructure and mechanical response of a magnesium alloy", Current Science, vol. 87(9), pp. 1218-1231, 2004.
69. Jeong Y., Young J. “Nucleation enhancement of Al alloys by high intensity ultrasound”, Japanese Journal of Applied Physics, vol. 48(07GM14), 2009.
70. Jian X., Meek T., Han Q., “Refinement of eutectic silicon phase of aluminum A356 alloy using high-intensity ultrasonic vibration”, ScriptaMaterialia, vol. 54, pp. 893-896, 2006.
71. Jian X., Xu H., Meek T., Han Q., “Effect of power ultrasound on solidification of aluminum A356 alloy”, Materials Letters, vol. 59, pp. 190-193, 2005.
72. Jin Q., Eom J., Lim S., Park W., You B., “Grain refining mechanism of a carbon addition method in a Mg-Al magnesium alloy”, ScriptaMaterialia, vol. 49, pp.1129-1132, 2003.
73. Khakbiz M., Akhlaghi, F., “Synthesis and structural characterization of Al-B_4C nano-composite powders by mechanical alloying”, Journal of Alloys and Compounds, vol. 479(1), pp. 334-341, 2009.
74. Kim Y., Yim C., You B., “Grain refining mechanism in Mg-Al base alloys with carbon addition”, ScriptaMaterialia, vol. 57(8), pp. 691-694, 2007.
75. Kulekci M., “Magnesium and its alloys applications in automotive industry”, The International Journal of Advanced Manufacturing Technology, vol. 39, pp. 851-865, 2008.
76. Lan J., Yang Y., Li X., “Microstructure and micro hardness of SiCnano particles reinforced magnesium composites fabricated by ultrasonic method”, Materials Science and Engineering A, vol. 386, pp. 284-290, 2004.
77. Langdon T., Furukawa M., Nemoto M., Horita Z. “Using equal-channel angular pressing for refining grain size.” Jom, vol. 52(4), pp. 30-33, 2000.
78. Langdon T., Furukawa, M., Horita, Z., Nemoto, M., “Using intense plastic straining for high-strain-rate superplasticity”, Jom, vol. 50(6), pp. 41-45, 1998.

79. Laurent V., Jarry P., Regazzoni G., Apelian D., “Processing-microstructure relationships in compo cast magnesium/SiC”, Journal of Materials Science, vol. 27, pp. 4447-4459, 1992.
80. Le Pen E., Baptiste D., Hug G. “Multi-scale fatigue behaviour modelling of Al–Al_2O_3 short fibre composites”, International Journal of Fatigue, vol. 24(2), pp. 205-221, 2002.
81. Lee C., “Effect of grain size on the tensile properties of magnesium alloy”, Materials Science and Engineering A, vol. 459(1), pp. 355-360, 2007.
82. Lee Y., Dahle A., StJohn D., “The role of solute in grain refinement of magnesium”, Metallurgical and Materials Transactions A, vol. 31(11), pp. 2895-2906, 2000.
83. Li H., Sritharan T., Lam Y., Leng N., “Effects of processing parameters on the performance of Al grain refinement master alloys Al-Ti and Al-B in small ingots”, Journal of Materials Processing Technology, vol. 66, pp. 253-257, 1997.
84. Li M., Tamura T., Miwa K., “Controlling microstructures of AZ31 magnesium alloys by an electromagnetic vibration technique during solidification: From experimental observation to theoretical understanding”, Acta Materialia, vol. 55(14), pp. 4635-4643, 2007.
85. Li X., Li T., Li X., Jin J., “Study of ultrasonic melt treatment on the quality of horizontal continuously cast Al-1pct Si alloy”, Ultrasonics Sonochemistry, vol. 13, pp. 121-125, 2006.
86. Li X., Tamura T., Miwa K., “Controlling microstructures of AZ31 magnesium al loys by an electromagnetic vibration technique during solidification: from experimental observation to theoretical understanding”, Acta Materialia, vol. 55, pp. 4635-4643, 2007.
87. Lim S., Ashby M., “Overview no. 55 Wear-Mechanism maps”, ActaMetallurgica, vol. 35(1), pp. 1–24, 1987.
88. Liu S., Gaof P., Zhang Q., Zhu X., Li W., “Fabrication of carbon nano tubes reinforced AZ91D composites by ultrasonic processing” Transactions of Nonferrous Metals Society of China, vol. 20, pp. 1222−1227, 2010.
89. Liu W., Koster U., “Microstructures and properties of interpenetrating alumina/aluminium composites made by reaction of SiO_2 glass performs with molten aluminium”, Materials Science and Engineering A, vol. 210(1), pp. 1-7, 1996.

90. Liu Z., Mao W., Zhao Z., “Effect of grain refining on primary α phase in semi-solid A356 alloy prepared by low superheat pouring and slight electromagnetic stirring”, Acta Metallurgica Sinica (English Letters), vol. 21(1), pp. 57-64, 2008.
91. Luo J., Acoff V., “Processing gamma-based TiAl sheet materials by cyclic cold roll bonding and annealing of elemental titanium and aluminum foils”, Materials Science and Engineering A, vol. 433(1-2)18, pp. 334-342, 2006.
92. Ma Z., Zhao W., Yan J., Li D., “Interfacial reaction of intermetallic compounds of ultrasonic-assisted brazed joints between dissimilar alloys of Ti-6Al-4V and Al-4Cu-1Mg”, Ultrasonics Sonochemistry, vol. 18, pp. 1062-1067, 2011.
93. Mabuchi M., Kubota K., Higashi K., “Effect of hot extrusion on mechanical properties of a MgSiAl alloy”, Materials Letters, vol. 19(5-6), pp. 247-250, 1994.
94. Mabuchi M., Kubota K., Higashi K., “Tensile strength, ductility and fracture of magnesium-silicon alloys”, Journal of Materials Science, vol. 31(6), pp. 1529-1535, 1996.
95. Mahato C., shamsuzzoha M. El-Kaddah N., “Solidification morphology and structure of cast Al-Li 2090 alloy at low superheats”, TMS-2004, solidification of aluminium alloys, pp. 321-328, 2004.
96. Mason T., “Sonochemistry and sonoprocessing: the link, the trends and (probably) the future”, Ultrasonics Sonochemistry, vol. 10, pp. 175-179, 2003.
97. Matin M., Lu L., Gupta M., “Investigation of the reactions between boron and titanium compounds with magnesium”, Scripta Materialia, vol. 45(4), pp. 479-486, 2001.
98. Matsunaga T., Ogata K., Hatayama T., Shinozaki K., Yoshida M., “Formation behavior of acoustic cavitation in molten aluminum alloys under ultrasonic vibration”, Journal Japan Institute of Light Metals, vol. 56(4), pp. 214-220, 2006.
99. Meidani A., Hasan M., “A study of hydrogen bubble growth during ultrasonic degassing of Al-Cu alloy melts” Journal of Materials Processing Technology, vol. 147, pp. 311–320, 2004.
100. Metals Handbook, “Metallography, structures, and phase diagrams”, American Society for Metals, Materials Park, OH, 8th ed., vol. 8, 1973.
101. Mondal D., Das S., Suresh K., Ramakrishnan N., “Compressive deformation behavior of coarse SiC particle reinforced composite: Effect of age-hardening and SiC content”, Materials Science and Engineering A, vol. 460–461, pp. 550–560, 2007.

102. Motegi T., “Grain-refining mechanisms of superheat-treatment of and carbon addition to Mg–Al–Zn alloys”, Materials Science and Engineering A, vol. 413, pp. 408-411, 2005.

103. Nandam S., Sankaran S., Murty B., “Precipitation Kinetics in Al-Si-Mg/TiB2 In-situ Composites”, Transactions of the Indian Institute of Metals, vol. 64, pp. 123-136, 2011.

104. Nastac L., “Modeling and Simulation of Microstructure Evolution in solidifying Alloys”, Kluwer Academic Publishers, pp. 262-265, 2004.

105. Nelson C., “Grain size behavior in magnesium casting alloys”, Trans AFS, vol. 56, pp. 1-23, 1948.

106. Nguyen-thi, H., Reinhart, G., Zhou, B., Billia, B., Liu, Q., Lyubimova, T., Roux, B. “Tailoring of dendritic microstructure in solidification processing by crucible vibration”, Journal of Crystal Growth, vol. 275(1), pp. e1579-e1584, 2005.

107. Nie K., Wang X., Wu K., Zheng M., Hu X., “Effect of ultrasonic vibration and solution heat treatment on microstructures and tensile properties of AZ91 alloy”, Materials Science and Engineering A, vol. 528(25), pp. 7484-7487, 2011.

108. Nimityongskula S., Jones M., Choi H., Lakes R., Kou S., Li X., “Grain refining mechanisms in Mg-Al alloys with Al_4C_3microparticles”, Materials Science and Engineering A, vol. 527, 2104–2111, 2010.

109. Oh S., Cornie J., Russell K., “Wetting of ceramic particle with liquid aluminium alloys. Part II: study of wettability”, Metallurgical and Materials Transactions A, vol. 20, pp. 533–541, 1989.

110. Pan J., Yoshida M., Sasaki G., Fukunaga H., Fujimura H., Matsuura M., “Ultrasonic insert casting of aluminum alloy”, Scripta Materialia, vol. 43, pp. 155-159, 2000.

111. Panigrahi S., Kumar K., Kumar N., Yuan W., Mishra R., DeLorme R., Davis B., Howell R., Cho K., “Transition of deformation behavior in an ultrafine grained magnesium alloy” Materials Science and Engineering A, vol. 549, pp. 123–127, 2012.

112. Paramsothy M., Tan X., Chan J., Kwok R., Gupta M., “Al_2O_3nano particle addition to concentrated magnesium alloy AZ81: Enhanced ductility”, Journal of Alloys and Compounds, vol. 545, pp. 12-18, 2012.

113. Patel B., Chaudhari G., Bhingole P., “Microstructural evolution in ultrasonicated AS41 magnesium alloy”, Materials Letters, vol. 66, pp. 335-338, 2012.

114. Peijie L., Nikitin V., Kandalova E., Nikitin K. “Effect of melt overheating, cooling and solidification rates on Al–16 wt.pct Si alloy structure”, Materials Science and Engineering A, vol. 332(1), pp. 371-374, 2002.

115. Petch N. “Clevage strength of polycrystals”, Journal of Iron Physics Society,Series B, vol. 64, 1951.

116. Polmear I. “Light Alloys: From Traditional Alloys to Nano crystals”, 4th ed., Elsevier/Butterworth-Heinemann, Oxford, U.K., 2006.

117. Puga H., Joaquim B., Seabra E., Ribeiro S., Prokic M., “The influence of processing parameters on the ultrasonic degassing of molten $AlSi_9Cu_3$ aluminium alloy”, Materials Letters, vol. 63(9), pp. 806-808, 2009.

118. Qian M, Peng C., “Discussions on grain refinement of magnesium alloys by carbon inoculation”, Scripta Materialia, vol. 52(5), pp. 415-419, 2005.

119. Qian M., Cao P., Easton M., McDonald S., StJohn, D., “An analytical model for constitutional supercooling-driven grain formation and grain size prediction”, Acta Materialia, vol. 58(9), pp. 3262-3270, 2010.

120. Ramirez A., Qian M., Davis B., Wilks T., StJohn D. “Potency of high-intensity ultrasonic treatment for grain refinement of magnesium alloys” Scripta Materialia, vol. 59(1), pp. 19-22, 2008.

121. Ramirez A., Qian M., Davis B., Wilks T., StJohn D., “Potency of high-intensity ultrasonic treatment for grain refinement of magnesium alloys”, Scripta Materialia vol. 59, pp. 19-22, 2008.

122. Rao Y., “Stoichiometry and thermodynamics of metallurgical processes”, Cambridge University Press, 2009.

123. Reddy G., Sekhar J., “Microstructure refinement with forced convection in aluminium and super alloys”, J. Materials Science, vol. 20, pp. 3535-3544, 1985.

124. Reddy G., Sekhar J., “Moderate pressure solidification: undercooling at moderate cooling rates”, Acta Metallurgica, vol. 37(5), pp. 1509-1519, 1989.

125. Renger K., Simon R., Proceedings of first international light metals technology conference 2003, (Brisbane, Australia):CAST Centre Pvt Ltd, pp. 231, 2003.

126. Rocher J., Quenisset J., Naslain R., “Wetting improvement of carbon or silicon carbide by aluminium alloys based on a K_2ZrF_6 surface treatment: application to composite material casting”, Journal of Materials Science, vol. 24(8), pp. 2697-2703, 1989.

127. Roy D., Basu B., Basu M., Manoj Kumar B., Ghosh S., "Understanding the unlubricated friction and wear behavior of Fe-aluminide reinforced Al-based in-situ metal–matrix composite", Composites Part A: Applied Science and Manufacturing, vol. 37(9), pp. 1464–1472, 2006.
128. Saito Y., Utsunomiya H., Tsuji N., Sakai T., "Novel ultra-high straining process for bulk materials-development of the accumulative roll-bonding (ARB) process", Acta Materialia, vol. 47(2), pp. 579-583, 1999.
129. Sarkar S., Banerjee M., Seal A., "Effect of vibration on the solidification of copper-tin alloys", Transactions of the Indian Institute of Metals, vol. 38(2), pp. 139-146, 1985.
130. Shukla D., Pandey P., Goel D., "Effect of vibration on the formation of porosity in aluminum alloy ingots", Metallurgical and Materials Transactions B, vol. 11B (1),pp. 166-168, 1980.
131. Shu-sen, Gu-zhong, Li-wan, Ping-an, You-mu M., "Microstructure and properties of rheo-diecast Al-20Si-2Cu-1Ni-0.4 Mg alloy with direct ultrasonic vibration process" Transactions of Nonferrous Metals Society of China, vol. 20, pp. s763-s767, 2010.
132. Sreekumar V., Pillai R., Pai B., Chakraborty M., "A study on the thermodynamics of in situ $MgAl_2O_4$/Al MMC formation using amorphous silica sources", Journal of Materials Processing Technology, vol. 192-193,pp. 588−594, 2007.
133. StJohn D., Qian M., Easton, M., Cao P., Hildebrand Z., "Grain refinement of magnesium alloys", Metallurgical and Materials Transactions A, vol. 36(7), pp. 1669-1679, 2005.
134. Su H., Gao W., Feng Z., Lu Z., "Processing, microstructure and tensile properties of nano-sized Al_2O_3 particle reinforced aluminium matrix composites", Materials and Design, vol. 36, pp. 590-596, 2012.
135. Suslick K., Price G., "Applications of ultrasound to materials chemistry", Annual Review of Materials Science, vol. 29 pp. 295-326, 1999.
136. Swallowe G., Field J., Rees C., Duckworth A., "A photographic study of the effect of ultrasound on solidification", Acta Materialia, vol.37(3), pp. 961-967, 1989.
137. Tiner N., "Superheating of magnesium alloys", Transactions of the American Institute of Mining, Metallurgical and Petroleum Engineers, vol. 161, pp. 242-264, 1945.
138. Tsunekawa Y., Suzuki H., Genma Y., "Application of ultrasonic vibration to in situ MMC process by electromagnetic melt stirring", Materials and Design, vol. 22, pp. 467-472, 2001.

139. Tyagi R., Nath S., Ray S., “Modelling of dry sliding oxidation modified wear in two phase materials”, Wear, vol. 255, pp.327-332, 2003.

140. Valiev R., Islamgaliev R., Alexandrov I., “Bulk nano structured materials from severe plastic deformation”, Progress in Materials Science, vol. 45(2), pp. 103-189, 2000.

141. Valiev R., Krasilnikov N., Tsenev N., “Plastic deformation of alloys with submicron-grained structure”, Materials Science and Engineering A, vol. 137, pp. 35-40, 1991.

142. Wang X., Jha A., Brydson R., “In situ fabrication of Al_3Ti particle reinforced aluminium alloy metal–matrix composites”, Materials Science and Engineering A, vol. 364(1–2), pp. 339–345, 2004.

143. Wood R., “The Foundryman”, pp. 98-99 and 256-61, 1953.

144. Xu H., Jian X., Meek T., Han Q., “Degassing of molten aluminum A356 alloy using ultrasonic vibration”, Materials Letters, vol. 58(29), pp. 3669-3673, 2004.

145. Yamada K., Takahashi T., Motoyama M. “EPMA state analysis of formation of TiC during mechanical alloying of Mg, Ti and graphite powder mixture”, Nippon Kinzoku Gakkaishi/Journal of the Japan Institute of Metals, vol. 60(1), pp. 100-105, 1996.

146. Yang Y., Lan J., Li X., “Study on bulk aluminum matrix nano-composite fabricated by ultrasonic dispersion of nano-sized SiC particles in molten aluminum alloy”, Materials Science and Engineering A, vol. A380(1-2), pp. 378-383, 2004.

147. Yang Z., Wang S., Gao M., Zhao Y., Chen K., Cui X., “A new-developed magnesium matrix composite by reactive sintering”, Composites Part A: Applied Science and Manufacturing, vol. 39(9), pp. 1427–1432, 2008.

148. Yano E., Yousuke T., Motegi T., Sato E., “Effect of carbon powder on grain refinement of an AZ91E magnesium alloy”, Materials Transactions (Japan), vol. 44(1), pp. 107-110, 2003.

149. YanoE., Tamura Y., Motegi T., Sato E.“Grain refining mechanism of cast magnesium alloy AZ91 by superheat treatment” Journal-Japan Institute of Light Metals, vol. 51(11), pp. 594-598, 2001.

150. Yao J., Li W., Zhang L., Wang F., Xue M., Jiang H., Lu J., “Wear mechanism for in situ TiC particle reinforced AZ91 magnesium matrix composites”, Tribology Letters, vol. 38(3), pp. 253-257, 2010.

151. Ye H., Liu X., “Review of recent studies in magnesium matrix composites”, Journal of Materials Science, vol. 39(20), pp. 6153-6171, 2004.

152. Ye H., Liu X., Luan B., “In situ synthesis of AlN in Mg-Al alloys by liquid nitridation”, Journal of Materials Processing Technology, vol. 166(1), pp. 79-85, 2005.
153. Yoshikazu G., Tsunekawa, Y., Okumiya, M., Mohri, N., “Incorporation of alumina particles with different shapes and sizes into molten aluminum alloy by melt stirring with ultrasonic vibration”, Materials Transactions-JIM, vol. 38(3), pp. 232-239, 1997.
154. Yu Z., Zhao N., Liu E., Shi C., Du X., Wang J., “Fabrication of aluminum matrix composites with enhanced mechanical properties reinforced by in situ generated $MgAl_2O_4$ whiskers” Composites Part A: Applied Science and Manufacturing, vol. 43(4), pp. 631–634, 2012.
155. Zhang F., Wang R., He X., Wang C., Ren L., “Interfacial shearing strength and reinforcing mechanisms of an epoxy composite reinforced using a carbon nanotube/carbon fiber hybrid”, Journal of Materials Science, vol. 44(13), pp. 3574-3577, 2009.
156. Zhang R., Acoff V., “Processing sheet materials by accumulative roll bonding and reaction annealing from Al/Nb elemental foils”, Materials Science and Engineering: A vol. 463(1-2) 37, pp. 67-73, 2007.
157. Zhang S., Zhao Y., Chen G., “In situ (Mg_2Si+ MgO)/Mg composites fabricated from AZ91-$Al_2(SiO_3)_3$ with assistance of high-energy ultrasonic field”, Transactions of Nonferrous Metals Society of China, vol. 20(11), pp. 2096-2099, 2010.
158. Zhang X., Liao L., Ma N., Wang H., “Mechanical properties and damping capacity of magnesium matrix composites”, Composites Part A: Applied Science and Manufacturing, vol. 37(11), pp. 2011–2016, 2006.
159. Zhao H., Zhou Z., Liu X., Guan S., “ Influence of Mg_3N_2 powder on microstructures and mechanical properties of AZ31 Mg alloy”, Journal of Central South University of Technology, vol. 15(4), pp. 459-462, 2008.
160. Zhi H., Xing y., “Review of recent studies in magnesium matrix composites” Journal of Materials Science, vol. 39(20), pp. 6153-6171, 2004.
161. Zhiqiang Z., Le Q., “Effect of high-intensity ultrasonic on solidification structure of Mg-Ca alloy”, Rare Metal Materials and Engineering, vol. 37(3), pp. 436-439, 2008B.
162. Zhiqiang Z., Le Q., “Influence of ultrasonic treatment on the morphology in $Mg_{17}Al_{12}$ of Mg-9Al binary magnesium alloy”, Rare Metal Materials and Engineering, vol. 37(1), pp. 173-175, 2008A.

163. Zhong G., Wu S., Jiang H., An P., " Effects of ultrasonic vibration on the iron-containing intermetallic compounds of high silicon aluminum alloy with 2% Fe" Journal of Alloys and Compounds, vol. 492(1), pp. 482-487, 2010.